The effect of surface modifications on the statics and dynamics of colloidal particles near a flat wall studied by scattering techniques based on evanescent wave illumination

Inaugural thesis presented to the Faculty of Mathematics and Natural Sciences

of Heinrich Heine University Düsseldorf

for the degree of

Doctor of Natural Sciences

by

José Alejandro Rivera Morán

from San Luis Potosi, Mexico

Düsseldorf, January 2026

From the Institute of Biological Information Processing, Biomolecular Systems and Processes (IBI-4) of Forschungszentrum Jülich GmbH.

Printed by permission of the Faculty of Mathematics and Natural Sciences of Heinrich Heine University Düsseldorf

Examiners:

1. Prof. Dr. Peter R. Lang

2. Prof. Dr. Jan K.G. Dhont

Date of the oral defence: 09 April 2026

Statutory Declaration

I declare under oath that I have produced my thesis independently and without any undue assistance by third parties under consideration of the 'Principles for the Safeguarding of Good Scientific Practice at Heinrich Heine University Düsseldorf, in accordance with *PromotionsOrdung* (15.06.2018) § 5 section 1b.

Additionally, this dissertation, in the form presented here or in a similar form, has not been submitted to any other institution nor faculty. Also, I have not previously made any unsuccessful attempts to obtain a doctorate.

_____

José Alejandro Rivera Morán

Included Publication

Part of this thesis has already been published in an international journal. Below, the related publication and my specific contributions are outlined. The content reproduced and adaptations, used in Subchapters 3.1 and 4.1, have been cited accordingly.

Publication: “The effect of morphology and particle-wall interaction on colloidal near-wall dynamics”.

> J. Alejandro Rivera-Morán, Yi Liu, Samuel Monter, Chiao-Peng Hsu, Pia Ruckdeschel, Markus Retsch, Maciej Lisicki and Peter R. Lang. *Soft Matter*, 2021, **17**, 10301-10311.
>
> Contribution: I performed all the experiments and data analyses for the colloidal systems described therein, excluding those regarding the hollow silica particles (Dr. Yi Liu). The experimental work was supported through discussions with Prof. Dr. Peter. R. Lang. I contributed to the review and editing of the original manuscript drafted by Prof. Dr. Peter. R. Lang.

Supervisor confirmation

In accordance with PromotionsOrdung (15.06.2018) § 6 section 3, I, Prof. Dr. Peter Lang, confirm that the doctoral researcher José Alejandro Rivera Morán contributed as indicated to the aforementioned publication and that some parts and adaptation are included in this thesis.

_____

Prof. Dr. Peter Lang

Abstract

The study of colloidal particles near interfaces has been pursued for decades due to its relevance across industrial applications and the natural sciences. Physical descriptions of particles near rigid interfaces (referred as walls) reveal that the dominant interactions arise from hydrodynamic effects and static interaction energies. The current theories describing particles in the vicinity of walls often lies on the ideal assumption of perfectly smooth surfaces. Although classical hydrodynamic and colloidal interaction models provide a robust framework for describing particle motion near smooth, hard walls, real systems exhibit some degree of surface heterogeneity, which in some drastic cases might differ from these assumptions. In this thesis, the static and dynamic behavior of colloidal particles with surface characteristics different from the ideal particles are measured at interfaces through highly sensitive experimental techniques.

In the first part of this contribution, the investigation of the near-wall dynamics of particles with different surface morphology is presented. By performing Evanescent Wave Dynamic Light Scattering experiments, the near-wall dynamics of silica particles having smooth and rough surface, as well as porous shells, were determined. The dynamics of smooth particles differ slightly from the prediction for hard spheres dynamics, whereas rough particles exhibit a significant slowdown compared to the model and opposite to the enhanced dynamics expected by hydrodynamic theory. Complementary numerical calculations for near-wall dynamics, accounting for polydispersity, aggregation and particle-wall static interactions, suggest that surface roughness of the particles modifies the particle-wall static interaction overcoming the hydrodynamic effects and impacting their diffusion.

In the second part, the static and dynamic properties of particle-wall systems with modified surfaces that may affect their interactions with the wall are presented, which include walls with hydrophobic properties and protein-coated particles. Through experiments based on Total Internal Reflection Microscopy, the interaction potential profiles and dynamic properties are measured at the single-particle level. The potential profiles of bare systems compared to hydrophobically coated wall do not show a notable difference except for the electrostatic amplitude, while the dynamic properties are not significantly affected by the coating. However, for both types of systems, the diffusion perpendicular to

the wall exhibit increased dynamics compared to no-slip boundary conditions due partial slip. On the other side, protein-coated particles display similar potential profiles and slight decrease in electrostatic amplitudes. Similarly, the normal diffusion shows some increase compared to dynamics with no-slip boundary conditions.

Additionally, the influence of unavoidable experimental noise effects on experimental results for both static and dynamic properties is addressed. While background noise can be reduced to a negligible contribution, the detector shot noise affects the most to the measured interaction potentials, mostly in the steep parts of the profile. Also, such errors do not affect drastically the calculation of the dynamic properties. However, it is also identified that sampling time determines the quality of the measured properties, where too long sampling times compromise the reliability of both static and dynamic properties at short separation distances.

Zusammenfassung

Die Untersuchung von kolloidalen Partikeln in der Nähe von Grenzflächen wird aufgrund ihrer Relevanz für industrielle Anwendungen und die Naturwissenschaften seit Jahrzehnten betrieben. Physikalische Beschreibungen von Partikeln in der Nähe von starren Grenzflächen (als Wände bezeichnet) zeigen, dass die dominierenden Wechselwirkungen aus hydrodynamischen Effekten und statischen Wechselwirkungsenergien resultieren. Die gängigen Theorien, die Partikel in der Nähe von Wänden beschreiben, basieren meist auf der idealisierenden Annahme vollkommen glatter Oberflächen. Während klassische hydrodynamische und kolloidale Wechselwirkungsmodelle einen robusten Rahmen für die Beschreibung der Partikelbewegung in der Nähe glatter, harter Wände bieten, weisen reale Systeme ein gewisses Maß an Oberflächenheterogenität auf, die in einigen drastischen Fällen von diesen Annahmen abweichen kann. In dieser Dissertation Beitrag wird das statische und dynamische Verhalten von kolloidalen Partikeln mit Oberflächeneigenschaften, die sich von idealen Partikeln unterscheiden, an Grenzflächen mit hochsensiblen experimentellen Techniken untersucht.

Im ersten Teil dieses Beitrags wird die Untersuchung der Wand-nahen Dynamik von Partikeln mit unterschiedlicher Oberflächenmorphologie dargestellt. Mittels dynamischer Lichtstreuung mit evaneszenter Beleuchtung wurde die Wand-nahe Dynamik von Silicapartikeln mit glatter und rauer Oberfläche sowie von porösen Silica-Kugelschallen bestimmt. Die Dynamik glatter Partikel weicht geringfügig von der Vorhersage für die Dynamik harter Kugeln ab, während raue Partikel im Vergleich zum Modell eine deutliche Verlangsamung aufweisen, was im Gegensatz zu hydrodynamischen Theorien steh nach der eine Zunahme der Dynamik erwartet wird. Ergänzende numerische Berechnungen für die Wand-nahe Dynamik, die Polydispersität, Aggregation und statische Wechselwirkungen zwischen Partikeln und Wänden berücksichtigen, deuten darauf hin, dass die Oberflächenrauhigkeit der Partikel die statische Wechselwirkung zwischen Partikeln und Wänden modifiziert, wodurch die hydrodynamischen Effekte überkompensiert werden und ihre Diffusion beeinflusst wird.

Im zweiten Teil werden die statischen und dynamischen Eigenschaften von Partikel-Wand-Systemen mit modifizierten Oberflächen bestimmt, darunter Wände mit hydrophoben Eigenschaften und

proteinbeschichtete Partikel. Mittels der Totalreflexionsmikroskopie werden die Wechselwirkungspotentialprofile und dynamischen Eigenschaften auf Einzelpartikelebene gemessen. Die Potentialprofile von unbeschichteten Systemen im Vergleich zu hydrophob beschichteten Wänden zeigen keinen nennenswerten Unterschied, außer in der elektrostatischen Amplitude. Die dynamischen Eigenschaften werden nicht wesentlich von der Beschichtung beeinflusst werden. Jedoch zeigt in beiden Fällen die Diffusion senkrecht zur Wand aufgrund teilweisen Schlupfs eine erhöhte Dynamik im Vergleich zu schlupffreien Randbedingungen. Auf der anderen Seite weisen proteinbeschichtete Partikel, im Vergleich zu unbeschichteten, ähnliche Potenzialprofile und eine leichte Abnahme der elektrostatischen Amplituden auf. In ähnlicher Weise zeigt die senkrechte Diffusion einen gewissen Anstieg im Vergleich zur Dynamik unter schlupffreien Randbedingungen.

Zusätzlich wird der Einfluss unvermeidbarer experimenteller Rauscheffekte auf die Messung der statischen und dynamischen Eigenschaften behandelt. Während das Hintergrundrauschen auf einen vernachlässigbaren Beitrag reduziert werden kann, wirkt sich das sogenannte Detektor-Schrotrauschen am stärksten auf das gemessene Wechselwirkungspotential aus, vor allem in den steilen Teilen des Profils. Allerdings haben solche Fehler keinen drastischen Einfluss auf die Berechnung der dynamischen Eigenschaften. Es wird jedoch auch festgestellt, dass die Abtastzeit die Qualität der gemessenen Eigenschaften bestimmt, wobei zu lange Abtastzeiten die Zuverlässigkeit sowohl der statischen als auch der dynamischen Eigenschaften bei kurzen Abständen beeinträchtigen.

Contents

1 Introduction

1.1 Background

Many everyday products, from foods, personal-care goods, to paints and lubricants are just a few examples which illustrate the relevance of the broad area of colloidal science. In addition, numerous biological substances fall into this category, for example, blood and proteins suspended in aqueous media are described as colloidal systems. In general, a colloidal system consists of particles ranging from some a few nanometers to several micrometers in size, dispersed in a continuum medium. Here in this work, the attention is focused particularly on solid particles suspended in aqueous solutions, which are commonly referred to as colloidal suspensions. The solid spherical particles are referred to as colloidal particles or colloids in short.

For such small particles, at low Reynolds numbers, local hydrodynamics applies, where viscous forces exerted by surrounding fluid onto the colloids dominate over inertial forces. The motion of colloidal particles is governed by Brownian forces, direct forces (e.g. due to charges carried by the colloids and mutually excluded-volume interactions), as well as hydrodynamic interactions mediated by the fluid in which the colloids are suspended. Far from confining boundaries and for sufficiently low colloid concentrations for which interparticle interactions can be neglected, the particles undergo “free” diffusion, characterized by isotropic motion. However, when colloids approach the boundary of a flat solid surface (in the following called the wall), their motion is altered by hydrodynamic interactions with the wall. The resulting wall-drag effect reduces particle mobility as the separation distance to the wall decreases and leads to directionally anisotropic diffusion [28, 37].

Furthermore, direct, static interactions play a fundamental role in determining whether or not particles stick to the wall and having a direct impact on the particles’ near-wall dynamics. In most cases, the main particle-wall static interactions arise from the combination of van der Waals attraction and screened electrostatic repulsion, which together constitute the basis of DLVO theory (named after Derjaguin, Landau, Verwey and Overbeek). The availability of analytical expressions for these

interactions in different particle-wall geometries has enabled the description of many phenomena at elevated concentrations encountered in colloidal systems.

Over the past decades, there have been developments on experimental techniques which allow the measurements of forces and energies of colloidal systems at the interface. Particularly, scattering methods based on the evanescent-wave illumination have been used to study the colloidal dynamics near interfaces [2, 32, 33, 36, 56, 60–62, 64–66, 81] and particle-wall interactions [7, 8, 29, 70, 71, 89, 92] from a fundamental point of view. Due to the distance-dependent strength of the evanescent field, both Evanescent Wave Dynamics Light Scattering (EWDLS) and Total Internal Reflection Microscopy (TIRM) offer great sensitivity in detecting femto-Newton forces and nanometric elevations that characterize colloidal behavior at interfaces.

Examples of applications of particle-wall systems studied using evanescent-wave scattering techniques span a wide range of interactions [98], including those involving copolymers adsorbed on particle and wall surfaces [69], protein-coated particles interacting with polymer brush layers [26, 95], depletion forces [34, 35, 45, 46, 49, 50], and interactions occurring near “soft” interfaces that combine biomolecules [16, 25, 84, 93, 94]. While modern video microscopy systems with evanescent wave illumination can measure the motion of large particles with sampling times on the order of milliseconds, light scattering methods have shown to measure particle systems with sub-millisecond resolution [10, 19, 20, 27, 56]. This provides great versatility for measuring a wide range of particle systems with sizes ranging from the nanoscale to the microscale.

However, unlike the idealized model particles assumed in most of the colloidal theory, real colloidal particles are not perfectly smooth but rather exhibit different degrees of roughness. Frequently, this characteristic has been partially ignored, particularly when the macroscopic behavior of the suspension still aligns with the expectations. Since the theory describing particles near walls are based on the assumption of perfectly smooth and spherical shape, the experimental static and dynamic data may be misinterpreted if the particles exhibit rough or irregular surfaces. Therefore, it is of interest to investigate whether such particles follow or deviate from the standard theoretical framework used for smooth particles.

Clear evidence of the implication of particle morphology has been observed in rheological studies, where suspensions of rough particles show shear thickening to be discontinuous and shifted towards lower volume fractions compared to suspensions of smooth particles [40]. This finding reflects the

difference in the static interactions occurring between colloids with different surface characteristics. Simulation studies in this regard support this view [9, 82, 83] upon finding that particles with asperities (rough surface) near a wall experience a distinguishable reduction in the electrostatic stabilization barrier. In addition, due to the reduction in the flow resistance on the rough surfaces which evokes a smaller effective hydrodynamic radius, an increase of near-wall diffusion of rough particles is predicted. However, experimental evidence showcasing the implications of roughness on the near-wall dynamics was still missing until recently [75].

On the other hand, the heterogeneity on particle surfaces has promising applications in biological systems, particularly when mimicking the irregular shapes of proteins and the rugosity of bio-membranes. As a case of relevance, streptavidin binding biotin proteins form one of the strongest known non-covalent bonds and become one of the most useful tools in molecular biology research. Thus, understanding how streptavidin interacts with model membranes is of fundamental interest. Although emerging investigations around the topic of macromolecules in soft matter, the inherent complexity of specific and non-specific biomolecular interactions makes it difficult to derive a unified framework for their description. Nonetheless, gaining experimental evidence is essential for continuing improving on understanding biomolecules at interfaces.

To that end, a variety of membrane-mimicking systems, ranging from single-lipid to mixed phospholipids-cholesterol compositions, have been developed such as liposomes (giant/small unillamelar vesicles), Langmuir films and supported lipid bilayers (SLBs). Particularly, as SLBs are flat phospholipid membranes, they are suitable for studies using scattering techniques based on evanescent wave illumination. Such techniques have already been applied to biologically relevant systems [16, 26, 55, 84, 100], and coated particles carrying biomolecules, which give a first approximation for probing intermolecular forces.

1.2 Motivation

As introduced above, investigations of colloidal particles with complex surface morphologies near interfaces are relatively limited, since theoretical descriptions have been developed for ideally smooth spheres. Thus, there is a gap which is being ignored in understanding the implications of how surface morphologies and modifications influence the behavior of colloidal particles near the wall.

With the recent development of methodologies for synthesizing colloidal particles with controlled asperity [38, 39, 99], the experimental investigation of the implications of roughness on the near-wall dynamics had become possible just recently. Hence, the scientific contribution in this thesis tests the applicability of conventional theory of particles near a wall but involving rough particles in the vicinity of the wall, since according to hydrodynamics, such particles are predicted to exhibit faster diffusion due to reduced flow resistance on their surfaces, evoking a particle with an effective smaller hydrodynamic radius. Addressing this gap is essential for assessing the limits of hydrodynamic models developed for smooth particles and for identifying cases where roughness fundamentally alters the dynamics.

Ultimately, this work contributes to advancing the field of colloids at interfaces by testing the boundaries of classical hydrodynamic descriptions and highlighting the role of surface morphology in near-wall dynamics. These findings become significant in colloidal dispersions because small-scale interactions critically determine macroscopic behavior. By understanding the implication of roughness in near-wall dynamics is key to providing insights that can be of relevant use in fields ranging from materials design to nanofluidics [51].

Beyond the fundamental interest of roughness on particles near an interface, which can be regarded as a specific type of surface modification, an equally important motivation lies in exploring other forms of particle and wall modifications, such as biologic systems. These systems may provide complementary perspectives on how interfacial chemistry and surface functionality influence particle dynamics near boundaries.

As many critical biological processes occur at or near membrane interfaces, the understanding of particle-membrane interactions and dynamics complement biological descriptions by identifying the underlying physical parameters that govern biological phenomena. Then, the knowledge of the physics around membranes enables the design and efficiency of drug delivery systems, particularly those relying on encapsulation or targeted delivery to cells. On the route to this goal, the use of knowledge developed in the area of soft matter physics for the study of biological membrane-like models provides a suitable approximation under a controlled physical framework. Thus, experimental evidence of the effect of surface modifications, together with established methodologies could be helpful in studying biological systems near interfaces.

Research in this topic is in constant growth [24–26], with e.g. new frameworks for describing brush-like systems being developed [22]. However, due to the non-specific nature of many biomolecular interactions, further experiments are required to better understand the broad spectrum of interactions among biomolecules. While biomolecular model systems combining liposomal particles with streptavidin proteins have been studied at the membrane structure level[63], direct measurements on the static and dynamic properties of proteins with model membranes are still missing. Then, as a second objective within this thesis, the implications of modified surfaces oriented towards biomolecules are addressed. In particular, it is explored how surface coatings on both particles and walls alter interaction potentials and near-wall dynamics based on the framework developed for particle-wall system studied by TIRM.

As a spin-off during this work, the study of sources of error inherent in TIRM, such as background and shot noise [17], that affect experimental measurements is addressed. Although background noise has been studied and is often omitted through signal correction [67], the combined effect of background and shot noise on the measured interaction potentials and dynamic properties remained poorly understood until recently [17, 74]. Then, a systematic exploration of these effects is therefore needed to improve the accuracy and reliability of TIRM analysis.

Finally, since the relevance of this research topic extends to its connection with biomembrane models, supported lipid bilayers (SLBs) represent a natural system to study using scattering techniques based on evanescent wave illumination. As SLBs are themselves surface coatings on flat substrates, their integration into sample cells used in TIRM is relatively straightforward, providing a direct means to study near-membrane physical properties. Hence, the implementation of this methodology in TIRM is presented at the end of this thesis.

The findings presented in the following are important because particles with nonclassical surface morphologies or modification, such as bare, hydrophobic, or protein-coated surfaces, exhibit static and dynamic properties that deviate notably from conventional expectations in the near-wall landscape. Also, these studies contribute with methodological insights into TIRM, emphasizing key parameters that must be carefully considered before experiments. Altogether, these contributions highlight the importance of systematically investigating colloidal interactions and dynamics near interfaces. Beyond their fundamental relevance in soft matter physics, particle-surface interactions are directly linked to processes occurring in material science, biology, and nanotechnology. For instance, they play a key role

in the stability of colloidal formulations, the controlled assembly of nanomaterials, the adhesion of proteins and cells to surfaces, and the design of functional membranes. These implications of systems with different surface characteristics make the basis for the present thesis, which aims to assess the limitations of theoretical models through experimental evidence complemented with numerical calculations and simulations of particle-wall systems. In the following section, the scope of the work is given as well as the outline.

1.3 Scope of the thesis

In this thesis, the investigation of the influence of particle-wall surface characteristics on the interaction potentials and dynamics, as compared to smooth surfaces, is presented. Here, two research studies are examined: (i) colloidal particles with controlled surface roughness interacting with hard and smooth walls, and (ii) systems where particles and walls are modified through hydrophobic coating and protein layers. These studies employ scattering techniques based on evanescent wave illumination, such as Evanescent Wave Dynamic Light Scattering (EWDLS) and Total Internal Reflection Microscopy (TIRM), and both are supported by numerical model calculations and simulations.

In the first part of the thesis, the effect of surface morphological characteristics of the particles is presented. There, the conventional theoretical framework of hydrodynamics near a hard smooth interface is tested in order to see the extent of applicability of the theory on particles with high degree of roughness. In particular, the parallel near-wall dynamics of particles with different surface morphology are measured using Evanescent Wave Dynamic Light Scattering and the experimental investigations are complemented by numerical model calculations.

In the second part of this thesis, the study on the effect of particle-wall surface modifications, which affect the particle-wall interactions, is presented. Here, the influence of surface characteristics is examined by measuring the particles' near-wall static and dynamic properties by means of the TIRM. To identify subtle distortions in the interaction potential profiles, the sources of noise are addressed by the implementation of Brownian dynamic simulations to identify the extent of their influence. The methodology developed here opens the way for exploring biomimetic systems such as particles interacting with SLBs.

Together, both studies contribute to the understanding of more realistic conditions in colloidal systems near the hard interfaces under non-idealized conditions. Although these systems may appear simple, the results highlight that not all experimental systems behave according to standard theoretical approaches, pointing out the need of complementary approaches and considerations to describe the experimental findings.

The structure of this thesis is the following. In Chapter 2, the fundamental theories that govern the interactions in macromolecular systems are presented. The van der Waals interaction together with the electrostatic interaction are presented in terms of the particle-wall systems, providing the foundations necessary to apply them directly to experimental methodologies. Then, the particles' near-wall dynamics is presented for both, stick and partial slip boundary conditions. Furthermore, the physical-mathematical approach that sustains the calculation for single particle dynamics near the wall measured in TIRM is shown.

Next in Chapter 3, the experimental techniques of evanescent wave dynamic light scattering (EWDLS) and total internal reflection microscopy (TIRM), used to investigate the colloidal systems, are presented along with the approaches used for data analysis. In a dedicated subsection, the noise present in TIRM experiments and how it is addressed is presented. The preparation of the samples, characterization and implementation of each methodology are also detailed.

Later in Chapter 4, the results together with the respective discussions and conclusions corresponding for each part are presented. Starting with the effect of particle morphology on particle-wall interaction and dynamics. Here, the results from EWDLS experiments on silica particles with different surface morphology are shown. The interpretation of the experiments is complemented with numerical calculations that account for particle shape, polydispersity, aggregation and static interactions. Systematically evaluating how each factor affects the resulting near-wall dynamics leads to the calculation of dynamics that resembles the experimental findings and revealing the major component influencing the near-wall dynamics.

In the second part of Chapter 4, the results of the effect of the particle-wall surface modifications on the static and dynamic properties, investigated by TIRM, are shown. Additionally, at the simulation level, the effect of noise sources on particles' near-wall static and dynamic properties are presented. Also, the influence of sampling time on the measurements and analysis is discussed.

Lastly, for the purpose of documenting the protocols on the topic of SLBs, the methodology and descriptive phenomenological results are briefly presented in the Supporting Information section. The protocol developed for creating SLBs using Langmuir-Blodgett and Langmuir-Schaffer techniques is described. Finally, the non-conclusive TIRM results obtained from SLB systems are presented.

2 Theoretical foundations

2.1 Static particle-wall interactions

In this section, the most relevant particle-wall interactions are introduced, forming the theoretical basis and framework of this research work. Also, it guides the subsequent data analysis.

When colloidal particles approach the boundaries of a flat surface (also referred to the wall), an interaction potential arises between them. The total interaction involves attractive and repulsive forces, governing the static and dynamic properties of the particles. The main contributors to the particle behavior near a wall are presented below, providing the essential concepts for understanding the physical phenomena investigated in this work.

2.1.1 Van der Waals interaction

The van der Waals forces are short-ranged interactions (typically < 5 nm) that arise from the interaction of dipoles within molecules, which in turn, form macroscopic bodies. According to quantum mechanics, non-polar elements and molecules have a time-averaged dipole moment of zero. However, instantaneous positions of electrons relative to the protons give rise to a finite dipole moment. In turn, this instantaneous dipole yields an electric field which polarizes neighboring molecules and inducing a dipole moment in them. The interaction between these atoms and molecules results in an instantaneous attractive force between them, which the time average of such force is finite.

2.1.1.1 Van der Waals interaction according to the additivity principle

The interaction between two molecules at distance r is described by the attractive pair potential $u(r) = -C/r^6$ due to the instantaneous and temporary dipoles that are induced between neighboring molecules. To upscale the interaction to macroscopic bodies, the principle of 'additivity' is applied, whereby the total potential $U(D)$ is computed by summing the single interactions between all pairs of molecules that constitute the bodies involved:

$$U(D) = \iint -\frac{C}{r^6}\rho_1 dV_1\,\rho_2 dV_2 \qquad (2.1)$$

where D is the separation distance of the macroscopic bodies, C is a constant determined by the physical properties of the molecules such as their mass, polarizabilities and ionizations, $\rho_{1,2}$ is the molecular number density and their respective volume element $dV_{1,2}$.

Analytic expressions have been derived for the interaction energies of different two-body systems based on the additivity principle. The simplest case considers the interaction between a single molecule at a separation distance D from a semi-infinite planar surface (wall). In particular, a molecule separated by a distance D from a ring of density ρ (Figure 2.1, left panel), their interaction is obtained by summing the contributions of all individual molecular interactions involved. If the distance between the single molecule to any other molecule of the ring, with radius x and volume $2\pi x\,dx\,dz$, is $r = \left(z^2 + x^2\right)^{1/2}$, then the molecule-wall interaction potential $U_{\mathrm{MW}}(D)$ is given by:

$$\begin{aligned} U_{\mathrm{MW}}(D) &= -2\pi C\rho \int_D^\infty dz \int_0^\infty \frac{x\,dx}{\left(z^2 + x^2\right)^3} \\ &= -2\pi C\rho/12D^3 \end{aligned} \qquad (2.2)$$

By replacing the single molecule with a flat surface, the interaction energy between these two planar surfaces is calculated as follows. Because the total energy between infinite surfaces diverges to infinity, the calculation is instead performed considering the energy per unit area, i.e. over a finite portion of the surface. This sheet lies in the xy plane with radius h and thickness dz, at a distance z from the

other planar surface of the same material. The total interaction energy between the two walls is then obtained by applying the additivity principle:

$$\begin{aligned} U_{\mathrm{WW}}(D) &= \int_D^{\infty} dz \int_0^h 2\pi\rho\, x\, dx\, U_{\mathrm{MW}} \\ &= -\frac{2\pi^2 h^2 \rho^2 C}{12} \int_D^{\infty} \frac{dz}{z^3} \\ U_{\mathrm{WW/A}}(D) &= \frac{U_{\mathrm{WW}}(D)}{area} = -\frac{\pi\rho^2 C}{12D^2} \end{aligned} \qquad (2.3)$$

Since the interaction energy is of the surface-to-surface type, it is expressed per unit area $U_{\mathrm{WW/A}}$ where $area = \pi h^2$. This expression is valid when $D \ll h$.

Other relevant systems are the sphere-wall and the sphere-sphere interactions. For the sake of brevity, the main expressions for the interactions are shown while their derivation is omitted but interested readers are referred to specialized literature [31, 42, 44].

By applying the same additivity principle, the sphere-wall interaction energy is built by summing all the contributions from all molecules in a circular layer $\pi\rho(2R-z)z\,dz$ of the sphere at a distance $D+z$ from the wall (Figure 2.1, right panel). For $D \ll R$, only small values of z contribute to the integral of the sphere-wall potential $U_{\mathrm{SW}}(D)$ and yield:

$$\begin{aligned} U_{\mathrm{SW}}(D) &= -\frac{2\pi^2 C\rho^2}{12} \int_0^{2R} \frac{(2R-z)\,z\,dz}{(D+z)^3} \\ &= \pi^2 C\rho^2 R/6D \end{aligned} \qquad (2.4)$$

When the case is $D \gg R$, van der Waals interaction is described as:

$$\begin{aligned} U(D) &= -\frac{2\pi^2 C\rho^2}{12} \int_0^{2R} \frac{(2R-z)\,z\,dz}{D^3} \\ &= \frac{\pi C\rho\left(4\pi R^3\rho/3\right)}{6D^3} \end{aligned} \qquad (2.5)$$

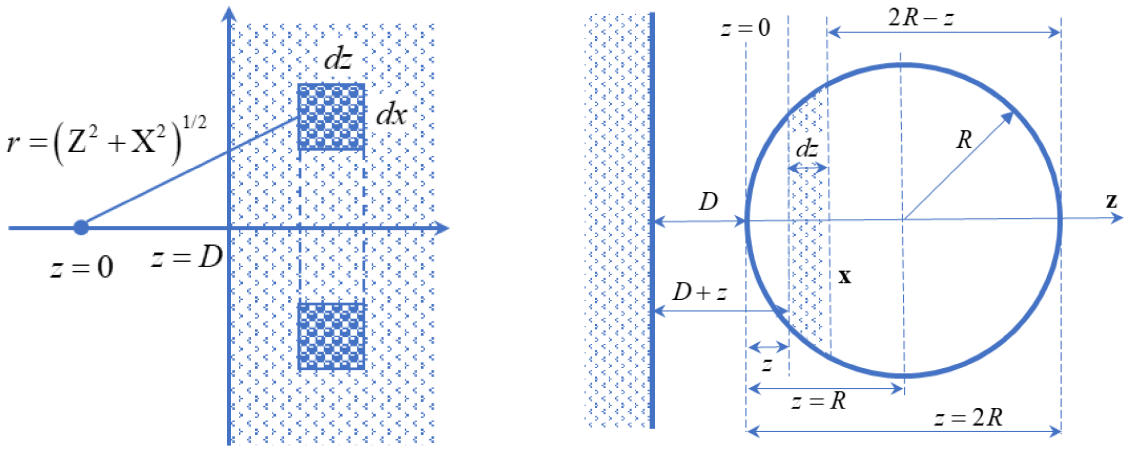

Figure 2.1. Geometric representation for calculating the interaction energy of the cases discussed in the main text. *Left*: molecule-wall interaction, shown as the cross-section of a ring with its center separated by a distance D from the molecule. *Right*: sphere-wall interaction, represented by a flat disc of a sphere near the wall. Adapted from reference [42].

2.1.1.2 Van der Waals attraction according to Hamaker

Originally, Hamaker [31] derived direct expressions, based on Eq. 2.1 for a sphere-sphere geometry, to calculate the magnitude of London-van der Waals interactions as a function of the radii and separation distance. Unlike the previous equations, Hamaker's expressions are reduced forms of the van der Waals potential derived in spherical coordinates to account for radial symmetry and are valid for both small and large separation distances.

The interaction potential between a sphere, with radius R, and separated by a distance z from a wall, is shown in Figure 2.2 left. This situation can be seen as the limiting case of the interaction between two spheres but one sphere becomes extremely large $R_i = \infty$ compared to the other sphere. In that case, the interaction between the sphere and the flat surface is given by:

$$\phi_{\mathrm{vdW}}(z) = -\frac{A_H}{6}\left[\frac{R}{z-R} + \frac{R}{z+R} + \ln\frac{z+R}{z-R}\right] \qquad (2.6)$$

where $A_H = \pi^2 C \rho_1 \rho_2$ is the Hamaker constant. Here, the notation for the interaction potential has changed to identify such expression which will be used for the calculation of the total interaction potential between a particle and a wall, as shall be described in the next chapter.

Regarding the nonretarded van der Waals interactions for the two-spheres system $U_{SS}(D)$, each sphere has a radius R_1 and R_2 respectively, and their centers are separated by a distance D as depicted in Figure 2.2 right [31]:

$$U_{SS}(D) = -\frac{A_H}{6}\left\{\frac{2R_1R_2}{D^2-(R_1+R_2)^2}+\frac{2R_1R_2}{D^2-(R_1-R_2)^2}+\ln\frac{D^2-(R_1+R_2)^2}{D^2-(R_1-R_2)^2}\right\} \qquad (2.7)$$

When the spheres are identical in radius ($R = R_1 = R_2$) and in composition ($\rho = \rho_1 = \rho_2$), Eq. 2.7 is simplified as:

$$U_{SS}(D) = -\frac{A_H}{6}\left(\frac{2R^2}{D^2-4R^2}+\frac{2R^2}{D^2}+\ln\left[1-\frac{4R^2}{D^2}\right]\right) \qquad (2.8)$$

where $A_H = \pi^2 C \rho^2$. This constant has a magnitude of $\sim 10^{-19}$ Joules (J) for interactions in vacuum, while in condensed media it is reduced $\sim 10^{-21}$ J.

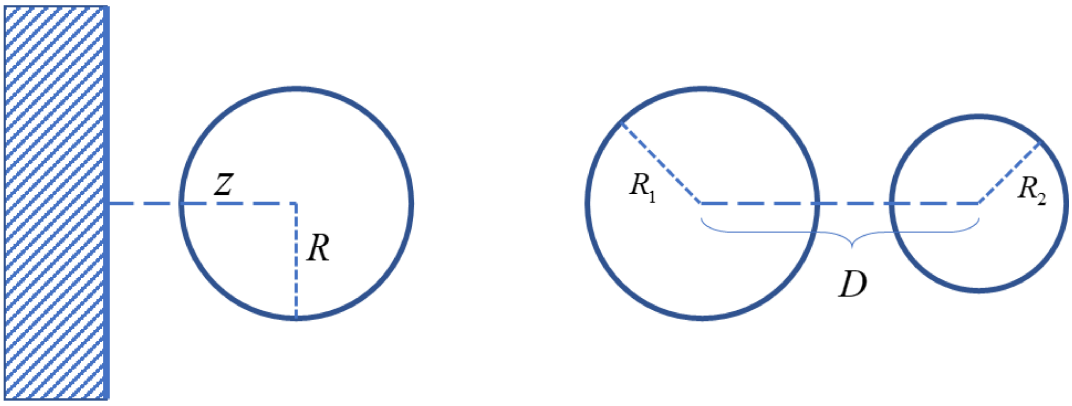

Figure 2.2. Sketches for the geometry used in the Hamaker expressions for the van der Waals interactions. *Left*: the sphere-wall system. *Right*: the two-spheres system.

In essence, the van der Waals equations presented earlier in Subsection 2.1.1.1 differ in their range of applicability in comparison with those shown here in Subsection 2.1.1.2. The first ones are valid when the separation distances are small compared to the particles size ($D \ll R$), while the latter apply when the particle size is comparable to the separation distance and are valid at all separations. For these reasons and given the particle-wall systems described in the next Subsection 3.4.1, Eq. 2.6 was selected for calculating the van der Waals potential as described later in Subsection 3.1.4.1.

2.1.1.3 Hamaker constant in the Lifshitz Continuum theory

The interaction potentials introduced above are based on pairwise additivity principle dictated by the dipole-dipole interactions. However, this approach ignores the interactions coming from neighbor molecules that are also affected by dipolar interactions. Hence, the additive principle does not account for multiple and complex interactions, e.g. macroscopic particles interacting within a medium.

In contrast, the Lifshitz theory addresses van der Waals forces between macroscopic bodies by describing them as continuous media, thus avoiding an atomic structure formalism. This approach is based on the quantum field theory where the interactions are treated as fluctuations of the electromagnetic field induced by neighboring molecules. These fluctuations are expressed in terms of the bulk dielectric properties, such as dielectric constants (ε) and refractive indexes (n). Within the Lifshitz framework, the analytical expressions for the distance dependence of the interaction energies remain unchanged, however, the Hamaker constant is calculated as a function of the dielectric properties of the interacting materials and medium.

In general, the Hamaker constant for two interacting particles with dielectric constants ε_1, ε_2 and refractive indexes n_1, n_2, respectively, both immersed in a medium with dielectric constant ε_3 and refractive index n_3, is given by the following equation, which accounts for nonretarded effects and within the framework of Lifshitz theory:

$$A_H \approx \frac{3}{4} k_B T \left(\frac{\varepsilon_1 - \varepsilon_3}{\varepsilon_1 + \varepsilon_3} \right) \left(\frac{\varepsilon_2 - \varepsilon_3}{\varepsilon_2 + \varepsilon_3} \right) + \frac{3h\nu_e}{8\sqrt{2}} \frac{\left(n_1^2 - n_3^2 \right)\left(n_2^2 - n_3^2 \right)}{\left(n_1^2 + n_3^2 \right)^{1/2} \left(n_2^2 + n_3^2 \right)^{1/2} \left\{ \left(n_1^2 + n_3^2 \right)^{1/2} + \left(n_2^2 + n_3^2 \right)^{1/2} \right\}} \quad (2.9)$$

Particularly, in the case of two identical particles of the same material interacting through a medium of different properties, the equation is reduced to simply:

$$A_H \approx \frac{3}{4} k_B T \left(\frac{\varepsilon_1 - \varepsilon_3}{\varepsilon_1 + \varepsilon_3} \right)^2 + \frac{3h\nu_e}{16\sqrt{2}} \frac{\left(n_1^2 - n_3^2 \right)^2}{\left(n_1^2 + n_3^2 \right)^{3/2}} \quad (2.10)$$

here, h is Plank's constant and ν_e the main electronic absorption frequency, which is assumed to be equal for the two material, in the range of UV/VIS electromagnetic spectrum. These equations for determining Hamaker constants are valid for the most common geometries of interacting macroscopic bodies, such as sphere-sphere, wall-wall and the wall-sphere, among others.

Additionally, the Lifshitz theory allows for a straightforward means of determining whether van der Waals interactions are attractive or repulsive. For any systems composed of two bodies with identical dielectric properties, the van der Waals interaction is always attractive when in vacuum. However, when a continuum medium is introduced, with dielectric properties n_3, its characteristics determine whether the van der Waals interaction is attractive or repulsive. Repulsion occurs when the dielectric properties of the medium lie in between those of the interacting bodies $n_1 < n_3 < n_2$. For an extensive treatment and derivation, the reader is referred to specialized literature [42].

Overall, the Hamaker constant of the interacting materials can be calculated analytically either from their molecular properties ($A_H = \pi^2 C \rho^2$) or from their bulk material properties (as in Eq. 2.9), with the two approaches differing by a factor of $3/4\pi$. While the Hamaker constant derived from Lifshitz theory is generally considered the most accurate, its calculation requires all the dielectric properties and refractive indexes of the materials involved. However, the numerical calculations carried out in the first

part of this thesis, the Hamaker constant was not computed analytically; instead, its magnitude was treated as a floating parameter in order to tune the van der Waals strength in the potential. The details of these numerical calculations are presented in Subsection 3.1.4.

On the other hand, since the Hamaker constant is typically on the order of 1×10^{-21} J (~ 0.25 $k_B T$) for most materials, the resulting van der Waals interactions are often negligible when the separation distance between macroscopic bodies exceeds a few nanometers. Therefore, for the TIRM experiments conducted on large colloids in the second part of this thesis, the van der Waals interactions were negligible in the total interaction potential.

2.1.2 Derjaguin approximation and particle-wall interaction

Alternatively, the interaction between macroscopic bodies can be expressed in terms of the forces rather than the interaction energy. Boris Derjaguin developed an approach that connects the theoretical plane-plane interaction energies with the forces which can be determined experimentally for two curved surfaces, and vice versa, since $F(D) = -\partial U(D)/\partial D$.

Particularly, it is assumed that two large spheres, having radii $R_1 \gg D$ and $R_2 \gg D$, are separated by a distance D. Then, the force can be calculated by integrating the forces between opposite discs, as the infinitesimal slices of a sphere, with an area of $2\pi x\,dx$, and separated by a distance $Z = D + z_1 + z_2$ as depicted in Figure 2.2. In this way, the force can be calculated in terms of the expression for the interaction of two planar surfaces (Eq. 2.3): $F(D)_{\text{sphere}} = 2\pi R U_{\text{WW}}(D)$. Thus, the total force between the spheres is given by:

$$F(D) = \int_D^\infty 2\pi\, x\, dx\; f_{\text{WW}}(Z) \qquad (2.11)$$

where $f_{\text{WW}}(Z)$ is the wall-to-wall normal force per unit area between the flat surfaces.

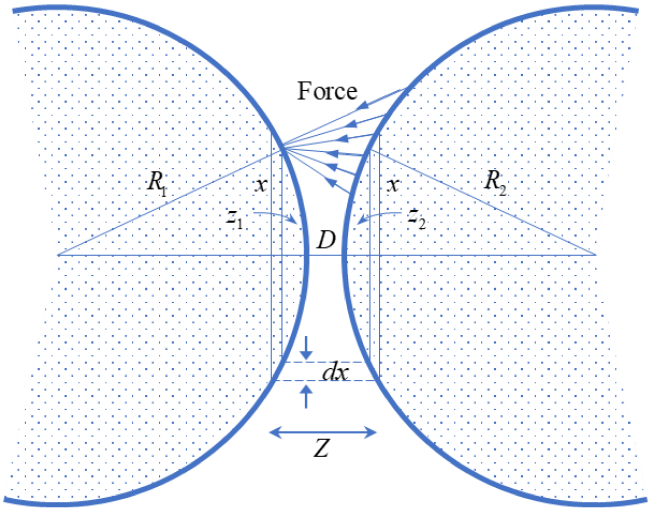

Figure 2.3. Sketch of the geometry used in the Derjaguin approximation. The force between two spheres is related as the energy, per unit area, between two flat discs facing each other. *Adapted from reference [42].*

At short distances when $z_{1,2} \ll R_{1,2}$, respectively, the chord theorem $x^2 \approx 2R_1 z_1 = 2R_2 z_2$, and with the separation distance between the discs, $Z = D + z_1 + z_2$, it gives $Z = D + \left(1/R_1 + 1/R_2\right) x^2/2$ and therefore $dZ = \left(1/R_1 + 1/R_2\right) x\, dx$. Then, (2.11 becomes:

$$F(D) = \int_D^\infty 2\pi \left(\frac{R_1 R_2}{R_1 + R_2} \right) f_{\mathrm{WW}}(Z)\, dZ \qquad (2.12)$$
$$= -2\pi \left(\frac{R_1 R_2}{R_1 + R_2} \right) U_{\mathrm{WW}}(D)$$

Such expression relates the existing force between two spheres to the energy, per unit area, between two flat surfaces distanced by D.

Then, to calculate the interaction energy between the spheres, the force given in the equation above is integrated:

$$U_{\mathrm{SS}}(D) = 2\pi \left(\frac{R_1 R_2}{R_1 + R_2} \right) \int_D^\infty U_{\mathrm{WW}}(Z)\, dZ \qquad (2.13)$$

This expression is valid only when $R_{1,2} \gg D$. As the interaction energy between two walls is $U_{\mathrm{WW/A}}(D) = -\pi \rho^2 C / 12 D^2$ (Eq. 2.3). Thus, substituting the appropriate terms and simplifications, the van der Waals interaction according to Derjaguin approximation is:

$$U_{\mathrm{SS}}(D) = \frac{\pi^2 \rho^2 C}{6D}\left(\frac{R_1 R_2}{R_1 + R_2}\right) \qquad (2.14)$$

2.1.3 Electrostatic repulsion

When colloidal particles are dispersed in an aqueous medium, they acquire surface charges through the interaction of their surface groups with the polar solvent which leads to the dissociation of ions. These surface charges prevent the aggregation of like-charged particles or walls by electrostatic repulsion. Meanwhile, the dissolved ions transform the direct electrostatic interaction between the macroscopic bodies into screened interactions, whose strength decays exponentially with distance. In the following, the screened electrostatic interaction between spheres and a wall is described according to the electrical double layer.

2.1.3.1 Screened electrostatic potential

The dissolved ions in the aqueous medium distribute near the surface according to the Boltzmann distribution according to the surface potential as:

$$\rho_i(\mathbf{r}) = \rho_i^0 \exp\left[-\frac{Z_i e \psi(\mathbf{r})}{k_B T}\right] \qquad (2.15)$$

where $\rho_i(\mathbf{r})$ is the ion concentration at any distance $\mathbf{r}$ from a surface, while ρ_i^0 is the concentration in bulk of species i. The electrostatic potential given by $\psi(\mathbf{r})$, the valency Z_i and the elementary charge is e. The Boltzmann constant as k_B and T the temperature in Kelvin.

In turn, the electrostatic potential $\psi(\mathbf{r})$ can be derived from Poisson equation:

$$\nabla^2\psi(\mathbf{r}) = -\frac{\rho(\mathbf{r})}{\varepsilon_0\,\varepsilon} \tag{2.16}$$

being ε_0 the permittivity in vacuum and ε the relative permittivity of the medium.

The number density of ions is given by:

$$\rho(\mathbf{r}) = \sum_j e\,Z_j\,\rho_j^0(\mathbf{r}) \tag{2.17}$$

Therefore, by combining the two above equations, it yields the Poisson-Boltzmann equation:

$$\nabla^2\psi(\mathbf{r}) = -\frac{e}{\varepsilon_0\,\varepsilon}\sum_j Z_j\,\rho_j^0 \exp\left[-\frac{Z_j\,e\psi(\mathbf{r})}{k_B T}\right] \tag{2.18}$$

For the scenario of a 1:1 symmetric electrolyte, e.g. NaCl, the valency and ion concentration are the same for both ion entities. Then,

$$\begin{aligned} Z &\equiv Z_+ = Z_- \\ \rho^0 &\equiv \rho_+^0 = \rho_-^0 \end{aligned} \tag{2.19}$$

and the Poisson-Boltzmann equation becomes:

$$\nabla^2\psi(\mathbf{r}) = -\frac{2e\rho^0 Z}{\varepsilon_0\,\varepsilon}\sinh\left[\frac{Z\,e\psi(\mathbf{r})}{k_B T}\right] \tag{2.20}$$

Moreover, when considering low potentials such as $\left(k_B T\right)^{-1} Ze\left|\psi\right| \ll 1$, which is known as the Debye-Hückel limit, the Poisson-Boltzmann equation becomes linearized:

$$\nabla^2\psi(\mathbf{r}) = \lambda_D^{-2}\,\psi(\mathbf{r}) \tag{2.21}$$

where the constant is the Debye length which characterizes the screening length of the electric field and is given by:

$$\lambda_D = \left(2e^2 \rho^0 Z^2 / \varepsilon_0 \varepsilon\, k_B T\right)^{-1/2} \qquad (2.22)$$

At this distance, the direct electrostatic interactions between charged macroscopic bodies drops $1/\mathbf{e}$ of the hypothetical value at contact. Here, $\mathbf{e} \approx 2.71828$ is the Euler number and it should not be confused with the elementary charge e.

Finally, considering a symmetric electrolyte distributed near planar surfaces with small surface potentials, the solution of the linearized Poisson-Boltzmann equation (Eq. 2.19) is:

$$\psi(x) = \psi_0 \exp\left[-x/\lambda_D\right] \qquad (2.23)$$

In the case where the spherical particle's radius is in the order of the Debye length, one has to consider the Poisson-Boltzmann equation in terms of the spherical symmetry [12]. For this case and for a 1:1 electrolyte, the solution has the form:

$$\psi(r) = \psi_0 \frac{R}{r} \exp\left[-(r-R)/\lambda_D\right] \qquad (2.24)$$

which represents the surface energy of a sphere of radius R.

In addition, to describe the pair interaction potential between two equal spheres, from an extensive derivation, yields [86]:

$$\psi(r)\beta = \lambda_B z_s^{\,2} \left(\frac{\exp[R\,\lambda_D^{-1}]}{(R+1)\lambda_D^{-1}}\right)^2 \frac{1}{r} \exp[-r/\lambda_D] \qquad (2.25)$$

where $\lambda_B = e^2/4\pi\varepsilon_0\varepsilon_r k_B T$ is the Bjerrum length, z_S the number of elementary charges at the surface and $r = 2R + D$ is the center-to-center separation distance. The expression above (Eq. 2.25) is known as Yukawa-type electrostatic potential.

2.1.3.2 Electrostatic repulsion between a sphere and wall

As two macroscopic objects approach each other, an interaction energy arises. For or two charged planar walls separated by a distance D , a repulsive contribution between the walls originates from the osmotic pressure $P(D)$ caused by a higher ion density in between the plates than the in the bulk rather than direct electrostatic interactions. For a monovalent electrolyte solution, such as NaCl, the excess of osmotic pressure generated by the ions confined in the gap gives rise to a force per unit area that follows:

$$P(D) = 64 k_B T \rho_0 \tanh^2\left(\frac{e\psi_0}{2k_B T}\right)\exp\left[-D/\lambda_D\right]. \qquad (2.26)$$

Subsequently, the interaction energy per area between the flat walls can be calculated by integrating the previous equation and yielding:

$$\begin{aligned} U^{\text{el}}_{\text{WW/A}}(D) &= \int_D^\infty P(D)\,dD \\ &= 64 k_B T \rho_0 \lambda_D \tanh^2\left(\frac{e\psi_0}{2k_B T}\right)\exp\left[-D/\lambda_D\right]. \end{aligned} \qquad (2.27)$$

Another system of interest is the sphere near a wall, where under the Derjaguin approximation, addressed earlier in Subsection 2.1.2, the force between them is proportional to the interaction energy of two walls $F_{\text{SW}}(D) = -\partial W_{\text{SW}}(D)/\partial D \approx 2\pi R U_{\text{WW/A}}(D)$. Then, to calculate the interaction energy between the sphere and the wall, the integration of the force $F_{\text{SW}}(D)$ through Eq. 2.26 is performed and resulting into:

$$U^{\text{el}}_{\text{SW}}(D) = 128\pi R k_B T \rho_0 \lambda_D \tanh^2\left(\frac{e\psi_0}{2k_B T}\right)\exp\left[-D/\lambda_D\right] \qquad (2.28)$$

and simplified into

$$\Phi_{\text{ER}}(D) = B_{\text{ER}} \exp\left[-D/\lambda_D\right]. \qquad (2.29)$$

Note that the notation for the potential has been changed to match the convention used in TIRM methodology described in the next section. This approximation (Eq. 2.29) is valid for the experimental conditions encountered in total internal reflection microscopy where the separation distances are short ($D \ll R$) and small Debye lengths ($\lambda_D \ll R$).

The typical Derjaguin approximation for the sphere-plane system becomes questionable when the condition of $R/\lambda_D \gg 1$ is not satisfied, as in cases involving small particles and/or low ionic strengths, due to the simplifications assumed in the initial expressions for the sphere-sphere limiting case of very large radius. Thus, limiting the applicability in sphere-plate systems outside the condition of $R/\lambda_D \gg 1$. However, such conditions are often encountered in EWDLS experiments. Under these circumstances, the linear superposition approximation (LSA), proposed by Lin et al. [57], provides a more appropriate description for the sphere-plate interactions. In LSA, the analytical expression for the sphere-plate electrostatic interaction is derived from the expression plate-plate interaction rather than the sphere-sphere limiting case, thus avoiding the simplifications that limit the applicability of Derjaguin approximation for sphere-plate systems. In simple terms, in the geometric representation used in the LSA, the sphere is divided into two hemispheres that interact with the wall. The sphere-plane electrostatic interaction is then obtained by summing the interactions of infinitesimal flat rings of each hemisphere with the wall. This is calculated by applying the Derjaguin approximation but using the expression for the plane-plane type potential, in two separate integrals with appropriate integration limits for each hemisphere. For sake of brevity, the detailed derivation is omitted here, and the reader is referred to dedicated literature [57]. In this framework, the electrostatic potential is given by:

$$\phi_{ER}(z) = B_{ER}\left[\begin{array}{l}\left(\exp\{-(z+R)/\lambda_D\} - \exp\{-(z-R)/\lambda_D\}\right) \\ +\dfrac{R}{\lambda_D}\left(\exp\{-(z+R)/\lambda_D\} + \exp\{-(z-R)/\lambda_D\}\right)\end{array}\right]. \qquad (2.30)$$

Here, the electrostatic repulsion is denoted as $\phi_{ER}(z)$ to distinguish it from the electrostatic potential defined in Eq. 2.29, $z = h + R$ is the distance from the wall to the sphere' center, while h is the shortest separation between the two surfaces. The coefficient B_{ER} is defined as:

$$B_{ER} = 64\,\pi\, R\, \varepsilon_0 \varepsilon\, \lambda_D\, \gamma_S\, \gamma_W \left(\frac{k_B T}{Ze} \right)^2 \qquad (2.31)$$

Here $\gamma_{S,W} = \tanh\left(Z_{S,W}\, e\, \Psi_{S,W} / 4 k_B T \right)$ with $\Psi_{S,W}$ being the surface potential and $Z_{S,W}$ the "valency" of the sphere and the wall, respectively.

2.1.4 Gravitational potential

In addition to the interactions presented above, there is still an external force that is present anywhere. The gravitational field acts over the macroscopic bodies as well, whether or not Brownian dynamics dominate their movement, gravity contributes to their total interaction potential.

Large macroscopic bodies are subjected to gravitational acceleration ($\mathbf{g}$) which results in a weight force. When these macroscopic particles are immersed in a solution, they also experience a buoyant force that opposes sedimentation due to gravity. In this case, the resulting buoyancy-corrected weight force G_{eff} is given by:

$$G_{\text{eff}} = m_{\text{eff}}\, \mathrm{g} \qquad (2.32)$$

where the effective mass $m_{\text{eff}} = \mathrm{v_P}\, \Delta\rho$, the particle's volume $\mathrm{v_P}$ and $\Delta\rho = \rho_{\text{particle}} - \rho_{\text{solvent}}$.

The contribution of the sphere's gravitational energy to the total interaction potential with a wall arises from the sphere's effective weight acting normal to the wall's surface. This contribution depends on the separation distance ($h = z - R$) from the wall and is expressed as:

$$\phi_G(h) = G_{\text{eff}}\, h\,. \qquad (2.33)$$

2.2 Hydrodynamic particle-wall interaction

In this section, the dynamic properties of colloidal particles are introduced, beginning with their behavior in bulk. Then, the particular case of the particle near the wall is shown. The theoretical contents presented provide the framework for analyzing the dynamics of colloids near the wall.

Typically, colloidal dispersions consist of macroscopic solid particles or droplets, ranging from a few nanometers to tens of micrometers in size, which are dispersed within a liquid medium. As presented in Section 2.1, interparticle interactions play an important role in determining the stability of the suspension and whether the colloids aggregate or remain dispersed. In addition, solvent molecules impart random forces on the colloidal bodies through the continuous collisions, resulting in random motion. This phenomenon is called Brownian motion, first observed and named after Robert Brown. Brownian motion is temperature-dependent since it is linked to the thermal kinetic energy of the solvent molecules. As the particle size decreases, Brownian motion becomes the dominant force, surpassing gravity in dictating particle dynamics.

Briefly, colloidal solid spheres when immersed in a fluid exhibit very low Reynolds number (Re), placing them in a viscous-dominated regime where the particle inertia is negligible. As a result, the fluid motion around the particle is smooth.

Here, a sphere of radius R moving freely in the solvent has a drag force ($\boldsymbol{F}_S$) of magnitude

$$F_S = 6\pi\eta R\mathrm{v} \qquad (2.34)$$

where η is the viscosity of the fluid and v is the particle's velocity. In addition, Stock's drag coefficient is defined as $\xi = 6\pi\eta R$.

Since Brownian motion relates to the random displacement, ($\mathbf{R}(t)$), of the particle in the three-dimensional space, this random force is modeled under the principle of random walk. In such approach, the mean displacement is zero while the mean squared displacement, $\left\langle \mathbf{R}(t)^2 \right\rangle$, is proportional to both the number of steps and the elapsed time. From this, the equation of motion of the particle is

$$m\frac{d^2\mathbf{R}}{dt^2}+\xi\frac{d\mathbf{R}}{dt}=F_{\text{random}} \tag{2.35}$$

with m being the particle's mass.

By assuming that the random force, and therefore the displacements, are isotropic in space i.e. uniformly distributed in space $\langle x\rangle^2=\langle y\rangle^2=\langle z\rangle^2$, Eq. 2.35 can be linearized as:

$$\frac{\xi}{2}\frac{dx^2}{dt}=x\,F_{\text{random}}-mx\frac{d^2x}{dt^2}. \tag{2.36}$$

After using identities and substitutions, this equation is rewritten as

$$\frac{\xi}{2}\frac{d\langle x^2\rangle}{dt}=x\langle F_{\text{random}}\rangle-m\frac{d}{dt}\left\langle x\frac{dx}{dt}\right\rangle+m\left\langle\left(\frac{dx}{dt}\right)^2\right\rangle \tag{2.37}$$

where the average of each term had been made.

Due to the fact that the random force is uncorrelated with the particle's position and its velocity is zero, the first and second term of Eq. 2.37 vanish, while the average of velocity squared is non zero . At this point, the equipartition theorem from statistical physics is brought, which states that the kinetic energy of a molecule or particle in thermal equilibrium averages $\frac{1}{2}m\langle v_x^2\rangle=\frac{1}{2}k_B\,T$ per degree of freedom. With this consideration, Eq. 2.37 becomes:

$$\frac{d\langle x^2\rangle}{dt}=2\frac{k_B\,T}{\xi} \tag{2.38}$$

and thus, the total mean squared displacement as a function of time in three dimensions is:

$$\langle\mathbf{R}^2\rangle=\frac{6\,k_B\,T}{\xi}t \tag{2.39}$$

Here, it is established that the mobility of a particle is diffusive and given by the Stokes-Einstein equation for the diffusion coefficient:

$$D_0 = \frac{k_B T}{6 \pi \eta R} \qquad (2.40)$$

which considers the motion for a spherical particle of radius R diffusing in the bulk of a solvent with viscosity η and at temperature T in Kelvin. This equation holds for dilute systems and far away from the effect of the boundaries. This latter scenario is presented in the next subsection.

To finish with the basic hydrodynamics of colloidal particles in bulk, it should be noted that a complete description of particle motion in a fluid requires solving the Stokes equations with appropriate boundary conditions. Such conditions must account for the nature of the particle's surface and its interaction with the solvent. These detailed formalisms lie beyond the scope of this thesis, however, interested readers are referred to standard textbooks on the subject [54].

2.2.1 Brownian motion near a wall

As a spherical particle approaches a hard, flat surface, its diffusion is strongly influenced by the wall through the hydrodynamic effects, in addition to direct particle-wall interactions, such as electrostatic and van der Waals interactions. The relative squeezing motion of the fluid in the narrow particle-wall gap, known as lubrication, generates an increase in hydrodynamic friction between the no-slip rigid surfaces. Consequently, the particle's diffusion becomes distance-dependent and slows as it gets closer to the wall. Furthermore, the particle's motion becomes anisotropic as compared to diffusion in bulk, splitting into the parallel ($D_{\parallel}$) and normal ($D_{\perp}$) diffusion relative to the wall surface. The mathematical expressions describing these effects, also referred to as correction factors, are presented below for both stick and partial slip boundary conditions.

Furthermore, the interaction between the particle and the surrounding fluid must be considered to establish a proper hydrodynamic framework. In Figure 2.4, a schematic representation of the so-called stick and slip boundary conditions for the Stokes equations is shown. The implications of these conditions that modify the particle's hydrodynamics are presented next. These terms are presented in a simplified form to explain the particle diffusion near a wall.

The stationary Stokes equation describes the fluid motion as:

$$\eta \nabla^2 \mathbf{v}(\mathbf{r}) - \nabla p(\mathbf{r}) = 0 \qquad (2.41)$$

and

$$\nabla \bullet \mathbf{v}(\mathbf{r}) = 0 \qquad (2.42)$$

where $\mathbf{v}(\mathbf{r})$ and $p(\mathbf{r})$ are the velocity and pressure of the fluid at position ($\mathbf{r}$), respectively. In the following, the boundary conditions applied for both the stick and slip models are presented.

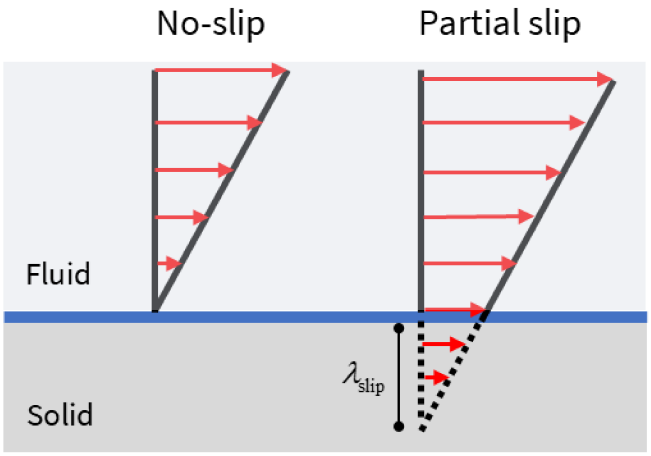

Figure 2.4. Schematic representation of stick-slip boundary conditions for fluid velocity (red arrows) at a solid interface. *Left*: the no-slip (stick) boundary condition, where the fluid is bound at the interface, resulting in zero velocity at the wall. The velocity increases with distance following a defined profile. *Right*: the partial slip boundary conditions, where the fluid at the interface is unbound and has a finite velocity. This behavior is characterized by the slip length, defined as the distance between the interface and the point where the extrapolated velocity profile would vanish inside the wall.

2.2.1.1 Stick (no-slip) boundary conditions

When a single sphere approaches a wall under no-slip conditions, its mobility decreases as the separation distance diminishes. The stick boundary condition describes the most common behavior of the motion of a fluid at smooth and impermeable interfaces, such as hard walls. The fluid velocity is

composed of the parallel and normal components $\mathbf{v} = \mathbf{v}_{\parallel} + \mathbf{v}_{\perp}$ and the corresponding boundary conditions at the interface $z = 0$:

$$\begin{aligned} \mathbf{v}_{\perp}|_{Z=0} &= 0 \\ \mathbf{v}_{\parallel}|_{Z=0} &= 0 \end{aligned} \qquad (2.43)$$

meaning that the fluid velocity at the interface surface is zero (Figure 2.4, left sketch), i.e. the fluid is attached at the interface and thus, having the same velocity as the particle or the wall.

Then, for the non-slip Brownian motion of a single sphere near a wall, correction factors for the friction coefficient, ξ, have been developed to account for the anisotropic diffusion coefficients in the parallel ($\xi_{\parallel}, D_{\parallel}$) and normal ($\xi_{\perp}, D_{\perp}$) components. For the parallel diffusion, a closed analytical approximation for the correction factor $\xi_{\parallel}$ on the separation distance was given by Faxén [28] from which the diffusion coefficient parallel to the wall is calculated as:

$$D_{\parallel}(z) = D_0\,\xi_{\parallel}(z) = D_0\left[1 - \frac{9R}{16z} + \frac{1}{8}\left(\frac{R}{z}\right)^3 - \frac{45}{256}\left(\frac{R}{z}\right)^4 - \frac{1}{16}\left(\frac{R}{z}\right)^5\right]^{-1}. \qquad (2.44)$$

Here, $z = h + R$ is the shortest distance from the particle center to the wall, h the surface-to-surface gap between the wall and the particle, and R the particle radius.

For the perpendicular direction the correction factor ($\xi_{\perp}$) can be described by an infinite series according to Brenner and coworkers [30, 37]:

$$\xi_{\perp}(z) = \frac{4\sinh\alpha}{3}\sum_{n=1}^{\infty}\frac{n(n+1)}{(2n-1)(2n+3)} \times \left[\frac{2\sinh\left[\alpha(2n+1)\right] + (2n+1)\sinh\left[2\alpha\right]}{\left(2\sinh\left[\alpha\left(n+1/2\right)\right]\right)^2 - \left((2n+1)\sinh\alpha\right)^2} - 1\right] \qquad (2.45)$$

where $\alpha = \cosh^{-1}(z/R)$. However, there exists a very good closed analytical approximation for such correction factor given by Bevan *et al.* [8], which if introduced to the diffusion expression for the perpendicular motion it gives:

$$D_{\perp}(z) = D_0 \xi_{\perp}(z) = D_0 \frac{6z^2 - 10Rz + 4R^2}{6z^2 - 3Rz - R^2}. \quad (2.46)$$

2.2.1.2 Partial slip

Boundary conditions for partial slip at fluid-solid interface (Eq. 2.47), also known as Navier boundary conditions, describe the perpendicular component of the fluid velocity at the surface to vanish, while parallel component is proportional to the tangential shear stress:

$$\begin{aligned} \mathbf{v}_{\perp} \mid_{Z=0} &= 0 \\ \mathbf{v}_{\parallel} \mid_{Z=0} &= \frac{\lambda_{\text{slip}}}{\eta} \sigma_{\text{xy}} \end{aligned} \quad (2.47)$$

where σ_{xy} the tangential component of the stress tensor and the slip length λ_{slip} . This last parameter defines the distance into the interior of the hard interface for which the near-surface velocity profile extrapolates to zero, thereby locating the effective no-slip plane at $z = -\lambda_{\text{slip}}$, as depicted in Figure 2.4, right. This means that the fluid at the interface carries a finite velocity parallel to the particle's surface.

Due to the roughness of the surface, the particles moving towards an interface can be described by using the model of stick-slip. The slipping is characterized by the slip parameter:

$$\zeta = \frac{\lambda_{\text{slip}}}{R + 3\lambda_{\text{slip}}} \quad (2.48)$$

where $0 \le \zeta \le 1/3$. In the limiting cased where $\zeta = 0$, the sphere is described as a smooth, hard surface with the surrounding fluid adhering to its surface. Conversely, when $\zeta = 1/3$, the particle is depicted with some degree of roughness, allowing the adjacent fluid to maintain a tangential velocity at the particle's surface, thereby reducing friction. Conceptually, the slip parameter defines the hydrodynamic radius as $R_H = (1-\zeta)R$, indicating that particles exhibiting slip diffuse more rapidly.

Ekiel-Jezewska and Wajnryb [21] described the mobility of a sphere in a fluid, with stick-slip boundary conditions through the inverse relation between the dimensionless mobility coefficient ($\mu = 6\pi\eta R\tilde{\mu}$) and the dimensionless friction coefficient $\varphi = 1/\mu$. This friction coefficient is determined as a function of the particle-wall distance and is numerically evaluated using the multipole expansion method, proposed by Cichoki et al. [13, 14]:

$$\varphi(z) = \sum_{n=0}^{N} R_n (1/z)^n \,. \qquad (2.49)$$

On the other hand, the corresponding lubrication expression for the friction coefficient φ of a particle exhibiting slip is given by the approximation [43]:

$$\varphi(\epsilon) = \frac{A}{\epsilon} - B\ln\epsilon + C - D\epsilon\ln\epsilon \qquad (2.50)$$

where $\epsilon = 1 - z$ is the dimensionless gap distance while the constants A, B, C, D depend on the slip parameter and the type of interface where the fluid binds. Particularly, for the flat hard wall case, the values of these constants were determined by Ekiel-Jezewska and Wajnryb by extensive numerical simulations. For a selection of slip parameters, the corresponding values are given in Table 2.1.

The diffusion coefficient normal to the wall, under partial slip conditions, is then calculated as:

$$D_{\perp}(z) = \frac{k_B T}{A/\epsilon - B\ln\epsilon + C - D\epsilon\ln\epsilon} \qquad (2.51)$$

ζ	A	B	C	D
1/12	0.25	3.5749	-6.2238	10.7
0.12	0.25	2.2	-2.6414	4.55
1/3	0.25	0.2	0.708214	0.033

Table 2.1. Constants used to calculate the friction coefficient related to a spherical particle approaching a flat and solid surface as a function of the slip parameter ζ . The calculated parameters for other slip parameters can be found in M.L. Ekiel-Jezewska and E. Wajnryb, 2018 [21].

A slip parameter of ζ = 1/3 corresponds to full slip while stick boundary conditions are characterized by ζ = 0. In the latter case, Eq. 2.51 and Eq. 2.46 produce the same results for large enough separation distances. However, for z/R < 1.04, Faxén's analytical expression returns values which deviate by more than 10 % from the more accurate numerical simulation data.

2.2.2 Particle dynamics from one-dimensional Brownian motion

When a colloidal sphere exhibits a one-dimensional Brownian motion, such as encountered in TIRM experiments, the one-dimensional Smoluchowski equation of motion is given by:

$$\frac{\partial P\left(z,z_0\,|\,t\right)}{\partial t}=\frac{\partial}{\partial z}\left[D_{\perp}\left(z\right)\left(\frac{\partial P\left(z,z_0\,|\,t\right)}{\partial z}+\beta\frac{d\,\Phi\left(z\right)}{dz}P\left(z,z_0\,|\,t\right)\right)\right] \qquad (2.52)$$

where $P\left(z,z_0\,|\,t\right)$ is the conditional probability function that describes the probability of finding the particle at a distance z at the time t , given it was located at a separation z_0 at time zero.

De Sio and co-workers (2018) derived a mathematical approach to resolve particle dynamics spatially [80]. From the particle one-dimensional traces, the first and second moments of the displacement distribution are calculated and plotted versus time. The initial slopes of these plots would correspond to the particle's drift velocity and diffusion normal to the wall, respectively.

In principle, the mean displacement $m\left(t,z_0\right)$ of a distribution $P\left(z,z_0\,|\,t\right)$ is defined as:

$$m\left(t,z_0\right)=\int_R^{\infty}dz\left(z-z_0\right)P\left(z,z_0,t\right) \qquad (2.53)$$

and the mean squared displacement $W\left(t,z_0\right)$ as:

$$W\left(t,z_0\right)=\int_R^{\infty}dz\left(z-z_0\right)^2P\left(z,z_0,t\right) \qquad (2.54)$$

By applying the right hand side of the Smoluchowski equation (Eq. 2.52) as the time derivatives on $m\left(t,z_0\right)$ and $W\left(t,z_0\right)$ one gets:

$$\frac{dm\left(t,z_0\right)}{dt}=\int_R^\infty dz\left(z-z_0\right)\frac{\partial}{\partial z}\left[D_\perp\left(z\right)\left(\frac{\partial P\left(z,z_0\mid t\right)}{\partial z}+\beta\frac{d\Phi\left(z\right)}{dz}P\left(z,z_0\mid t\right)\right)\right] \tag{2.55}$$

and

$$\frac{dW\left(t,z_0\right)}{dt}=\int_R^\infty dz\left(z-z_0\right)^2\frac{\partial}{\partial z}\left[D_\perp\left(z\right)\left(\frac{\partial P\left(z,z_0\mid t\right)}{\partial z}+\beta\frac{d\Phi\left(z\right)}{dz}P\left(z,z_0\mid t\right)\right)\right] \tag{2.56}$$

respectively.

The simplification of both equations by implementing a two-fold integration by parts leads to

$$\left\langle v_{\text{drift}}\left(z\right)\right\rangle=\frac{dm\left(t,z_0\right)}{dt}=\int_R^\infty dz\,P\left(z,z_0\mid t\right)\left[\frac{dD_\perp\left(z\right)}{dz}-\beta D_\perp\left(z\right)\frac{d\Phi\left(z\right)}{dz}\right] \tag{2.57}$$

where the drift velocity is identified as

$$v_{\text{drift}}\left(z\right)=\frac{dD_\perp\left(z\right)}{dz}-\beta D_\perp\left(z\right)\frac{d\Phi\left(z\right)}{dz} \tag{2.58}$$

while the mean squared displacement derivate is simplified as:

$$\begin{aligned}\frac{dW\left(t,z_0\right)}{dt}&=2\int_R^\infty dzP\left(z,z_0\mid t\right)\left[D_\perp\left(z\right)+\left(z-z_0\right)v_{\text{drift}}\right]\\&=2\left\langle\left[D_\perp\left(z\right)+\left(z-z_0\right)v_{\text{drift}}\right]\right\rangle\end{aligned} \tag{2.59}$$

By introducing the Taylor expansions for small displacements into equations Eq. 2.55 and Eq. 2.56 and solving the integrals yields:

$$\frac{dm(t,z_0)}{dt} = v(z_0) + m(t,z_0)\frac{dv_{\text{drift}}(z_0)}{dz_0} + \frac{1}{2}W(t,z_0)\frac{d^2v_{\text{drift}}(z_0)}{dz_0{}^2} + \dots \tag{2.60}$$

and

$$\begin{aligned}\frac{dW(t,z_0)}{dt} &= 2D_{\perp}(z_0) + 2m(t,z_0)\left(\frac{dD_{\perp}(z_0)}{dz_0} + v_{\text{drift}}(z_0)\right) \\ &+2W(t,z_0)\left(\frac{1}{2}\frac{d^2D_{\perp}(z_0)}{dz_0{}^2} + \frac{dv_{\text{drif}}(z_0)}{dz_0}\right) + \dots\end{aligned} \tag{2.61}$$

With this, the short-time evolution of the mean displacement and mean squared displacement can be obtained by taking the generic short-time expansions of $m(t,z_0) = a_{11}t + a_{12}t^2$ and $W(t,z_0) = a_{21}t + a_{22}t^2$ to then perform their derivation with respect to time. By comparing and matching the coefficients with those in Eq. 2.60 and Eq. 2.61, it finally yields:

$$m(t,z_0) = v_{\text{drift}}(z_0)t + \frac{1}{2}\left[v_{\text{drift}}(z_0)\frac{d\,v_{\text{drift}}(z_0)}{d\,z_0} + D_{\perp}z_0\frac{d^2\,v_{\text{drift}}(z_0)}{d\,z_0{}^2}\right]t^2 \tag{2.62}$$

and

$$\begin{aligned}&W(t,z_0) = 2D_{\perp}(z_0)t \\ &+\left[v_{\text{drift}}(z_0)\left(\frac{d\,D_{\perp}(z_0)}{dz_0} + v_{\text{drift}}(z_0)\right) + D_{\perp}(z_0)\left(\frac{d^2\,D_{\perp}(z_0)}{dz_0{}^2} + 2\frac{d\,v_{\text{drift}}(z_0)}{dz_0}\right)\right]t^2\end{aligned} \tag{2.63}$$

In this way, the equations above establish the relationship between the first and second moments of the particle's displacement distribution and the dynamic properties of drift velocity and perpendicular diffusion, respectively. These properties can be determined from the initial slopes of the mean displacement and mean squared displacement versus time curves, respectively, when evaluated at short times.

3 Experimental and numerical methods

In order to address the particles' near-wall interactions and dynamics, measurements of their scattered light near solid-liquid interfaces were measured by Evanescent Wave Dynamic Light Scattering (EWDLS) and Total Internal Reflection Microscopy (TIRM). These techniques use evanescent waves, produced by the total internal reflection of a laser beam, as the illumination source near interfaces. Given the relationship between the wall-particles' separation distance with the exponentially decaying illumination profile, both techniques are depth-sensitive and suitable to measure either static interaction potentials or/and dynamic properties at the nanoscale. In a general picture, from these techniques it is possible to acquire the light scattered by probe spheres near a glass wall, which carry the raw information that can be analyzed to determine the particles' near-wall interactions and dynamics.

In the present chapter, both evanescent wave-based experimental techniques and their respective analyses are explained. Additionally, numerical simulations were developed for the purpose of complementing the experimental findings and expanding the explanations. Furthermore, a subsection dedicated to experimental noise considerations (shot and background noise) is included. Such noises are inherent in any scattering technique but here analyzed for TIRM. In the end, there is a description of samples used in each experimental method.

3.1 Evanescent Wave Dynamic Light Scattering (EWDLS)

EWDLS allows the study of dynamic properties of colloidal particles undergoing Brownian motion close to a glass-aqueous solution interface. The measurement principle of EWDLS is equivalent to conventional dynamic light scattering in the sense that time auto-correlation functions of the scattered

intensity from an ensemble of particles are measured. However, the illumination of the scattering volume is fundamentally different in EWDLS and as a consequence the analytical formulation of the scattering vector is significantly more complicated. These aspects are discussed in the following.

As previously mentioned, the evanescent wave illuminates the near-wall particles up to a certain distance characterized by the so-called penetration depth (introduced later). Nevertheless, the retrieved dynamic information represents a quantity which is averaged over the illuminated volume where an ensemble of particles is present. As discussed in the “Theoretical Background” chapter, the Brownian motion of particles near an interface is slower than in the bulk due to hydrodynamic interactions with the surface, with the extent of this slowdown depending on the particle-wall separation distance, hereafter termed “height”. Further the motion becomes spatially anisotropic, i. e. generally motion parallel to the interface is faster than in the normal direction. Owing the characteristics of the evanescent illumination, the experimental diffusion coefficients are integrated over heights and particles size distributions. Different from other EWDLS set-ups, the one used in this work has the particularity of measuring independently the geometric components of particles’ diffusion constants near the wall, i. e. diffusion constant parallel $\langle D_{\parallel} \rangle$ and normal $\langle D_{\perp} \rangle$ to the wall (the pointed brackets indicate averaging over the evanescent illumination profile), by decomposing experimentally the scattering vector into its parallel ($Q_{\parallel}$) and normal ($Q_{\perp}$) components, respectively. In the following, a detailed description of the experimental set-up, data analysis and numerical calculations is presented.

3.1.1 EWDLS conceptualization and analytical foundation

EWDLS requires a coherent and monochromatic light source which will be scattered by the colloidal particles in the sample cell. In order to illuminate the colloidal suspension near the wall, the technique relies on the evanescent wave, produced by the total internal reflection of a laser beam at the glass/solution interface (Figure 3.1 left panel). The laser beam travels within a dense dielectric medium, which has a refractive index n_1, and gets totally reflected when it hits the less dense second medium ($n_2 > n_1$). At the interface, the beam has an incident angle α_i such that $\alpha_i \geq \alpha_C$ where α_C is the

critical angle for total internal reflection and is given by Snell's Law: $\alpha_C = \sin^{-1}\left[n_2/n_1\right]$. Then, an evanescent wave is created at the interface which propagates along the interface for a short distance of the order of the wavelength. The electric field of this wave extends into the less dense medium which in this case is the colloidal suspension. The associated field strength, $E(z)$, decays exponentially with distance Z along the normal interface:

$$E = E_0 \exp\left[\frac{-\kappa}{2} z\right] \tag{3.1}$$

where $\kappa/2$ is the inverse of the penetration depth of the evanescent field, which in turn, depends on the refractive indexes, the incident angle α_i and the laser's vacuum wavelength λ_0:

$$\frac{\kappa}{2} = \frac{2\pi}{\lambda_0}\sqrt{\left(n_1 \sin\alpha_i\right)^2 - n_2^2} \tag{3.2}$$

The evanescent wave has an associated wave vector $\boldsymbol{k}_E$ along the interface in the direction of propagation. The wave vector of the scattered light $\boldsymbol{k}_S$ has the same magnitude as $\boldsymbol{k}_E$ and its direction is determined by the position of the detecting unit as shown in Figure 3.1 right panel. The difference between these two vectors is the scattering vector $\boldsymbol{Q} = \boldsymbol{k}_S - \boldsymbol{k}_E$ and its magnitude is $Q = \sqrt{Q_{\parallel}^2 + Q_{\perp}^2}$.

The scattering vector is then geometrically separated into its components: the parallel scattering vector and the normal scattering vector. The parallel scattering component is given by

$$Q_{\parallel} = \frac{2\pi n_2 \sqrt{1 + \cos^2\alpha_r - 2\cos\theta\cos\alpha_r}}{\lambda_0} \tag{3.3}$$

and the normal component follows:

$$Q_{\perp} = \frac{2\pi n_2 \sin\alpha_r}{\lambda_0} \tag{3.4}$$

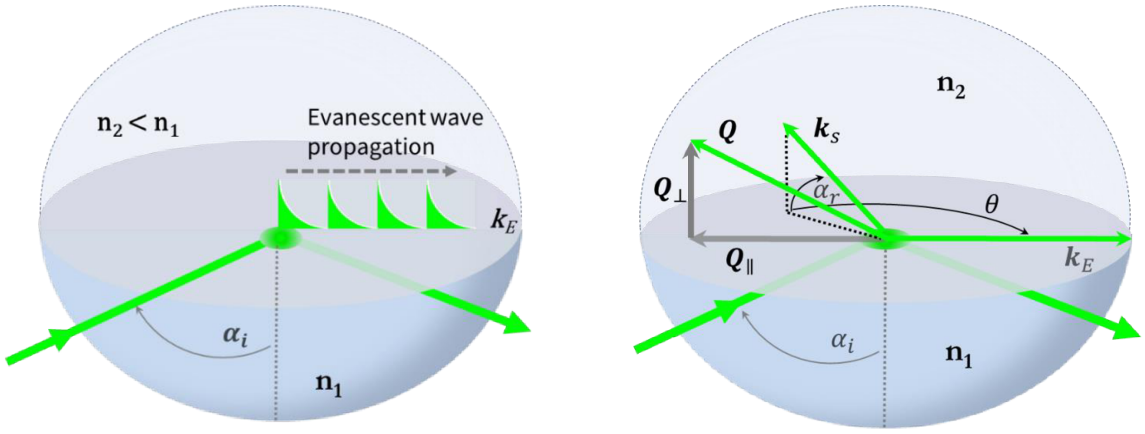

Figure 3.1. Scheme of EW formation inside the sample cell. The spherically shaped cell is built by two parts: the upper part is a hemispherical dome shell which contains the colloidal suspension (n_2). The bottom part is a hemisphere made of high refractive index solid quartz glass (SF10, n_1). Left panel: a laser beam hits the bottom side of the glass/solution interface with a particular angle of incidence $\alpha_i > \alpha_C$ to achieve total internal refraction. The created evanescent wave has an exponentially decaying field strength $E(z)$ as stated in Eq. 3.1. Right panel: sketch of sample cell and the resulting scattering vector $\boldsymbol{Q} = \boldsymbol{k}_S - \boldsymbol{k}_E$. Additionally, the decomposition of $\boldsymbol{Q}$ into its geometric components parallel ($\boldsymbol{Q}_{\parallel}$)and normal ($\boldsymbol{Q}_{\perp}$) components is shown.

The experimental set up' configuration allows for varying angles θ and α_r independently. In this way, it is possible to experimentally change only one of the scattering vector components while the other remains constant. Eventually, this results in measurements of the averaged diffusion constats parallel and normal to the wall separately. As will be explained soon, the initial slopes of the experimental intensity auto-correlation functions depend linearly on the squared scattering vector components, $Q_{\parallel}$ or $Q_{\perp}$ with slopes that are proportional to $\langle D_{\parallel} \rangle$ and $\langle D_{\perp} \rangle$.

3.1.2 EWDLS experimental set-up, sample cell and alignment

The experimental set-up is built in-house based on a three-axis goniometer (Huber Diffraktionstechnik, Rimsting, Germany). One goniometer is used to manipulate the incident angle of the laser source and

the other two are used to change the angles (θ, α_r) for the detector's position. A sketch of the experimental set-up is shown in Figure 3.2.

The goniometer arm, which carries the light source (Nd/Yag laser; wavelength in vacuum λ_0 = 532 nm; nominal power value 0.3 W, Excelsior, Spectra Physics) moves around the *x*-axis normal to the paper plane allowing the change of the angle of incidence α_i. Consequently, the penetration depth changes according to Eq. 3.2. Further this arm holds a grey density filters carousel, a $\lambda/2$ plate, a polarizer and a lens.

Then in the center of the set-up, sits an ensemble of devices: a goniometer (ω, turning the sample around the vertical z-axis), two circle segment cradles (χ_1, χ_2, tilting the sample cell with respect to the x- and y-axis respectively) and three linear stages (translating the sample along the x-, y- and z-axis). Each device serves the sample cell alignment by rotation, inclination and translation, respectively. The proper alignment sets the center of the sample cell at the intersection of the three axes of the set-up and the reflecting surface parallel to the xy-plane.

The detector unit consists of an ALV/SO-SIPD single photon counting unit equipped with an internal 50/50 beam splitter and two single photon detecting photo-multiplier tubes. Both devices are mounted on the goniometer arm opposite the laser. The detector's arm is mounted on two goniometers that move the detector's position along the θ angle (horizontal plane) and α_r angle (outside the horizontal plane) allowing independent changes of the magnitude of scattering vector components $Q_{\parallel}$ and $Q_{\perp}$.

The photomultipliers' signal is cross correlated by a LS Instruments (LSI) multiple-τ correlator to yield the time auto correlation function of the scattered intensity. The whole hardware of the experimental set-up is controlled by a LS Instruments box through the EWDLS Manager v1.0.2.2 software (custom made, LS Instruments AG, Switzerland). With that, all the motor-controlled stages and goniometers can be moved either for alignment or setting-up experiments.

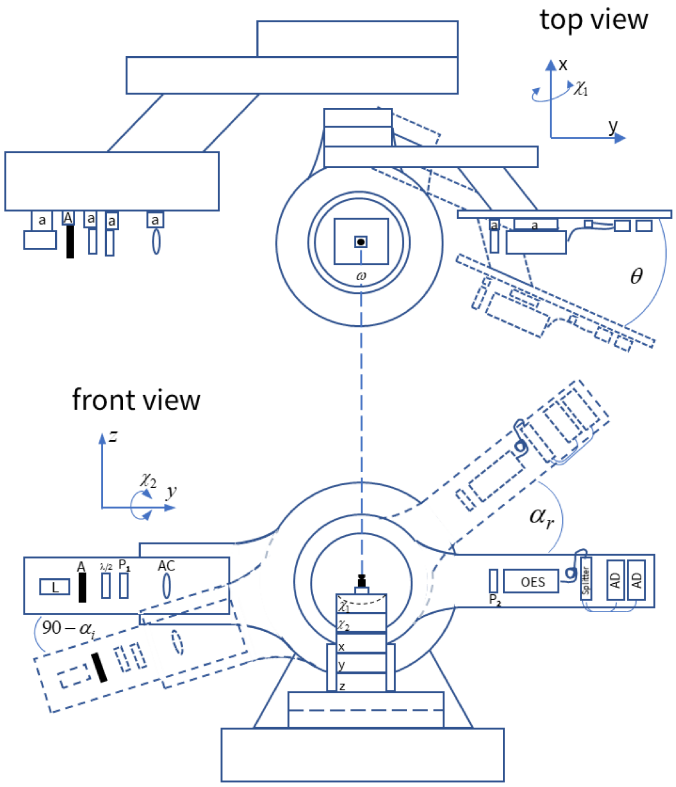

Figure 3.2. Design sketch of the EWDLS experimental set-up and its geometry. The following components are labeled in the sketch: laser (L), neutral density filter wheel (A), a $\lambda/2$ plate, polarizers (P1,2), detector unit (OES), a fiber splitter, a pair of avalanche diodes (AD) and various positioning units (a). Reproduced from Ref. [59] in which, different from the current work, avalanche diodes were used as photon counting units.

The sample cell, shown in Figure 3.1, consists of two parts: a semi spherical glass lens as the bottom part (SF10 glass, $n_1 = 1.736$ at the used λ_0) and, a hemispherical dome on top completing the spherical shape of the sample cell. Both glass parts were custom-made by Hellma GmbH, Müllheim, Germany. The volume between the flat face of the lens and the dome is filled with colloidal suspension. Typically, the solvent's refractive index is $n_2 = 1.333$. A complete description of the colloidal suspensions used is presented in Subsection 3.4.1.

For reproducible positioning of the measuring cell, the lower lens part is glued to a kinematic three-point bearing. The flat surface of the lens is precisely adjusted into the apparatus, then the upper part of the cell is placed on top and filled with the sample solution. The alignment of the bottom part is done as follows: firstly, the laser arm is set to $\alpha_i = 0$ and the detector is moved to the position where the

maximum intensity from the attenuated laser beam is recorded by scanning θ and α_r. The resulting detector's angles are set as θ = 0 and α_r = 0. Then, the sample cell without the dome, is placed in the set-up first aligned concerning its tilt. To that end, the following steps are performed:

(i) The planar face of the cell must be aligned to the horizontal plane, as defined by θ. To check this, the laser is positioned in a way that the beam hits the lens' plane surface from above, and the reflected beam is projected onto a screen on a wall a few meters away. Then, the sample cell is turned around the axis, defined by ω, from 0 to 180° degree, which will typically lead to vertical displacements of the projected beam on the screen. Then the χ_1 cradle is inclined to the angle $\Delta\chi$ at which the mentioned displacement is removed and finally the cradle position is set to $\chi_1 = \Delta\chi/2$. The same procedure is repeated for the angles ω = 90° and 270° and with the χ_2 cradle. The entire process involving the two cradles is repeated until a full 360 degree turn of ω will not cause any displacement of the laser spot on the screen. With this procedure it is assured that the deviation of the reflecting plane from the machine internal xy-plane is smaller than 0.3 mrad in either direction.

(ii) The height of the reflecting surface must be levelled with the laser beam. To this end, the laser angle α_i and the detector's angle α_r, are first set to zero (devices on the horizontal plane and opposite to each other) and, the position of the beam on the detector arm is marked with a pinhole, then both arms are moved to the same angle above the surface. If the point of impact of the laser has travelled away from the pinhole as a result, the height of the cell's flat surface is corrected by tuning the z-stage until the laser hits the pinhole again. After this step, the deviation of the planar surface's *z*-position from the machine internal z = 0 position is of the order of 1 micrometer.

(iii) For the alignment of the x- and y- positions of the cell, a similar procedure as for the correction of the inclination is applied. This time, the laser is reflected from the bottom side of the interface and displacements of the spot on the screen due to turns around ω are corrected by adjusting the x- and y-stages. This procedure results in the poorest alignment

accuracy of all steps, since the laser beam is significantly expanded by travelling through the lens-shaped bottom part. The errors in the x- and y-position of the sample cell may be as large as 0.1 mm

Once the bottom part of the sample cell is aligned, the dome is put on top and sealed with a non-soluble vacuum grease. Then, it is filled with the sample solution through tubes mounted in the pole region of the cell.

3.1.3 Analysis of dynamic properties

In the EWDLS technique, the scattering signal from the colloidal particles which are close to the interface is acquired. The temporal fluctuation of the scattered intensity carries information about the dynamics of the particles close to the wall. A correlator device computes the intensity correlation function $g_2(t)$, which in turn is then used to calculate the field autocorrelation function $g_1(t)$, being t the lag time. The latter is directly related to physical properties of the particles, such as their diffusion coefficient. The analytical basis of the necessary computation is described below.

In the case of intensity autocorrelation function $g_2(t)$ (Figure 3.3 top panel) measured in an EWDLS experiment, it is considered that the scattered intensity has a contribution coming from colloidal particles and another from the surface roughness. Then, it is expected to acquire a mix of homodyne and heterodyne detection. The mathematical expression for this case of the intensity autocorrelation function follows the generalized Siegert relation [32, 33, 75]:

$$g_2(t) = 1 + 2C_1 g_1(t) + \left(C_2 g_1(t)\right)^2 \qquad (3.5)$$

where $C_1 = C_2 - C_2^2$ and $C_2 = 1 - \sqrt{1-A}$ being A the intercept of the experimental intensity autocorrelation function $g_2(t)$. Next, $g_2(t)$ is translated to the field autocorrelation function $g_1(t)$ by means of Eq. 3.5.

The short time part of the $g_1(t)$ curves (Figure 3.3 bottom panel) are fitted using a nonlinear least square fitting routine, where the field-autocorrelation function is approximated as a time-decaying single exponential function given by:

$$g_1(t) = (1 - B_1)\exp[-\Gamma t] + B_1 \qquad (3.6)$$

where B_1 is a baseline, used for the larger relaxation times in the curve, and Γ is the initial decay rate of the field autocorrelation function. Additionally, B_1, is related to the baseline B_2 of the intensity autocorrelation function by $B_1 = \left[\left(C_1/C_2\right)^2 + B_2/C_2^2\right]^{1/2} - C_1/C_2^2$. Consequently, there are three independent parameters to fit: A, B_2 and Γ.

To increase the reliability of the best fitting parameters, the curves are fitted for short times, starting with a manually chosen number data points, N_p. After the fit converges, the fitting process restarts but with two less data points at the long-time end. The process is done repeatedly and the fitting parameters with the resulting mean squared deviations, δ^2, are plotted as a function of N_p. These plots typically show regions in which neither the parameters nor δ^2 vary significantly with the number of points. The Γ values found within this range are established as the initial slope of $g_1(t)$. To this end, an executable tool, developed in-house and described in detail elsewhere [75] was employed, which does the conversion from $g_2(t)$ to $g_1(t)$ and the fitting automatically.

On the other hand, the initial slope is directly related to the diffusion constants, parallel and normal to the wall, as follows [58]:

$$\Gamma = Q_{\parallel}^2 \langle D_{\parallel} \rangle_{\kappa} + \left(Q_{\perp}^2 + \frac{\kappa^2}{4}\right)\langle D_{\perp} \rangle_{\kappa} \qquad (3.7)$$

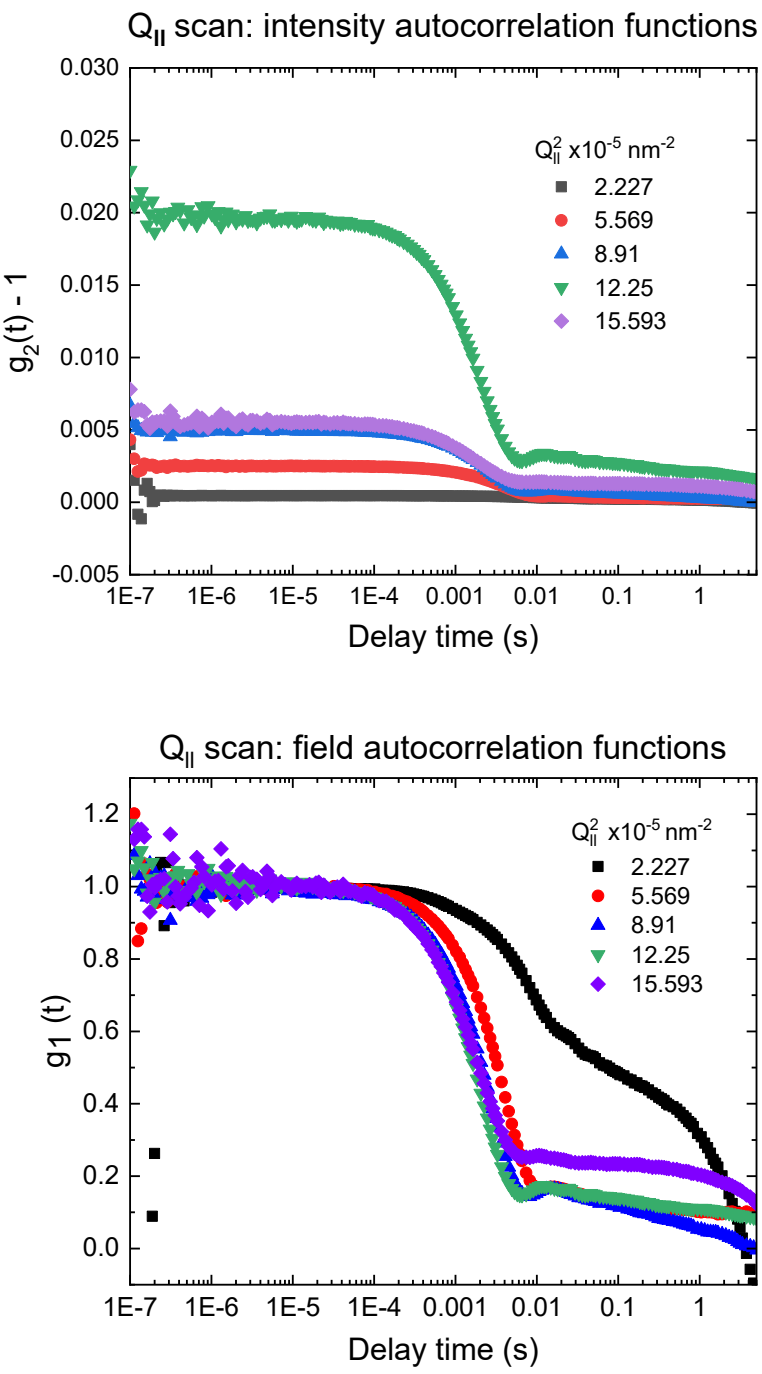

Figure 3.3. *Top panel*: intensity autocorrelation functions measured on the same sample but at different parallel scattering vectors while the normal scattering vector component remains fixed. *Bottom panel*: field autocorrelation functions of the same sample but at different parallel scattering vectors. The curves are fitted according to Eq. 3.6 in order to get the initial slope Γ at those scattering vectors.

As mentioned before, the advantage of changing θ while fixed α_r independently is to allow the variation of the parallel scattering vector's magnitude while the normal component is kept constant. This means that one can determine the parallel component of the diffusion constant as the slope of a plot of Γ vs $Q_{\parallel}^2$ at fixed $Q_{\perp}^2$. For this, the measurements are performed at least three times to obtain an averaged $\langle \Gamma \rangle$ with standard deviations. Next, the averaged initial decay rates $\langle \Gamma \rangle$ are plotted (Figure 3.4) as a function of $Q_{\parallel}^2$. Then, the linear fit to these points is done and the slope is twice the diffusion constant value $\langle D_{\parallel,\perp} \rangle_{\kappa}$ at the pre-set penetration depth. Then, the process is repeated for different penetration depths.

This procedure applies as well to the computation of the diffusion constants normal to the wall, where the out-of-plane angle α_r and in-plane angle θ are moved to maintain the $Q_{\parallel}^2$ values fixed, according to Eq. 3.3, 3.4 and 3.7.

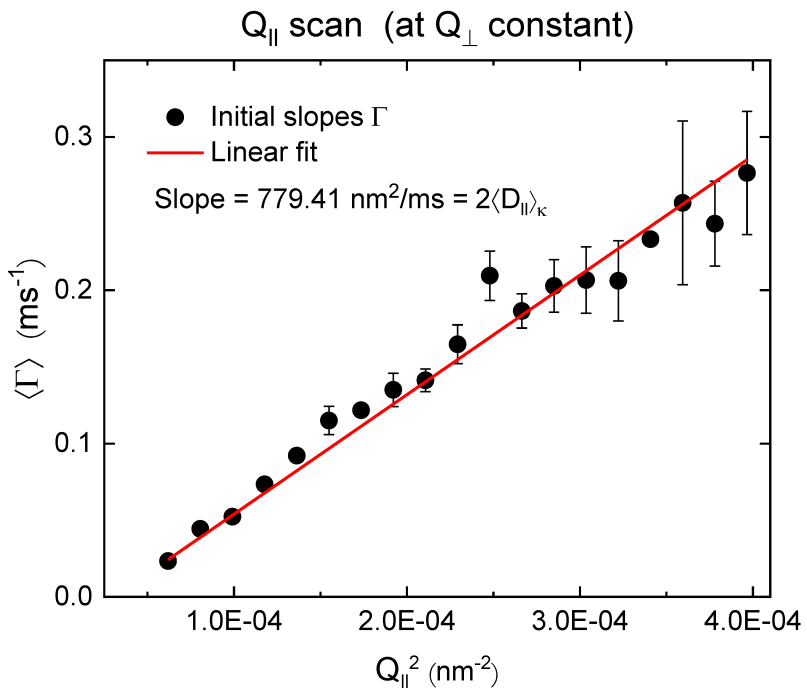

Figure 3.4. Average initial slopes vs. parallel scattering vector component squared. Points are experimental data obtained at a particular penetration depth. The red line is a linear fit, the slope of which is the diffusion constant parallel to the wall $\langle D_{\parallel} \rangle_{\kappa}$. A similar process is done when calculating the normal diffusion constant (omitted in the graph for simplicity).

The whole procedure is repeated for all the penetration depths, i.e. for different incident angles α_i in order to obtain the near-wall dynamics profile along the normalized distances as shown in Figure 3.5. The process is followed for both components of diffusion: parallel and normal to the interface.

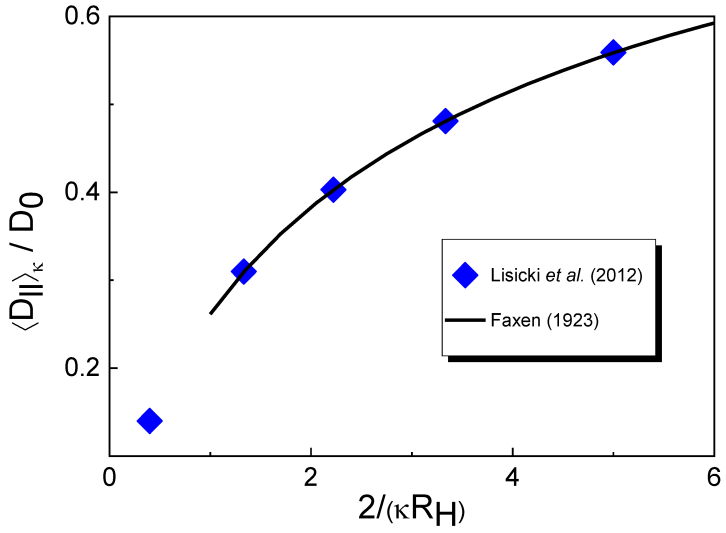

Figure 3.5. Example of near-wall dynamics of hard spheres where their normalized mean diffusion coefficients parallel to the surface as a function of normalized penetration depth is shown. Analytical data from Lisicki et al. 2012 (blue rhomboids) and Faxen model [28] (solid line) for near-wall dynamics of hard spheres.

3.1.4 Calculations of the colloidal near-wall diffusion constants

As the diffusion coefficients are associated to the initial slope of the field autocorrelation functions through their decay rate, Γ, these quantities are analytically calculated as follows:

$$\Gamma = \frac{\int_R^\infty \exp\{-\beta\phi(z)\}\exp\{-\kappa z\}\left[D_\parallel(z)Q_\parallel^2 + D_\perp(z)\left(Q_\perp^2 + \kappa^2/4\right)\right]dz}{\int_R^\infty \exp\{-\beta\phi(z)\}\exp\{-\kappa z\}\,dz} \qquad (3.8)$$

which reduces to the linear relation shown in Eq 3.7, describing Γ as a function of the diffusion coefficients averaged over the decaying illumination profile for the case of non-interacting monodisperse particles. As for the analytical expressions for the diffusion constants, the parallel component is given by Eq. 2.44 and the normal component by Eq. 2.46 presented in Subsection 2.2.1.1.

3.1.4.1 Particle-wall interaction potential

The total interaction potential $\phi(z)$ between the particles and the wall is modeled as the superposition of three major contributions: an attractive van der Waals term, $\phi_{\mathrm{vdW}}(z)$, a repulsive electrostatic term, $\phi_{\mathrm{E}}(z)$, and the attractive gravitational term $\phi_{\mathrm{G}}(z)$. All these potentials are described in detail in Section 2.1.

The distance dependence of the attractive van der Waals term between a spherical body and a flat surface, is given by

$$\phi_{\mathrm{vdW}}(z) = -\frac{A_{\mathrm{H}}}{6}\left[\frac{R}{z-R} + \frac{R}{z+R} + \ln\left(\frac{z+R}{z-R}\right)\right] \qquad (3.9)$$

where the strength of the interaction is given by the Hamaker constant A_{H}, which is mainly determined by the dielectric constants of the colloid, the wall and the solvent [42]. In the numerical calculations, this parameter is varied to systematically increase or decrease the strength of the attractive component of the total potential.

The electrostatic repulsion expression is based on the linear superposition approximation by Lin *et al.* [57]:

$$\phi_{ER}(z) = B_{ER}\left[\begin{array}{l}\left(\exp\{-(z+R)/\lambda_D\} - \exp\{-(z-R)/\lambda_D\}\right) \\ +\dfrac{R}{\lambda_D}\left(\exp\{-(z+R)/\lambda_D\} + \exp\{-(z-R)/\lambda_D\}\right)\end{array}\right] \qquad (3.10)$$

with B_{ER}, described in Eq. 2.31, as an adjustable parameter to vary the repulsive component of the total interaction potential.

The gravitational potential is calculated by the buoyancy-corrected mass of a sphere, having the expression:

$$\phi_{\mathrm{G}}(z) = \frac{4}{3}\pi R^3 \Delta\rho_m \, g \, z \qquad (3.11)$$

being $\Delta\rho_m$ the difference of mass density of the particle and the solvent and g the acceleration of gravity.

3.1.4.2 *Considerations of polydispersity and particle morphology*

In the cases where the particles are not smooth spheres and/or if they are polydisperse in size, the expression for the decay rates, in Eq. 3.8, becomes more complex due to the introduction of two factors: the near-wall scattering amplitude, $B_{\mathrm{NW}}(Q,R)$, and the size distribution function $P(R)$, being a Gaussian normal distribution function with mean value μ and standard deviation σ.

The general expression for the decay rates with the previous considerations is given by:

$$\langle\Gamma\rangle_R = \frac{\int_0^\infty B_{\mathrm{NW}}^2(Q,\kappa,R)\,P(R)\,dR \int_R^\infty \exp\{-\beta\phi(z)\}\exp\{-\kappa z\}\; D(Q,\kappa,R)\,dz}{\int_0^\infty B_{\mathrm{NW}}^2(Q,\kappa,R)\,P(R)\,dR \int_R^\infty \exp\{-\beta\phi(z)\}\exp\{-\kappa z\}\,dz} \qquad (3.12)$$

being $D(Q,\kappa,R) = D_{\|}(z)\,Q_{\|}^2 + D_{\perp}(z)\left(Q_{\perp}^2 + \kappa^2/4\right)$.

The form amplitude of a spherical particle in an exponential illumination profile, is given by [75]:

$$B_{\mathrm{NW}}(Q,\kappa,R) = 2\pi R^3 \left[\begin{array}{l} \int_{-1}^{1} d\mu \int_0^1 y^2 \cos(Q_{\perp} y \mu R)\exp\{y\mu\kappa R/2\}\, J_0\left(Q_{\|}\sqrt{1-\mu^2}\, yR\right) dy \\ +i\int_0^1 y^2 \sin(Q_{\perp} y \mu R)\exp\{y\mu\kappa R/2\}\, J_0\left(Q_{\|}\sqrt{1-\mu^2}\, yR\right) dy \end{array}\right] \qquad (3.13)$$

where J_0 is the zero order Bessel-function of the first kind.

The hollow shell can be thoght as a core-shell particle with a core of radius R_C with scattering length density ρ_C while the outer shell part has a radius R and a scattering length density of ρ_S. The form amplitude for a core shell particle with $\vartheta = R_C/R$ is given by:

$$B_{NW}\left(Q_{\|},Q_{\perp},\kappa,R_C,R\right) = 2\pi R^3 \left(\int_{-1}^{1} \rho_C \, d\mu \left[\begin{array}{l} \int_0^{\vartheta} y^2 \cos\left(Q_{\perp} y\mu R\right) \exp\left\{\frac{-y\mu\kappa R}{2}\right\} J_0\left(Q_{\|}\sqrt{1-\mu^2}\, yR\right) dy \\ +i\int_0^{\vartheta} y^2 \sin\left(Q_{\perp} y\mu R\right) \exp\left\{\frac{-y\mu\kappa R}{2}\right\} J_0\left(Q_{\|}\sqrt{1-\mu^2}\, yR\right) dy \end{array} \right] + \rho_S \left[\begin{array}{l} \int_{\vartheta}^{1} y^2 \cos\left(Q_{\perp} y\mu R\right) \exp\left\{\frac{-y\mu\kappa R}{2}\right\} J_0\left(Q_{\|}\sqrt{1-\mu^2}\, yR\right) dy \\ +i\int_{\vartheta}^{1} y^2 \sin\left(Q_{\perp} y\mu R\right) \exp\left\{\frac{-y\mu\kappa R}{2}\right\} J_0\left(Q_{\|}\sqrt{1-\mu^2}\, yR\right) dy \end{array} \right] \right) \quad (3.14)$$

For hollow penetrable shells, the scattering length density ρ_C has to be set to the value of the solvent.

The rough particles used in some of the experiments can be thought of as the limiting case of core shell particles where the size of the spherical core is very large compared to the asperities, which in turn, are distributed randomly over the spherical surface. Thereby creating an effective outer layer with a very small thickness compared to the used wavelength, and a scattering length density between the values of the solvent and the particle material. For this kind of particles, the form amplitude can be approximated by Eq. 3.14 using an adjustable value for the scattering length density of the shell.

3.2 Total Internal Reflection Microscopy (TIRM)

This technique allows the measurement of the static interaction potential of a single colloidal sphere with a hard wall, which in this case is a glass surface. Additionally, the measured intensity trace can be used to compute the particles' near-wall dynamics, specifically the normalized diffusion coefficient $D_{\perp}(h)/D_0$ and the drift velocity $v_{\text{drift}}(h)$, both perpendicular to the wall. In the following, the fundamentals of the technique and its experimental implementation are presented. At the end of the

subchapter, the methodological approach to tackling inevitable noise effects (shot and background) in TIRM experiments is shown.

3.2.1 TIRM conceptualization and analytical foundations

In a TIRM experiment, a colloidal sphere located within the evanescent field scatters this electromagnetic radiation in the form of light ($I \propto E^2$). The intensity is expressed in photon counts per second, and units typically in kHz. Changes in the particle-wall separation distance h, are seen as fluctuations in the intensity of the scattered light I_S. Meanwhile, it is assumed that parallel motion does not affect intensity. The relation between the intensity of the scattered light with height is given by:

$$I_S(h) = I_0 \exp\left[-h/\kappa\right] \qquad (3.15)$$

where I_0 is the maximum scattered intensity when the particle is touching the glass: $I_S(h=0) \equiv I_0$.

It is important to note that h is the shortest surface to surface separation, differently from the distance z used in EWDLS experiments. The two quantities are related by $z = R + h$, with R being the particle's radius.

In a typical experiment, a time intensity trace with a large number of intensity data points (~1E6) and a time resolution of Δt = 2 ms is acquired to build the histogram of intensities using small bin widths. The purpose of measuring large data sets is to make the histogram a good approximate the probability density function of intensities, which can be related to the distribution of heights (Figure 3.6) using the following relation to convert the intensity values (center bin values) to separation distances:

$$h = \kappa^{-1} \ln\left(\frac{I_0}{I_S}\right) \qquad (3.16)$$

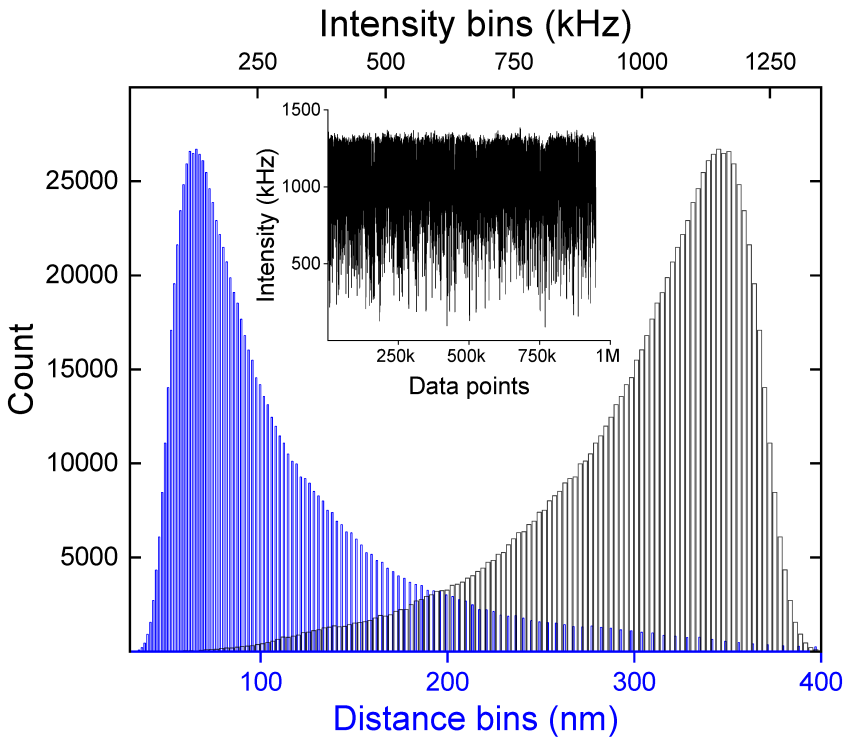

Figure 3.6. From the intensity trace (insert), a histogram of intensities (black) is obtained from which a histogram of distances (blue) is constructed via Eq. 3.16. For small enough bin widths both distributions are good approximations for probability density functions of the respective quantities. For the calculation of the interaction potential the most frequent value needs to be identified.

3.2.1.1 Particle-wall interaction potential measured by TIRM

The probability to observe any intensity value is equal to the probability that the particle is at the corresponding height:

$$p\left(I_S(h)\right)\, d\, I_S(h) = p(h)\, dh \qquad (3.17)$$

with the approximation that the histogram of intensities is a good representation of the probability density, this can be rewritten as:

$$p(h) \approx \frac{N\left(I_S\left(h_i\right)\right)}{\sum_i N\left(I_S\left(h_i\right)\right)} \frac{\partial I_S(h)}{\partial h} \tag{3.18}$$

where the first factor on the right side represents an approximation of the probability distribution of intensities as a function of height. It is determined by the ratio of occurrences of the intensity $I_S\left(h_i\right)$ with the total number of acquired intensities. Then, applying the indicated partial derivative to the expression in Eq. 3.15, the approximation becomes:

$$p(h) \approx -\left(\kappa^{-1}\right) I_0 \exp\left\{-\left(\kappa^{-1}\right) h\right\} \frac{N\left(I_S\left(h_i\right)\right)}{\sum_i N\left(I_S\left(h_i\right)\right)} \approx -I_S(h)\left(\kappa^{-1}\right) \frac{N\left(I_S\left(h_i\right)\right)}{\sum_i N\left(I_S\left(h_i\right)\right)} \tag{3.19}$$

On the other hand, the probability density function $p(h)$ is related to its potential energy by Boltzmann's law. This relation is given by:

$$p(h) = p\left(h_{\text{ref}}\right) \exp\left\{-\frac{\Delta\phi(h)}{k_B T}\right\} \tag{3.20}$$

where h_{ref} is an arbitrary chosen separation distance as reference, $\Delta\phi(h) = \phi(h) - \phi\left(h_{\text{ref}}\right)$ is the potential difference between separation distance h and h_{ref}, respectively. The thermal energy unit, $k_B T$, is given by the Boltzmann constant times the temperature T in Kelvin.

Thus, it is possible to compute the difference of the potential $\Delta\phi(h)$ in thermal units, by solving Eq. 3.20 for it. Since, Eq. 3.19 is valid for all separation distances, including the one where the potential has its minimum $h_{\min} = h_{\text{ref}}$, the ratio $p\left(h_{\min}\right) / p(h)$ can be calculated, and the potential difference is determined by:

$$\frac{\Delta\phi(h)}{k_B T} = \ln \frac{p\left(h_{\min}\right)}{p(h)} \approx \ln \frac{N\left(I\left(h_{\min}\right)\right) I\left(h_{\min}\right)}{N\left(I(h)\right) I(h)} \tag{3.21}$$

Figure 3.7 shows the potential interaction between a probe particle and the glass wall, obtained by applying the previous equation to measured data.

The particle-wall potential is mainly given by the superposition of an attractive gravitational potential $\phi_G(h)$ (Eq. 2.33) in combination with the repulsive electrostatic potential $\phi_{ER}(h)$ (Eq. 2.29). The resulting total potential has a single local minimum which is given by the particle's weight being large enough to outweigh the electrostatic repulsion force beyond a certain separation distance. For typical polystyrene probe particles, with a density difference to the solvent of $\Delta\rho$ = 55 g/ml, this is possible if their radius is in the micron range. Then, the range of the electrostatic repulsion is much smaller than the particle radius and Derjaguin approximation [42] can be applied with which the expression for the total potential simplifies to:

$$\phi(h) = B_{\mathrm{ER}} \exp\left[-h/\lambda_{\mathrm{D}}\right] + G_{\mathrm{eff}}\, h \qquad (3.22)$$

where G_{eff} is the buoyance corrected weight of the spherical particle. In some particular experiments, weak optical tweezers might be applied to avoid lateral particle motion. Then, the external force caused by the photon pressure should be included in the total interaction potential.

The electrostatic amplitude B_{ER} is a complicated variable to measure experimentally since the surface potentials of the wall and the particle are involved. However, according to Eq. 3.21, the interaction potential can be determined by the difference of potentials: $\Delta\phi(h) = \phi(h) - \phi(h_{\min})$. Noticing that Eq. 3.22 has a single minimum at $h_{\min}/\lambda_D = \ln\left[B_{\mathrm{ER}}/G_{\mathrm{eff}}\,\lambda_D\right]$ [71], the potential difference can be expressed without explicit dependence on B_{ER}:

$$\Delta\phi(h) = G_{\mathrm{eff}}\,\lambda_D\left[\exp\left\{-\left(h-h_{\min}\right)/\lambda_D\right\}-1\right] + G_{\mathrm{eff}}\left(h-h_{\min}\right) \qquad (3.23)$$

Note that in this form both sides of the equation are expressed in absolute energy units. To obtain the potential difference in thermal energy units, as required by Eq. 3.21, both sides must be divided by $k_B T$.

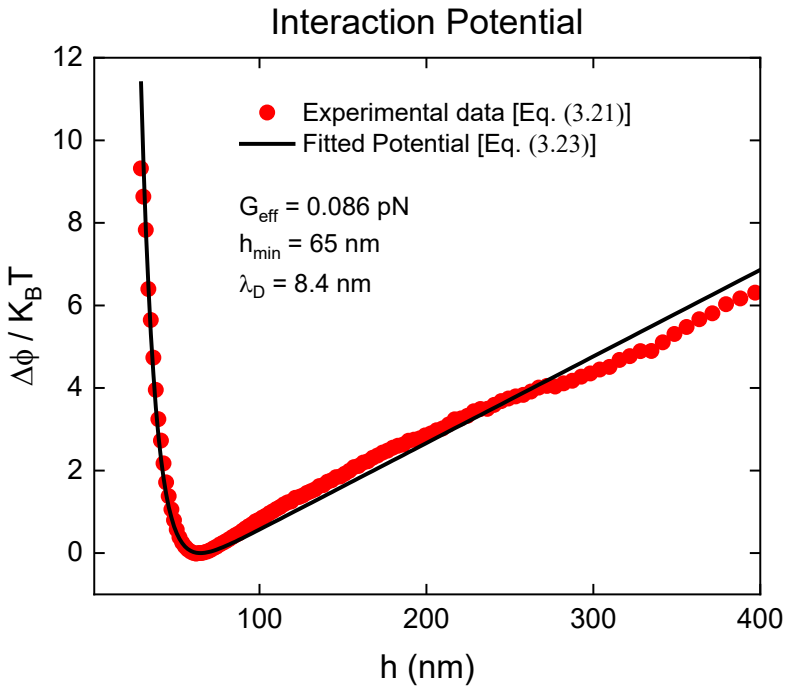

Figure 3.7. Experimentally determined interaction potential (red dots) as a function of separation distance for a Polystyrene particle with radius R = 3 µm. The solid black line is computed from non-linear least squares fitting of the model potential in Eq. 3.23. The parameters describing the potential are determined from such fitting as floating parameters: effective gravitational force (G_{eff}), height of equilibrium (h_{min}) and Debye length (λ_D).

In practice, the output of the TIRM instrument is a single row file of intensities values as photomultiplier count rates. For data analysis these were imported into the OriginPro software (version2019, 64 Bit) to use the built-in tool to make the histograms and calculate the interaction potentials according to Eq. 3.21. The physical properties describing the potential, Debye screening length (λ_D), effective gravitational force (G_{eff}) and the separation distance from the potential minimum (h_{min}), are determined by non-linear least-squares fitting, according to Eq. 3.23. An example is shown in Figure 3.7. The fitting is performed with either with the fitting tool built into OriginPro or with an algorithm coded in-house which allowed for the simultaneous fitting of multiple potentials.

3.2.1.2 Single particle near-wall dynamics measured by TIRM

The intensity traces measured with a TIRM set-up were recorded with a sampling time $\Delta t = 2$ ms and then translated into one-dimensional trajectories using Eq. 3.16. From these trajectories, the spatially resolved dynamic properties of the colloid near the wall can be calculated, specifically the local diffusion coefficient normal to the wall, $D_{\perp}(h)$, and the local drift velocity, $v_{\text{drift}}(h)$.

For simplicity, the following mathematical description is detailed according to the distance z, where $z = h + R$, being h the surface-to-surface separation distance and R the particle's radius. The results for these dynamic properties will be shown with respect to h as is customary in literature on TIRM.

As stated in Section 2.2.2, the analytical approach for single particle near-wall dynamics was proposed by de Sio *et al*. [80]. This approach is based on the derivation of a short time expansion for the mean, $m(t,z)$, and the mean-squared one-dimensional displacements, $W(t,z)$ of the particle along the surface normal. The expressions are:

$$m(t,z) = v(z)t + \frac{1}{2}\left[v(z)\frac{\partial v(z)}{\partial z} + D_{\perp}(z)\frac{\partial^2 v(z)}{\partial z^2} \right] t^2 \qquad (3.24)$$

and

$$W(t,z) = 2D_{\perp}(z)t + \left[v(z)\left(\frac{\partial D_{\perp}(z)}{\partial z} + v(z) \right) + D_{\perp}(z)\left(\frac{\partial^2 D_{\perp}(z)}{\partial z^2} + 2\frac{\partial v(z)}{\partial z} \right) \right] t^2 \qquad (3.25)$$

respectively.

It is important to note that $D_{\perp}(h)$ represent spatially resolved values of the average quantity $\langle D_{\perp} \rangle_{\kappa}$, which is measured in the EWDLS experiments. For better distinguishability, we use different notations.

Practically, $D_{\perp}(h)$ and $v_{\text{drift}}(h)$ are determined from the trajectories in two steps as sketched in Figure 3.8. Firstly, the probability distribution $p(z - z_0)$ for a particle displacement $\Delta z = z - z_0$ during a delay time is determined for a selected starting value z_0. The first and second moments of these

distributions are the mean displacement $m(t,z)$ and mean squared displacement $W(t,z)$, respectively. This procedure is repeated for various delay times.

Secondly, the initial slopes of $m(t,z_0)$ and $W(t,z_0)$ as a function of t are identified as $v_{\text{drift}}(z_0)$ and $2D_{\perp}(z_0)$ according to Eq. 3.24 and 3.25, where the subscript '0' is omitted for convenience of notation. The data analysis, for both experimental and simulated data (presented in the next subsection), is performed by using an executable program "TIRMDyn.exe", coded inhouse by Peter R. Lang, which follows the described methodology.

Analytically, the particle's drift velocity arises as a consequence of the hydrodynamic and static interactions between that particle with the wall. Then, the drift velocity is described as:

$$v_{\text{drift}}(z) = \frac{\partial D_{\perp}(z)}{dz} - \beta D_{\perp}(z) \frac{\partial \phi(h)}{\partial h} \qquad (3.26)$$

where $\beta = 1/k_B T$ is the inverse of thermal unit and the height-dependent normal diffusion coefficient, $D_{\perp}(z)$ depends on the closest distance between the particle's center of mass and the wall $z = h + R$.

The normal diffusion is calculated using the approximation by Bevan et al. [8] in Eq. 2.46, which can also be expressed in terms of the closest surface to surface separation, which is typically used in TIRM:

$$D_{\perp}(h) = D_0 \frac{6h^2 + 2hR}{6h^2 + 9hR + 2R^2} \qquad (3.27)$$

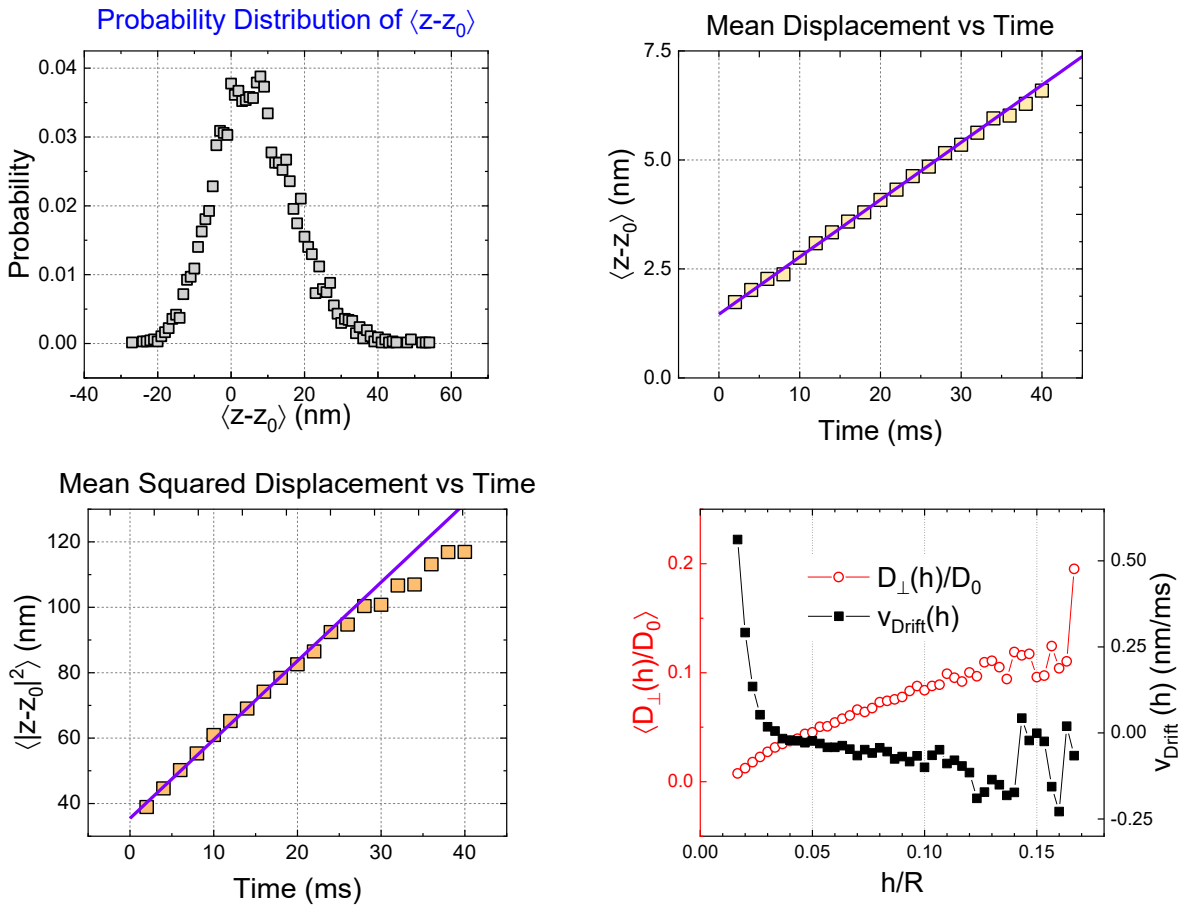

Figure 3.8. Derivation of the dynamic properties of the system. From the intensity traces, the probability distribution for displacements $z - z_0$ (top left) is calculated for a given time Δt, and repeated for progressive times. Then, the means of the distribution $\langle z - z_0 \rangle$ as a function of time are determined (top right), whereby the slope of their linear extrapolation for short times gives the drift velocity at the given h_0. Iterations over different h_0 yield the drift velocity dependence on the separation distance (bottom right, black squares). In parallel, the mean squared displacement $\langle | z - z |^2 \rangle$ as a function of delay times are computed (bottom). The slope from the linear extrapolation for short times results into twice the local normal diffusion coefficient at that given h_0. Consecutive calculations for different separation distance determine the normal diffusion profile over the separation distances (bottom right, red circles).

Recalling from Subsection 2.2.1.1, these expressions for normal diffusion and drift velocity are valid for hydrodynamic stick boundary conditions. However, as mentioned in previous chapter, due to a variety of reasons, among which roughness of the particles and/or the wall surface, can affect the friction coefficient and cause partial slip. For this case, Jeffrey and Onishi [43] introduced an expression for the

friction normal to the wall which can be translated to the near wall diffusion coefficient under partial slip conditions:

$$D_{\perp}(z)=\frac{k_B T}{A/_{\in}-B\ln(\in)+C-D\in\ln(\in)} \qquad (3.28)$$

with $\in = z/R-1$ and the parameters A to D, computed for a limited number of slip parameters (ζ) by Ekiel-Jezewska and Wajnryb [21], given in Table 2.1.

3.2.1.3 Simulated data of a particle near the wall

The simulation of a single particle diffusing near a wall is based on the algorithm suggested by Sholl et al for Brownian dynamics simulations, which in turn, it is adapted from Ermak and Buckholz [23] Brownian dynamics simulation algorithm for particles diffusing with inhomogeneous friction coefficients. There, it is considered the separation distance between the particle and the wall is only a fraction of its radius [79]. The computation of the vertical displacements of a sphere, within a time interval, considers the following: i) a distance-dependent friction coefficient; ii) a force acting on the sphere due to the static interaction with the wall, and; iii) a random term caused by Brownian motion. In this scenario, the particle displacement is given by:

$$\Delta z=-\xi^{-1}(z)\frac{\partial\phi(z)}{\partial z}\Delta t+\frac{\partial D_{\perp}(z)}{\partial z}\Delta t+\Theta\sqrt{2D_{\perp}(z)\Delta t} \qquad (3.29)$$

where $\Delta z = z(t+\Delta t)-z(t)$ is the displacement, $\xi^{-1}(z)$ is the height-dependent friction coefficient, $\phi(z)$ is the potential and Θ is a random number from a Gaussian distribution with mean zero.

In typical simulation, traces with 1E6 data points were calculated with a sampling time Δt =2 ms, among other parameters, to reproduce the conditions in a TIRM experiment. After the simulation of the one-dimensional trajectories, these are translated into scattered light traces. These can be analyzed in the same way as described above for the experimental data. Additionally, an important assumption is that within the sampling time interval the forces acting on the particle remain constant; a concept that will

be revisited later. Finally, the starting positions in the simulation were chosen to be the most probable positions which are related to the minimum value in the interaction potential.

3.2.2 TIRM experimental set-up and sample cell

The experimental set-up, built in-house, (Figure 3.9) has a 15 mW HeNe laser (λ_0 = 632.8 nm, Melles Griot, NY, USA) as the light source. The laser is mounted on a motorized goniometer (Linos, Germany), allowing precise and reproducible adjustments of the incident laser angle θ_{laser} relative to the horizontal. If necessary, a neutral density (ND) filter can be placed at the laser output to reduce illumination intensity.

The laser beam is directed onto a dove prism (n_{glass} = 1.51, BK7 glass, Edmund Optics, NJ, USA) at an incident angle and then refracted through the glass. The sample cell, made of BK7 cover slips, is attached to the prism using index-matching oil (n_{oil} = 1.51, Immersol™ 518F, Carl Zeiss Jena GmbH, Germany) to ensure continuity in refractive index between sample cell and prism. In this way, the beam travels unaffected until it reaches the glass/water interface, where total internal reflection occurs if the incident angle is properly set.

Above the sample cell, the microscope-detector system is clamped onto an X-95 rail system (Linos, Germany). An infinity corrected 40X SCLPlanFI objective (f = 6.5-8.3, NA = 0.55, Olympus, Japan) is placed over the sample cell to collect the scattered light. Additionally, this objective is used to create an optical tweezer (OT) when required, by illuminating it through its back focal plane with a green laser beam (λ_{OT} = 532 nm, Verdi V2 solid state Nd:Yag, Coherent, CA, USA).

Sitting above the objective, a dichroic mirror transmits the red light towards the detector while it reflects the green laser beam out from the observation path. Then, a 50:50 beam splitter is placed to direct equal fractions of the scattered light towards two detection systems: a photomultiplier tube (PMT) (Hamamatsu H7421-40, Hamamatsu, Japan) which is read out by a digital counter card (National Instruments, NI-6602, TX, USA), and to a CCD camera (Photometrics Cascade 1 K, AZ, USA). To optimize the signal-to-noise ratio, an 800 µm pinhole is placed in front of the PMT as spatial filter, and an

interference filter blocks unwanted wavelengths different from 632 nm. Additionally, a white light lamp is positioned below the setup allowing illumination for visualization of the sample and selecting particles for experiments.

The experimental set-up is managed by three different software packages. The planar stages, on which the set-up sits, and the goniometer on which the laser is held, are moved by the software M40Demo1 which is used for alignment and sample repositioning. To operate the camera, Micromanager 1.3 (ImageJ) allows to set the camera's parameters for live mode observation or to acquire single frames. The experiments are designed in the TIRM0.03beta.vi software, based on LabView 8.6 (National Instruments, TX, USA). With this the variables sampling time, number of data points and optical tweezer's nominal laser power can be tuned for a single or series of measurements.

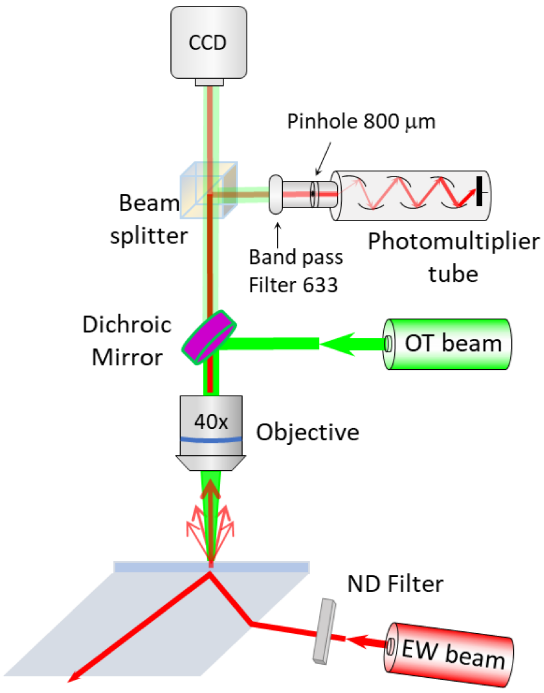

Figure 3.9. Cartoon of the TIRM experimental set-up. The totally internal reflected beam at the interface produces an evanescent wave. A colloidal particle in the vicinity of the wall scatters light, with an intensity depending on the separation distance. The scattered light is collected by an objective and guided towards a detector which measures the intensity in terms of photon counts per time.

3.2.2.1 Geometry and beam path for total internal reflection

Below, the beam path and geometry in the set-up is sketched where the total internal reflection and, consequently, the creation of the evanescent wave at the interface occurs.

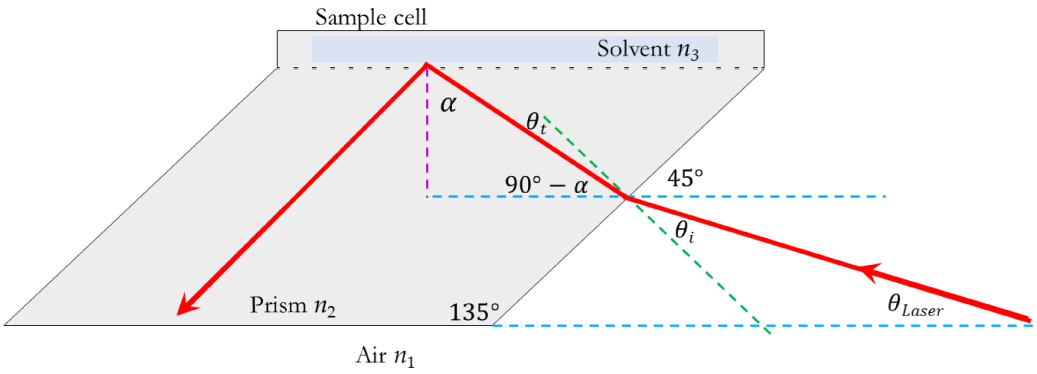

Figure 3.10. Beam path relating the laser beam direction with the incident angle for total internal reflection. Full description in the text.

The laser beam is directed at an angle θ_{laser}, with respect to the horizontal (blue dashed lines), towards the prism face where the term horizontal implies the plane of the reflecting surface. The beam hits the air/glass interface at an incidence angle θ_{i}, with respect to its normal (green dashed line) and is refracted through the glass at an angle θ_{t}, according to Snell's law. The laser beam impinges on the bottom of the sample cell, at an angle α with respect to the normal (magenta dashed line), where it is not refracted because the prism, the index-matching oil and the glass of the sample cell have the same refractive index. Thus, the beam hits the glass/solvent interface at the angle α. According to Snell's law, total internal reflection and therefore the creation of the evanescent wave occurs if, $\alpha > \alpha_C$ where $\alpha_C = \sin^{-1}\left(n_3/n_2\right)$ is the critical angle of total reflection.

In Figure 3.10, a geometrical sketch is presented to analyze geometrically the relation of angle α in terms of the laser's angle θ_{laser}. First, the laser beam, the horizontal and the normal to the prism face form a triangle with an obtuse angle of 135°, thus, $\theta_{\text{i}} = 45° - \theta_{\text{laser}}$. Next, the direction of the beam within the prism is calculated by Snell's law:

$$\theta_t = \sin^{-1}\left[\frac{n_1}{n_2}\sin\theta_i\right]$$

Further, θ_t can be related to α by analyzing the right-angled triangle made by the horizontal line at the center, the vertical line and the beam propagation line as the hypotenuse. The interior angles α, $90° - \alpha$ and the right angle, define this triangle as shown in the figure. It follows thus:

$$\alpha = 45° + \theta_t$$

Eventually, the relationship between the angles θ_{laser} and α through θ_t is obtained by combining the previous expressions:

$$\theta_{\text{laser}} = 45° - \sin^{-1}\left[\frac{n_2}{n_1}\sin(\alpha - 45°)\right] \quad (3.30)$$

Or inversely,

$$\alpha = \sin^{-1}\left[\frac{n_1}{n_2}\sin(45° - \theta_{\text{laser}})\right] \quad (3.31)$$

In this way, it is possible to experimentally adjust the laser's incident angle to achieve a specific incident angle at the interface, and hence, the required penetration depth.

3.2.2.2 Sample cell

The sample cell is built using BK7 squared coverslips (Menzel-Gläser, Germany) 20x20 mm^2 as for the bottom part and 18x18 mm^2 for the top cover. These coverslips are centered and glued together by means of a double-sided adhesive spacer with 120 µm thickness (SecureSeal imaging spacers, sku: 654008, Grace Bio-Labs, OR, USA) leaving two open sides as illustrated in Figure 3.11, and in this way, facilitates the filling of the cell. In the following the cleaning procedure and assembly process of the sample cell are described.

The glass coverslips are cleaned before assembly following this procedure: the coverslips are placed in a Teflon rack (Wash-N-Dry™ coverslip rack, Merck KGaA, Germany) inside a glass beaker. The container is filled with Milli-Q grade water and placed into a sonication bath for 45 minutes. Afterwards, the glasses are rinsed three times with pure Milli-Q water (electrical resistivity = 18.2 MΩ cm and total organic counts: 2 ppb). Next, the water is exchanged for ethanol, and the sonication and rinsing steps are repeated following the same procedure as for the water step. The water/ethanol cleaning cycle is performed three times. After that, each coverslip is dried by blowing dry nitrogen gas at high pressure along the surface. Finally, the glasses are treated in a plasma cleaner (miniFlecto-PC-MFC, Plasma Technology GmbH, Germany) for five minutes under vacuum (0.2 mbar) to remove any residues from the previous steps.

The sample cell assembly is carried out as follows: as shown in Figure 3.11, a complete piece of spacer is cut into four equal pieces along the shorter length, resulting in smaller strips with two holes in each one. Then, one of these strips is cut in half again along the new longer side. Next, these strips are placed on the opposite edges of the smaller coverslip. After removing the protective plastic film from the spacer strips, the smaller coverslip is carefully placed and centered on top of the larger coverslip. In this way, there is enough space between the coverslips which can be filled with approximately 40 µl of the suspension containing the probe particles. Finally, the openings are sealed by adding small amounts of UV-curable glue (Norland Optical Adhesive 81, NJ, USA) along the slits. The sample cell is then placed under a UV-lamp for about two minutes to harden the glue.

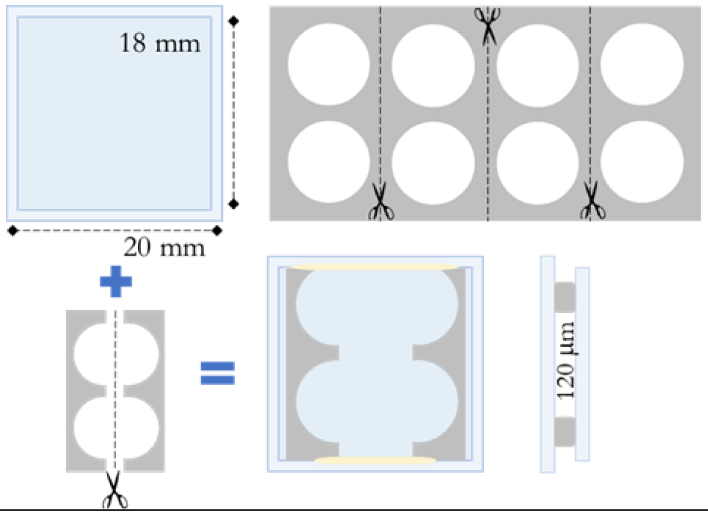

Figure 3.11. Material elements that make up the TIRM sample cell. Two centered cover slips are glued together by a spacer. The space inside can be filled with 40-45 µl colloidal suspension. The sealing (yellow patches) is done by adding UV-curable glue along the openings and placing the sample cell under a UV light source for two minutes.

3.2.2.3 Experimental procedure

Typically, in a TIRM experiment, the penetration depth of the evanescent field, κ^{-1}, can be set in a range between 100 to 400 nm by varying the incident angle α. For the experiments discussed here, the incident angle was set to reach κ^{-1} ~ 200 nm. This value was later refined through a calibration process, where the experimental potential data of a spherical particle with a known radius and mass density, suspended in a NaCl solution of known concentration, was fitted according to Eq. 3.23. Then, κ^{-1} was varied until the fitted parameters matched the expected values for the particle's weight force and the Debye screening length of the aqueous medium. Explicitly, a Polystyrene (PS) particle of 3 µm nominal radius experiences a buoyancy-corrected weight force G = 55 fN when immersed in a 1 mM NaCl aqueous solution, which has a λ_D = 9.6 nm. As a result of this procedure, a value of κ^{-1} = 200.4 nm was found to yield the expected nominal parameters. The precise determination of the penetration depth is crucial since it directly affects the calculation of interaction potentials, and hence, the dynamic properties of the system.

The sampling time for all experiments was chosen to Δt = 2 ms since both, literature and prior experience, indicate that this time frame is reasonable to measure accurate potential profiles for particles with a 3 µm radius. To ensure a reliable statistical analysis, the number of data points to

measure were set to 1E6 (duration of ~33 min at that given Δt). Having this huge number of points ensures that the histogram of scattered intensities is a good approximation for their probability density.

The reference intensity value, I_0, is needed for later TIRM data analysis and is performed by measuring probe particles in a dedicated sample. To prepare such a sample cell, the bottom coverslip is placed on a hot plate at 50 °C (below polystyrene melting temperature). Then, 40 µl of the colloidal suspension in pure water is deposited onto the coverslip, allowing the liquid to evaporate. During this step, a beaker is placed over the coverslip to avoid contamination by dust. Once the liquid residues are no longer visible, the sample cell is assembled as previously described and filled with the aqueous solution used in the experiments. This sample is then placed in the TIRM setup to measure the intensity of light scattered by individual immobile particles that have adhered to the glass/solution interface. By following the above-mentioned experimental settings, the intensity traces are measured from at least five different particles and averaged to yield the reference intensity value.

Finally, the sample of interest is placed into the set-up and a single particle has to be identified. Ideally, if a particle is isolated from other particles within the field of view, it is selected for the experiment. Then, weak optical tweezers are introduced to prevent the particle from diffusing parallel to the wall. To check whether the particle is mobile (i.e. not adsorbed to the interface), a short preliminary test is performed accumulating 1.5E5 data points (~5 min). Afterwards, a background signal measurement resulting in 6E4 data points (~2 min) is done to ensure that background scattering is $\leq$ 1% of the test's average signal. Subsequently, series of measurements are performed by increasing progressively the optical tweezer power: starting at 10 mW and continuing with 30 mW up to 60 mW in steps of 5 mW. In the end, a measurement without optical tweezers (00 mW) is made. Once finished, the experiment is repeated on at least four additional particles within the same sample cell.

3.3 Examination of background and shot noise in TIRM experiments

In any TIRM experiment, inherent technical noises are always present while measuring, affecting the raw intensity traces. Here, the two unavoidable noise sources are the background noise, and the

detector shot noise. These artifacts influence the reliability of the measured parameters that describe the static interaction potential of a particle near the wall.

Background noise arises from uncorrelated scattered light originating from other entities different from the particle [67]. The background noise contribution can be minimized down to a range significantly smaller than 1% of the particle scattered light. Meanwhile, shot noise results from the detector's statistical nature of photon detection [17]. For this case, within a given time interval in a measurement, the probability of detecting ' n ' photons follows a Poisson distribution which has a finite width. This means an introduction of intrinsic uncertainty. Unlike background noise, shot noise cannot be reduced experimentally.

To investigate the impact of these noise contributions on the static and dynamic properties of systems measured by TIRM, Brownian dynamic simulations with additional considerations were carried out. To this end, the noise is introduced at the intensity trace level by making use of Eq. 3.15 to convert simulated trajectories into time-trace intensities. For shot noise, an intensity value $I_S(t_i)$ is replaced by a random value from a Poisson distribution with a mean value $I_S(t_i)$. Likewise, background noise is implemented by first running a short simulation (1E4 data points) to calculate the mean intensity value $\langle I_S(test)\rangle$. Then, a random intensity value $I_S(t_i)$ is substituted by another from a Poisson distribution with a mean value of $(1-S/N)\times\langle I_S(test)\rangle$, where the ratio S/N is the particle's scattering intensity (signal) over the averaged background intensity (noise). Subsequently, the noisy intensity traces are translated into height trajectories by means of Eq. 3.16, allowing for further analysis of the system's static and dynamic properties as described in Section 3.2.1.

3.4 Samples and characterization

3.4.1 Silica particles with different morphology used in EWDLS experiments: smooth, rough and hollow silica particles

Briefly, the rough silica particles (RSi) are produced in a two-step process of hetero aggregation, where smaller silica particles are added onto the bigger smooth silica particles (SSi). Then, a thin smoothing

coating layer is applied to control the asperities and prevent the small particles from detachment [40, 99]. The hollow silica particles (HSi) particles are synthesized by growing a silica shell around monodisperse polystyrene particles which, in a subsequent step, are calcinated leaving behind the porous hollow shells (two-step Stöber synthesis protocol) [76].

To remove dust contaminants and eliminate clusters of particles, the suspensions containing one particle type were dispersed in Milli-Q grade water (electrical resistivity = 18.2 MΩ cm; MerckMillipore, Merkc KGaA, Germany) and treated with three cycles of gentle centrifugation at 800 rpm for 16 hours (GA-6 fixed angle 35°, radius 137 mm; Allegra 6R, Beckman Coulter). After each cycle, taking the supernatant was collected, leaving the contaminants and clusters at the bottom. Due to unavoidable carbon dioxide adsorption into the water, the relative ion concentration is estimated to be C_{CO_2} ~10^{-5} mol/ L resulting in approximate Debye length of λ_D = 96 nm.

Further, complementary characterization of particles in suspension is performed by means conventional static (SLS) and dynamic light scattering (DLS) with a commercial instrument from ALV-Laservertriebsgesellschaft (Langen, Germany) equipped with a 632.8 nm HeNe Laser as the light source, an automated attenuation system, a PerkinElmer avalanche diode and an ALV-6000 correlator. The aim is to determine the particles' diffusion coefficient in bulk, D_0, and the hydrodynamic radius R_H. Furthermore, the cryo-TEM experiments give visual evidence of particles' morphology (Figure 3.12) and, their sizes listed in Table 3.1.

	Smooth particles (SSi)	**Rough particles (RSi)**	**Hollow particles (HSi)**
$\langle R_H \rangle$	77	86	154
$\langle R \rangle_{SLS}$	69 +/- 0.05	-	142 +/- 0.02
$\langle R \rangle_{TEM}$	65 +/- 0.08	65 +/- 0.15	142 +/- 0.03

Table 3.1. Averaged values of the particles' radii measured with different techniques. The hydrodynamic radii R_H determined by DLS are in the first row. Second row for measurements determined by SLS experiments. Third row displays the values obtained by analyzing TEM images.

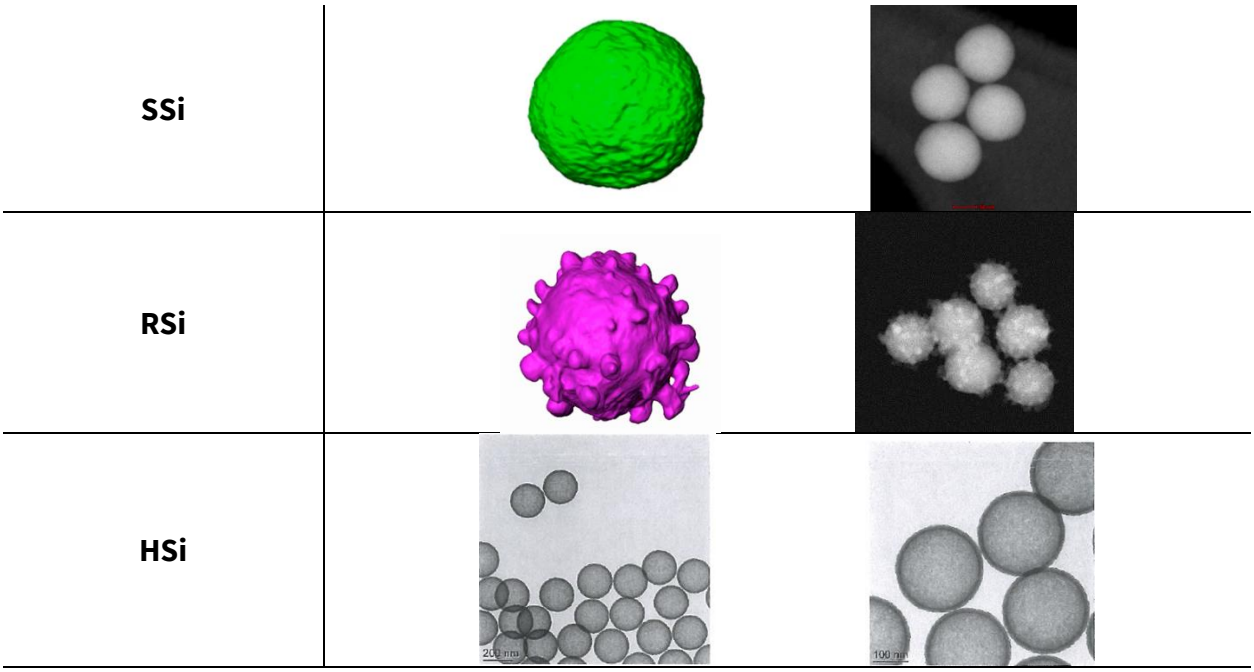

Figure 3.12. *Top and middle row*: Three-dimensional reconstructed images (left) and micrographs (right) of the smooth (top) and rough (middle) silica particles. *Bottom row*: TEM images of the hollow particles at different magnification. Reproduced from Ref. [75] with permission from the Royal Society of Chemistry under the CC BY-NC 3.0 license.

3.4.2 Micron-sized Polystyrene particles and walls used in TIRM experiments

3.4.2.1 Colloidal polystyrene particles

Two different colloidal suspensions were investigated in the experiments. The first sample consisted of polystyrene (PS) spheres with nominal radius of 3 µm (Cat. No. 4206A, Duke Scientific Cooperation, USA) which were previously dialyzed against milli-Q grade water (Resistivity = 18 MΩ cm, Merck KGaA, Germany) and diluted for a concentration of 0.1 % w/solids.

The second colloidal sample consisted of Streptavidin-coated PS particles with nominal radius of 2.5 µm (Cat. No. CP01006, Bangs Laboratories, Inc., USA). These particles were cleaned according to manufacturer's recommended procedure [4], which involves pelleting by centrifugation and resuspension cycles for particles larger than 500 nm. Specifically, for protein-coated particles between 1 to 5 µm in diameter, the applicable relative centrifugal force range should be 5500 to 8000 G's, which corresponds to 8210 to 9900 RPM for a 7.3 cm radius centrifuge.

However, these suggestions were adapted and performed as follows: an aliquot from the stock solution at 1% is diluted 100-fold in milli-Q water to a final volume of 1 ml in a plastic centrifuge tube (European Cat. No. 211-0319, VWR International, LLC., USA). The tubes were placed in a benchtop centrifuge (Eppendorf 5417R, rotor FA-45-30-11, max radius 9.5 cm and fixed angle 45°, Eppendorf Corporate, Germany) and spun at 5500 G for 7 minutes at a constant temperature of 6 °C. After centrifugation, 500 µl of the supernatant was removed, and the pellet was resuspended by adding 500 µm of fresh aqueous solution. This procedure was repeated three times before using the particles in TIRM experiments.

The cleaning process was tested using different aqueous solutions to assess their feasibility for TIRM experiments and their impact on the protein coating, which was examined using TEM. The washing solutions tested were Milli-Q grade water, Phosphate Buffer Saline (PBS) (tablet-based, item: 00-3002, Invitrogen, USA), and PBS diluted 1000-fold (~1.5 mM NaCl and 0.1 mM PO_4^{-3}).

Initial DLS measurements gave insights into the stability of the samples. The PBS-containing samples exhibited wide intensity correlation functions with broad distribution of decay times and high intensity peaks. This indicated instabilities due to particle aggregation, suggesting that PBS might not be an ideal washing solution for maintaining colloidal stability.

For TIRM tests, the previously mentioned prepared samples were further diluted with their corresponding washing solutions to reach a particle concentration of 1E-3% w/solids. The samples were then observed in TIRM setup in a sample cell with uncoated walls. The tests showed that PBS and diluted PBS-samples were unsuitable, as the colloids stuck to the bottom surface, being immobile and then unusable for experiments. As a result, only particles suspended in water were considered for further studies.

The in-depth visualizations of these particles were performed using an in-house TEM microscopy setup (Zeiss Libra 120, 120 kV, Carl Zeiss AG, Germany). For this purpose, carbon-coated cupper grids (Art. No. S160, Plano GmbH, Germany) were used to load both bare PS particles or Streptavidin-coated PS particles. TEM images (Figure 3.13) revealed morphological differences between the two types of particles. Bare PS particles exhibited a nearly circular shape whereas Streptavidin-coated particles showed some surface irregularities, appearing with noticeable bumps. Interestingly, no appreciable differences were observed between unwashed and centrifuge-washed particles, suggesting that the variations in the surface morphology are likely to be due to differences in synthesis quality between the

two manufacturers rather than the washing procedure. Additionally, the protein layer was not visibly distinguishable at the micron size range.

As a result of the previous tests, and in addition with the requirement to have a defined electrolyte concentration present in the solvent, the preparation of the final colloidal suspensions was done by diluting the cleaned particles ten times to a final concentration of 1E-3% w/s in 1 mM NaCl aqueous solution.

	PS particles	**Streptavidin-coated PS particles**
Centrifugation	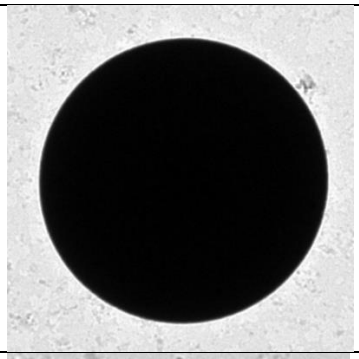	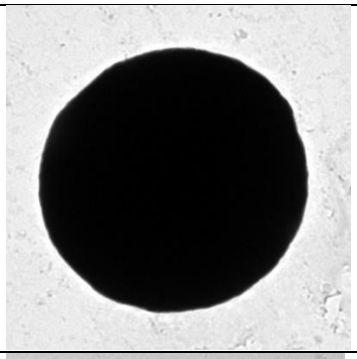
No Centrifugation	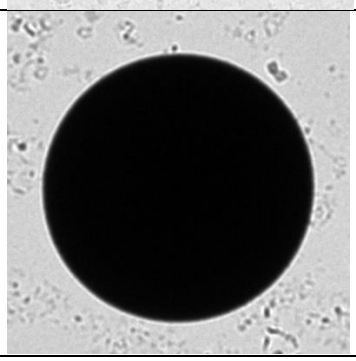	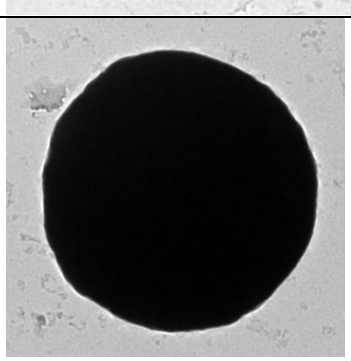

Figure 3.13. Images obtained by Transmission Electron Microscopy (TEM) of colloidal polystyrene particles (3 µm nominal radius) and Streptavidin-coated polystyrene particles (2.5 µm nominal radius), compared when washed and unwashed.

3.4.2.2 Coated walls

To investigate the influence of the wall characteristics, the bottom glass of the sample cell was pre-treated to achieve specific surface functionalization. Three types of sample cells having distinct surface properties were prepared. The first surface was the bare glass (coverslips borosilicate hydrolytic class

1, ThermoFisher Menzel-Gläser, Germany), cleaned as previously described. The second surface consisted of hydrophobically coated glass, treated with Sigmacote® (Sigma-Aldrich Co. LLC, Merck KGaA, Germany) which gives hydrophobic properties. And for documentation purposes (see 6.2 Supplementary Information), a third surface consisted of supported lipid bilayers (SLB) of 1,2-dipalmitoyl-sn-glycero-3-phosphocholine (DPPC) phospholipids, fabricated using the Langmuir-Blodgett and Langmuir-Schaefer techniques.

For the bare glass and the hydrophobically coated glass, the sample cells were assembled as usual according to the procedure described earlier. However, the preparation of SLB and its assembly onto the sample cell required a different protocol, as shown in 6.2 Supplementary Information. Below, the preparation and characterization of the hydrophobically coated glass is presented.

Sigmacote-coating on glass

Procedure: Sigmacote® is a ready-to-use product consisting of a siliconizing liquid reagent, (chlorinated organopolysiloxane in heptane). Upon application to glass surfaces, it instantly forms a thin organic film due to covalent bonds, providing hydrophobic properties on such surfaces. Additional information and chemical specifications about this product are not available due to patent restrictions and a vague product description. However, this product is widely used to avoid the adhesion of cells onto glass surfaces.

The procedure for coating pre-cleaned glass with Sigmacote® is the following: A freshly plasma-cleaned coverslip glass is placed on a disposable weighing tray (Rotilabo^{R}, Carl Roth GmbH+Co. KG, Germany), and a sufficient amount of Sigmacote® is applied to fully cover the surface. Then, after resting for one minute, the glass is flipped over and left in contact with the reagent for an additional minute. Next, the glass is removed from the solution and thoroughly rinsed on both sides with Milli-Q grade water until any ring-shaped light patterns or stain-like residues are no longer visible. Finally, the glass is blow dried with dry nitrogen and stored in a coverslips rack covered with a beaker and sealed until use.

Characterization method: The coating on the coverslip glass and the bare glass walls were characterized by means of X-ray reflectivity (XRR) measurements, performed in in-house in cooperation with JCNS 2/ PGI 4, of Forschungszentrum Jülich GmbH. Briefly, in XRR experiments [15, 53, 77], the specular intensity of a monochromatic and collimated X-ray beam that is partially reflected at the sample surface or interface is measured under specular conditions. This means that the incident and

reflected beams lie in the same plane and the resulted scattering vector, $\boldsymbol{Q}_Z$, is oriented perpendicular to the surface (Figure 3.14 top left). To meet these conditions, the incident beam has an angle θ_i (typically less than 5°) and the reflected angle satisfies $\theta_i = \theta_f$ when in total external reflection conditions $\theta_i < \theta_C$, being θ_C the critical angle that depends on the material refractive index and X-ray wavelength.

When the incident beam is $\theta_i > \theta_C$ impinging a single, homogeneous and flat layer, it is reflected and refracted at the interfaces (Figure 3.14 top right). These beams interfere constructively and destructively, producing oscillations in the reflected intensity known as Kiessig fringes, whose periodicity is directly related to the layer thickness. The amplitude and shape of the reflectivity curve are influenced by surface/interface roughness and electron density (Figure 3.14 bottom panel). In this way, XRR allows for the characterization of surfaces, layered-surfaces and interfaces through the fitting the experimental reflectivity to determine thickness, roughness and electron density.

Reflectivity profiles are usually presented according to the wave vector Q_Z perpendicular to the surface. This is defined as the difference between the incident ($\boldsymbol{k}_i$) and reflected ($\boldsymbol{k}_f$) beam wave vectors: $\boldsymbol{Q}_Z = \boldsymbol{k}_f - \boldsymbol{k}_i$. Since the magnitude of the wave vector $|\boldsymbol{k}| = 2\pi / \lambda$, the magnitude of $|\boldsymbol{Q}_Z| \equiv Q_Z = 4\pi \sin(\theta_i)/\lambda$.

Instrumentation: The setup consists of a Brucker AXS reflectometer D8 Advance (Brucker Corporation, Germany) with an X-ray wavelength of λ_0 = 1.54 Angstrom (Å), corresponding to Cu-Kα line. There, the X-ray beam is directed at small angles (θ_i) toward a solid surface and the reflected intensity is measured under specular conditions ($\theta_i = \theta_f$). For layered structures, the measured intensity is modulated by the interference of reflections at the interfaces between the layers, allowing for the retrieval of information about layers thickness and roughness.

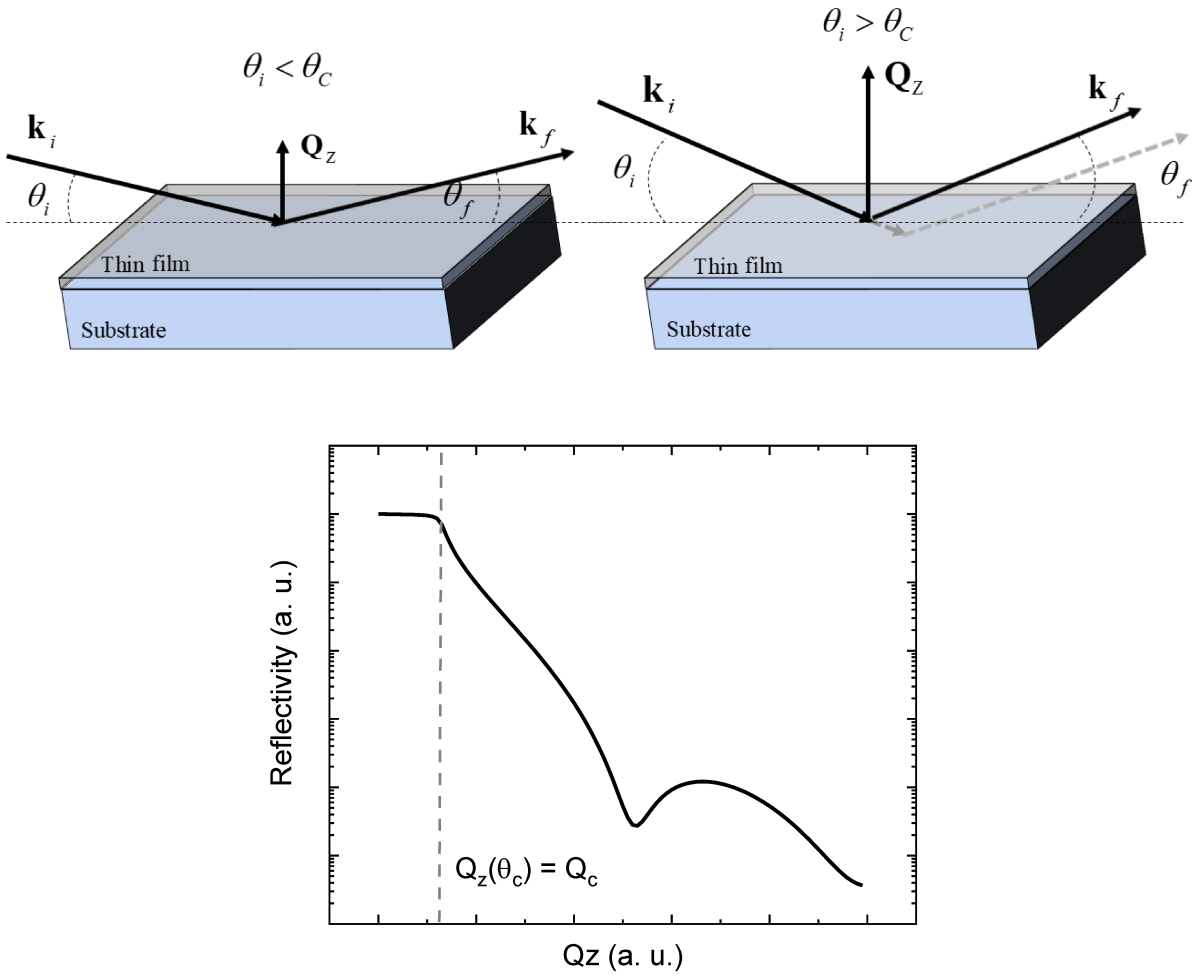

Figure 3.14. Sketch of the geometry involved in X-ray reflectivity. Top left: the incident wave vector of the beam (k_i) has with it an angle smaller than the critical angle (θ_C), resulting in total external reflection at the surface with a wave vector k_f. Top right: the incident wave vector has with it an angle above the critical angle, leading to partial refraction and reflection at the next interface. Bottom: calculated reflectivity curve for a hypothetical single-layer sample. The position of the critical wave vector, corresponding to the critical angle, is indicated with a dashed line.

The samples were tested in "$\theta - 2\theta$ scanning" mode, starting from 0.1° to 7° in steps of 0.02°, with the critical angle at 2θ = 0.4°. Data analysis was done using Parratt32 "The Reflectivity Tool" v1.5.2 software (1997-99 Christian Braun, Hahn-Meitner-Institut, Berlin Neutron Scattering Center, Germany) which fits the curves following the Parratt formalism [68].

Resulting parameters: X-ray reflectivity measurements were performed on each type of substrate at the air interface, and the corresponding reflectivity curves were averaged. The mean reflectivity curve of the bare glass was fitted to determine the bulk's SLD. For the Sigmacote-coated glass, it was assumed that Sigmacote coating formed a single layer of carbon-hydrogen being on top of the bulk. In both cases, a constant background noise of 1E-6 was included.

Typically, the composition of borosilicate is 75% SiO2, 10% B2O3, 6% NaO+K2O, 5% Al2O3 [1]. By using the NIST calculator [48], the scattering length density (SLD) for this composition (*75SiO2 10B2O3 5NaO 1K2O 5Al2O3*) was determined based on a mass density of 2.23 g/cm3 [48], thickness of 1 cm and "Cu Ka" as the X- ray source (λ = 1.54 Å). The calculated SLD values were 19E-6 $Å^{-2}$ for the real part and 0.278E-6 $Å^{-2}$ for the imaginary part.

For the bare glass samples (bulk), the input parameters were SLD = 19E-6 $Å^{-2}$, roughness of 5 Å and the SLD imaginary part of 1.05E-11 $Å^{-2}$ (default value). The reflectivity curves are displayed in Figure 3.15 top panel while the parameters obtained from the fitting are listed in Table 3.2. Then, it turned out that the bulk exhibited a SLD = 23E-6 $Å^{-2}$ and zero roughness.

The input parameters for the Sigmacote-coated glass samples introduced the substrate's SLD = 23E-6 $Å^{-2}$ as fixed parameter. The input parameters for the layer included a starting thickness of 20 Å and a fixed SLD = 8.5E-6 $Å^{-2}$, which is related to that of a layer of carbon-hydrogen, as expected the hydrophobic coating to follow. The SLD imaginary part of 1.05E-11 $Å^{-2}$ (default value) and a roughness of 5 Å. The related reflectivity curves are shown in Figure 3.15 bottom panel while the parameters obtained from the fitting are listed in Table 3.2. The resulting parameters of the hydrophobic coating yielded a thickness of 15 Å and zero roughness.

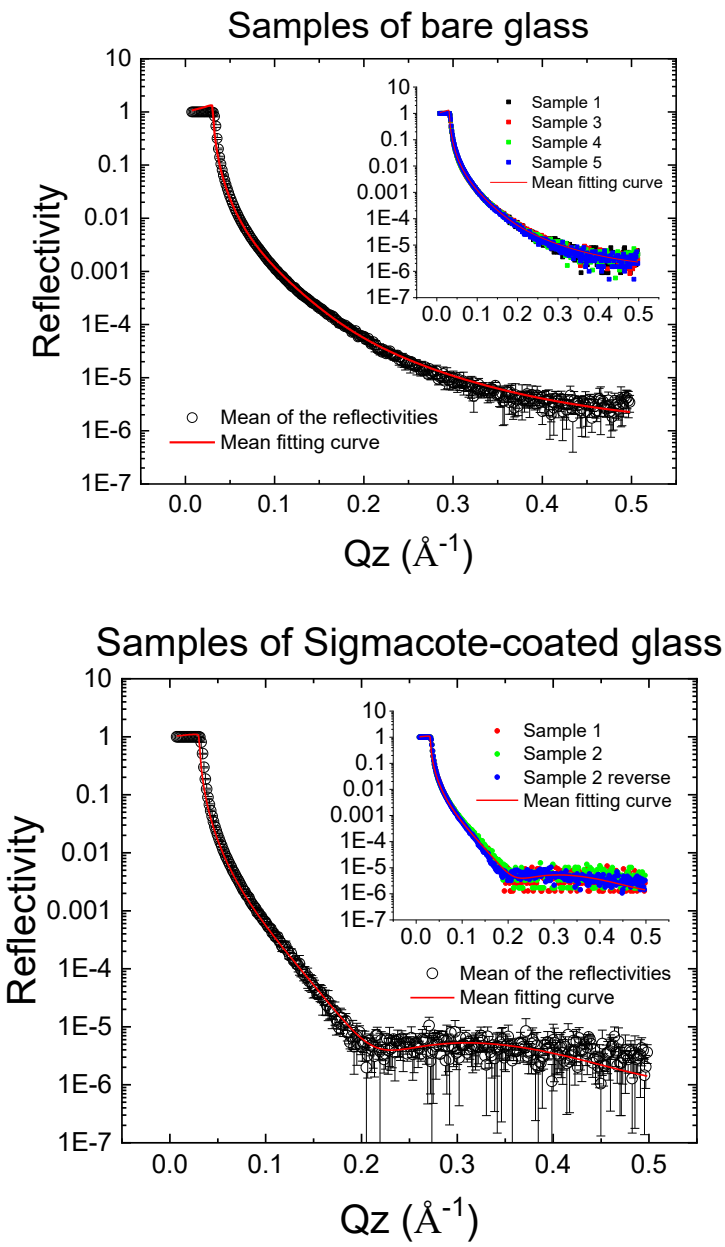

Figure 3.15. Mean reflectivity curves of the samples bare glass (top) and Sigmacote-coated glass (bottom) fitted accordingly as described in the main text. Insets: Individual reflectivity curves along with the mean fitting curve (red line).

Samples		Thickness (Å)	SLD (Å^{-2})	Roughness (Å)
Bare glass	Bulk	N/A	23E-6	0
Sigmacote-coated glass	Layer 1	15	8.5E-6	0
	Bulk	N/A	23E-6	0

Table 3.2. Parameters determined by fitting the mean of the reflectivity profiles of the samples.

4 Results

The first study explores the near-wall dynamic behavior of silica particles with different surface morphology by means of evanescent wave dynamic light scattering. The probe particles of interest had smooth and rough surfaces while others were porous, hollow shells. Their diffusion coefficient components parallel and normal to the interface were measured. While smooth surface particles followed Brenner's model prediction for near-wall dynamics with stick boundary conditions within the experimental error, the major finding was the significant slowdown of rough particles' dynamics compared to the aforementioned model [28, 37]. Such difference in dynamics contrasts with theoretical hydrodynamic expectations [52] since it is expected that rough surfaces reduce the hydrodynamic resistance, thus, rough particles would move faster than smooth particles with the same hydrodynamic radius. To tackle this controversy, numerical calculations for near-wall dynamics, based on particle-wall interaction potentials, were performed. The numerical calculations showed that, in order to reproduce the experimental behavior of rough particles, an increase in the attractive part of the potential has to be considered. This means a reduction of the stabilization barrier amplitude of the DLVO potential occurs, allowing the particles to get closer to the wall and by that reducing their dynamics.

The second research project aims to investigate the effects of surface modifications (particle and the wall) on the interaction potential and the near-wall dynamics at a single particle level. By means of total internal reflection microscopy (TIRM), the systems' interaction potentials and dynamics (diffusion coefficients and drift velocity) were determined. These properties of the system bare polystyrene colloidal particles near the bare glass wall were compared to those of similar particles near hydrophobically coated glass. Similarly, Streptavidin-coated polystyrene particles close to both types of walls were measured to determine their near-wall properties. However, the protein-coated particles showed a peculiar behavior in the vicinity of hydrophobically coated walls that required to change the experimental conditions to measure their near-wall properties properly.

4.1 The effect of surface morphology and particle-wall interactions on the near-wall dynamics

4.1.1 Experimental near-wall dynamics

The near-wall diffusion constants, parallel and normal to the wall, of small sized colloidal particles in suspensions were measured by evanescent wave dynamic light scattering (EWDLS). Polystyrene beads (S-PS) were used to test the methodology. Then, silica particles that have specific morphology of interest, smooth (SSi), rough surfaces (RSi) and porous shells (HSi), were investigated. The experimental parallel diffusion constants $D_{\parallel}$ are shown in Figure 4.1 top panel and the normal diffusion constants $D_{\perp}$ in Figure 4.1 bottom panel. To facilitate comparison of the datasets, both diffusion constants components are displayed normalized with the diffusion coefficient in bulk D_0 and the penetration depth is normalized by the particles' hydrodynamic radius in bulk R_H.

4.1.1.1 Models and experimental reference data

To illustrate the reliability and the error range of the method, the results of the near-wall dynamics of polystyrene particles (S-PS) in suspension with Debye lengths of λ_D = 30 nm (black rhombus), and λ_D = 3 nm (red rhombus) [33] are presented in Figure 4.1. Data on the parallel diffusion of S-PS at λ_D = 3 nm, within the experimental error, followed the theoretical prediction (solid line) and numerical calculations (blue asterisks) for the near-wall dynamics of hard spheres [28]. The data of S-PS experimental with λ_D = 30 nm, except for an outlier at the smallest penetration depth, closely followed the numerical calculations by Holmqvist *et al.* (2007) [33] (dotted line), which combines the hydrodynamics of a hard sphere and the increased range of the electrostatic repulsion (with an amplitude of $B_{ER} = 100\, k_B T$) between the wall and the particles. Therefore, experimental information acquired by EWDLS is considered to be reliable to a certain extent.

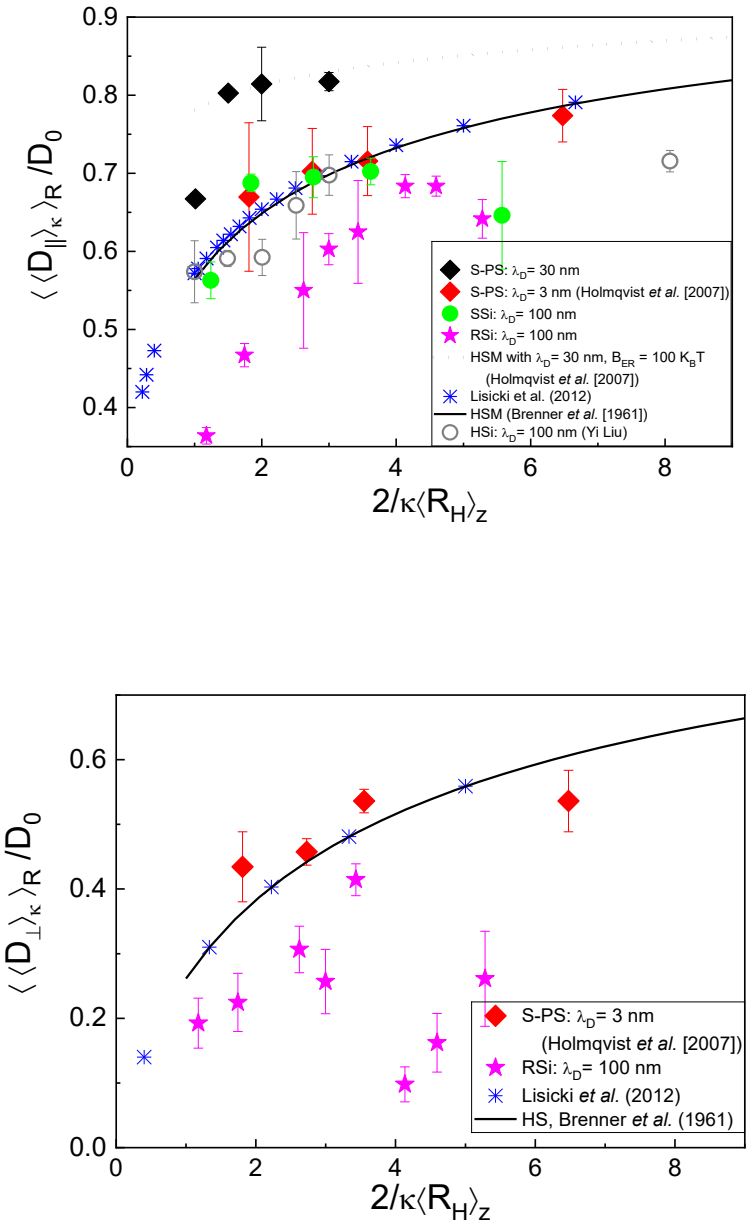

Figure 4.1. Top panel: normalized parallel diffusion coefficients versus normalized penetration depth for various kinds of colloidal particles (see legend). Reproduced from Ref. [75] with permission from the Royal Society of Chemistry under the CC BY-NC 3.0 license. Additionally, calculated data for hard spheres' model (Eq. 3.8 and 3.9) [28, 37], Liscki et al. (2012) [58] and Holmqvist et al. (2007) [33] are displayed for comparison. Symbols are averages of the results of three consecutive measurements while the error bars represent the corresponding standard deviation. Bottom panel: normalized normal diffusion coefficients versus normalized penetration depth of selected particle systems (see legend) with additional calculated reference data in Faxen (1923); Brenner (1961); Lisicki et al. (2012); Holmqvinst et al. (2007).

4.1.1.2 *Experimental data of particles of interest*

The data for smooth silica particles shown in Figure 4.1 top panel (SSi, green circles), except for the last point at the largest normalized penetration depth, exhibited dynamics similar to the Brenner's theoretical model for hard spheres. Such resemblance is observed despite the difference in the Debye lengths of approximately 90 nm. In the case of hollow particles (HSi in open gray circles; data from Yi Liu [75]), the data followed the trend of the hard sphere dynamics but slightly slower. On the other hand, the diffusion constants of rough silica particles (RSi, magenta stars) significantly exhibited slower and steeper trend in their dynamics compared to the hard sphere model. Here, the last two points at large penetration depths are off from the trend of increasing diffusion with normalized penetration depth. However, the diffusion constants determined at large penetration depths are likely compromised due to a leakage of the primary beam into the solution which is often seen at such large penetration depths.

However, the case of RSi is of special interest. Theoretically, the hydrodynamics of rough particles have been described by the use of a hydrodynamic penetration depth due to flows going through the asperities. This reduces the flow resistance in comparison with a solid sphere with a radius R_T, being equal to the distance between the particle center and the tips of the asperities, which causes an effective reduction of the particle hydrodynamic radius. In consequence, according to Stokes-Einstein equation of diffusion, the dynamics of such rough particles is expected to be faster than the smooth particles with the nominal radius R_T. Thus, the finding that RSi particles presented slower near-wall dynamics than the SSi conflicts with hydrodynamic expectations [52, 87, 92].

Regarding the particles' diffusion constants normal to the wall (Figure 4.1, bottom panel), the available experimental data also presented similarities as their parallel counterparts: The S-PS particles (red rhomboids) resembled the model for near-wall dynamics of hard spheres (solid line and blue asterisks). On the other side, at short penetration distances, RSi particles (magenta stars) also exhibited slower diffusion than the hard sphere model. However, once again at large penetration depths, the farthest three data points broke the tendency of increasing diffusion and showed a drop of the diffusion values.

These uncertain tendencies of the normal diffusion constants can qualitatively be attributed to the fact that the light intensity acquired while measuring $g_2(t)-1$ during a $Q_\perp$-scan is even smaller than

during a $Q_{\parallel}$-scan. Thus, such low intensities can compromise the reliability of those measurements. Once mentioned these drawbacks in determining the normal diffusion coefficients from an EWDLS experiment, only the parallel diffusion coefficients are discussed in the following.

4.1.2 Numerical calculations of the near-wall dynamics

Numerical calculations for the particles' near-wall dynamics were conducted to provide a physical interpretation of the unexpected behavior exhibited by RSi particles in experiments which deviate from the predictions established by hydrodynamic theory. Briefly, the numerical calculations (Subsection 3.1.4) were based on analytical expressions for polydispersity, aggregation and particle-wall interaction potentials. Then, these factors were tuned one by one in order to elucidate their impact in the diffusion coefficients $D_{\parallel}$. Afterwards, the calculated parallel diffusion constants that closely resembled those found in the experiments were calculated by fixing the Debye length (matching the experimental value), and adjusting the parameters of polydispersity and aggregation, in addition to the potential's parameters B_{ER} and A_{H}. Finally, the physical interpretation of parameter combinations allowed to derive a qualitative explanation for the experimental observations. It is emphasized that the numerical calculations were performed, compared and discussed only for the case of $D_{\parallel}$ since the obtained experimental $D_{\perp}$ presented a considerable degree of unreliability.

4.1.2.1 The effect of polydispersity on the near-wall dynamics

The effect of polydispersity on the particles' near-wall dynamics is shown in Figure 4.2. These calculations in Eq. 3.12 and Eq. 3.13, considered the corresponding particles' near-wall scattering form amplitude $B_{\mathrm{NW}}\left(Q,R\right)$, a Gaussian-type size distribution function $P\left(R\right)$ with a mean μ, relative standard deviation σ, and the interaction potential $\phi_{\mathrm{HS}}\left(z\right)$ of hard spheres. For meaningful comparisons with the experimental data, the z-average of the diffusion coefficients resulting from the distribution of particle sizes $\left\langle\left\langle D_{\parallel}\right\rangle_{K}\right\rangle_{R}$ were determined and normalized by the z-averaged bulk diffusion

coefficient $\left\langle D_0 \right\rangle_Z$. Meanwhile, the penetration depth $2/\kappa$ was normalized by the z-average of the distribution of particle radii $\left\langle R \right\rangle_Z$.

Concerning SSi particles' dynamics, two main results are described next. In Figure 4.2 top left, the variation of the mean radius (μ = 50, 100 and 150 nm) at a constant standard deviation (σ = 0.1) is displayed. Here, at small penetration depths, these three datasets showed great similarity to the dynamics of monodisperse hard sphere model. Meanwhile, at large penetration depths, small deviations were observed where the calculated values were slightly slower than those of the hard sphere model. However, such deviations were smaller than the typical experimental error.

On the other hand, in Figure 4.2 top right, it is shown the effect of increasing standard deviation values from σ = 0 to 0.15, at a constant mean radius μ = 100 nm. The variation of standard deviation led to a systematic decrease of the mean diffusion constants compared to the monodisperse hard sphere model. When comparing both ways of modifying polydispersity, the tuning of standard deviation had a greater influence on the dynamics than the mean radius. Nevertheless, in both cases, the trend of the dynamics is not much different from the monodisperse hard spheres case.

The dynamics of HSi particles were calculated using the form amplitude of a core-shell particles according to Eq. 3.12 and 3.14, yielding the results shown in Figure 4.2 bottom panel. In this case, variations in σ showed larger influence on the particles' dynamics calculations than when tuning μ. Although the HSi diffusion constants followed similar trends as the hard sphere model, they were slightly slower than for the hard sphere case at short penetration depths. In the range between 1 and 1.5 in the normalized penetration depth, there was a crossover of the calculated dynamics and those of the HSi particles became faster than the reference system.

According to the arguments presented in Subsection 3.1.4 for calculating RSi dynamics, these particles were modelled as core shell particles with an outer thin shell. In this case, the outer radius of the shell is considered to be equal to the hydrodynamic radius of the particles, the z-average of which is used for the normalization of the penetration depth. Therefore, with regard to the adjustment of polydispersity parameters, the resulting trend of RSi was expected to follow similar dynamics as exhibited in Figure 4.2 bottom panel for the HSi case.

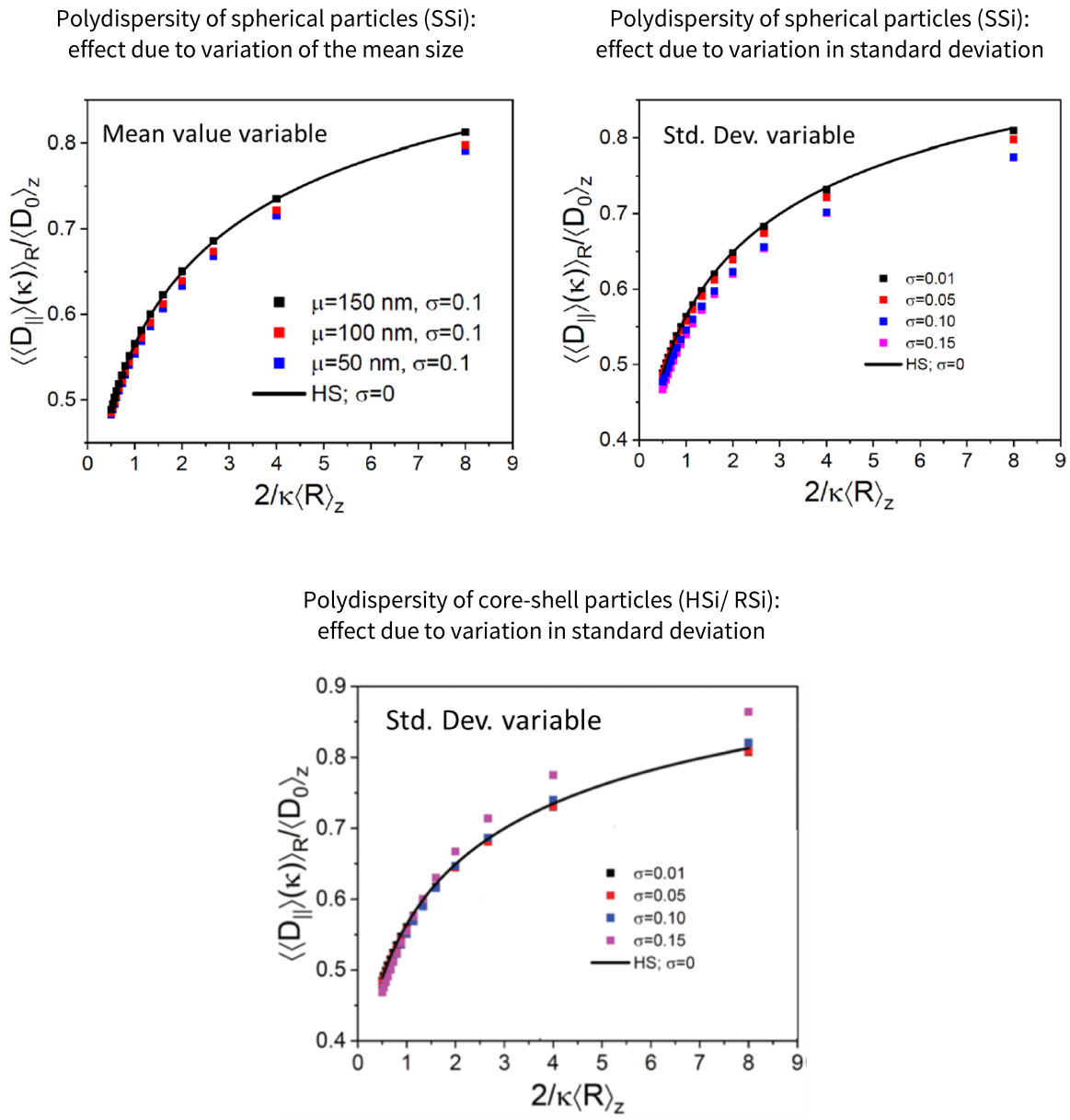

Figure 4.2. The normalized parallel diffusion constants with respect to normalized penetration depth are shown for polydisperse spherical particles changing the mean size at constant standard deviation (top left) and varying standard deviation at constant average radius (top right). The variation in the dynamics for core-shell particles due to changing the standard deviation is shown in bottom panel. In all cases, hard spheres near-wall dynamics with stick boundary conditions is presented as reference model [28]. Reproduced from Ref. [75] with permission from the Royal Society of Chemistry under the CC BY-NC 3.0 license.

4.1.2.2 The effect of aggregation on the near-wall dynamics

The next factor considered for influencing the near-wall dynamics was particle aggregation. This contribution was implemented by substituting the monomodal size distribution, $P(R)$ in Eq. 3.12, by a bimodal distribution. There, the large population was represented by single particles with mean size μ and standard deviation σ. Meanwhile, the aggregates were considered in the second population described by a mean size, μ_{agg} being an integer multifold value of μ, and a relative standard deviation σ_{agg}. The proportion of aggregates was established by their relative volume fraction ϕ_{agg}. In this case, the interaction potential followed the hard sphere model while the factor $B_{NW}(Q,R)$ for spherical particles was used for both populations. The effect of particle aggregation on the calculated parallel diffusion constants, as a function of normalized penetration depth, is shown in Figure 4.3.

As a result of increasing the size ratio μ_{agg}/μ, at fixed σ_{agg} = 0.05 and ϕ_{agg} = 0.05 (Figure 4.3 left panel), an evident decrease in particle diffusion near the wall was observed. Such reduction in diffusion was even appreciable for small aggregates that had averaged radii twice that of the of single particles. Here, the effect of increasing the aggregates size caused the flattening of the gradient in the dynamics. On the other hand, changing the relative volume fraction of aggregates ϕ_{agg}, at a fixed size of $\mu_{agg} = 2\mu$ and σ_{agg} = 0.05, also caused a clear slowing down of diffusion which became more pronounced as the volume fraction grew (Figure 4.3 right panel). However, in this last situation, the dynamics kept a similar gradient between the different values of ϕ_{agg} but shifted towards smaller diffusion constants with increasing ϕ_{agg}.

Calculations for larger aggregates and larger populations were not performed. This was unnecessary as the presence of aggregates was minimized by experimental precautions in the real samples. These were tested before and after the EWDLS experiments in bulk DLS, where neither sedimentation nor clustering or turbidity were detected.

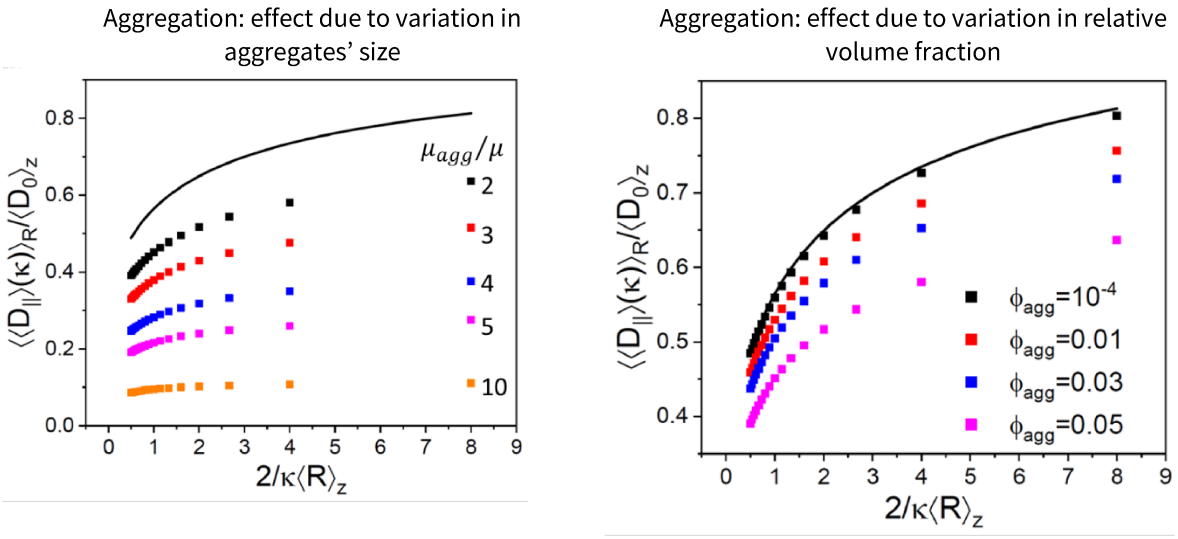

Figure 4.3. Normalized parallel diffusion coefficients vs normalized penetration depth for systems mimicking aggregation by considering systems of spheres with bimodal Gaussian size distribution. For these calculations, the larger population of spheres had a mean size of μ = 100 nm and the standard deviations of both populations were $\sigma = \sigma_{agg}$ = 0.05. Left panel: Effect of the variation of μ_{agg} as indicated in the legend (numbers behind the colored squares are values of μ_{agg}/μ) and the theoretical model for monodisperse spheres (full black line, [28]). Right panel: Effect of the variation of ϕ_{agg} at a mean aggregate size fixed at $\mu_{agg} = 2\mu$. Reproduced from Ref. [75] with permission from the Royal Society of Chemistry under the CC BY-NC 3.0 license.

4.1.2.3 Effect of static particle-wall interactions on near-wall dynamics

The last factor considered for the calculations was the static particle-wall interaction potential determined according to Subsection 3.1.4. The results of modifying the static interactions in the calculations are presented in Figure 4.4. Generally speaking, the resulting interaction potential could have a relatively high stabilization barrier if the electrostatic amplitude B_{ER} was chosen to be larger than the Hamaker constant A_H. Or on the contrary, the stabilization barrier could be very low or even vanishing by increasing A_H over B_{ER}. The near-wall dynamics data calculated with interaction potentials with variable B_{ER} and fixed A_H = 0.5 $k_B T$ are depicted in Figure 4.4 left panel. In this case,

the diffusion constants, at very short penetration depths, showed slower values than the reference hard sphere model. Then, as the normalized penetration depth increased, the dynamics rapidly sped approaching the hard sphere model curve and became faster than that for the cases when B_{ER} considerably exceeds the fixed value of A_{H}. It is also seen that depending on the magnitude of B_{ER}, the crossing point with the model curve occurs at smaller penetration depth as B_{ER} increases.

Figure 4.4 right panel shows the near-wall dynamics data calculated with interaction potentials with variable A_{H} and fixed $B_{\mathrm{ER}} = 1 k_B T$. Here, it was found that the calculated dynamics stayed slower than the reference model for all cases with a finite Hamaker constant. Also, it was observed that the diffusion constants were even smaller than those of the hard sphere model as A_{H} increases. The steepness of the slopes in the near-wall dynamics resembled the ones observed experimentally for the RSi particles.

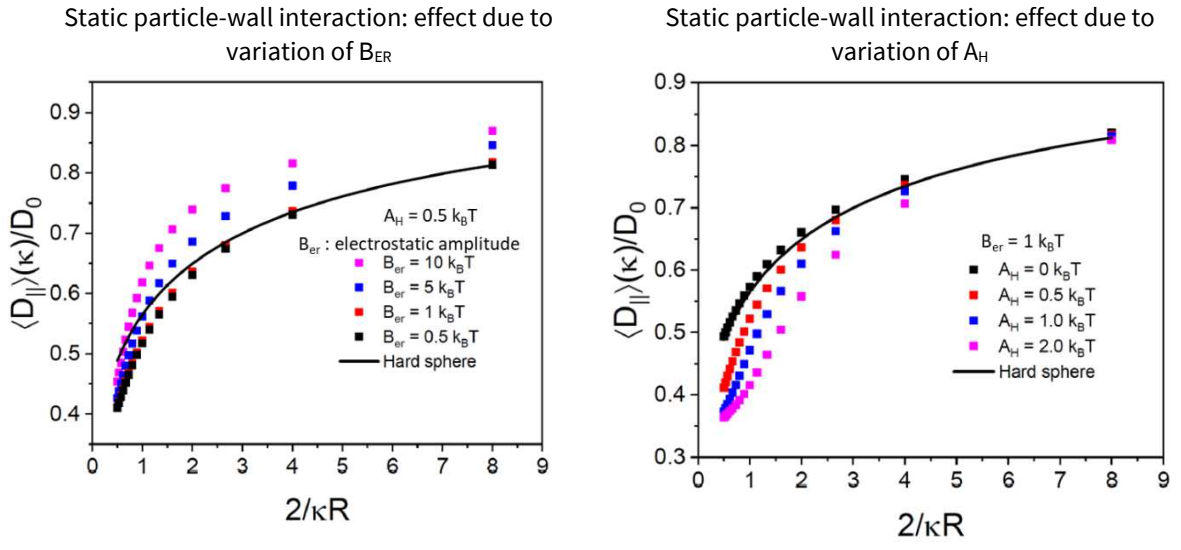

Figure 4.4. Normalized parallel diffusion coefficients versus normalized penetration depth for particles having radii R = 100 nm, with a sphere-wall interaction potential considering the parameters λ_D ~100 nm and $\Delta\rho_{\mathrm{m}}$ = 1 g/ml, compared to the hard sphere model predictions shown as solid line. Left panel: calculations with fixed A_{H} = 0.5 $k_B T$ and B_{ER} variable as stated in the legend. Right panel: calculations with fixed $B_{\mathrm{ER}} = 1 k_B T$ and A_{H} variable as stated in the legend. Reproduced from Ref. [75] with permission from the Royal Society of Chemistry under the CC BY-NC 3.0 license.

4.1.2.4 Converging numerical calculations to experimental findings

In summary, calculations performed by varying the polydispersity parameters showed that the standard deviation had more impact on the near-wall dynamics than the mean size, although such influence remained within the experimental error. Also, the calculations demonstrated that the particles' near-wall diffusion was highly susceptible to particle aggregation, where the diffusion dropped considerably with respect to the hard sphere model. Further, in the calculations considering the influence of the static particle-wall potential on the dynamics, the increasing Hamaker constant, while keeping the electrostatic amplitude fixed, led to a reduction in the near-wall diffusion compared to the reference model. There, at high Hamaker constants, a reversal in the curvature of the diffusion versus penetration depth curves was observed, which is qualitatively similar to the experimental data for the RSi particles.

Nevertheless, in a real EWDLS experiment, all three factors discussed above are present and then contribute to the results to a certain extent. Therefore, calculations incorporating the effects of polydispersity, aggregation, and particle-wall interactions were performed to obtain comparable results as those seen for SSi, HSi, and RSi in experiments. For this purpose, the following criteria were applied: (i) the inclusion of a small fraction of aggregates modelled as a bimodal distribution with $\mu_{\mathrm{agg}} = 2\mu$ and identical standard deviation $\sigma_{\mathrm{agg}} = \sigma$ for both populations; (ii) the particle-wall interacting potential was a DLVO potential with a Debye length of λ_D = 96 nm; (iii) sedimentation was included by considering an excess mass density of $\Delta\rho_{\mathrm{m}}$ = 1 mg/ml and; (iv) the particles mimicking aggregates had the same static particle-wall interaction potential as the monomer particles. Particle-particle interactions were neglected. As the interaction potential was the key factor that influences the dynamics, model calculations were done systematically varying the parameters B_{ER} and A_{H} until the calculated data eventually closely matched the experimental results. The parameters that yielded the diffusion coefficients closest to the experimental data are listed in Table 4.1, with the corresponding dynamics plotted in Figure 4.5.

Particle	$\mu(\mathrm{nm})$	σ	$B_{ER}(k_BT)$	$A_H(k_BT)$	ϕ_{agg}
SSi	71	0.05	1.5	0.5	0.005
HSi	154	0.05	1.0	0.25	0.030
RSi	80	0.05	1.5	2.75	0.005

Table 4.1. Parameters used in numerical calculations for the near-wall dynamics displayed in Figure 4.5 that yielded the best agreement with the dynamics found in experiments.

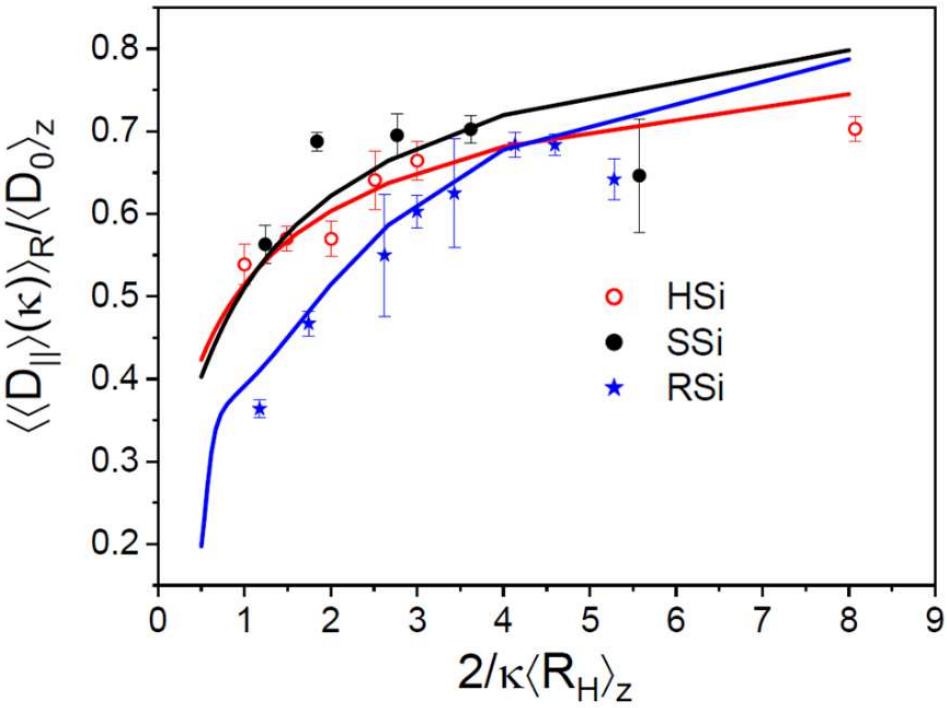

Figure 4.5. Normalized parallel diffusion coefficients versus normalized penetration depth. Experimental data (symbols) is shown in combination with numerical calculations (solid lines) which are based on the values listed in Table 4.1. The SSi system is represented in black color, HSi system is in red color and RSi system in blue color. Reproduced from Ref. [75] with permission from the Royal Society of Chemistry under the CC BY-NC 3.0 license.

4.1.3 Discussion and conclusions of the effect of particle morphology on the near-wall dynamics

The electrostatic amplitude values shown Table 4.1 ranged from B_{ER} = 1 $k_B T$, for the HSi system to B_{ER} = 1.5 $k_B T$ for the SSi and RSi systems. This similarity in B_{ER} values between the different systems is to be expected, since the chemical components of the particles' surface and the wall remain unchanged in all cases. Further, the pH of the suspending medium (milli-Q water) is the same in all suspensions, and consequently, the surface charge densities should be of the same order in all three cases. Likewise, the B_{ER} values are related to an effective surface potential of $\Psi_{\mathrm{p,w}}$ ~ -2 mV which is the combination of the particle's surface and the wall's surface potential.

Although the effective surface potential of $\Psi_{\mathrm{p,w}}$ ~ -2mV was similar across the particle systems, this value seems to conflict with the experiments, since the measured zeta potentials of all three systems were found to lie in the range of -30 to -40 mV. Further, according to total internal reflection microscopy measurements found in literature [41, 96, 97], the interaction potential between 2 µm Stöber-Silica particles with fused silica surfaces, used as microscopy slides, suggest an effective surface potential of the order of $\Psi_{\mathrm{p,w}}$ ~-20 mV. However, in the present case, the wall consists of a special high refractive index quartz glass (SF10) for which there are indications in the literature [78] that its surface charge density might be significantly smaller than that of silica [5]. Thus, the obtained small value of B_{ER} is very likely due to the low surface potential of the wall.

On the other side, the Hamaker constants embedded in the attractive term of the potential showed more differences between the three different systems. In the case of SSi particles, the A_{H} values required to match the calculated data to the experimental data were found to be lower than one $k_B T$. This is in qualitative accordance with the non-retarded van der Waals interaction according to the Lifshitz theory for silica interacting with quartz through water [6]. Additionally, the relative volume fraction of aggregates was as low as ϕ_{agg} = 0.005.

For the case of HSi particles, the A_H resulting in the best agreement between calculated and experimental data was in the same order of magnitude as that for the SSi system. This similarity is to be expected considering the chemical equivalence of the participating components. However, the small difference in A_H may be due to the fact that only the HSi particles' outer shell is made of silica, while the core consists of water. This will necessarily lead to weaker van der Waals attraction than between two full silica spheres. Nevertheless, this effect would probably not be detectable in an experiment.

The required volume fraction to achieve a close approximation of the calculated with the experimental data was significantly higher than for the SSi system with ϕ_{agg} = 0.030. This considerable difference can be related to the particles' synthesis process that involves a calcination step to remove the organic core from an intermediate polystyrene-silica core-shell system. This process reduces the likelihood that all particles can be re-dispersed. Attempts were made to remove these aggregates by centrifugation, but this method can never be completely successful. Therefore, it is more likely to find aggregates in the HSi suspensions than in the other two systems.

For the RSi particles, the major contributor to the deviation of the calculated dynamics from the hard sphere reference system was the Hamaker constant. To approximate the calculations to the experimental values A_H needed to be one order of magnitude larger than that for the HSi system and 5 times for the SSi case. At first glance, this finding is astonishing as the SSi and the RSi system are chemically identical and their Hamaker constants should therefore be the same. The only difference between the silica particles is their surface morphology. This implies that the roughness of the RSi particles has a significant influence on the interaction potential and, in this way, impacts their near-wall dynamics.

There are reports [91] indicating that asperities on spherical particles can reduce the so-called stabilization barrier of the DLVO pair interaction by approximately 10-15% due to the difference of the distance-dependence (hyperbolic versus exponential decay) of attraction and repulsion. Similarly, data reported in the literature show evidence that the global minimum of the DLVO pair interactions may vanish for particles with asperities on their surface [9]. This might explain why the RSi particles don't stick to the wall irreversibly, despite the large Hamaker constant. The quoted simulation studies support our observation that chemically identical particles may have significantly different interaction

potentials with a wall, due to different surface morphologies. Therefore, it has to be concluded that the deviation of the RSi dynamics data from the hard sphere model is mainly due to the variation of the interaction potential, since the hydrodynamic effect of surface roughness is rather expected to speed up diffusion.

Finally, it is concluded that the near-wall dynamics depend significantly on the particles' surface morphology, i.e. smooth, porous or rough surface. The last case is of particular interest because arguments based on theoretical hydrodynamics predicted faster dynamics due to the reduction of the flow resistance on the surface of rough particles. On the contrary, it is shown through experimental evidence that the near-wall dynamics are reduced. Additionally, systematic numerical calculations supported the experimental findings, indicating that increasing attractive particle-wall interactions, such as those introduced by surface asperities, contribute most significantly to the slowing down of particle dynamics.

4.2 The effect of surface modifications on the particle-wall interactions and dynamics

In this subchapter, the static and dynamic experimental findings of micron-size colloidal particles interacting with bare and coated glass surfaces are presented. First, the particle-wall interaction potentials are shown together with the parameters describing them. Then, the corresponding near-wall dynamics are presented. Additionally, static and dynamic information obtained by Brownian dynamics simulations are shown in the corresponding subsection. These simulations complement the experimental findings by considering background and shot noises, as source of errors.

Recapitulating the methodology presented in Subsection 3.2.1, from the measured light scattering intensities, histograms are determined and converted to distances according to Eq. 3.16. Subsequently, the interaction potential values are computed by means of Eq. 3.21. Then, by performing a least squares fit of the potential, based on Eq. 3.23, the parameter values of the Debye length λ_{D}, the equilibrium distance h_{min}, and the effective gravitational force G_{eff} are obtained. From these parameters, the

amplitude of the electrostatic potential can be determined as $B_{\mathrm{ER}} = \exp\left[\left(h_{\min}/\lambda_{\mathrm{D}}\right)\right] \times G_{\mathrm{eff}}\,\lambda_{\mathrm{D}}$ in the Derjaguin approximation.

Furthermore, for the calculation of the dynamic properties $D_{\perp}(h)$ and $v_{\mathrm{drift}}(h)$, the intensity traces, whether they are experimental or simulated, are converted into 1-D trajectories. From these, the probability densities of particle displacements at a given delay time are constructed. The first moment of this distribution is the mean displacement. The initial slope of the mean displacement versus delay time yields the particle's drift velocity $v_{\mathrm{drift}}(h)$ at a given separation distance, according to the first term of Eq. 3.24. The second moment is the mean square displacement, and its initial slope versus delay time gives twice the normal diffusion coefficient $2D_{\perp}(h)$ at the given position, according to the first term of Eq. 3.25. This procedure was applied to the intensity traces from two types of colloidal particles (bare Polystyrene and Streptavidin-coated Polystyrene) when interacting with the two types of surfaces (bare glass and hydrophobically coated glass).

4.2.1 Static interaction potential of particles near the walls

4.2.1.1 *Experimental interaction potentials*

The interaction potentials of single polystyrene (PS) particles (nominal radius of 3 μm suspended in 1 mM NaCl aqueous solution) with the bare glass and a hydrophobically coated glass, were measured and are shown in Figure 4.6. The top panel refers to PS particles near the bare glass wall while the bottom panel shows PS particles near a hydrophobically coated glass. It is important to note that, for each system, the six measured potentials were obtained from six different particles, all of which were contained within the same sample cell. Therefore, the experimental conditions for the six measurements were identical. The parameters λ_{D}, G_{eff} and $h_{\min}$ were determined by fitting the experimental data using Eq. 3.23, which in turn, was used to construct the model potentials displayed as lines in the graphs. The extracted parameters for the PS particles near the bare wall (glass) and the hydrophobically coated wall (glass) are listed below in Table 4.2.

At first glance, the interaction potentials of PS particles near the bare glass presented different distances from their potential minima $h_{\min}$ but similar shapes. The Debye lengths λ_D ranged from 9.2 to 11.8 nm. This interval of λ_D matched reasonably with the expected value for particles in a 1 mM NaCl solution. According to the Debye-Hückel approximation, a 1:1 electrolyte solution has $\lambda_D \cong 0.304/\sqrt{c_S}$ = 9.6 nm. The buoyancy-corrected gravitational force acting on the particles, which was determined from the slope of the potential at large distances, spanned from 57 to 67.1 fN. The expectation value for this parameter was calculated to lie between 56 fN and 67 fN, by using the nominal diameter of 6 µm, the density of polystyrene which varies from 1.05 to 1.06 g/cm^3, and the acceleration of gravity. Further, if taking into account the particles' diameter distribution (5.99 ± 0.07 µm) the experimental values for the gravitational force can be considered as agreeing very well with the expectations. On the other side, as the particles' equilibrium distances $h_{\min}$ ranged from 66 to 125 nm, the electrostatic amplitude had to vary drastically from particle to particle. Such notable differences are due to the exponential relationship between B_{ER} and $h_{\min}$ according to $B_{ER} = \exp(h_{\min}/\lambda_D) \times G_{\text{eff}}\,\lambda_D$. Consequently, the values of B_{ER} differed by almost two orders of magnitude between the profiles. This indicates that either different particles, different spots on the glass surface, or both at the same time, can present different local charge densities.

In the case of the PS particles near the hydrophobic glass (Figure 4.6 bottom panel), the parameters of the interaction potentials showed similar values as in the previous case, falling within the expected ranges for λ_D and G_{eff}. However, λ_D seemed to tend slightly to higher values than those obtained in the bare wall case. Likewise, the effective attraction forces G_{eff} were found in the range expected for a polystyrene particle with a nominal radius of 3 µm. Thus, differences in G_{eff} compared to the previous case are not significant. Regarding their equilibrium position, the distances $h_{\min}$ on average showed larger values and less fluctuations than those observed in the bare wall case.

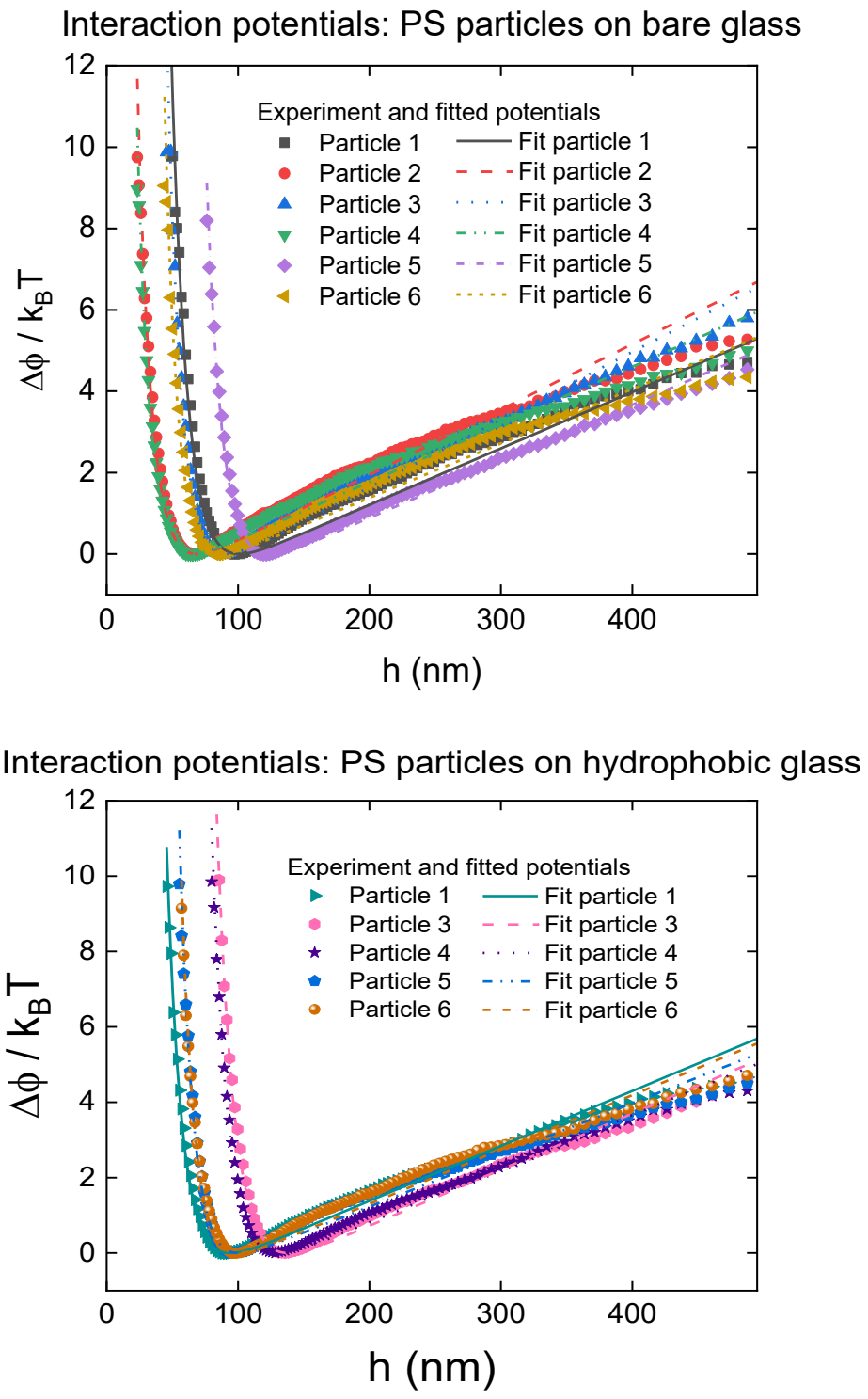

Figure 4.6. Experimentally determined interaction potentials profiles of polystyrene particles (3 µm radius), immersed in 1 mM NaCl aqueous solution, with two different walls. Upper panel: the wall is bare glass. Bottom panel: the wall is a glass surface coated with a hydrophobic layer (Sigmacote™). Lines represent model function calculated with parameters resulting from non-linear least squares fits with Eq. 3.23. The corresponding parameter values are listed in Table 4.2.

Particle No.	$\lambda_D\,(\mathrm{nm})$		$G_{\mathrm{eff}}\,(\mathrm{f\,N})$		$h_{\min}\,(\mathrm{nm})$		B_{ER}/k_BT	
	Bare glass	Coated glass	Bare glass	Coated glass	Bare glass	Coated glass	Bare glass	Coated glass
1	11.8	*11.2*	57.0	*59.2*	101	*93.8*	873	*688.5*
2	10.5	-	66.1	-	68.5	-	118	-
3	9.3	*13.0*	67.9	*60.8*	89	*138.3*	2297	*8004.6*
4	9.7	*12.0*	60.1	*60.0*	65.9	*131.0*	122	*9814.8*
5	11.8	*10.0*	58.1	*56.5*	124.5	*100.5*	6524	*2876.3*
6	9.2	*10.0*	61.7	*59.7*	86.2	*100.0*	1631	*3252.6*

Table 4.2. Best fitting parameters that describe the interaction potentials between bare PS colloidal particles (3 µm nominal radius) with two different types of walls: bare glass (black font) and hydrophobic-coated glass (font in italic and purple). As reference, for a PS particle with radius of 3 µm and a density of 1.055 g/cm^3 immersed in a 1 mM NaCl aqueous solution, a buoyancy-corrected weight force G_{eff} = 61.6 fN and a Debye length λ_{D} = 9.6 nm are expected.

Consequently, the values of B_{ER} were slightly higher on average and more uniform in this case. This implies that the charge density on the hydrophobically coated surface is more homogenously distributed but higher than on the bare glass. Especially the latter conclusion is somewhat surprising, as the coating is designed to make the surface hydrophobic. However, it should be noted that the chemical composition of the coating reagent and its mode of action are kept confidential by the manufacturer.

Next, a third system was measured in TIRM. This sample consisted of Streptavidin-coated polystyrene particles (nominal diameter of 5 µm immersed in a 1 mM NaCl aqueous solution) floating above a bare glass wall. The experimental interaction potential profiles are displayed in Figure 4.7 together with the best fits according to Eq. 3.23. The resulting parameters are listed in Table 4.3. Additionally, Streptavidin-coated polystyrene particles, here after called as protein-coated PS particles, moving above a hydrophobically coated wall were also measured. However, due to experimental constraints which required adjustments of the experimental conditions, data from these experiments are shown separately and discussed at the end of the chapter.

According to the parameter values in Table 4.3, the protein-coated particles experienced interaction potentials with potential minimum at $h_{\min}$ = 78 nm and above. These equilibrium distances were in a similar range as in the previous case of bare PS particles near the bare glass. The effective weight G_{eff} tended to be slightly higher than the expected for a PS particle of 2.5 μm nominal radius (35 fN), where it was considered that the protein layer's mass is negligible compared to the particle core's (~ 5%) [3]. However, the standard deviation of the size distribution is 0.2 μm measured by the manufacturer. Therefore, expectation values of G_{eff} range from 27 to 44 fN and the experimental values were considered to be in very good agreement with expectations. Likewise, λ_{D} presented values from 1.7 up to 4.1 nm above the expected value of λ_{D} = 9.6 nm for the 1 mM NaCl aqueous solution. As a result, the electrostatic amplitudes B_{ER} calculated from the previous parameters fall within a range difference of less than 100 $k_B T$ with one exception. All the electrostatic amplitudes observed for this system were much smaller than in the previous cases of bare PS particles.

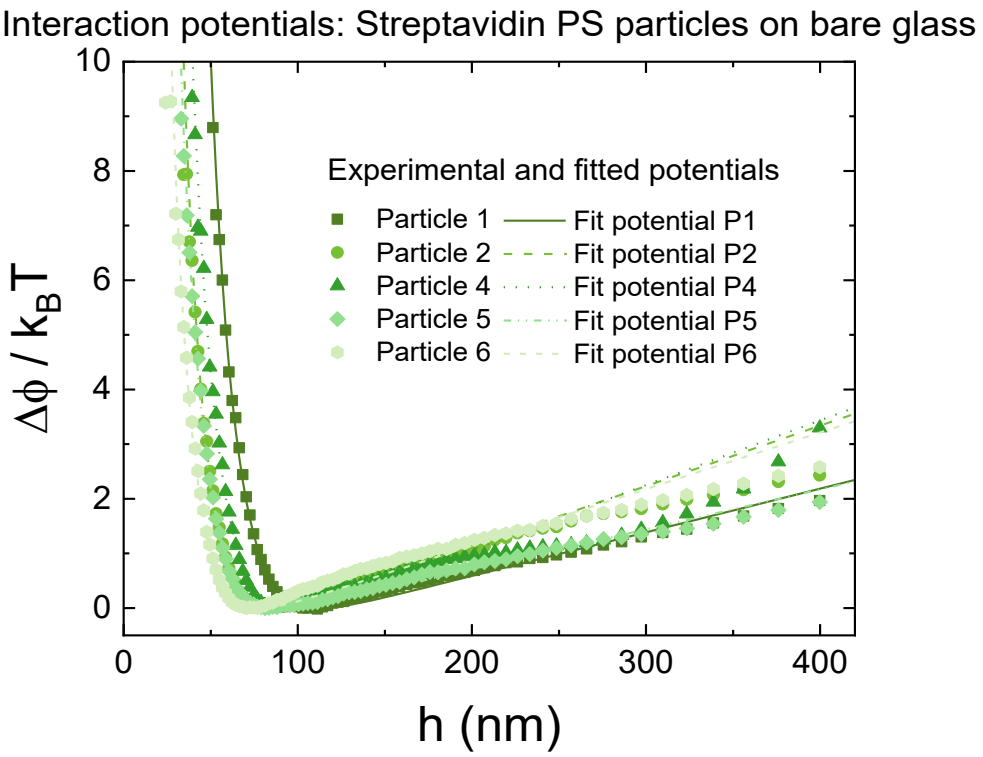

Figure 4.7. Experimentally determined interaction potentials profiles (symbols) with the bare wall of Streptavidin-coated PS particles (2.5 μm radius) suspended in a 1 mM NaCl aqueous solution. Lines represent model function calculated with parameters resulting from non-linear least squares fit (Eq. 3.23). The resulting parameters are listed in Table 4.3.

Particle No.	$\lambda_D\,(\mathrm{nm})$	$G_{\mathrm{eff}}\,(\mathrm{fN})$	$h_{\mathrm{min}}\,(\mathrm{nm})$	$B_{ER}/k_B T$
1	13.7	32.3	112.7	411.70
2	11.7	44.7	86.3	202.61
4	13.5	47.9	96.4	205.09
5	12.2	29.6	91.1	156.36
6	11.3	41.9	78.5	120.29

Table 4.3. Experimental parameters describing the interaction potentials between Streptavidin-coated particles (2.5 μm nominal radius) with the glass wall (Figure 4.7) obtained by curve fitting using Eq. 3.23 to the experimental data. As reference, for a PS particle with radius of 2.5 μm and density of 1.055 g/ml immersed in 1 mM NaCl aqueous solution, a buoyant-corrected weight G_{eff} = 35 fN and λ_{D} = 9.6 nm are expected.

4.2.1.2 Discussion and conclusions of experimentally determined interaction potentials

In general, for the three systems described above, it was found that the parameters λ_D and G_{eff}, matched the expected values within experimental error. Small discrepancy in G_{eff} can be attributed to size and density variations between individual particles due to polydispersity. The differences in the Debye length are potentially due to two effects: (i) small deviations of the penetration depth from the value that was set based on the measuring cell geometry and, (ii) inevitable experimental noise, which is likely the more important effect. This last effect will be investigated and discussed in the context of simulated interaction potentials in the next subsection. Both effects lead to a systematic deviation in the direction of the electrostatic parameters, as was observed in all cases. The dispersion of the values was 20 % around the respective mean value. This is due to the fact that only relatively few measuring points in the potentials were available in the short range of distances, which is dominated by the exponential decay, making the fit less reliable in that range.

The three systems differ drastically regarding the amplitude of the electrostatic repulsion, which were calculated from the above parameters and the position of the potential minimum. The mean values of $\langle B_{ER} \rangle / k_B T$ differ by a factor of about 25 between the three systems and the measured values on one system vary by up to ± 50 %. The corresponding values are collected in the following Table 4.4.

System	Average $\langle B_{ER} \rangle / k_B T$	Standard deviation of $\Delta B_{ER} / k_B T$
Bare PS spheres / bare glass	1930	900
Bare PS spheres / hydrophobically coated glass	4930	1530
Protein coated spheres / bare glass	220	45

Table 4.4. Average values $\langle B_{ER} \rangle / k_B T$ and variation $\Delta B_{ER} / k_B T$ of the electrostatic amplitude measured in three different sphere / wall systems.

The measured potentials of the protein-coated particles near the bare glass showed the smallest electrostatic amplitude. This is very likely caused by Streptavidin having an isoelectric point of pH 6.2, similar to that of the surrounding environment, and therefore, this protein will be very weakly charged under the experimental conditions. Also, the variation of $\left\langle B_{\mathrm{ER}} \right\rangle / k_B T$, being on relative or absolute scale, is significantly smaller for this system than in the bare sphere-bare wall system.

On the other hand, PS particles near the hydrophobically coated glass had the largest B_{ER} among the systems. This implies that the coated surface has a higher charge density than the uncoated glass. This is inconsistent with the Sigmacote manufacturer's claim that treating a glass surface with this product should produce a neutral hydrophobic coating. Visual observations of the contact angle of water confirmed this claim. Since the manufacturer does not provide any information about the specific nature of the Sigmacote reagent, it is not possible to explain the experimental findings for this system within the framework of the model used for interaction potentials.

In addition, the electrostatic amplitude values varied between not only different systems but also among single particles within the same sample. This variation was more pronounced in the systems comprising bare PS particles than in those with protein coated particles. Probably, the major reason lies in the manufacturing procedure of the bare PS spheres. The used particles were commercially manufactured with an extremely small polydispersity of sizes. The relative standard variation of the size distribution is of the order of 10^{-4}, which cannot be achieved by standard polymerization procedures. According to the manufacturer, these particles originate from different synthesis batches whose products were fractionated and collected according to size classes in order to achieve sufficiently large sample quantities and very narrow widths of the size distribution. The fact that particles within a stock suspension originate from different approaches can explain their different charge densities.

On the other hand, the protein-coated particles have a relative width of the size distribution in the range of 10 % indicating that they were synthesized in a single batch. This immediately explains why the variation of the electrostatic amplitude is the smallest among the three systems, which is still of the order ± 20%. While one might expect the particles to share similar electrostatic amplitude properties before the protein coating, the particles may exhibit topological defects known as surface roughness, inhomogeneous protein coverage and, in a more realistic scenario, the combination of both [72, 73, 90]. Also, a realistic glass wall is likely to have corrugations and charge density inhomogeneities. The

combination of these effects causes the electrostatic amplitude values to show significant variations among several single-particle experiments.

Another minor factor to consider when analyzing the physical parameters is the numerical inaccuracies related to the fitting of the experimental data. Artifacts as error propagations in combination with the selection of data points could generate small differences in the best fitting parameters. In particular, minor errors in the determination of $h_{\min}$ significantly impact on the B_{ER} values due to their exponential relationship.

4.2.1.3 Simulated interaction potentials and the effect of noises

In recent years, the notion of shot noise has come into TIRM considerations while analysing experimental data due to its effect at the time of detection that impacts the shape of the potential [17, 67, 88]. In addition, if it is not properly managed, background noise has also been observed to influence the scattered light signal. Therefore, to complement the experimental findings it is necessary to assess whether the previously observed potentials were only determined by the system parameters or partially influenced by the above-mentioned errors. For this purpose, Brownian dynamics simulations were performed to calculate interaction potentials in dependence of the experimental parameters and adding the inevitable shot noise and background noise.

The procedure consisted of obtaining an averaged potential by simulating five independent potentials using the experimental parameters of a selected particle of each system. The background noise and shot noise were also added when simulating the intensity traces. For easy appreciation, only the case of Bare PS particle near the bare glass is shown since it reveals the main effects of these noises which are similar in all systems.

The simulated interaction potentials of the bare PS particle near bare glass are presented in Figure 4.8, together with the associated experimental data. In the top panel, five independent simulated potentials (solid symbols) and the resulting averaged potential (open circles) are shown. For the simulated data 5% of background noise (BN) and shot noise (SN) were considered. This level of background noise represents the maximum threshold below which experimental measurements are considered reliable.

These simulations were done by using the best fitting parameters for the experimental data (black solid line): λ_D = 9.2 nm, G_{eff} = 61.7 fN and $B_{ER}/k_B T$ = 1631.

In general, the simulated potentials with added noise (Figure 4.8 top panel) agreed well with the experimental data for separation distances larger than the position of the minimum. There, the difference between the slopes of the linear parts is smaller than 5%. For distances below the equilibrium position, where the potential is steeper, the differences between the simulated and experimental potentials were clearly distinguishable. The simulated potentials showed slightly smaller gradients than the experimental data. These deviations from the best fitting potential are in line with the observations related to shot noise found firstly by F. Cui and D. J. Pine [17].

In order to quantify the extent of the noise contributions in the potentials, simulations with different noise contributions were performed (Figure 4.8 bottom panel). Since the effect of noise is mainly evident at short distances in the potential, the following discussion is focused on this region of interest. At a glance, the averaged noise-free simulated potential (black squares) and the experimental data (blue stars) fall close to each other and to the fitting potential (blue line). The noise-free simulated potential tends to deviate to a small extent from the fitting potential at short distance to the wall. The background noise (red circles), with a strength of 5% signal-to-noise ratio, reduced the gradient of the repulsive part of the potential. This is translated as an increase in λ_D and a reduction of $B_{ER}/k_B T$. Similarly, shot noise tended to decrease the potential gradient (green triangles) but with a stronger effect compared to background noise of 5%. In consequence, the combination of both sources (light blue rhomboids and light broken blue line), named as full noise, reinforced these effects on the potential.

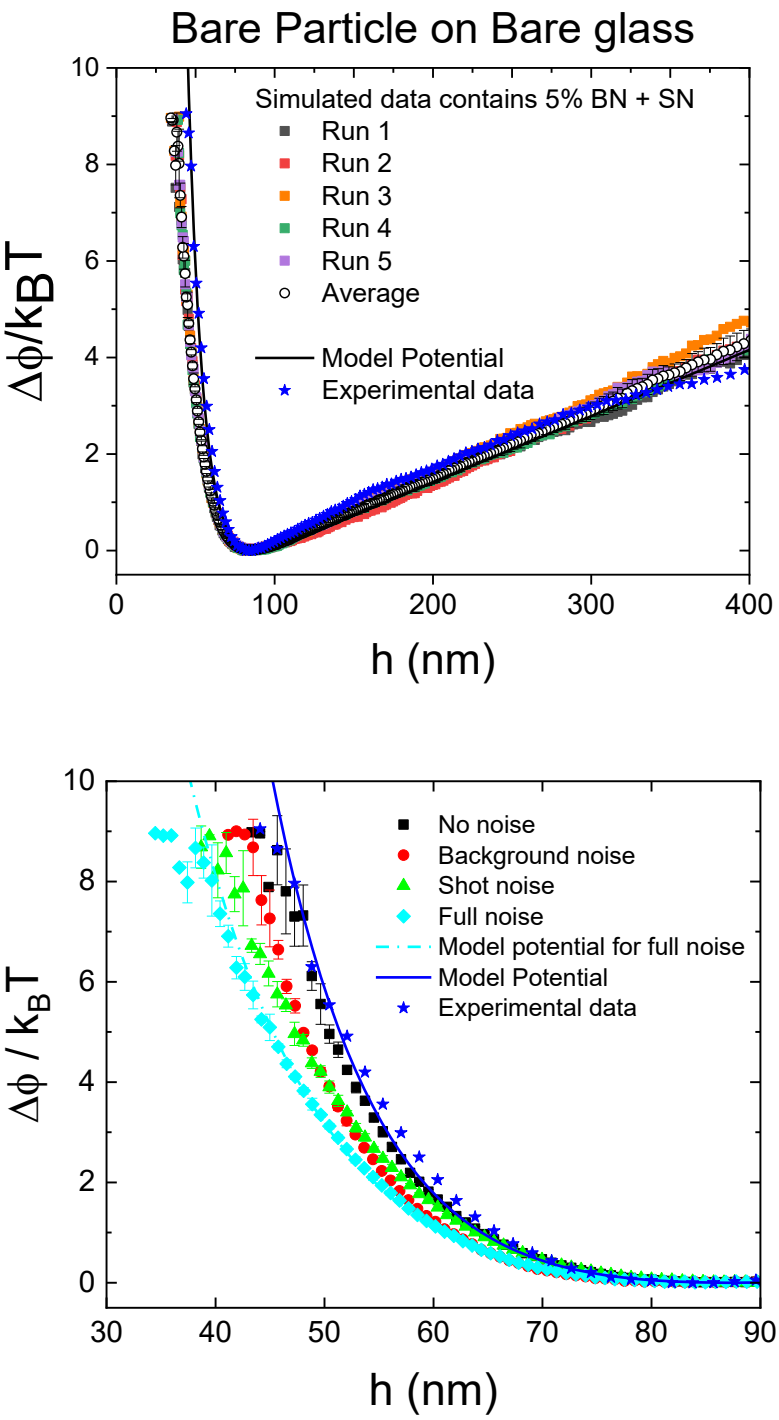

Figure 4.8. Simulated interaction potentials between a bare polystyrene particle (3 μm radius) with the bare glass wall are shown in comparison with experimental data. The parameters used in the simulation come from the particle listed as No. 6 in Table 4.2 which are λ_D = 9.2 nm, G_{eff} = 61.7 fN and h_{min} = 86.2 nm. Top panel: five independent simulated potentials and their average compared to the experimental data. Bottom panel: simulated potentials at short distances with various noise contributions as indicated in the legend shown together with experimental data.

These two sources of noise are always present in experiments and therefore the interaction potential measurements are slightly biased towards shallower profiles, according to the findings above. Thus, larger λ_{D} and smaller $B_{\mathrm{ER}}/k_B T$ are being measured, along with slightly smaller G_{eff} values, compared to those determined from hypothetical noise-free experiment. If the experiments are performed cautiously, the background noise can be reduced to 1-2% of the signal reducing the resulting uncertainty to a certain extent. However, shot noise cannot be manipulated since it is caused by inevitable quantum fluctuations of the detector. Thus, these inherent noise contributions will always distort the interaction potential profile as mentioned.

As shown above, the noise-free simulated potential presented slight deviations from the model potential at short distances, whereas in principle the two curves should lay exactly on top of each other. The deviations can be attributed to the fact that the electrostatic repulsive force causes a high drift velocity of the particle away from the surface within the short-distance region. Under these conditions, the implicit assumption that the potential is constant over the sampling time is not valid. Thus, to fulfil this assumption shorter times must be considered.

Since the effect of sampling time is a factor that is frequently referred to during this research, this topic is addressed in detail in Subsection 4.2.3. Briefly, simulations having a reduced sampling time Δt = 0.2 ms resulted in a better match of data with the model potential than the simulations with Δt = 2 ms. However, performing experiments at Δt = 0.2 ms would reduce the count-rate by a factor of ten and amplify the effect of shot noise. To counteract this effect, the illumination intensity would require a tenfold increase compared to real experiments, which in turn, would lead to detector over-illumination and dead time losses. Therefore, the implementation of such small sampling times in real measurements is unfeasible.

Below in Figure 4.9, simulated data (solid symbols) for representative potentials for each experimental system are shown. For these simulated potentials, the parameters determined by fitting the experimental potentials were used but with the addition of 1% of background noise (BN) and shot noise (SN), resembling the experimental noise conditions. As reference, experimental data of the three systems, (open symbols), are displayed together with their corresponding fitted potentials (continuous lines) calculated by using the extracted parameters listed in Table 4.5.

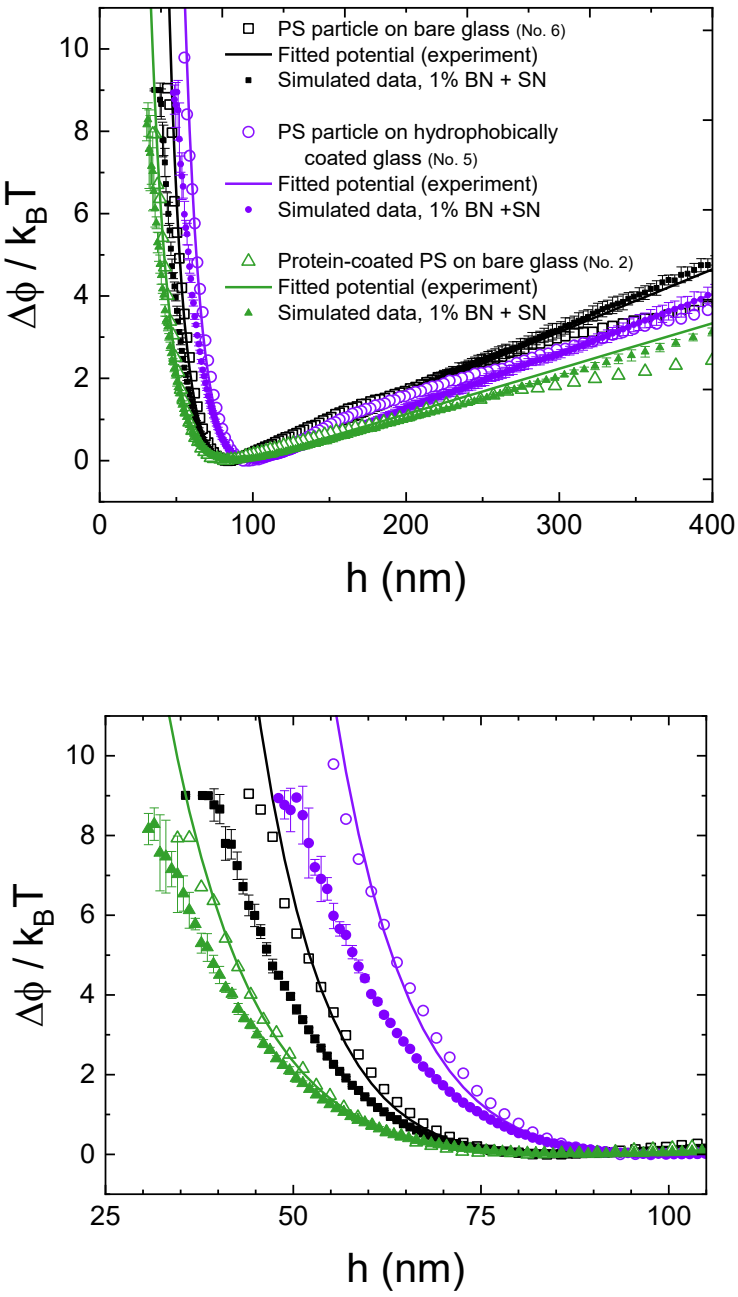

Figure 4.9. Experimental (open symbols) and simulated (full symbols) interaction potentials from representative particles of each system as denoted in the legend. The parameters obtained from fitting the experimental potentials (solid lines), listed in Table 4.5, were used to calculate the corresponding averaged simulated data with additional noise. Full symbols represent the average result of five independent simulations, and the error bars indicate their standard deviations. Top panel: the potentials are shown over a wide range of distances from the wall. Bottom panel: close-up view at shorter distances to distinguish the simulated potentials from the experimental ones and the models. For visual clarity, the fitting potentials for the simulated data are ommited but their parameters are listed in Table 4.5.

Sample	$\lambda_D\,(\mathrm{nm})$		$G_{\mathrm{eff}}\,(\mathrm{fN})$		$h_{\mathrm{min}}\,(\mathrm{nm})$		$B_{ER}/k_B T$	
	exp	*sim*	**exp**	*sim*	**exp**	*sim*	**exp**	*sim*
Bare PS particle (No. 6)-Bare glass	**9.2**	*12.4*	**61.7**	*66.7*	**86.2**	*88.5*	**1631**	*255.8*
Bare PS particle (No. 5)-hydrophobic-coated glass	**10**	*12.9*	**56.5**	*59.1*	**100.5**	*102.5*	**2876.3**	*513.8*
Protein-coated PS particle (No.2)-Bare glass	**11.7**	*14.3*	**44.7**	*43.3*	**86.3**	*90.5*	**202.6**	*85*

Table 4.5. Parameters of the model potentials extracted from experimental ("exp" columns in bold font) and simulated data ("sim" columns in Italic font) which includes 1% background and shot noise.

The simulations of the interaction potentials showed that noise consistently reduced the gradients in the potential profiles across all three systems. Therefore, the broader profiles led to significantly smaller electrostatic amplitude $B_{\mathrm{ER}}/k_B T$ and larger λ_{D} values as described previously. This suggests that in real TIRM experiments, where these inherent noise sources are present, measurements of the particle-wall potential are subject to the same systematic errors. Thus, physical parameters determined for these three types of systems are overestimated due noises ruling out any influence of the particles' surface composition on the potentials. The noises could explain the deviation of the experimentally determined screening length from the expected values based on the electrolyte concentration. Further, it has to be assumed that the values of the electrostatic amplitude are always underestimated in a TIRM experiment.

4.2.1.4 Conclusion of simulated interaction potentials and noise

Simulations that incorporated inherent experimental noises, background noise and shot noise, have shown a measurable impact on the accuracy of interaction potential profiles measured with TIRM. These provided insights into the separate and combined effect of noises on the interaction potentials. As in experiments, background noise can be minimized as low as 1% but shot noise remains inevitable while it contributes the most to broaden the interaction potential profiles. This distortion affects the

steepest part of potential profile most severely and consequently, the misestimation of the derived parameters λ_D and B_{ER}. The effect on G_{eff} is smaller and not significant with respect to the experimentally measured parameter. Therefore, simulations of the static interaction potential are needed to complement the experimental data and estimate the degree of error due to the noise effects. And so, the values of the parameters that describe the potential could be better assessed.

Also, simulated potentials with both noise-free and noise-added when compared to the potential built with experimental parameters led to identifying the role of sampling time. While noise tends to broaden the potential profile, in principle noise-free potential should coincide with the potential built by using the experimental parameters. However, notable differences are still observed in the steepest part of the potentials. These differences are attributed to the violation of the assumption of constant forces acting on the particles within the sampling time. As will be presented in the next subsection, simulated potentials with reduced sampling time reach a better agreement with the fitted potential. While in simulations it is possible to tune this parameter to shorter times, in actual experiments technical complications arise, thus limiting the accuracy of measurements at short separation distances.

As expected, the simulations showed the same influence of noise for all three particle types, since the simulation algorithm does not process any information about the particles' surface properties. However, the simulations provide a qualitative measure of the factor $C = B_{\mathrm{ER}}^{\mathrm{exp}} / B_{\mathrm{ER}}^{sim}$ by which the experiments overestimate the electrostatic amplitude. If this factor is applied to the values of the mean amplitudes and error bars from Table 4.3, it can be shown that the value of the B_{ER} in the case of the protein-coated particles is significantly smaller than the corresponding values for the other two particle types which is shown by the calculated values in Table 4.6.

This shows that the protein-coated particles have a significantly lower charge density than the uncoated particles. However, based on the experiments conducted, it is not possible to conclude whether this is an effect of the coating or if these particles had a comparatively low charge density prior to coating.

Sample	$C = B_{\mathrm{ER}}^{\mathrm{exp}} / B_{\mathrm{ER}}^{sim}$	$C\langle B_{\mathrm{ER}} \rangle / k_B T$	$C\,\Delta B_{\mathrm{ER}} / k_B T$
Bare PS particle (No. 6)-Bare glass	0.16	303	141
Bare PS particle (No. 5)-hydrophobic-coated glass	0.18	881	273
Protein-coated PS particle (No.2)-Bare glass	0.42	92	19

Table 4.6. Average experimental values $\langle B_{\mathrm{ER}} \rangle / k_B T$ and variation $\Delta B_{\mathrm{ER}} / k_B T$ of the electrostatic amplitude of three different sphere / wall systems corrected by the facto $C = B_{ER}^{\mathrm{exp}} / B_{ER}^{sim}$ as determined by simulations.

4.2.2 Dynamic properties of particles near different surfaces

4.2.2.1 Experimental dynamic properties

The dynamic properties of particles near the different types of walls, diffusion coefficients $D_{\perp}(h)$ and drift velocities $v_{\mathrm{drift}}(h)$ normal to the interface were calculated from the measured intensity traces, as described in chapter section 3.2. The $D_{\perp}(h)$ experimental results of bare PS particles near both, the bare glass and hydrophobically coated wall, are shown in Figure 4.10 alongside with theoretical models as references. Meanwhile in Figure 4.11, the $v_{\mathrm{drift}}(h)$ experimental data along with calculated model values are presented. On the other hand, dynamic data for protein-coated PS particles near the bare glass is displayed separately in Figure 4.12. In all graphs the dynamic data are plotted as a function of the dimensionless separation distance $h/R = (z-R)/R$.

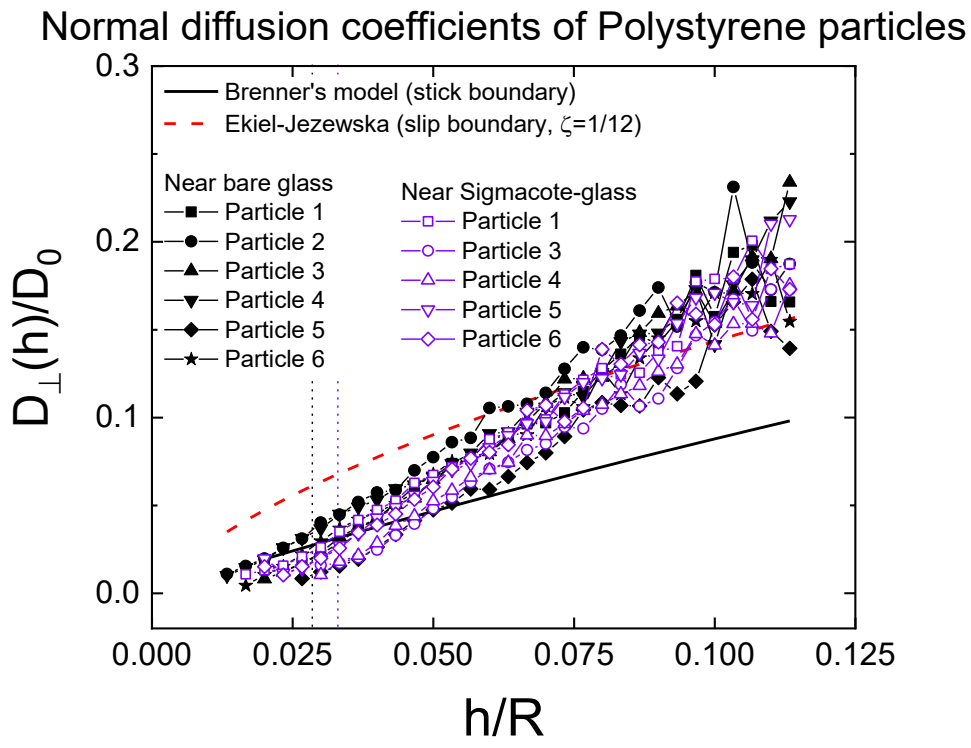

Figure 4.10. Experimentally determined normalized diffusion coefficients perpendicular to the wall as a function of the normalized separation distance for polystyrene particles near two different walls: bare glass (solid black symbols) and Sigmacote-coated glass (open purple symbols). The theoretical model for $D_{\perp}(h)/D_0$ of a sphere (R = 3 μm), based on Brenner's prediction for stick boundary conditions (Eq. 3.27), is represented by the black solid line. The red dashed line corresponds to $D_{\perp}(h)/D_0$ but following partial slip boundary conditions, based on precise numerical calculations by Ekiel-Jezewska's et al. (Eq. 3.28), with a slip parameter of ζ =1/12. The lubrication constants implemented for Eq. 3.28 are listed in Table 2.1. The vertical dotted lines indicate the potential minimum, according to the samples' color code.

According to Figure 4.10, the $D_{\perp}(h)/D_0$ of both systems did not follow completely Brenner's near-wall diffusion model, which assumes stick boundary conditions with the wall. At very short distances, both systems of particles exhibited slower diffusion than the reference model (solid black line). However, beyond a certain separation distance, their $D_{\perp}(h)/D_0$ steeply increased above Brenner's prediction and eventually exceeded it by roughly a factor of two for long distances. A similar behavior, where particles exhibit faster normal diffusion near hard walls, has also been reported in systems influenced by depletion interactions with rods [80]. In addition, PS particles near the hydrophobically coated glass

(purple open symbols) did not show a clear trend as to whether their diffusion is slightly slower or faster compared to those near the bare glass (black full symbols).

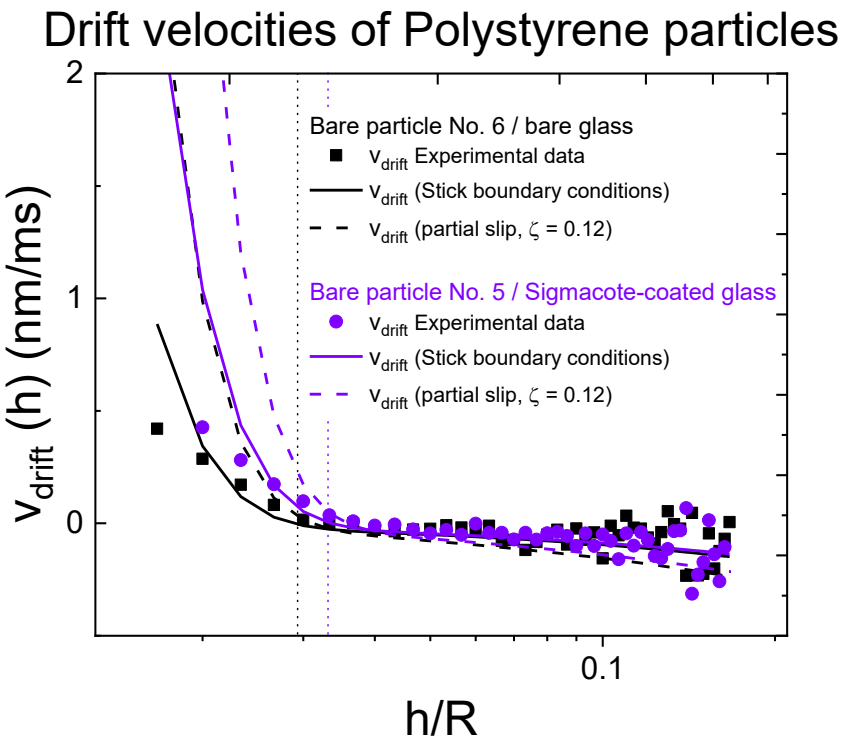

Figure 4.11. Representative data sets for PS particles' drift velocities with respect to normalized separation distance. Experimental data for particles near to two different walls: bare glass (black squares) and Sigmacote-coated glass (purple circles) is shown. Calculated values (Eq. 3.26) for the particle near the bare wall (black lines) and particle near Sigmacote-coated glass (purple lines), both computed following stick boundary conditions (full lines) and partial slip boundary conditions (broken lines). The lubrication constants implemented for Eq. 3.26 are listed in Table 2.1. The vertical dotted lines indicate the potential minimum, according to the samples' color code.

The observed increase of particle dynamics near the walls suggests an alternative interpretation based on particle motion under stick-slip boundary conditions between the particles with the wall [21]. This approach involves calculating friction coefficients by using lubrication expressions that incorporate a slip parameter ζ. Thus, normal diffusion coefficients were calculated assuming partial slip boundary conditions with a slip parameter $\zeta = 0.12$ using Eq. 3.28 and parameters listed in Table 2.1. The

calculated values are shown as the red dashed line in Figure 4.10. These analytical values presented faster dynamics than the experimentally measured constants at short distances but ended meeting at larger separation distances. This disparity, as will be shown in the next Subsection 4.2.3, can be attributed to the effects of too long sampling times. Hypothetically, an agreement between calculated data for stick-slip prediction and experimental data, at short distances, could be achieved by reducing the sampling time. However, in an experiment the sampling time cannot be reduced to the required small values for the reasons briefly mentioned in Subsection 4.2.1 and discussed in detail in Subsection 4.2.3.

Likewise, calculated values for $v_{\mathrm{drift}}(h)$ of bare PS particles near both types of walls were computed by means of Eq. 3.26 and the parameters listed in Table 2.1 and Table 4.5. In Figure 4.11, only a representative data set of each system is shown for visual clarity. In general, the measured $v_{\mathrm{drift}}(h)$ for both systems (symbols) seems to closely followed the analytically calculated values for stick boundary conditions (full lines). At longer distances, significant error bars of the measured data occurred around the analytical curves but due to low statistics while measuring the intensity trace. Besides these similarities, the data related to the hydrophobic wall system was shifted toward larger separation distances.

In parallel, the protein-coated particles near the bare glass (Figure 4.12), exhibited a similar trend of the dynamic quantities as the previous two systems. The experimentally measured $D_{\perp}(h)/D_0$ values (Figure 4.12 top panel) seem to follow the non-slip diffusion model at very short distances, while at long distances, the values surpassed this model. Then, near-wall diffusion with partial slip was considered with a slip parameter of ζ = 1/12 (red dashed line). Under this condition, the experimental data aligned well at intermediate and large distances.

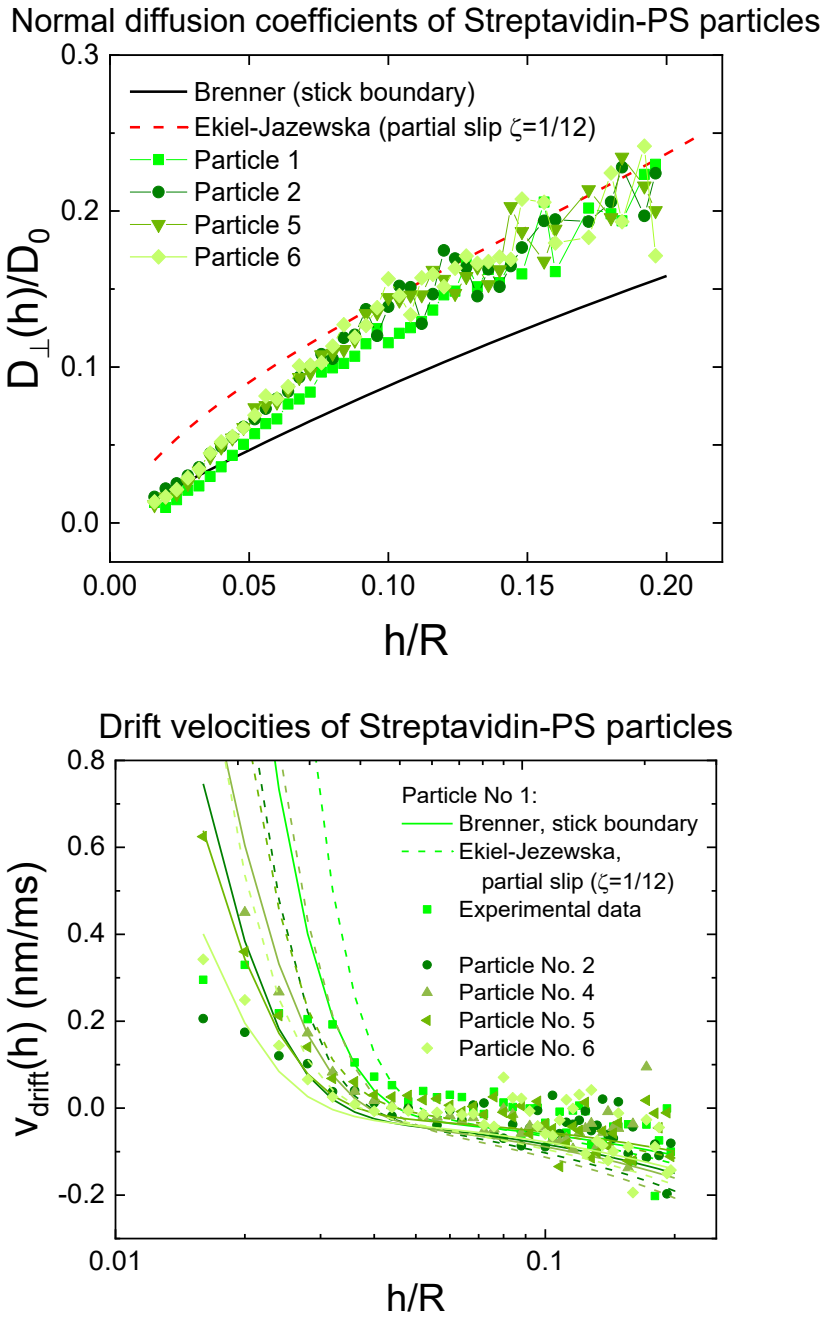

Figure 4.12. *Top*: experimentally determined normal diffusion coefficients as a function of separation distance of Streptavidin-coated PS particles near the bare wall (greenish symbols). Theoretical near-wall dynamics model of a hypothetical sphere (R = 2.5 µm) near a flat wall following stick boundary conditions (hard spheres, black solid line) and partial slip boundary conditions with slip parameter ζ = 1/12 (Ekiel-Jezewska, red dashed line). *Bottom*: experimentally determined drift velocities with respect to normalized separation distance (greenish symbols). The analytical determined values are shown as greenish lines, which were calculated either using stick boundary conditions (solid lines) or partial slip boundary conditions (broken lines) with ζ = 1/12, and the corresponding potential parameter for each particle.

The drift velocities of Streptavidin-coated particles (Figure 4.12 bottom panel) are presented alongside analytical values calculated for both stick (solid lines) and partial slip boundary conditions (dashed lines). The experimental data (symbols) were above both calculated curves for stick and partial slip conditions, exhibiting faster drift velocities at intermediate and large distances. Even so, the experimental data seems to follow the calculated values for stick boundary conditions (solid lines), except for points located at very short distances. However, as will discuss in Subsection 4.2.3, this observation is affected by the role of long sampling times and noise effects at the moment of measurements.

4.2.2.2 Conclusion of experimental dynamic properties

In general, the experiments on the studied three systems exhibited dynamic trends that are not significantly different despite the composition on their surfaces. This indicates that any particle from any system is likely to exhibit dynamics similarly to those from another system. Complementary, analytical calculations of their perpendicular diffusion and drift velocities, based on their interaction potential parameters, were shown as reference. Experimental diffusion constants from the three systems showed some agreement to the analytical calculations for partial slip boundary conditions at separation distances larger their $h_{\min}$. On the other hand, the experimental drift velocities seem to agree better with the analytical prediction for hard sphere with stick boundary conditions. However, this apparent mismatch of the particles' dynamic properties following different models can be solved by the effect of too long sampling times in the experiments. This statement will be addressed in the next Subsection 4.2.3.

4.2.2.3 Simulated dynamic properties

To further investigate the implications of noise and the potential effect of slip, as factors contributing to the discrepancy between measured data and theoretical predictions, Brownian dynamic simulations incorporating these noises were performed and the results are presented next. For easy visualization, simulated data for the dynamics of the simplest case of PS particle near the bare glass is first shown. In this case, the dynamic properties of the system bare PS particle near the bare glass with the progressive

addition of slippage with constant noise (1% background noise plus shot noise) were determined from simulated data. These diffusion constants (Figure 4.13 top panel) and drift velocities (Figure 4.13 bottom panel) perpendicular to the wall are presented below both as a function of normalized separation distance.

In the first plot (Figure 4.13 top panel), simulated normal diffusion constants (symbols) are presented. There, the noise-free data with no slippage (black squares) closely followed the prediction for stick boundary conditions. Similarly, simulated data accounting for stick boundary condition but incorporating full noise (open black squares) matched the same prediction as well. However, at short distances both data sets showed minor deviations from the prediction of hard spheres with stick boundary conditions, and they presented low dispersion around the model line at greater distances.

Diffusion constants that included partial and full slip (ζ = 0.12 and 1/3) with noises also matched their corresponding analytical predictions at intermediate and large distances, with error bars widening as the slip parameter and distance increased. This tendency is simply statistical and does not indicate a deviation from the expected behavior. Meanwhile, at short distances, the simulated diffusion values were noticeable smaller than their corresponding analytical values (broken lines). In general, it was observed that by increasing systematically the slip parameter led to greater differences between the simulated data and the analytical values at short and large dispersion of data at large distances.

Similarly, simulated drift velocities (Figure 4.13 bottom panel) aligned with their corresponding analytical models at distances larger than the equilibrium distance $h_{\min}$, regardless of noise and slip conditions. Also, there was an increase of data scattered around the models and wide error bars. However, this dispersion is due to statistical artifacts and does not indicate a deviation from the expected behavior. However, at short separation distances, noticeable deviations from the analytical curves occurred in all cases, as seen previously with the experimental data. Here, the degree of mismatch between simulated data with their corresponding analytical model also increased with increasing slip parameter.

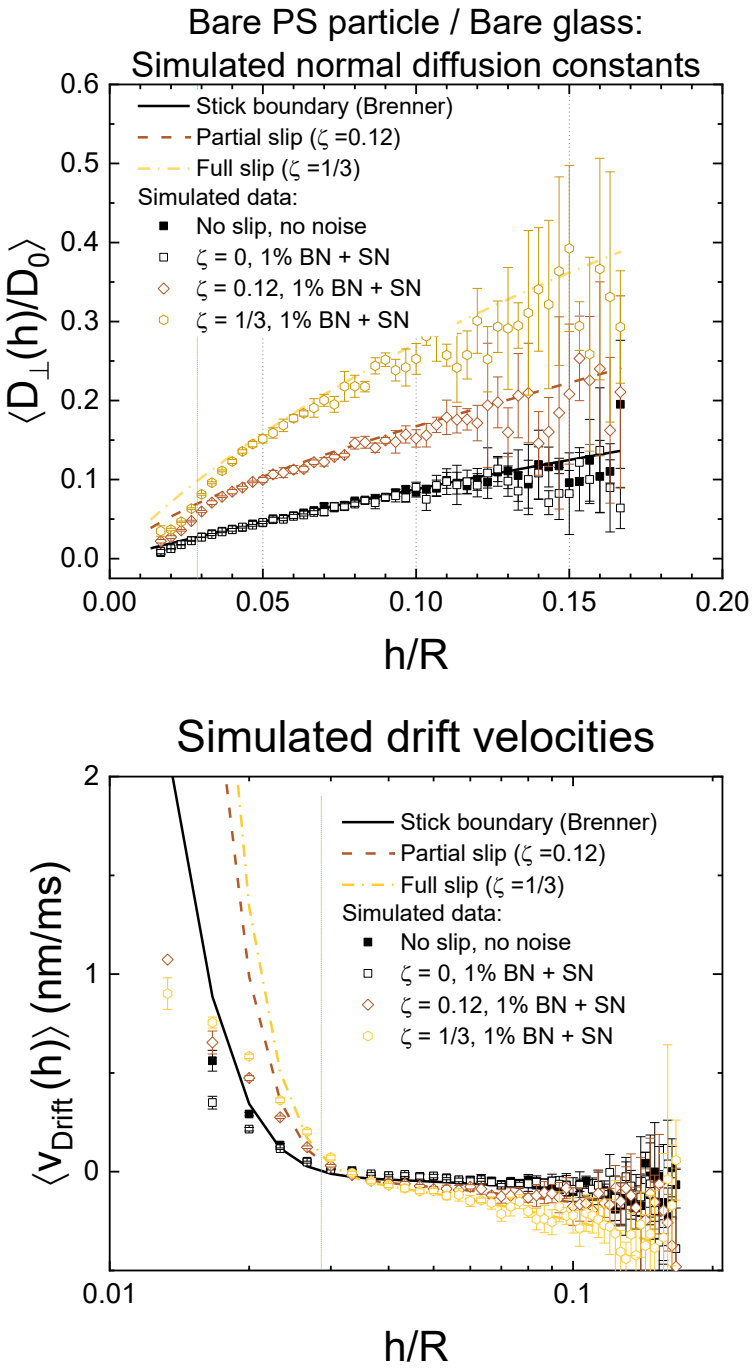

Figure 4.13. Simulated normalized diffusion coefficients (upper panel) and drift velocities (bottom panel) perpendicular to the wall as a function of normalized separation distance. Simulated data (symbols) generated using the experimental parameters of the bare PS-particle No. 6 (Table 4.2) with equilibrium distance located at h/R = 0.029 (vertical green dashed line) and Δt =2 ms. Simulations include 1% background noise (BN) and shot noise (SN), while incorporating different slip conditions: zero slip, partial slip (ζ = 0.12) and full slip (ζ = 1/3). Moreover, calculated dynamic profiles based on hard spheres stick boundary conditions (solid line) and partial slip conditions (broken lines) are presented for reference.

Then, these simulations suggest that noise does not impact drastically on the dynamic properties but susceptible at short distances. However, these deviations at short distances are expected to have their origin in the dominance of large repulsive forces acting on the particles, which violate the assumption of constant forces over the sampling time. Therefore, the sampling time variable is reintroduced to address these discrepancies in the dynamic properties at short distances later in Subsection 4.2.3.

Dynamic properties of the particle-wall systems of interest were computed according with simulated traces based on their experimental conditions. These simulations considered the stick boundary conditions, partial slip (ζ = 0.12) and full slip (ζ = 1/3) in combination with full noise. The experimental parameters used for the simulations were taken from Table 4.5 for selected particles and the sampling time Δt = 2 ms. The resulting normal diffusion constants are presented in Figure 4.14 top panel and the drift velocities in the bottom panel.

In Figure 4.14 top panel, the simulated diffusion coefficients (open symbols) showed comparable results as those in Figure 4.13. For $D_{\perp}/D_0$ with stick boundary conditions (ζ = 0), no noticeable difference was observed between the three particle-wall systems and all closely followed the corresponding model within the error. By increasing the slip parameter to ζ = 0.12, an appreciable difference between simulated data and the analytical values was noticed at very short separation distances. From distances above $h_{\min}$, the simulated data followed the analytical line for partial slip with slight dispersion. Simulated $D_{\perp}/D_0$ with full slip, ζ = 1/3, exhibited evident reduction in the normal diffusion at short separation distances compared to the corresponding analytical line. From distances above $h_{\min}$, simulated data fell into the reference line within the statistical error. To conclude, the simulated $D_{\perp}/D_0$ of the investigated systems did not show any evidence that indicate their surface characteristics influence their dynamics as they showed no significant differences between them. Instead, simulations allowed to identify the subtle systematic effects of noise and slip on the simulated diffusion constants.

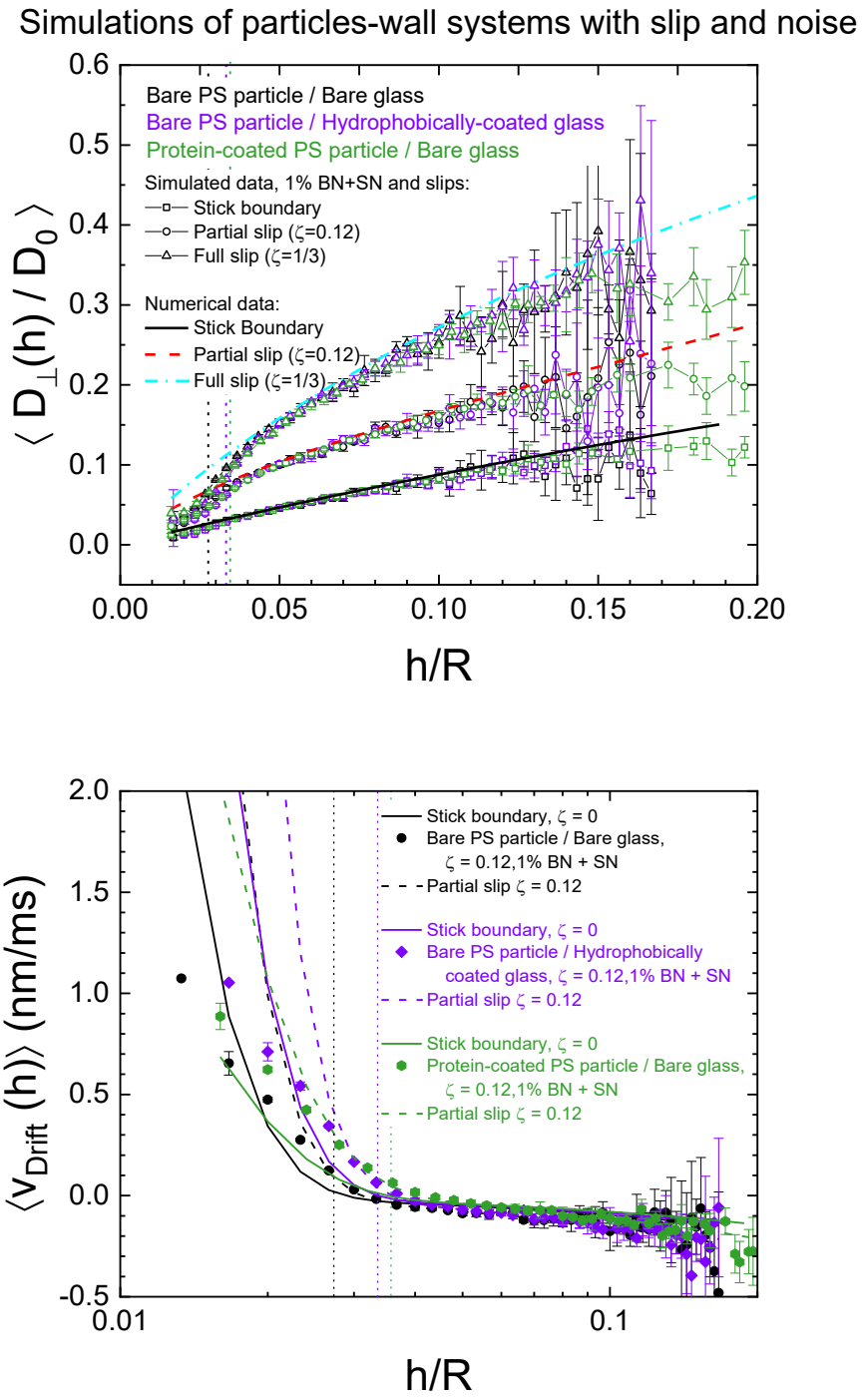

Figure 4.14. Simulated diffusion coefficients (upper panel) and drift velocities (bottom panel) perpendicular to the wall as a function of normalized separation distance of the three studied systems. The simulated data is based on the parameters listed in Table 4.5. The positions of the potential minima are indicated by vertical dotted lines in color-coded as shown in the legend. Simulations incorporate stick boundary conditions and slip boundary conditions, with the addition of 1% background noise (BN) plus shot noise (SN) as stated in the legend. For visual clarity, the cases of simulated drift velocities implementing stick boundary and full slip conditions are displayed in 6.1 Supplementary Information.

According to Figure 4.14 bottom panel, the simulated $v_{\mathrm{drift}}(h)$ with partial slip (full symbols), matched the analytical values for the respective slip parameter (ζ = 0.12, dashed lines) within the error at distances larger than h_{min}. However, as described above, significant deviations from the analytical values were present below h_{min} where the electrostatic repulsion dominates the potential.

In general, for all three systems, the dynamic properties determined by simulations incorporating partial and full slip (ζ = 0.12, ζ = 1/3), showed agreement with the analytical values at separation distances larger than the position of the potential minimum. However, noticeable discrepancies between all simulated data and their respective analytical values arose when the separation distance between the particle and the wall decreased, showing an apparent slowing down of the near-wall dynamics.

Below in Subsection 4.2.3, it will be shown that reducing the sampling time can remove this deviation. This means in turn that the experimental data for all three systems would rather likely approach the prediction for partial slip with ζ = 0.12, if they could be measured with sufficiently small sampling times. Consequently, it is probable that the protein coating of the particles and the hydrophobic coating of the wall did not significantly alter the dynamic properties of the particles, but rather they exhibited partial slip dynamics.

4.2.2.4 Conclusion of simulated dynamic properties

Simulations determining the dynamic properties of particles near the wall showed that inevitable experimental noise does not cause significant deviations of the normal diffusion constants from theoretical predictions based on stick-slip boundary conditions (see Figure 4.13). The drift velocities are affected to a small extent which can be considered negligible in comparison to the effect of other artefacts (see Subsection 4.2.3) Instead, these findings indicate that the effect of noise can be disregarded in the experimental determination of diffusion coefficients and drift velocities, if the scattered light intensities are significantly higher than the noise signals. This can be attributed to the Poisson distribution defining the intensity error, which becomes nearly symmetrical when sufficiently large intensity counts are collected per sampling time.

Further, simulations incorporating slip boundary conditions were performed to evaluate the impact of slip on dynamic properties, as experimental data showed qualitative agreement with partial slip models, particularly at larger separation distances. As expected, the introduction of slip in the simulations resulted in enhanced diffusion coefficients and drift velocities when compared to the non-slip models. However, since neither the simulations in absence of noise nor slip could recover the simulated data matching the analytical models at short distances, the source of such gap is attributed to the use of long sampling times.

The analysis of samples from different particle-wall systems suggests that, despite their particular surface characteristics, there is no significant variation in the distance-dependent diffusion constants or drift velocities. In other words, the near-wall dynamics of these systems appear to be similar between them and follow near-wall dynamics under partial slip conditions.

Finally, the repeatedly observed deviations at short distances are certainly attributed to the use of long sampling times in the experiments. This means that the intrinsic assumption for data evaluation, being that the particle does not move noticeably during the sampling time, is violated if large forces act on the particle. As will be discussed in the next subsection, reducing the sampling time improves the agreement between simulated data and analytical models. However, unlike simulations, sampling time in experiments cannot be reduced arbitrarily due to technical limitations. An alternative strategy could involve using larger probe particles, since a phenomenological relationship links sampling time to particle radius. As a practical guideline, the following equation should be used to estimate the minimum particle size and sampling time when planning future TIRM experiments:

$$v_{\max}(h) \approx \frac{\Delta h}{\Delta t_{\max}} = \frac{\partial \phi(h)}{\partial h} \frac{\lambda^{-1}}{6\pi\eta R}$$

Here, Δh is the experimental spatial resolution. According to the experimental set-up (Subsection 3.2.2), Δh is typically in the range of 0.2 nm approximately, with an intensity resolution of the detector of about 1 kHz. The velocity $v_{\max}(h)$ is given by Stoke's law modified with the near-wall friction contribution. As an example, using typical potential parameters from Table 4.2, a maximum permissible sampling time can be estimated. For a particle-to-wall distance of 50 nm, this is in the order of 0.2 ms, which is approximately one order of magnitude shorter than the time used.

Other than that, the simulations provided important insights about the implications of noise, slip and sampling time that should be considered for the interpretation of the dynamic information obtained by TIRM experiments.

4.2.3 Effect of sampling time on the particles near-wall interaction potential and near-wall dynamics

4.2.3.1 Sampling time in particle-wall static interactions

The noise-free simulations of interaction potentials revealed another factor involved in the deviations from the model potential at short distances, whereas in principle, both of them should coincide. This deviation is attributed to the fact that large forces acting on the particle cause a high drift velocity. In the present case, electrostatic repulsive forces dominate the short-distance region. Under these conditions, the distance a particle travels during sampling time can become so large that the potential can no longer be assumed to be constant. Thus, to fulfil the assumption of constant potential which is implicit in TIRM data evaluation shorter times must be applied.

In Figure 4.15, simulated data addressing the effect of varying sampling time for the calculation of the particle-wall potential interaction is shown. The parameters used for the simulations refer to those found experimentally for the bare PS particle/bare glass system, listed in Table 4.5. The simulated interaction potential profiles were deduced from simulation runs with decreasing sampling time steps.

Simulations demonstrated that reducing the sampling time improves the agreement between the simulated interaction potential and the model potential derived from experimentally determined parameters. Starting from a typical sampling time of $\Delta t = 2$ ms, noise-free simulations reproduced the previously observed deviations at short distances (Figure 4.8, bottom panel). However, when the sampling time was reduced by an order of magnitude ($\Delta t = 0.2$ ms), the simulated potential closely matched the analytical model. In a similar way, simulations with the shortest sampling time tested ($\Delta t = 0.2$ ms) showed excellent agreement with the model potential. On the other hand, simulated potentials incorporating noise (1% background noise and shot noise) at these sampling times exhibited broadened potential profiles, consistent with the expected effect of such noise sources.

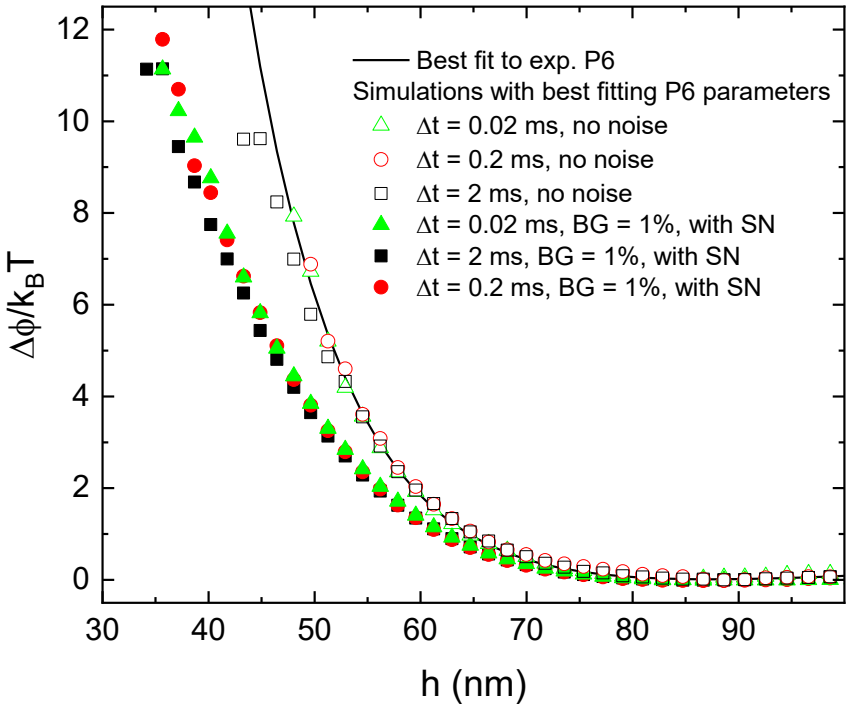

Figure 4.15. Simulations varying the sampling time of noise-free interaction potentials (open symbols) along with the noisy interaction potentials (full symbols) versus separation distances as stated in the legend. The simulated interaction potentials were computed by using the parameters listed in Table 4.5 for the bare PS particle/bare glass system which is displayed as the solid line.

4.2.3.2 Sampling time in the particle near-wall dynamics

The following subsection demonstrates how the reduced sampling times affect the normal diffusion (Figure 4.16) and drift velocity (Figure 4.17) for the bare PS particle near the bare glass surface.

The simulated data for $D_{\perp}(h)/D_0$ in Figure 4.16, showed that by reducing the sampling time systematically from $\Delta t = 2$ ms to 0.2 ms, significantly improved the agreement between simulated values and the analytical prediction at small distances. As expected, simulated values in the absence of noise converged slightly better toward the analytical curve at the short distances with decreasing

sampling time. Nevertheless, simulations for the shortest sampling time (open triangles) exhibited increased dispersion around the analytical line for partial slip. This issue is attributed to poor statistics rather than having any physical origin.

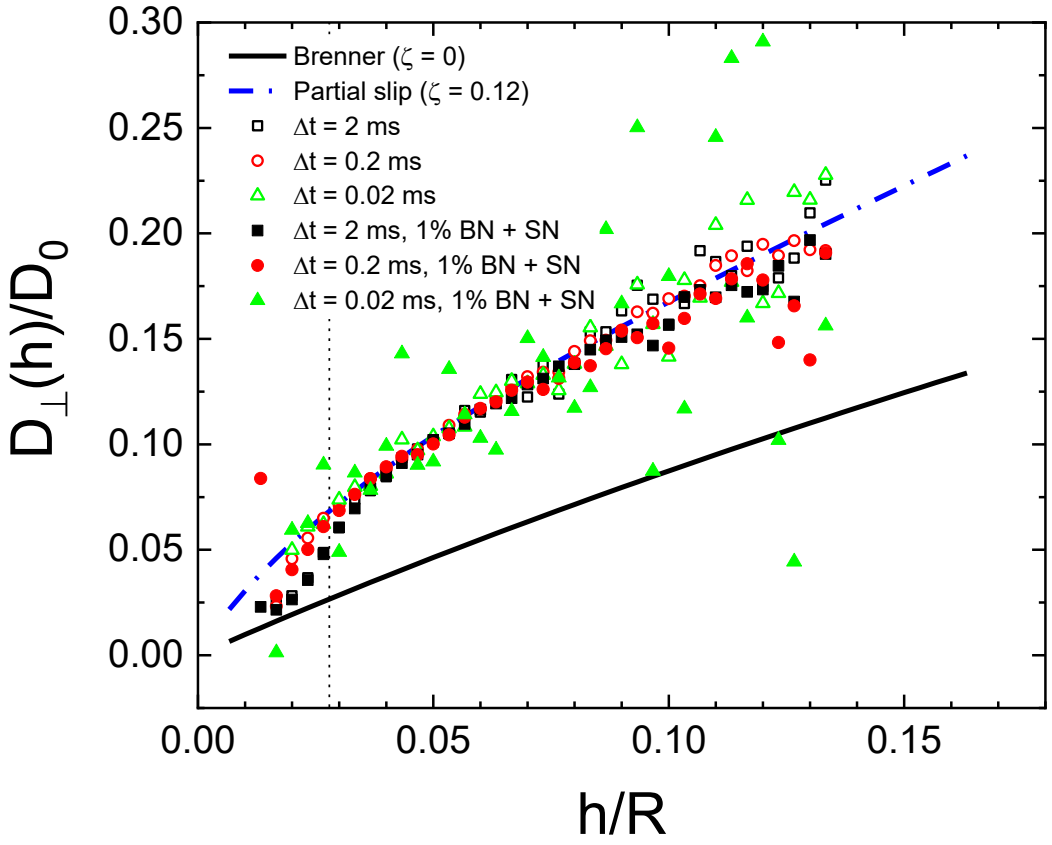

Figure 4.16. Results of simulations with varying sampling time of normal diffusion coefficients under partial slip boundary conditions ($\zeta = 0.12$) disregarding noise (open symbols) and considering noise (full symbols) as a function of normalized separation distances as stated in the legend. Simulated data is based on the parameters listed in Table 4.5 for the bare PS particle (No. 6) near the bare glass. Additionally, Brenner's model for stick boundary dynamics (solid line) and the dynamics following slip boundary conditions ($\zeta = 0.12$, dashed-dotted line) are shown as reference. The position of the potential minimum is indicated by a vertical black dotted line.

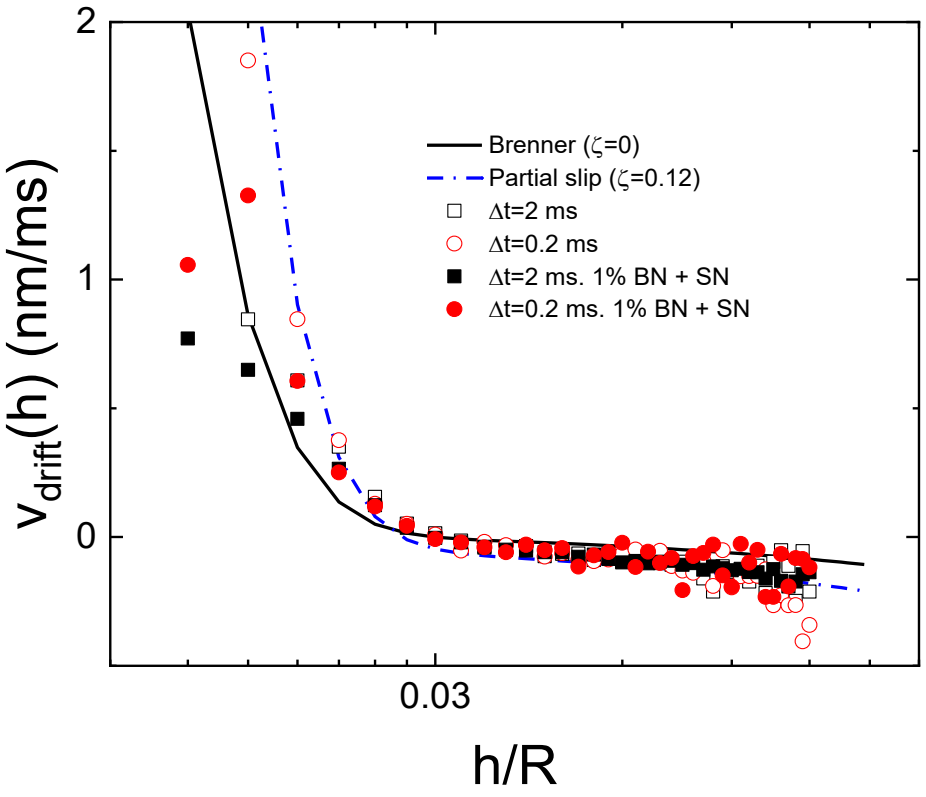

Figure 4.17. Results of simulations with varying sampling times of drift velocities under partial slip boundary conditions ($\zeta = 0.12$) disregarding noise (open symbols) and considering noise (full symbols) as a function of normalized separation distances as stated in the legend. Simulated data is based on the parameters listed in Table 4.5 for the bare PS particle (no. 6) near the bare glass. Additionally, Brenner's model for stick boundary dynamics (solid line) and the dynamics following partial slip boundary conditions ($\zeta = 0.12$, dashed-dotted line) are displayed as reference. The data points for the shortest sampling time are omitted here for the sake of clarity, since they scatter widely.

In Figure 4.17, simulated $v_{\text{drift}}(h)$ in the absence of noise (open symbols), showed better agreement to the partial slip line as decreasing systematically the sampling time from $\Delta t = 2$ ms (squares) to 0.2 ms (circles). There, simulations with a sampling time of 0.2 ms without noise almost reach perfect match with the analytical data for partial slip. Then, if the combination of noises is considered (solid symbols), the simulated data clearly differs from the analytical reference of partial slip, as explained in previous sections. However, here is shown that the as shorter the sampling time is, the closer the simulated data gets to the reference line.

This clarifies the misleading observation of the apparent agreement between the experimental $v_{\text{drift}}(h)$ values with the model for stick boundary conditions. Then, it is presumed that the measured $v_{\text{drift}}(h)$ follow the model for partial slip, matching the diffusion coefficients following the same model (see e. g. Figure 4.12). Thus, the apparent reduction of dynamics at short distance is caused by the combined effects of excessive sampling times and, to a lesser extent, experimental noise.

4.2.3.3 Conclusions on the effect of sampling time

With the implementation of simulations with varying systematically the sampling time, it was possible to unmask the wrong apparent agreement of experimental drift velocities with stick boundary conditions, where in reality, it was a visual coincidence. Then, distortion of the measured drift velocities at short distance are given by the sum of noise and, mainly, too long sampling times. Thus, these simulations support the observation that both $D_{\perp}(h)/D_0$ and $v_{\text{drift}}(h)$ follow partial slip conditions.

The discrepancies between both experimental and simulated data relative to analytical predictions have been emphasized. These inconsistencies arise from the dominant strong repulsive forces acting on the particles. These lead to a significant directed movement of the particles, which causes a violation of the assumption of constant forces during the sampling time. To minimize these deviations and improve accuracy, shorter sampling times should be considered while determining the system's properties with TIRM.

The simulations demonstrate that reducing the sampling time can minimize the discrepancies between simulated results and analytical almost quantitatively. Experimentally, achieving a short sampling time from of $\Delta t = 2$ ms to 0.2 ms would reduce the photon count rate by the same factor and amplify the impact of shot noise. Compensating for this would require a tenfold increase in illumination intensity, which in turn would lead to detector overexposure and dead time losses. Consequently, implementing such short sampling times in real measurements is unfeasible with the current set-up.

Simulations allow for distinguishing the separate effect that noise and sampling time have on the static and dynamic properties of individual particles near a wall. In practice, these combined simulations also advert that even reducing sampling time by 10 times, the inherent noise still prevents the simulated data from aligning completely with analytical predictions. This leads to the conclusion that in a real

TIRM experiment investigating electrostatic repulsion, the Debye length will always be overestimated, and the electrostatic amplitude will always be underestimated.

4.2.4 Streptavidin-coated particles near hydrophobically coated walls (phenomenological and qualitative description)

As briefly mentioned in Subsection 4.2.2, the system of protein-coated PS particles near the hydrophobically coated glass were measured as well. With this system it was impossible to maintain the same experimental conditions of ionic strength as the other systems (I = 1 mM), since the particles became immobile near the surface at the resulting Debye length. Consequently, the intensity traces became almost flat with minimal fluctuations which didn't carry any information about particle motion. Therefore, to enable meaningful measurements of fluctuating intensities, the experimental conditions were changed.

The ionic strength of the suspending solution was reduced by an order of magnitude to address the issue of motionless protein-coated particles at the hydrophobically coated glass. The colloidal suspension was prepared at 0.1 mM NaCl solution corresponding to an estimated Debye length of λ_D = 30.4 nm, to prevent particle adhesion at the interface. However, under these conditions, the particles tended to drift too far away from the wall, resulting in low scattering intensities and low contrast against the background. Therefore, weak optical tweezers (OT) were applied to gently push the particle toward the interface, allowing for reliable detection of the scattered light.

As a consequence of changing these experimental parameters, both the static and dynamic measurements obtained from this system cannot be directly compared to those from the previously studied systems. The resulting interaction potentials for three protein-coated particles near the hydrophobic glass are presented in Figure 4.18 while the corresponding dynamic properties are displayed in Figure 4.20.

4.2.4.1 *Particle-wall interaction potentials and normal diffusion of Streptavidin-coated particles near a hydrophobically coated glass wall*

The interaction potentials of protein-coated PS particles near the hydrophobically-coated glass, immersed in 0.1 mM NaCl and held with OT at 10 mW nominal laser power (open symbols, Figure 4.18), were fitted according to Eq. 3.23. The resulting fit parameters are listed in Table 4.7.

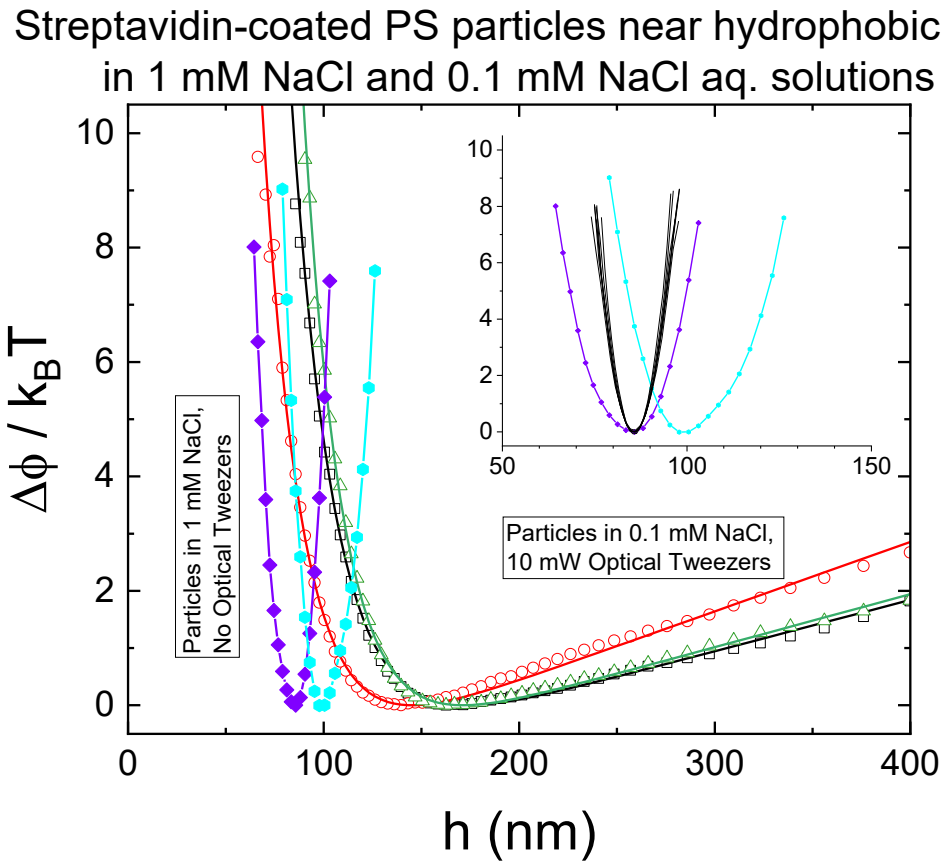

Figure 4.18. Experimentally determined interaction potentials profiles of Streptavidin-coated PS particles near the hydrophobic wall under different experimental conditions. Particles immersed in a 0.1 mM NaCl solution are shown in open symbols, along with their corresponding fitted model potentials (solid lines). Particles suspended in a 1 mM NaCl solution are shown with solid symbols. Inset: comparison between interaction potentials at 1 mM NaCl and the profiles of particles stuck at the interface, measured for the determination of I_0. For visual clarity, the stuck particle potentials have been shifted to match the $h_{\min}$ of the potential in green.

From the interaction potentials curves, two out of three particles showed G_{eff} values closely related to the expected weight of a free polystyrene (PS) particle with nominal radius of 2.5 μm (~35 fN). This value excludes the contribution of the thin outer protein layer since it is negligible, representing just ~5% of the particle's weight. Particle No.2 presented a large mismatch in its effective weight compared to the others. Considering the standard deviation of 0.2 μm of the particles' radius distribution, the corresponding standard deviation of the weight distribution ranges from 27 to 44 fN. But also knowing that ~95% of particle sizes are within a range of two standard deviations, the weight distributes from 20 to 55 fN. Thus, the effective weight of particle No. 2 fell within the expected range. However, since for all particles G_{eff} also includes the effect of the OT photon pressure, their actual weight may be slightly lower.

On the other hand, the measured Debye lengths were smaller than the expected value of λ_{D} = 30.4 nm, ranging from 19.6 to 21.9 nm. These values were 30% lower than that one for a monovalent salt solution at a concentration of 1×10^{-4} M. Additionally, the potential minimum was found at separation distances of approximately 145 and 172 nm. As a result, electrostatic amplitude values were quite different among these particles, differing by a factor of two to three.

Particle	λ_{D} **[nm]**	$h_{\min}$ **[nm]**	G_{eff} **[fN]**	$B_{\text{ER}}/k_B T$
No. 1	21.9	172.9	36.3	520.4
No. 2	19.7	145.0	49.1	376.8
No. 4	19.6	170.9	37.5	1100.2

Table 4.7. Experimental parameters describing the interaction potentials profiles of protein-coated particles (2.5 μm nominal radius) with a hydrophobic wall, determined using non-linear least squares fitting based on Eq. 3.23. The experimental conditions include 0.1 mM NaCl and weak photon pressure. For reference, for a PS particle with a nominal radius of 2.5 μm and density of 1.05 g/ml, immersed in a 0.1 mM monovalent salt solution, a buoyancy corrected weight force G_{eff} = 35 fN and a λ_{D} = 30.4 nm are expected.

Interestingly, these protein-coated PS particles near the hydrophobically coated glass exhibited two distinct behaviors when the ionic strength of the solution was reduced by an order of magnitude. In a 1 mM NaCl solution, the particles appeared trapped in a narrow parabolic potential (solid symbols, Figure 4.18), with their equilibrium positions around 100 nm from the interface, indicating strong confinement without adhesion to the surface. In contrast, when the particles were suspended in a 0.1 mM NaCl solution, they could not be detected due to the absence of scattering contrast with the background. This implies that their equilibrium distance is very far from the surface. Upon applying weak optical tweezers, the particles were pushed toward the interface, revealing typical interaction potential profiles with minima located beyond 140 nm (open symbols). These observations suggest that ionic strength plays a critical role in shaping the interaction potential. However, given the limited dataset, further experimental repetitions are necessary to understand the precise role of ionic strength on this system.

Figure 4.19 shows the comparison of these protein-coated PS particles in the vicinity of different surfaces, bare glass *vs* hydrophobically coated glass, at the same ionic strength (1 mM NaCl), where two different interaction potential profiles were distinguished. In the first case, the particles exhibited a typical near-wall potential profile when near the bare glass (open symbols). In the latter case, the particles were trapped in narrow parabolic potential when close to the hydrophobically coated glass (solid symbols). Interestingly, the equilibrium distances in both systems were found to lie within a similar range: 78 to 110 nm for the bare glass case and 85 to 100 nm for the hydrophobic surface. This comparison suggests that the hydrophobic coating on the wall may influence the attractive component of the interaction potential. However, further experiments are required to confirm this effect.

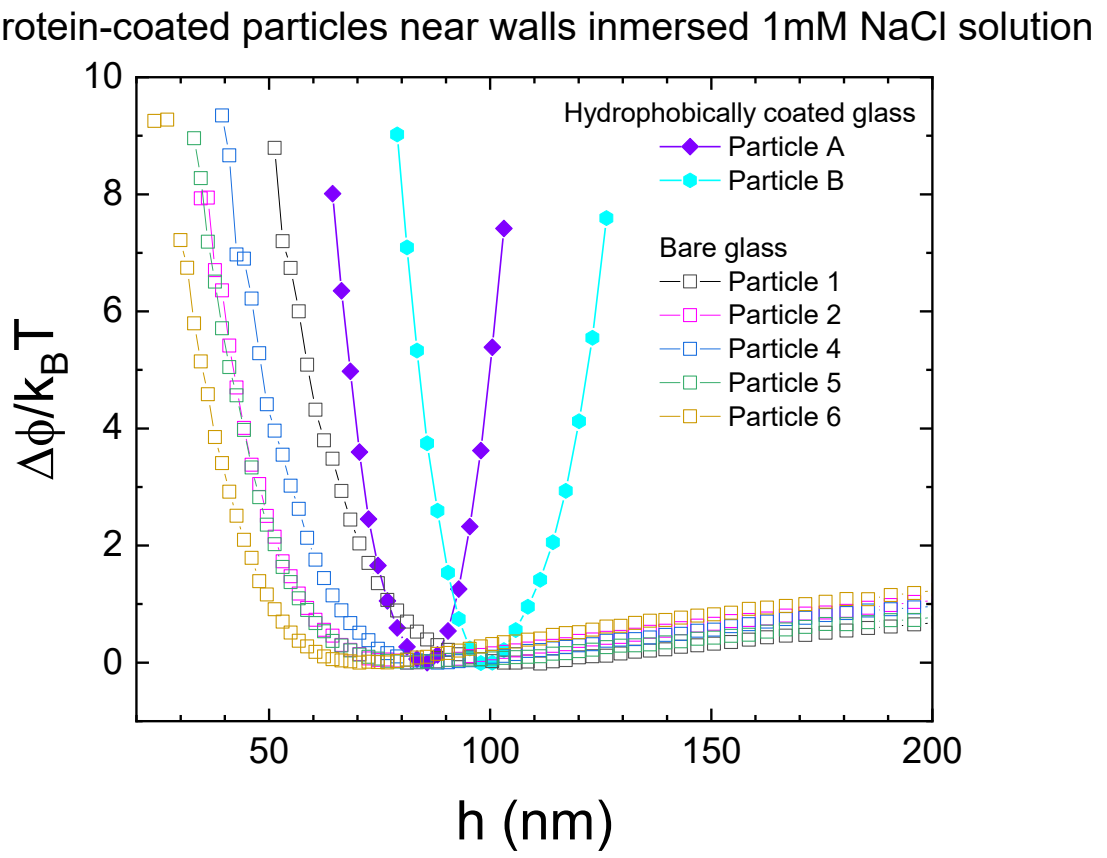

Figure 4.19. Experimentally determined interaction potentials profiles of Streptavidin-coated PS particles, immersed in a 1 mM NaCl solution, near the bare glass (open symbols) and the hydrophobically coated glass (solid symbols).

Differently, the static interaction potentials of the protein-coated particles with a hydrophobically coated wall show peculiarities which cannot be understood on the basis of the currently available data. Therefore, further experiments on this system are necessary to reach a better understanding of this interesting phenomenon. Moreover, similar unexpected interaction profiles were observed in systems involving particles near a supported DPPC lipid bilayer. Only for documentation purposes, this data is included in Supplementary Information. These observations suggest that there may be additional, yet unidentified, contributions to the interaction potential that go beyond the conventional DLVO framework, particularly when the glass wall is modified with a hydrophobic coating.

The near-wall dynamics of the protein-coated particles were examined to evaluate their mobility close to the hydrophobically coated glass under the aforementioned experimental conditions. The diffusion coefficients (Figure 4.20 top panel) were determined from experimental intensity traces and analytical values incorporating partial slip were calculated. The drift velocities (Figure 4.20 bottom panel) were computed and compared with analytical predictions for the slip regime that closely matched the observed diffusion coefficients.

The normal diffusion coefficients $D_{\perp}(h)/D_0$ appeared to approach the analytical values for partial slip with ζ = 1/12 (dashed green line), for separation distances above the potential minimum. This slip parameter of ζ = 1/12 seemed to define a limiting behavior for the particle dynamics. At distances smaller than the potential minimum, the experimental data exhibited smaller values than the reference partial slip curve. According to the previous Subsection 4.2.3, this reduction at short distances is very likely related to the long sampling time used in experiments (Δt = 2 ms), which affects the reliability of measurements in regions dominated by steep potential gradients.

On the other hand, the experimental drift velocities $v_{\text{drift}}(h)$ (Figure 4.19 bottom panel) seemed to follow the partial slip model with ζ = 1/12 (dashed lines) beyond the equilibrium positions. At small separation distances, the experimental data appear to closely follow the model curve for stick boundary conditions (solid lines). However, in light of the discussion in Subsection 4.2.3, it can also be assumed here that this is an artifact caused by too long sampling times and experimental noise.

Excluding artifacts at short distances, probably caused by long sampling times and to a smaller extend by noise, $D_{\perp}(h)/D_0$ and $v_{\text{drift}}(h)$ of protein-coated particles near the hydrophobically coated glass followed a slower partial slip (ζ = 1/12) than those observed for the other systems (ζ = 0.12, see e. g. Figure 4.13).

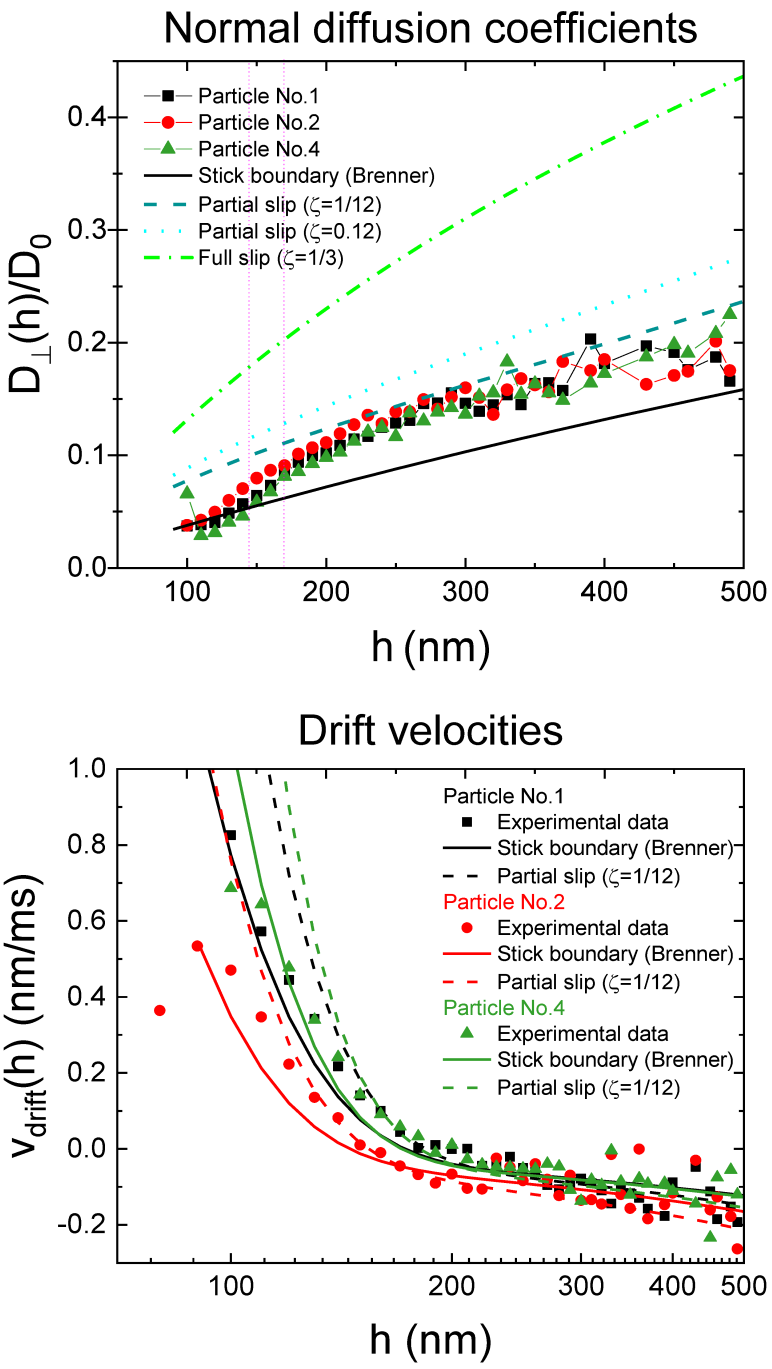

Figure 4.20. Experimentally determined normal diffusion coefficients (upper panel) and drift velocities (bottom panel) as a function separation distance h for Streptavidin-coated PS particles near a hydrophobically coated glass. The particles' normalized diffusion constants are shown along with analytical predictions for different slip conditions: partial slips with ζ = 1/12 (dashed dark green), ζ = 0.12 (dotted light blue light) and full slip ζ = 1/3 (dot-dashed light green line), while Brenner's prediction for stick boundary conditions is presented by a solid line. The measured particles' drift velocities are presented together with analytical models for partial slip conditions with ζ = 1/12 (color-coded broken lines) and stick boundary conditions (color-coded solid lines).

5 Summary and Outlook

The scientific work presented in this thesis contributes to the understanding of colloidal particle systems near walls by providing experimental evidence that deviates from the classical hard sphere model. Unlike ideal spherical particles, those with non-conventional surface morphologies exhibited dynamic properties different from those expected by the theory for smooth spheres near the wall.

The near-wall dynamics of three different colloidal systems of silica particles near a hard wall were measured using EWDLS, and their parallel diffusion coefficients were determined at different normalized penetration depths. The SSi and HSi displayed near-wall dynamics similar to the model for hard spheres. In contrast, the RSi particles exhibited a pronounced reduction in their parallel diffusion, contrary to an expected enhanced dynamics due to the reduced flow resistance on the RSi surface.

To elucidate this behavior, numerical calculations for near-wall dynamics considering factors for polydispersity, aggregation and particle-wall static interactions were conducted, with a particular focus on the RSi system. The systematic exploration in polydispersity factors determined that this variable had a negligible role on the particle dynamics. Meanwhile, aggregation factors showed notable effects on the particle dynamics that decrease the near-wall dynamics but failed to reproduce the trend of RSi in experiments. However, adjusting the static interactions for an attractive potential reduced the near-wall dynamics and brought it closer to the experimental trend for RSi particles. Subsequently, systematic numerical calculations were performed aiming for replicating the experimental data. While SSi and HSi could be described by reasonable physical parameters, the RSi particles required significant attractive contribution in their interaction potential to match the experimental observations. These findings demonstrate that the near-wall dynamics of particles are prone to surface roughness. For particles with pronounced surface roughness, the related attractive particle-wall interaction overcomes the expected hydrodynamic reduction of the flow resistance, resulting in the slowdown of their near-wall dynamics.

Since the fabrication of rough particles can be produced with controlling asperities on the particles' surface, it should be possible to identify the threshold asperity ratio at which particle-wall static interactions begin to surpass the hydrodynamic effects on the near-wall dynamics. In this sense, further systematic investigations for RSi near-wall dynamics are needed in which the degree of roughness is varied to observe the evolution and transition as the particle becomes rougher.

Regarding the static and dynamic properties of surface-modified systems consisting of single particles interacting with the wall were measured by TIRM. The investigated systems included bare particle-wall, bare particles near hydrophobically coated wall, and protein-coated particles near a bare wall. While the overall shapes of the interaction potentials did not differ significantly among the systems, the calculated electrostatic amplitudes varied considerably. The measured diffusion perpendicular to the wall showed faster near-wall dynamics than the prediction for hard spheres under no-slip boundary conditions but aligned better to partial slip approximations.

Due notable discrepancies in both measured static and dynamic properties at short separation distances led to perform Brownian dynamics simulations to assess the effect of unavoidable noise sources: background and shot noise. Experimentally, background noise can be reduced to a negligible contribution in the scattering signal whereas shot noise cannot. Simulations showed that shot noise contributes is the dominant source of distortion in the interaction potential profiles. Although these noises do not contribute significantly on the dynamics, the sampling time was identified as a key parameter in the accuracy for measuring potential interactions and dynamics. Long sampling times lead to an underestimation of the interaction potentials and diffusion constants at short separation distances. If the reduction of sampling time is about 0.2 ms yields accurate estimations at short distances. However, the implementation of such sampling time is unfeasible in experiments due to technical limitations and associated measurements artifacts.

Additionally, the intrigue of non-conclusive results of protein-coated particles near the hydrophobically coated wall (Subsection 4.2.4) demand further experiments on this system to reach a better understanding of the observed phenomenon. So far, such observations suggest additional, yet unidentified, contributions to the interaction potential that go beyond the conventional DLVO framework.

With the refinement and characterization of SLBs with methodologies an additional line of future investigation becomes feasible. Once a robust protocol for the preparation of SLBs using the Langmuir

techniques, proper charged phospholipids may be used to create repulsive barrier in the static particle-SLB interactions. and measure n-w particle motion. Such controlled membrane-like systems would enable accurate measurements of near-wall particle motion under biologically relevant conditions. This direction not only expands the experimental framework toward mimicking real cell-membrane environments but also provides a basis for probing how soft, charged interfaces modulate colloidal dynamics and particle-membrane interactions.

6 Supplementary information

6.1 Results on simulated dynamic properties

6.1.1 Bare PS Particles and Streptavidin-coated PS particles near walls

Dynamic simulations examining the effects of noise and slip on particles near-wall dynamics were presented in Subsection 4.2.2. Here, the complete sets of simulated $v_{\text{drift}}(h)$ are shown for the three different systems: bare PS particle near bare glass, bare PS particle near hydrophobically coated glass, and protein-coated PS particle near the bare glass. For visual clarity, $v_{\text{drift}}(h)$ considering different slip parameters are presented separately.

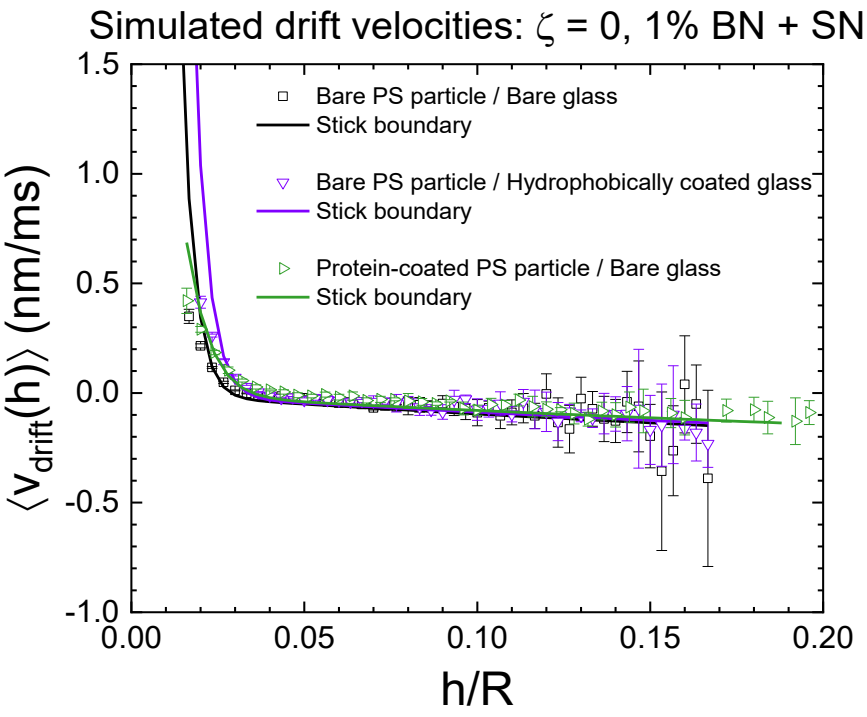

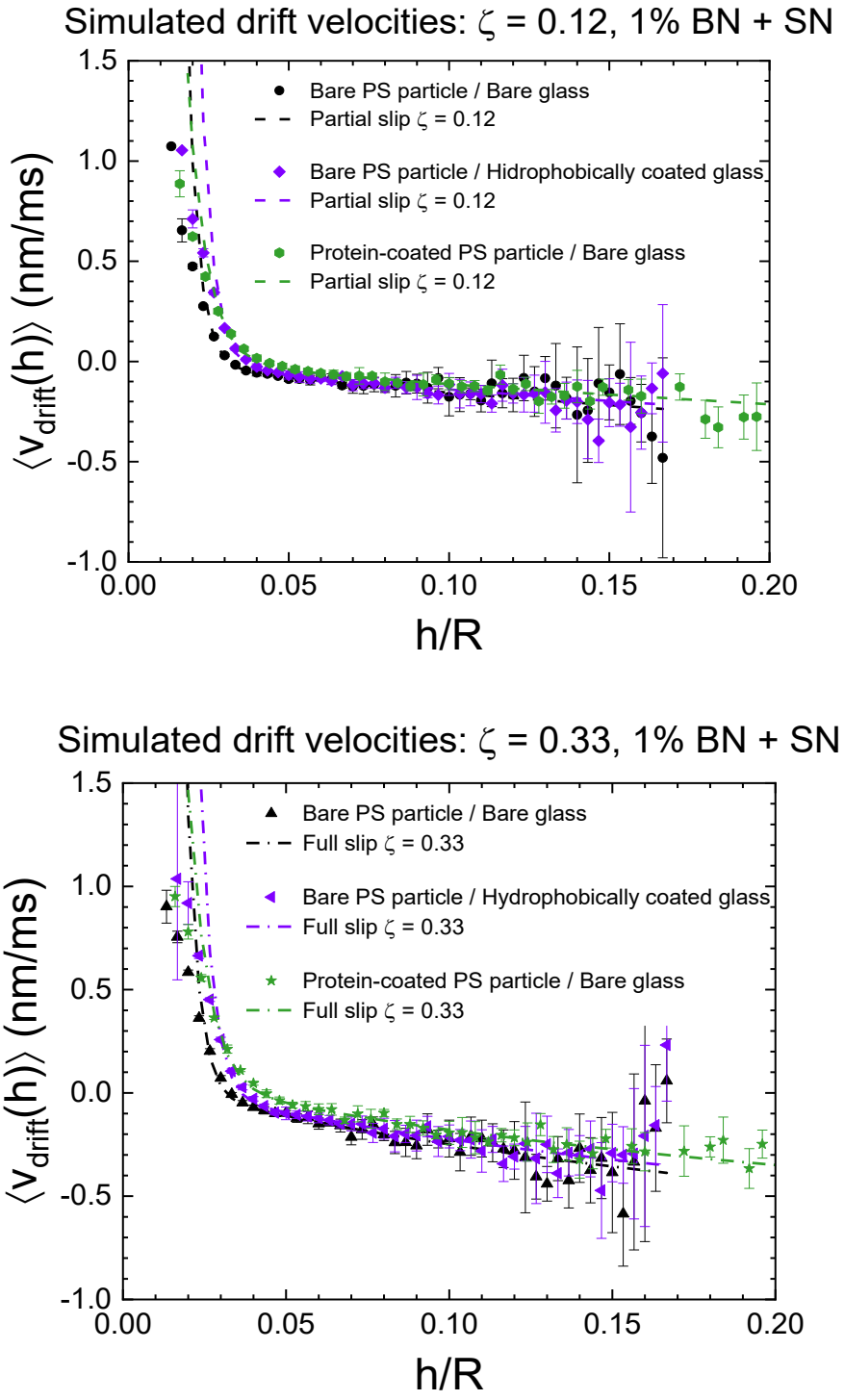

Figure S1. Simulated drift velocities as a function of normalized separation distance. These simulations are based on the parameters listed in Table 4.4 and computed at a sampling time of $\Delta t = 2$ ms. Simulations incorporate stick boundary conditions (top panel), partial slip (middle panel) and full slip (bottom panel) boundary conditions, with the addition of 1% background noise (BN) plus shot noise (SN), as stated in the legends.

6.2 Particles near a supported lipid bilayer (SLB)

6.2.1 Preparation and sample cell assembly

As the name indicates, SLB are phospholipid bilayers supported on solid surfaces, often glass or mica. SLBs were fabricated by consecutively applying the Langmuir-Blodgett (LB) [11] and Langmuir-Schaefer (LS) [85] techniques. The floating lipid film was composed of DPPC (1,2-dipalmitoyl-sn-glycero-3-phosphocholine, Avanti Polar Lipids, LLC, Alabama, USA) on a water surface which were transferred twice onto the glass substrate, being BK7 squared coverslips (Menzel-Gläser, Germany).

Instrumentation: The preparation of lipid mono- and bilayers was carried out using a Langmuir trough (Microtrough G2, Kibron Inc. Oy, Finland) operated via the *FilmWare X* software package (Kibron Inc. Oy, Finland). The trough is equipped with two PTFE barriers and force balance system that utilizes DyneProbe™ (cylindrical analog of Wilhelmy thin plates), which is in contact with the subphase (milli-Q grade water). A motorized dip-coating elevator operated separately by *LayerX* software package (Kibron Inc. Oy, Finland). The elevator supports mounting either a mechanical clamp, which holds the coverslips with their flat surface vertically for LB coating, or a vacuum clamp (Layer X LS-clamp vacuum, Kibron Inc. Oy, Finland) which secures the coverslips horizontally for LS coating.

Setting the phospholipid film: Using the mechanical clamp, a cleaned coverslip is vertically immersed into the trough well. The trough is then filled with Milli-Q grade water to a level slightly above the edge of the trough. The interface cleanliness is then checked by doing compression-relaxation cycles and looking that the surface pressure variation does not exceed 0.1 mN/m over values less than zero. If these conditions are not met, indicating the presence of contaminants, the barriers must be set in the closed position (minimal area) to thoroughly clean the surface of the inner space using an aspirator. This process is repeated until the cleaning conditions are satisfied.

Monolayer preparation by LB technique: Once cleaned, the barriers are opened to their relaxation position (maximum area), and an aliquot of 30 µl DPPC lipid solution (1 mg/ml in Chloroform), is carefully spread onto the water surface. After allowing 30 minutes for complete evaporation of the solvent, the lipid monolayer is compressed using PTFE barriers at rate of 5.1 mm^2/min until a target

surface pressure of 40 mN/m is achieved and remains constant, forming an equilibrated condensed-structure film.

To deposit the phospholipid layer, the motorized elevator raises the coverslip vertically at similar rate of 5.1 mm^2/min, allowing it to pass through the lipid film at the interface. As the glass ascends, the monolayer is transferred onto its surface. To maintain uniform coverage during this transfer, the film area is dynamically reduced via a software-controlled feedback loop that compensates for material loss while maintaining constant film pressure. Once the coverslip has fully crossed the interface, the Langmuir-Blodgett process is complete, resulting in a single phospholipid layer on each side of the glass, with the hydrocarbon chains facing outward (toward air).

Bilayer preparation by LS technique: Since SLB requires to be kept in a liquid environment, this technique is ideal for performing the second transfer while maintaining SLB in such an environment at all times. The top part of the TIRM sample cell (a top coverslip with spacer) is placed into a specially designed tray and submerged in the trough when setting the instrument. Then, once LB transfer is complete and the floating phospholipid film is restored to the condense structure and constant surface pressure, the monolayer-coated coverslip is held flat and parallel to the lipid film using the vacuum suction clamp. As illustrated in Figure S2-A, the glass is carefully centered and aligned above the submerged top coverslip of the sample cell. Using the motorized elevator, the monolayer-coated glass is lowered to until it comes into contact with the floating film and passes through it. Thus, deposition of the second lipid layer and the assembly of the TIRM sample cell is achieved in a single step.

Subsequently, the remaining lipid film at the water surface is removed by aspiration, and the tray holding the sample cell is carefully extracted from the trough (Figure S2-B). Once outside, the external surfaces of the glass are gently dried using lint-free wipes. Coordinately, the sample cell is filled with the colloidal suspension by pipetting through one of the side openings, while the water inside is dragged from the opposite end using a lint-free wipe, as shown in Figure S2-C. Finally, the cell is sealed with UV-curable glue, as described previously in Methods chapter.

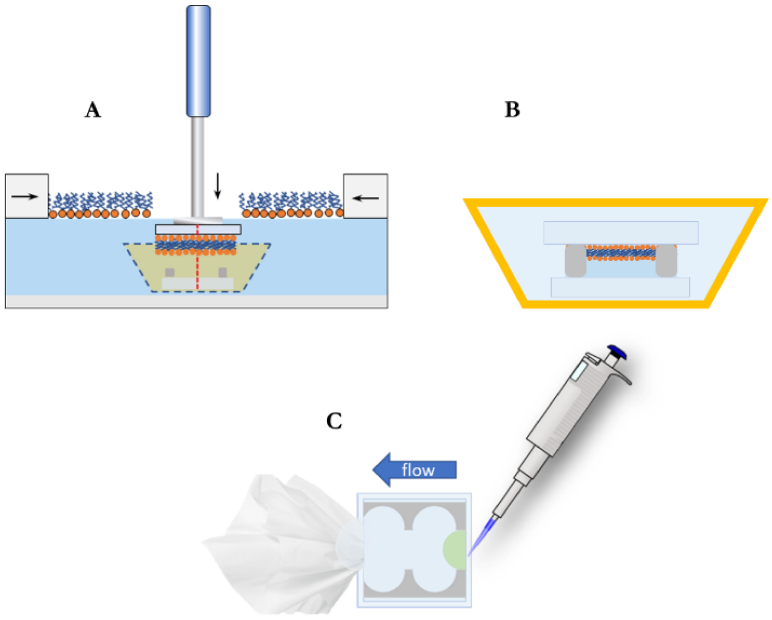

Figure S2. Final steps of the supported lipid bilayer preparation and sample cell assembly. A) The second lipid layer is transferred by the Langmuir-Schaefer procedure and the SLB is pushed all the way down to join the top part of the sample cell placed inside a specially designed tray. B) In the complete sample cell, the SLB is covered by water preserving the SLB integrity inside the chamber. C) The colloidal suspension is injected into the sample cell from the smaller inlet while the water is blotted from the other side using a paper tissue.

6.2.2 Phenomenological results

Polystyrene particles on DPPC supported lipid bilayer

Polystyrene particles with a nominal radius of 3 μm , immersed in a 1 mM NaCl aqueous solution, were introduced into the SLB sample cell. Then, TIRM experiments were conducted as a preliminary investigation to measure the particle-bilayer interaction potentials. The measured potential profiles are displayed in Figure S3.

Initially, the particles were not located near the interface but far from the interface. To overcome this, a weak optical tweezer (10 mW output power) was used to push the particles closer to the bilayer. The particle measured in the first sample (blue squares) exhibited a parabolic potential with an equilibrium distance of 70 nm, where its perpendicular movement was constrained within a narrow range. Further measurements with increased strength of the OT showed similar potential profiles, which are not shown for visual clarity.

In contrast, another particle from a second sample was measured while systematically varying the optical tweezers' power from 60 to 10 mW in steps of 5 mW. The potentials showed three distinct profile configurations which are highlighted in Figure S4 with the solid symbols and the three different colors. First, the potential at 60 mW, the potential exhibited a broad profile with two local minima.

As the tweezers' strength was gradually reduced, 55 mW (tilted green triangles) to 45 (open green symbols), the potentials showed typical near-wall profiles, all with the same $h_{\min} \approx 70$ nm.

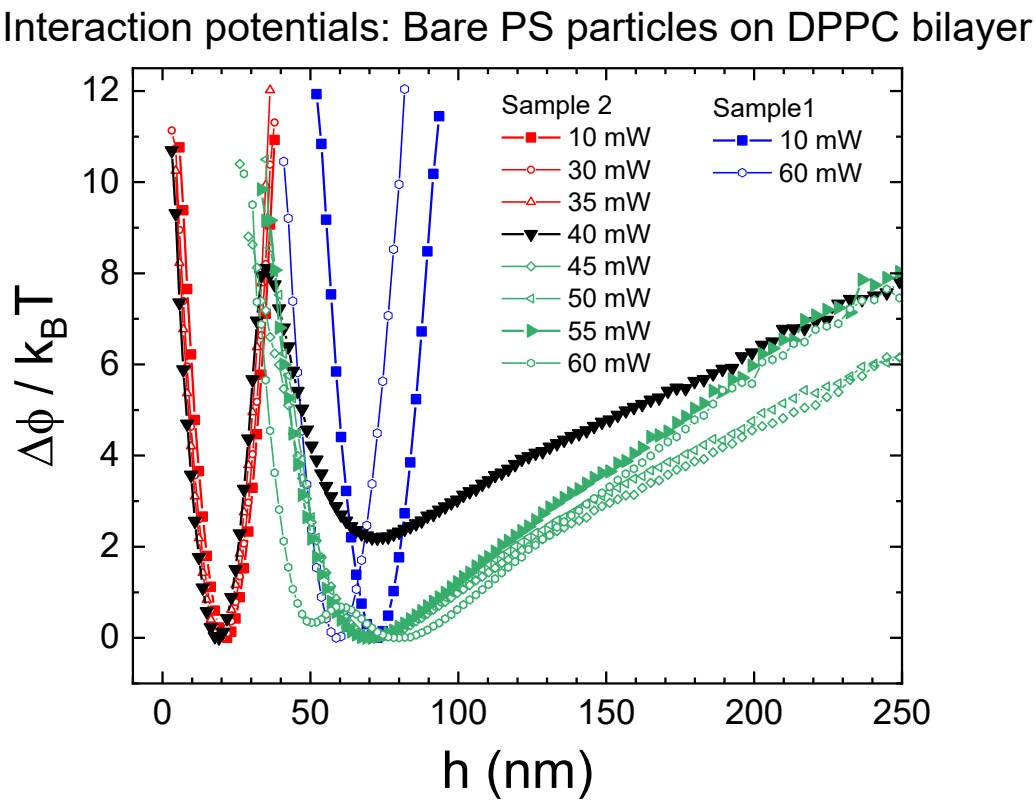

Figure S3. Experimentally determined interaction potentials as a function of separation distance from the SLB of bare PS particles immersed in 1mM NaCl aqueous solution. For visual clarity, only selected potential profiles are shown for Sample 1 (blue symbols) while the complete set of potential profiles of Sample 2 are presented as indicated in the legend.

Additionally, a progressive reduction in the slope of the linear part of the potential was observed, consistent with the reduction of the tweezers' strength. At 40 mW (black inverted triangles), a "transition" of the potential occurred, changing from typical near-wall potential with $h_{\min}$ ≈ 70 nm to a parabolic shape with the minimum at $h_{\min}$ ≈ 20 nm. After this "transition", subsequent measurements at low powers (35 mW to 10 mW, red symbols), consistently displayed parabolic potentials with a minimum located at $h_{\min}$ ≈ 20 nm, suggesting that the particle was likely stuck onto the bilayer. The drop in the equilibrium positions of the potentials might be directly related to the presence of the DPPC bilayer. Since DPPC molecules are electrically neutral (pI_{DPPC} : pH ~4 [47]) at the solvent's pH (~ 5), is likely that net surface charge of the SLB was reduced. And consequently, electrostatic repulsion would be diminished, allowing the particles to approach closer to the SLB. Further experimentation needs to be done for the first sample to support the observed behavior.

The inconsistency between samples, along with the wide variability in interaction potentials profiles exhibited by individual particles, highlights the need for a complementary characterization technique to assess the bilayer's homogeneity and surface potential. Moreover, the presence of multiple interaction potential shapes makes it unfeasible to describe these complex interactions using the previously applied theoretical framework. Consequently, since the obtained near-wall interaction potentials did not follow completely the theoretical model used so far (Eqs. 3.22 and 3.23), it was not possible to extract the physical parameters that describe the particle-wall interaction. To establish a clearer understanding of the interactions between PS particles and the DPPC-supported lipid bilayer, further measurements are required along with the consideration of alternative theoretical models.

Streptavidin-coated PS particles on DPPC supported lipid bilayer

Having seen the apparent immobility of the PS particles observed in the previous system, due to likely diminished surface charges, these protein-coated PS particles were prepared in 10 mM NaCl solution and adjusted to a final pH of 2 using HCl. By lowering the pH to this level, the isoelectric points of both Streptavidin proteins ($pI_{Streptavidin}$: pH ~ 6 [18]) and DPPC molecules (pI_{DPPC} : pH ~4 [47]) were surpass allowing them to acquire positive electrical charges. This resulting electrostatic repulsion could prevent the particles from becoming stuck to the membrane. Then, exploration experiments for the interaction

potentials of Streptavidin-coated PS particles near the DPPC-supported lipid bilayer (Figure S4) were performed.

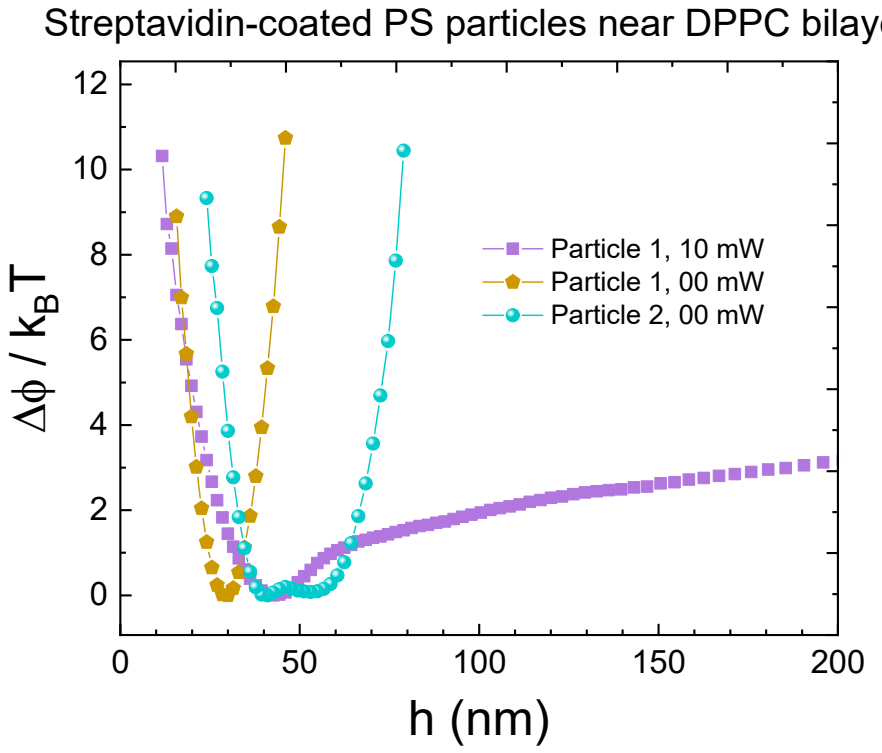

Figure S4. Experimentally determined interaction potentials as a function of separation distance from the supported lipid bilayer of protein-coated PS particles immersed in 10 mM NaCl aqueous solution and adjusted to a pH of 2.

Particle No. 1 was measured under an additional optical tweezer power of 10 mW (purple squares) and revealed a near-wall interaction potential characterized by two distinct slopes in the attractive part of the potential, resembling the potentials of systems with depletant agents. The potential minimum was located at $h_{\min}$ ~ 40 nm. The steeper slope near the potential minimum indicates a strong attractive force between the particle and the wall, while the least steep slope at larger distances, is directly associated with the particles' buoyant weight. However, when this particle was measured without the influence of optical tweezers (orange pentagons), its behavior changed, exhibiting a parabolic potential

with $h_{\min}$ ~ 30 nm, suggesting that the particle had likely become stuck at the bilayer interface. Nevertheless, given that this separation distance is larger than the typical bilayer's thickness (~ 5-7 nm), it is questionable regarding the integrity and composition of the bilayer.

Particle No.2 was measured in the absence of optical tweezers (blue spheres). The resulting interaction potential displayed a broad parabolic profile, suggesting that the particle had become immobile. Additionally, the potential exhibited two adjacent local minima at $h_{\min}$ = 40 nm and $h_{\min}$ = 55 nm, both with equal depth.

These three potential profiles lack consistency in their shape, making it unsuitable to apply the model potential used throughout this work. Consequently, extracting the physical parameters within this theoretical framework is not feasible. To address the challenges encountered during the experiments and initial findings under the given conditions, future studies should consider using charged phospholipids. This approach would help establish well-defined electrostatic repulsion while maintaining a reasonable ionic strength in the solution

References

[1] Anderson, O., Daalderop, G. H. O., and Bange, K. 1997. X-ray reflectivity investigations of glass surfaces produced by float and draw techniques. *Microchimica Acta* 125, 1, 63–67.

[2] Antoniou, E., Voudouris, P., Larsen, A., Loppinet, B., Vlassopoulos, D., Pastoriza-Santos, I., and Liz-Marzán, L. M. 2012. Static and dynamic plasmon-enhanced light scattering from dispersions of polymer-grafted silver nanoprisms in the bulk and near solid surfaces. *The Journal of Physical Chemistry C* 116, 6, 3888–3896.

[3] Avvakumova, S., Colombo, M., Galbiati, E., Mazzucchelli, S., Rotem, R., and Prosperi, D. 2018. Chapter 6 - Bioengineered Approaches for Site Orientation of Peptide-Based Ligands of Nanomaterials. In *Biomedical Applications of Functionalized Nanomaterials : Micro and Nano Technologies*, B. Sarmento and J. das Neves, Eds. Elsevier, 139–169. DOI=10.1016/B978-0-323-50878-0.00006-9.

[4] Bangs Laboratories, Inc. *Washing microspheres" technote 203, Rev #005*. https://bangslabs.com/wp-content/uploads/BLI_TN203_WashingSeparation.pdf.

[5] Behrens, S. H. and Grier, D. G. 2001. The charge of glass and silica surfaces. *The Journal of Chemical Physics* 115, 14, 6716–6721.

[6] Bergström, L. 1997. Hamaker constants of inorganic materials. *Advances in Colloid and Interface Science* 70, 125–169.

[7] Bevan, M. A. and Prieve, D. C. 1999. Direct Measurement of Retarded van der Waals Attraction. *Langmuir* 15, 23, 7925–7936.

[8] Bevan, M. A. and Prieve, D. C. 2000. Hindered diffusion of colloidal particles very near to a wall: Revisited. *The Journal of Chemical Physics* 113, 3, 1228–1236.

[9] Bhattacharjee, S., Ko, C.-H., and Elimelech, M. 1998. DLVO interaction between rough surfaces. *Langmuir* 14, 12, 3365–3375.

[10] Biondi, S. A. and Quinn, J. A. 1995. Direct observation of hindered brownian motion. *AIChE Journal* 41, 5, 1324–1328.

[11] Blodgett, K. B. 1935. Films Built by Depositing Successive Monomolecular Layers on a Solid Surface. *Journal of the American Chemical Society* 57, 6, 1007–1022.

[12] Butt, H. J. and Kappl, M. 2010. *Surface and Interfacial Forces*. Wiley-VCH, Federal Republic of Germany.

[13] Cichocki, B., Felderhof, B. U., Hinsen, K., Wajnryb, E., and Bl/awzdziewicz, J. 1994. Friction and mobility of many spheres in Stokes flow. *The Journal of Chemical Physics* 100, 5, 3780–3790.

[14] Cichocki, B., Jones, R. B., Kutteh, R., and Wajnryb, E. 2000. Friction and mobility for colloidal spheres in Stokes flow near a boundary: The multipole method and applications. *The Journal of Chemical Physics* 112, 5, 2548–2561.

[15] Colombi, P., Agnihotri, D. K., Asadchikov, V. E., Bontempi, E., Bowen, D. K., Chang, C.-H., Depero, L. E., Farnworth, M., Fujimoto, T., and Gibaud, A. 2008. Reproducibility in X-ray reflectometry: results from the first world-wide round-robin experiment. *Applied Crystallography* 41, 1, 143–152.

[16] Cui, F., Marbach, S., Zheng, J. A., Holmes-Cerfon, M., and Pine, D. J. 2022. Comprehensive view of microscopic interactions between DNA-coated colloids. *Nature communications* 13, 1, 2304.

[17] Cui, F. and Pine, D. J. 2021. Effect of photon counting shot noise on total internal reflection microscopy. *Soft matter* 18, 1, 162–171.

[18] Diamandis, E. P. and Christopoulos, T. K. 1991. The biotin-(strept)avidin system: principles and applications in biotechnology. *Clinical Chemistry* 37, 5, 625–636.

[19] Dufresne, E. R., Altman, D., and Grier, D. G. 2001. Brownian dynamics of a sphere between parallel walls. *Europhysics Letters* 53, 2, 264.

[20] Eichmann, S. L., Anekal, S. G., and Bevan, M. A. 2008. Electrostatically confined nanoparticle interactions and dynamics. *Langmuir* 24, 3, 714–721.

[21] Ekiel-Jeżewska, M. L. and Wajnryb, E. 2018. Motion of a particle with stick-slip boundary conditions towards a flat interface: hard wall or free surface. Physicochemical Problems of Mineral Processing; ISSN 2084-4735.

[22] Ellingson, M. O. and Bevan, M. A. 2024. Direct measurements & simplified models of colloidal interactions & diffusion with adsorbed macromolecules. *Soft matter* 20, 34, 6808–6821.

[23] Ermak, D. L. and Buckholz, H. 1980. Numerical integration of the Langevin equation: Monte Carlo simulation. *Journal of Computational Physics* 35, 2, 169–182.

[24] Everett, W. N., Beltran-Villegas, D. J., and Bevan, M. A. 2010. Concentrated diffusing colloidal probes of Ca2+-dependent cadherin interactions. *Langmuir : the ACS journal of surfaces and colloids* 26, 24, 18976–18984.

[25] Everett, W. N. and Bevan, M. A. 2014. kT-Scale interactions between supported lipid bilayers. *Soft matter* 10, 2, 332–342.

[26] Everett, W. N., Wu, H.-J., Anekal, S. G., Sue, H.-J., and Bevan, M. A. 2007. Diffusing colloidal probes of protein and synthetic macromolecule interactions. *Biophysical journal* 92, 3, 1005–1013.

[27] Faucheux, L. P. and Libchaber, A. J. 1994. Confined brownian motion. *Phys. Rev. E* 49, 6, 5158.

[28] FAXEN, H. 1923. Die Bewegung einer starren Kugel langs der Achse eines mit zaher Flussigkeit gefullten Rohres. *Arkiv for Matemetik Astronomi och Fysik* 17, 1–28.

[29] Frej, N. A. and Prieve, D. C. 1993. Hindered diffusion of a single sphere very near a wall in a nonuniform force field. *The Journal of Chemical Physics* 98, 9, 7552–7564.

[30] Goldman, A. J., Cox, R. G., and Brenner, H. 1967. Slow viscous motion of a sphere parallel to a plane wall—II Couette flow. *Chemical Engineering Science* 22, 4, 653–660.

[31] Hamaker, H. C. 1937. The London—van der Waals attraction between spherical particles. *physica* 4, 10, 1058–1072.

[32] Holmqvist, P., Dhont, J. K. G., and Lang, P. R. 2006. Anisotropy of Brownian motion caused only by hydrodynamic interaction with a wall. *Physical review. E, Statistical, nonlinear, and soft matter physics* 74, 2 Pt 1, 21402.

[33] Holmqvist, P., Dhont, J. K. G., and Lang, P. R. 2007. Colloidal dynamics near a wall studied by evanescent wave light scattering: experimental and theoretical improvements and methodological limitations. *The Journal of Chemical Physics* 126, 4, 44707.

[34] Holmqvist, P., Kleshchanok, D., and Lang, P. R. 2007. Unexpected slow near wall dynamics of spherical colloids in a suspension of rods. *Langmuir* 23, 24, 12010–12015.

[35] Holmqvist, P., Kleshchanok, D., and Lang, P. R. 2008. Interaction potential and near wall dynamics of spherical colloids in suspensions of rod-like fd-virus. *The European physical journal. E, Soft matter* 26, 1, 177–182.

[36] Hosoda, M., Sakai, K., and Takagi, K. 1998. Measurement of anisotropic Brownian motion near an interface by evanescent light-scattering spectroscopy. *Phys. Rev. E* 58, 5, 6275–6280.

[37] Howard Brenner. 1961. The slow motion of a sphere through a viscous fluid towards a plane surface. *Chemical Engineering Science* 16, 3, 242–251.

[38] Hsiao, L. C., Jamali, S., Glynos, E., Green, P. F., Larson, R. G., and Solomon, M. J. 2017. Rheological state diagrams for rough colloids in shear flow. *Physical review letters* 119, 15, 158001.

[39] Hsiao, L. C. and Pradeep, S. 2019. Experimental synthesis and characterization of rough particles for colloidal and granular rheology. *Current Opinion in Colloid & Interface Science* 43, 94–112.

[40] Hsu, C.-P., Ramakrishna, S. N., Zanini, M., Spencer, N. D., and Isa, L. 2018. Roughness-dependent tribology effects on discontinuous shear thickening. *Proceedings of the National Academy of Sciences* 115, 20, 5117–5122.

[41] Iracki, T. D., Beltran-Villegas, D. J., Eichmann, S. L., and Bevan, M. A. 2010. Charged Micelle Depletion Attraction and Interfacial Colloidal Phase Behavior. *Langmuir* 26, 24, 18710–18717.

[42] Israelachvili, J. N. 2011. *Intermolecular and surface forces*. Academic press.

[43] Jeffrey, D. J. and Onishi, Y. 1984. Calculation of the resistance and mobility functions for two unequal rigid spheres in low-Reynolds-number flow. *Journal of Fluid Mechanics* 139, 261–290.

[44] Jones, R. A. L. 2002. *Soft condensed matter*. Oxford University Press.

[45] July, C., Kleshchanok, D., and Lang, P. R. 2012. Shear-affected depletion interaction. *The European physical journal. E, Soft matter* 35, 7, 60.

[46] July, C. and Lang, P. R. 2010. Depletion interactions effected by different variants of fd virus. *Langmuir* 26, 24, 18647–18651.

[47] Karwowska, K., Skrodzka, E., Kotyńska, J., and Petelska, A. D. 2020. Equilibria in DPPC-Diosgenin and DPPC-Diosgenin Acetate Bilayer Lipid Membranes: Interfacial Tension and Microelectrophoretic Studies. *Coatings* 10, 4.

[48] Kienzle, P. 2025. *Neutron activation and scattering calculator*. NIST Center for Neutron Research, 2013-04-17 v1.3.8.

[49] Kleshchanok, D., Tuinier, R., and Lang, P. R. 2006. Depletion interaction mediated by a polydisperse polymer studied with total internal reflection microscopy. *Langmuir* 22, 22, 9121–9128.

[50] Kleshchanok, D., Tuinier, R., and Lang, P. R. 2008. Direct measurements of polymer-induced forces. *Journal of Physics: Condensed Matter* 20, 7, 73101.

[51] Kunert, C. and Harting, J. 2007. Roughness induced boundary slip in microchannel flows. *Physical review letters* 99, 17, 176001.

[52] Kunert, C., Harting, J., and Vinogradova, O. I. 2010. Random-roughness hydrodynamic boundary conditions. *Physical review letters* 105, 1, 16001.

[53] Lang, P. 1999. Amphiphiles at interfaces studied by surface sensitive x-ray scattering. *Surfactant science series*, 377–416.

[54] Lang, P. and Liu, Y. 2016. *Soft Matter at Aqueous Interfaces* 917. Springer International Publishing, Cham.

[55] Li, W., Cao, F., He, C., Ohno, K., and Ngai, T. 2018. Measuring the interactions between protein-coated microspheres and polymer brushes in aqueous solutions. *Langmuir* 34, 30, 8798–8806.

[56] Lin, B., Yu, J., and Rice, S. A. 2000. Direct measurements of constrained Brownian motion of an isolated sphere between two walls. *Phys. Rev. E* 62, 3, 3909.

[57] Lin, S. and Wiesner, M. R. 2010. Exact analytical expressions for the potential of electrical double layer interactions for a sphere-plate system. *Langmuir : the ACS journal of surfaces and colloids* 26, 22, 16638–16641.

[58] Lisicki, M., Cichocki, B., Dhont, Jan KG, and Lang, P. R. 2012. One-particle correlation function in evanescent wave dynamic light scattering. *The Journal of Chemical Physics* 136, 20.

[59] Liu, Y. 2016. *Near-wall dynamics of colloidal particles studied by evanescent wave dynamic light scattering*. Dissertation, Heinrich-Heine Universität Düsseldorf.

[60] Liu, Y., Bławzdziewicz, J., Cichocki, B., Dhont, Jan KG, Lisicki, M., Wajnryb, E., Young, Y.-N., and Lang, P. R. 2015. Near-wall dynamics of concentrated hard-sphere suspensions: comparison of evanescent wave DLS experiments, virial approximation and simulations. *Soft matter* 11, 37, 7316–7327.

[61] Loppinet, B., Dhont, J. K., and Lang, P. 2012. Near-field laser Doppler velocimetry measures near-wall velocities. *The European physical journal. E, Soft matter* 35, 7, 62.

[62] M. I. M. Feitosa and O. N. Mesquita. Wall-drag effect on diffusion of colloidal particles near surfaces: A photon correlation study.

[63] Manley, S., Horton, M. R., Lecszynski, S., and Gast, A. P. 2008. Sorting of streptavidin protein coats on phase-separating model membranes. *Biophysical journal* 95, 5, 2301–2307.

[64] Michailidou, V. N., Petekidis, G., Swan, J. W., and Brady, J. F. 2009. Dynamics of concentrated hard-sphere colloids near a wall. *Physical review letters* 102, 6, 68302.

[65] Michailidou, V. N., Swan, J. W., Brady, J. F., and Petekidis, G. 2013. Anisotropic diffusion of concentrated hard-sphere colloids near a hard wall studied by evanescent wave dynamic light scattering. *The Journal of Chemical Physics* 139, 16.

[66] N. Garnier and N. Ostrowsky. 1991. Brownian dynamics in a confined geometry. Experiments and numerical simulations. *J. Phys. II France* 1, 10, 1221–1232.

[67] Odiachi, P. C. and Prieve, D. C. 2004. Removing the effects of additive noise from TIRM measurements. *Journal of colloid and interface science* 270, 1, 113–122.

[68] Parratt, L. G. 1954. Surface studies of solids by total reflection of X-rays. *Physical review* 95, 2, 359.

[69] Petroff, M. G., Garcia, E. A., Herrera-Alonso, M., and Bevan, M. A. 2019. Ionic strength-dependent interactions and dimensions of adsorbed zwitterionic copolymers. *Langmuir* 35, 14, 4976–4985.

[70] Piech, M., Weronski, P., Wu, X., and Walz, J. Y. 2002. Prediction and measurement of the interparticle depletion interaction next to a flat wall. *Journal of colloid and interface science* 247, 2, 327–341.

[71] Prieve, D. C. 1999. Measurement of colloidal forces with TIRM. *Advances in Colloid and Interface Science* 82, 1-3, 93–125.

[72] Rajagopalan, R. and Chu, R. Q. 1982. Dynamics of adsorption of colloidal particles in packed beds. *Journal of colloid and interface science* 86, 2, 299–317.

[73] Richmond, P. 1975. Electrical forces between particles with discrete periodic surface charge distributions in ionic solution. *J. Chem. Soc., Faraday Trans. 2* 71, 0, 1154–1163.

[74] Rivera-Morán, J. A. and Lang, P. R. 2023. Analysing Sources of Error in Total Internal Reflection Microscopy (TIRM) Experiments and Data Analysis. *Polymers* 15, 21.

[75] Rivera-Morán, J. A., Liu, Y., Monter, S., Hsu, C.-P., Ruckdeschel, P., Retsch, M., Lisicki, M., and Lang, P. R. 2021. The effect of morphology and particle–wall interaction on colloidal near-wall dynamics. *Soft matter* 17, 45, 10301–10311.

[76] Ruckdeschel, P., Dulle, M., Honold, T., Förster, S., Karg, M., and Retsch, M. 2016. Monodisperse hollow silica spheres: An in-depth scattering analysis. *Nano Res.* 9, 5, 1366–1376.

[77] Rücker, U. D 2 Scattering under Grazing Incidence from Surfaces and Interfaces.

[78] Shen, X., Wang, A. E., Sankaran, R. M., and Lacks, D. J. 2016. First-principles calculation of contact electrification and validation by experiment. *Journal of Electrostatics* 82, 11–16.

[79] Sholl, D. S., Fenwick, M. K., Atman, E., and Prieve, D. C. 2000. Brownian dynamics simulation of the motion of a rigid sphere in a viscous fluid very near a wall. *The Journal of Chemical Physics* 113, 20, 9268–9278.

[80] Sio, S. de, July, C., Dhont, J. K. G., and Lang, P. R. 2018. Near wall dynamics of a spherical particle in crowded suspensions of colloidal rods - dynamic information from TIRM revisited. *Soft matter* 14, 45, 9232–9242.

[81] Sofikitis, D., Bougas, L., Katsoprinakis, G. E., Spiliotis, A. K., Loppinet, B., and Rakitzis, T. P. 2014. Evanescent-wave and ambient chiral sensing by signal-reversing cavity ringdown polarimetry. *Nature* 514, 7520, 76–79.

[82] Suresh, L., et al. Direct Measurement of the Effect of Surface Roughness on the Colloidal Forces between a Particle and Flat Plate.

[83] Suresh, L., et al. Effect of Surface Roughness on the Interaction Energy between a Colloidal Sphere and a Flat Plate.

[84] Swavola, J. C., Edwards, T. D., and Bevan, M. A. 2015. Direct Measurement of Macromolecule-Coated Colloid-Mucus Interactions. *Langmuir : the ACS journal of surfaces and colloids* 31, 33, 9076–9085.

[85] Tamm, L. K. and McConnell, H. M. 1985. Supported phospholipid bilayers. *Biophysical journal* 47, 1, 105–113.

[86] Verwey, E., Overbeek, J., and van Nes, K. 1948. *Theory of the Stability of Lyophobic Colloids: The Interaction of Sol Particles Having an Electric Double Layer*. Elsevier Publishing Company.

[87] Vinogradova, O. I. and Belyaev, A. V. 2011. Wetting, roughness and flow boundary conditions. *Journal of Physics: Condensed Matter* 23, 18, 184104.

[88] Volpe, G., Helden, L., Brettschneider, T., Wehr, J., and Bechinger, C. 2010. Influence of noise on force measurements. *Physical review letters* 104, 17, 170602.

[89] Walz, J. Y. 1997. Measuring particle interactions with total internal reflection microscopy. *Current Opinion in Colloid & Interface Science* 2, 6, 600–606.

[90] Walz, J. Y. 1998. The effect of surface heterogeneities on colloidal forces. *Advances in Colloid and Interface Science* 74, 1, 119–168.

[91] Walz, J. Y. and Sun, N. 2023. Effects of surface roughness on van der Waals and electrostatic contributions to particle-particle interactions and particle adhesion. In *Particles on Surfaces: Detection, Adhesion and Removal, Volume 7*. CRC Press, 151–169.

[92] Walz, J. Y. and Suresh, L. 1995. Study of the sedimentation of a single particle toward a flat plate. *The Journal of Chemical Physics* 103, 24, 10714–10725.

[93] Wang, Z., Gong, X., and Ngai, T. 2015. Measurements of long-range interactions between protein-functionalized surfaces by total internal reflection microscopy. *Langmuir : the ACS journal of surfaces and colloids* 31, 10, 3101–3107.

[94] Wang, Z., He, C., Gong, X., Wang, J., and Ngai, T. 2016. Measuring the surface–surface interactions induced by serum proteins in a physiological environment. *Langmuir* 32, 46, 12129–12136.

[95] Wang, Z., Luan, Y., Gan, T., Gong, X., Chen, H., and Ngai, T. 2017. Long-range interactions between protein-coated particles and POEGMA brush layers in a serum environment. *Colloids and Surfaces B: Biointerfaces* 150, 279–287.

[96] Wu, H.-J. and Bevan, M. A. 2005. Direct Measurement of Single and Ensemble Average Particle−Surface Potential Energy Profiles. *Langmuir* 21, 4, 1244–1254.

[97] Wu, H.-J., Pangburn, T. O., Beckham, R. E., and Bevan, M. A. 2005. Measurement and Interpretation of Particle−Particle and Particle−Wall Interactions in Levitated Colloidal Ensembles. *Langmuir* 21, 22, 9879–9888.

[98] Wu, J., Liu, W., and Ngai, T. 2023. Total internal reflection microscopy: a powerful tool for exploring interactions and dynamics near interfaces. *Soft matter* 19, 25, 4611–4627.

[99] Zanini, M., Hsu, C.-P., Magrini, T., Marini, E., and Isa, L. 2017. Fabrication of rough colloids by heteroaggregation. *Colloids and Surfaces A: Physicochemical and Engineering Aspects* 532, 116–124.

[100] Zhang, P., Zhou, L., Wang, R., Zhou, X., Jiang, J., Wan, Z., and Wang, S. 2022. Evanescent scattering imaging of single protein binding kinetics and DNA conformation changes. *Nature communications* 13, 1, 2298.

Acknowledgements

At this stage of my academic path, I would like to thank Dr. Peter Lang for giving me the opportunity to work here in the group and on such an interesting topic. I value his constant support, both inside and outside the laboratory. I would also like to express special thanks to Dr. Jan Dhont for the chance to join IBI-4 at that time and for the valuable discussions that supported this research work. My special gratitude goes to Angelika Schmitz for her constant help in every circumstance which contributed to creating a smooth working place. I also thank Manolis Stiakakis for his friendly career-life advice and jokes. Also, I would like to thank all members of the IBI-4 group, past and present, as well as the staff who in one way or another help me throughout my chapter in this group, leveling up my skills and work experience.

I am especially grateful to the friends I met when I first joined the group: Zihan, Shilpa, Amir, Katarina, and Mehrnaz, for the memorable moments at the institute and the many happy times we shared outside of work. I would also like to thank the friends I met during the final stage of my time at the institute: Theodora, Binny, Michelle, and Margot, who not only made me laugh more than ever, but also helped me stay motivated and supported me in bringing this work to completion.

Finally, my deepest gratitude to my beloved people, Eli and my family (my mother, grandma, brothers, and father), for their unconditional and constant support throughout the most challenging moments of this journey. For this reason, I dedicate this thesis and all effort behind it to them, and to the memory of my grandfather.

Volume 17
Number 45
7 December 2021
Pages 10163–10396

Soft Matter

rsc.li/soft-matter-journal

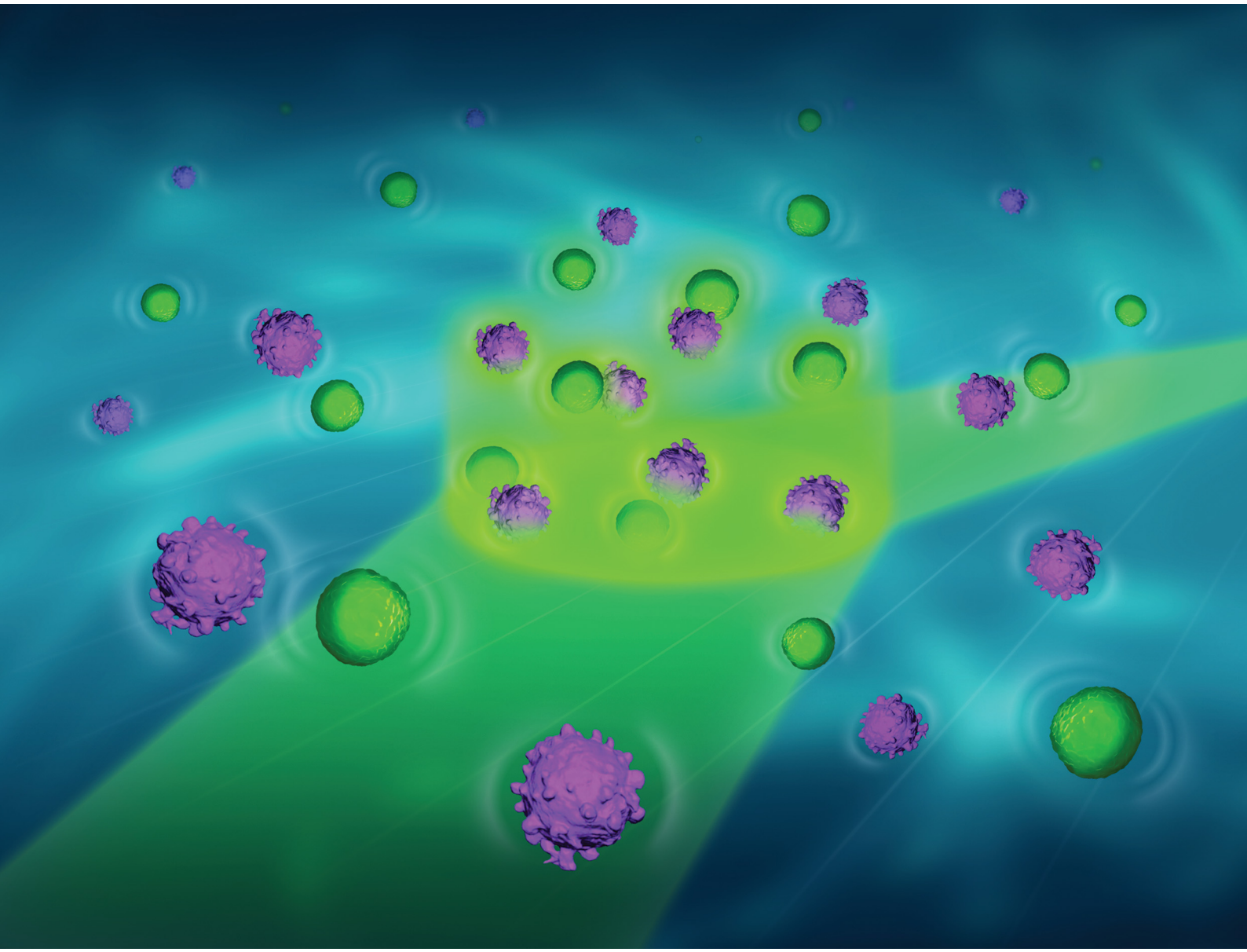

ISSN 1744-6848

ROYAL SOCIETY OF CHEMISTRY

PAPER
Peter R. Lang *et al.*
The effect of morphology and particle–wall interaction on colloidal near-wall dynamics

Soft Matter

PAPER

View Article Online
View Journal | View Issue

Cite this: *Soft Matter*, 2021, **17**, 10301

The effect of morphology and particle–wall interaction on colloidal near-wall dynamics†

J. Alejandro Rivera-Morán, [a] Yi Liu,[a] Samuel Monter, [ab] Chiao-Peng Hsu, ‡[c] Pia Ruckdeschel,[d] Markus Retsch, [d] Maciej Lisicki [e] and Peter R. Lang *[a]

Received 14th August 2021,
Accepted 28th September 2021

DOI: 10.1039/d1sm01191j

rsc.li/soft-matter-journal

We investigated the near-wall Brownian dynamics of different types of colloidal particles with a typical size in the 100 nm range using evanescent wave dynamic light scattering (EWDLS). In detail we studied dilute suspensions of silica spheres and shells with a smooth surface and silica particles with controlled surface roughness. While the near wall dynamics of the particle with a smooth surface differ only slightly from the theoretical prediction for hard sphere colloids, the rough particles diffuse significantly slower. We analysed the experimental data by comparison with model calculations and suggest that the deviating dynamics of the rough particles are not due to increased hydrodynamic interaction with the wall. Rather, the particle roughness significantly changes their DLVO interaction with the wall, which in turn affects their diffusion.

1 Introduction

The low Reynolds-number dynamics of particles near a flat interface is generally slower than in bulk and directionally anisotropic due to an increased flow resistance caused by hydrodynamic interaction between particles and the interface. The first theoretical investigations of this effect date back to the early twentieth century,[1,2] while the first experimental verifications[3] only became available in the 1980s. With the modern microscopy and evanescent wave scattering methods[4] that are now available, there have been numerous investigations of colloidal dynamics in the ultimate vicinity of glass surfaces during the last three decades.[5–20] With a few exceptions,[7,8,18] in most of these investigations, data-analysis and interpretation is based on the assumption of particles with smooth surfaces and no static interaction with the wall other than excluded volume. Similarly, in most studies concerning static particle–particle or particle–wall interactions, flat and homogeneous surfaces are assumed.[21–24] Only since synthesis methods have been available, which allow the batch production of particles with controlled surface roughness,[25–27] have systematic studies on the effect of particle roughness become possible.

The rheological behaviour and particle deposition on various kinds of surfaces have been intensively investigated. It was found that in suspensions of rough particles the onset of discontinuous shear thickening is shifted towards lower volume fractions and critical stresses as compared to particles with smooth surfaces.[26,28,29] This effect is commonly attributed to additional tangential stresses caused by hydrodynamic interaction or solid contacts of asperities. The deviation between experientially observed particle deposition rates and values predicted assuming DLVO interaction between bodies with smooth surfaces has been attributed to the neglect of roughness for a long time. Analytical expressions for the interaction potential between rough particles are not available, but simulations suggest that the stabilization barrier of DLVO potentials is significantly reduced by surface roughness.[30,31] An analytical approximation for the interaction energy between a rough particle and a flat surface was given by Suresh *et al.*[32] and verified by total internal reflection microscopy experiments.[33] Jin *et al.*[34] provided the first numerical model for particle deposition including the impact of surface roughness, merging modified expressions for DLVO interactions between rough surfaces and hydrodynamic interaction.

So-called hairy colloids, *i.e.* core–shell particles consisting of a hard particle core carrying polymer brushes, may be regarded as a limiting case of rough particles with extremely pointed asperities and high surface coverage. However, such particles show a qualitatively different rheology, *e.g.*, the presence of the brushes suppresses shear thickening.[35,36] This is attributed to the fact that the brush behaves like a porous shell, reducing the flow resistance as compared to a compact sphere with the same outer radius. The hydrodynamics of such particles can be described by invoking a hydrodynamic penetration length

[a] *Forschungszentrum Jülich, IBI-4, Jülich, Germany. E-mail: p.lang@fz-juelich.de*
[b] *Universität Konstanz, Germany*
[c] *ETH-Zürich, Switzerland*
[d] *Universität Bayreuth, Germany*
[e] *University of Warsaw, Poland*

† Electronic supplementary information (ESI) available. See DOI: 10.1039/d1sm01191j

‡ Present address: Technische Universität München, Germany.

which reduces the effective hydrodynamic radius to a value smaller than the outer radius of the core shell particle.[37–39] The same concept can be generally applied to flows past rough surfaces at low Reynolds numbers.[8,40,41] Consequently, rough particles and porous shell particles are expected to show faster near-wall dynamics as compared to smooth particles with the same outer radius.

In our investigation we employed full spherical particles with a smooth surface, micro-porous spherical shells and spherical particles with surface roughness to test this prediction. We used evanescent wave dynamic light scattering (EWDLS) experiments supported by numerical model calculations to study the Brownian particle dynamics parallel to a flat glass wall. After a thorough introduction to the materials and methods in Section 2 and the numerical model in Section 3, we discuss our findings in Section 4.

2 Experimental

2.1 Materials

We investigated three different types of silica particles, namely standard spheres with a smooth surface (SSi), spherical hollow shells (HSi) and spheres with controlled surface roughness (RSi). The HSi particles were synthesized in a three-step procedure consisting of the synthesis of a monodisperse polystyrene latex core by emulsifier-free emulsion polymerisation which was covered by a silica shell applying a Stöber synthesis protocol. After purification and drying the resulting core–shell particles were calcined to burn off the core. The RSi were produced through hetero-aggregation of small particles onto the surface of a large core. Here we used a combination of particles of 150 nm and 8 nm in diameter. In a second step, a smoothing layer was applied to adjust the height of the asperities. The coverage of the RSi was determined by the number ratio of core and asperity particles. The roughness was controlled by adjusting the thickness of the smoothing layer, which also prevents the detachment of asperity particles. Here we applied a 5 nm thick smoothing layer. The synthesis routes to these particles are described in the literature for the HSi[42] and RSi,[25,28] while the SSi are the same as the large particles used in the first step of the two-step procedure leading to the RSi.

All colloids were suspended either in pure (Mili-Q grade) water which has an approximate electrolyte concentration of $c_S \approx 10^{-5}$ mol L^{-1} due to carbon dioxide absorption, corresponding to a Debye screening length of $\lambda_D^{-1} \approx 100$ nm. At larger electrolyte concentrations, all types of particles would aggregate inevitably. To exclude distortions and misinterpretation of evanescent wave DLS data by the formation of aggregates over the experiment duration and their preferred sedimentation, all samples were characterized by bulk DLS before and after the EWDLS experiments. In no case did we find variations of the hydrodynamic radius, beyond experimental error. Prior to DLS and EWDLS measurements, all sample solutions were centrifuged at 800 rpm for about 16 hours to spin down dust and potential aggregates as far as possible.

Table 1 Particle sizes and relative standard deviations determined by different methods. $\langle R_H \rangle$: hydrodynamic radius measured by DLS; $\langle R_G \rangle$, $\langle R \rangle_{SLS}$, $\langle R_C \rangle_{SLS}$: radius of gyration, particle outer radius and core radius determined by SLS; $\langle R \rangle_{TEM}$, $\langle R_C \rangle_{TEM}$: particle outer radius and core radius determined by electron microscopy. All size parameters are given in units of nm and relative standard deviations σ_{SLS}, σ_{TEM} refer to the line above them

Particle type	Smooth, full silica	Hollow silica	Rough silica
Acronym	SSi	HSi	RSi
$\langle R_H \rangle$	77	154	86
$\langle R_G \rangle$	55	(176)	74
$\langle R \rangle_{SLS}$	69	142	—
σ_{SLS}	0.05	0.02	—
$\langle R_C \rangle_{SLS}$	—	128	—
$\langle R \rangle_{TEM}$	65	142	65
σ_{TEM}	0.08	0.03	0.15
$\langle R_C \rangle_{TEM}$	—	132	—

The particle size parameters and their standard deviations measured with different methods are listed in Table 1.

2.2 Methods

2.2.1 Static and dynamic light scattering. Static (SLS) and dynamic (DLS) light-scattering experiments in bulk were performed on a commercial instrument by ALV-Laservertriebsgesellschaft (Langen, Germany), equipped with a 632.8 nm HeNe Laser as the light source, an automated attenuation system, a PerkinElmer avalanche diode and an ALV-6000 correlator. Static scattering intensities $I(Q)$ were obtained over an angular range from 16 to 150 degrees, by measuring diode count rates which were corrected for attenuation, and scattering volume. Experimental particle form factors, $P(Q)$ were determined by normalizing the scattered intensities with the intensity at zero angle which was obtained by extrapolation. Time auto-correlation functions of the scattered intensity $g_2(Q, t)$ were recorded in a range of scattering angles $20^\circ \leq \theta \leq 150^\circ$ in steps of five degrees. Here the scattering vector is $Q = 4\pi n_S \sin(\theta/2)/\lambda_0$ with the solvent refractive index, n_S, and the laser vacuum wavelength λ_0. To determine the particles' Stokes–Einstein diffusion coefficient, D_0, the initial slope of the correlation function $\Gamma = -D_0 Q^2$ was identified by a non-linear least squares fit to a stretched exponential and plotted *vs.* Q^2. The initial slope of this representation is $2D_0$. The particles' hydrodynamic radii, $\langle R_H \rangle$, were calculated *via* the Stokes–Einstein relation, $\langle R_H \rangle = k_B T/6\pi\eta\langle D_0 \rangle$ using $T = 293$ K and $\eta = 1.0$ mPa s for the solvent viscosity, where $k_B T$ is the thermal energy unit. It is understood that for polydisperse samples $\langle R_H \rangle$ is the *z*-average of the radius distribution and $\langle D_0 \rangle$ is the corresponding averaged diffusion coefficient.

2.2.2 Cryo transmission electron microscopy: cryo-TEM. Bright field TEM images were acquired on a ThermoFisher Tecnai Osiris TEM operated at 200 kV. Mean particle radii $\langle R \rangle_{TEM}$ and relative standard deviations σ were determined by averaging over 100 particles at minimum. Since conventional TEM images correspond to two-dimensional (2D) projections of three-dimensional (3D) objects, electron tomography in high angle annular dark field scanning transmission electron microscopy mode was performed to investigate the morphology of the colloidal particles.[43] A series of 2D projections was acquired

while tilting the specimen around an axis perpendicular to the electron beam over the range from −72 to 72 with an increment of 3 degrees. After cross correlation alignment, the 2D images were reconstructed by Expectation Maximization.[44]

2.3 Evanescent wave dynamic light scattering

2.3.1 EWDLS set-up. EWDLS experiments were performed with an instrument built in-house, based on a triple axis diffractometer by Huber Diffraktionstechnik, Rimsting, Germany, which has been described in detail elsewhere.[14] A frequency doubled Nd/Yag Laser (Excelsior; Spectra Physics) with a vacuum wavelength of λ_0 = 532 nm and a nominal power output of 300 mW is used as a light source. The scattering geometry and the definition of the scattering vector and its components parallel and normal to the interface are sketched in Fig. 1. The sample cell (custom-made by Hellma GmbH, Müllheim, Germany) consists of a hemispherical lens as the bottom part, made of SF10 glass, with an index of refraction n_1 = 1.736 at the used wavelength. The lens is covered by a hemispherical dome which contains the colloidal suspension. The incident beam is totally reflected at the flat wall surface of the hemisphere thereby creating an evanescent wave. The evanescent field extends into the particle suspension and is used as the illumination for the dynamic light scattering experiment. The evanescent wave has a wave vector $\mathbf{k}_e$ lying in the intersection of the interface and the plane spanned by incident and reflected beam. The scattering vector $\mathbf{Q} = \mathbf{k}_s - \mathbf{k}_e$, where the wave vector of the scattered light, $\mathbf{k}_s$, can be varied by changing the two angles θ and α_r which define the position of the detecting unit.

The reciprocal penetration depth of the evanescent field is determined by the angle of incidence α_i, the refractive index of the glass n_1 and that of the suspension n_2 as $\kappa/2 = 2\pi\sqrt{(n_1 \sin\alpha_i)^2 - n_2^2}\big/\lambda_0$. The magnitude of the scattering vector component parallel to the interface is given by

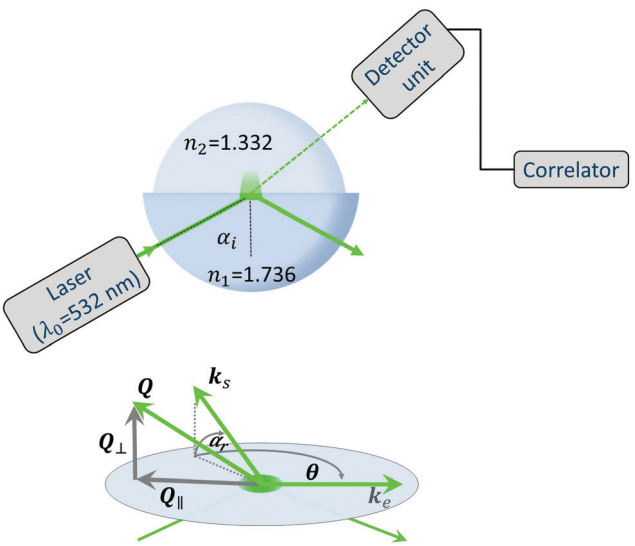

Fig. 1 Sketch of the scattering geometry of an EWDLS experiment with spherical symmetry.

$Q_\parallel = 2\pi n_2\sqrt{1+\cos^2\alpha_r - 2\cos\theta\cos\alpha_r}\big/\lambda_0$ while the normal component is $Q_\perp = 2\pi n_2 \sin\alpha_r/\lambda_0$. Here θ is the in-plane and α_r the off-plane angle defining the position of the detector unit with respect to the reflecting interface. The two scattering vector components can be varied independently of each other by changing θ and α_r. To determine the particle dynamics parallel to the interface at a given penetration depth, a series of correlation functions is recorded at a fixed α_r varying $Q_\parallel$ by changing θ. The initial slopes of the correlation functions Γ are determined by converting the experimental curves to field correlation functions, $g_1(t)$, and fitting their short time parts repeatedly with a single exponential starting from a manually chosen number of data points, N_p. When a single fit has converged, N_p is reduced by two and the remaining data are fitted again. With this procedure it is possible to identify a limited range of N_p's where the best fitting values are essentially independent of N_p.[14] The Γ-values from these ranges are plotted *versus* $Q_\parallel{}^2$ to yield a linear slope which according to eqn (6) is the diffusion coefficient parallel to the interface $\langle D_\parallel\rangle(\kappa)$. The latter is a function of the penetration depth, since the experiment integrates over the z-coordinate, normal to the interface, as indicated by the angle brackets. Examples of original correlation functions and data analysis are presented in the ESI.†

3 Model for numerical calculations

3.1 Near wall dynamics

Suspended particles close to a solid interface show slower Brownian dynamics than in bulk suspension due to hydrodynamic interaction with the wall. Approximations for the resulting friction coefficients in the low Reynolds number limit parallel and normal to the wall were published by Brenner and co-workers.[45,46] Although there are more accurate, but non-analytical expressions *e.g.* ref. 37, we use here the closed approximation to calculate the diffusion coefficient parallel to the wall

$$D_\parallel(z) = D_0\left[1 - \frac{9}{16}\frac{R}{z} + \frac{1}{8}\left(\frac{R}{z}\right)^3 - \frac{45}{256}\left(\frac{R}{z}\right)^4 - \frac{1}{16}\left(\frac{R}{z}\right)^5\right]. \quad (1)$$

For a sphere moving normal to the wall we replaced Brenner's infinite series[46] by the very good closed analytical approximation by Bevan *et al.*[47] to calculate the normal diffusion coefficient.

$$D_\perp(z) = D_0\frac{6z^2 - 10Rz + 4R^2}{6z^2 - 3Rz - R^2}, \quad (2)$$

where z is the shortest distance between the wall and the sphere centre. Since in the EWDLS experiment particles at different distances are illuminated with an exponentially decaying field strength, the experimentally determined diffusion constant is an average over z, weighted with the local field strength. For monodisperse spherical particles that do not experience static interactions with the wall except for excluded volume interactions (hard spheres), the averaged diffusion

constants are

$$\langle D_{\parallel,\perp}\rangle(\kappa) = \kappa\int_R^\infty \mathrm{d}z\, D_{\parallel,\perp}(z)\exp\{-\kappa(z-R)\}. \quad (3)$$

If the particles interact with the wall by a static potential $\Phi(z)$ their number density is not independent of z and the average in eqn (3) has to be additionally weighted by the local density, which is written as the Boltzmann factor of the potential *i.e.*

$$\langle D_{\parallel,\perp}\rangle(\kappa) = \frac{\int_R^\infty \mathrm{d}z\exp\{-\beta\Phi(z)\}\exp\{-\kappa z\}D_{\parallel,\perp}(z)}{\int_R^\infty \mathrm{d}z\exp\{-\beta\Phi(z)\}\exp\{-\kappa z\}}, \quad (4)$$

where $\beta = 1/k_BT$ is the reciprocal thermal energy unit. Under the conditions considered so far, the initial slope of the scattered field correlation function can be identified[14] as

$$\Gamma = \frac{\int_R^\infty \mathrm{d}z\exp\{-\beta\Phi(z)\}\exp\{-\kappa z\}\left[D_\parallel(z)Q_\parallel{}^2 + D_\perp(z)\left(Q_\perp{}^2+\kappa^2/4\right)\right]}{\int_R^\infty \mathrm{d}z\exp\{-\beta\Phi(z)\}\exp\{-\kappa z\}} \quad (5)$$

which results in the linear relation

$$\Gamma = \langle D_\parallel\rangle(\kappa)Q_\parallel{}^2 + \langle D_\perp\rangle(\kappa)\left(Q_\perp{}^2+\frac{\kappa^2}{4}\right) \quad (6)$$

with the definitions of diffusion coefficients averaged over the illumination profile given by eqn (4).

3.2 Particle–wall interactions

The interaction potential of the investigated particles with the adjacent glass wall is modelled as a superposition of three contributions,

$$\Phi(z) = \Phi_{\mathrm{vdW}}(z) + \Phi_{\mathrm{er}}(z) + \Phi_{\mathrm{g}}(z) \quad (7)$$

with the van der Waals attraction, $\Phi_{\mathrm{vdW}}(z)$, the electric double layer repulsion, $\Phi_{\mathrm{er}}(z)$, and a gravitational contribution $\Phi_{\mathrm{g}}(z)$ causing particle sedimentation.

The strength of the van der Waals attraction is given by the Hamaker constant, A_{H}, and the dependence on separation distance can be calculated for the sphere wall geometry[48] to yield

$$\Phi_{\mathrm{vdW}}(z) = -\frac{A_{\mathrm{H}}}{6}\left[\frac{R}{z-R}+\frac{R}{z+R}+\ln\left(\frac{z+R}{z-R}\right)\right]. \quad (8)$$

To model the electrostatic repulsion we exploited the linear superposition approach by Lin *et al.*[49]

$$\begin{aligned}\Phi_{\mathrm{er}}(z) &= B_{\mathrm{er}}[(\exp\{-\lambda_{\mathrm{D}}(z-R)\}+\exp\{-\lambda_{\mathrm{D}}(z+R)\})\\ &\quad+(R\lambda_{\mathrm{D}})^{-1}(\exp\{-\lambda_{\mathrm{D}}(z+R)\}-\exp\{-\lambda_{\mathrm{D}}(z-R)\})]\end{aligned} \quad (9)$$

where the amplitude B_{er} is related to the dielectric properties of the medium between the particle and wall and their surface potentials by

$$B_{\mathrm{er}} = 64\pi R\varepsilon\gamma_{\mathrm{p}}\gamma_{\mathrm{w}}\left(\frac{k_BT}{Ze}\right)^2$$

Here, $\varepsilon = \varepsilon_r\varepsilon_0$ where ε_0 is the vacuum permittivity and ε_r is the relative permittivity of the medium, Z is the valency of a single charged site (assumed to be $Z = 1$ in the following), e is the electron unit charge and $\gamma_{\mathrm{p,w}} = \tanh(Ze\Psi_{\mathrm{p,w}}/4k_BT)$ where $\Psi_{\mathrm{p,w}}$ is the surface potential of the particle and the wall, respectively. Since we have no means to assess the surface potential of the wall, we used an effective value $\gamma^2 = \gamma_{\mathrm{p}}\gamma_{\mathrm{w}}$.

The expression of Lin *et al.* is more accurate for the given sphere–wall geometry for all values of λ_DR than the expression which can be derived using Derjaguin's approximation. It is however worthwhile to note that the two expressions differ only by a constant in λ_DR. The ratio of the two expressions is given by $1 - 1/\lambda_DR + (1 + 1/\lambda_DR)\exp\{-2\lambda_DR\}$.

The gravitational contribution to the potential is determined by the buoyancy corrected particle mass

$$\Phi_{\mathrm{g}}(z) = \frac{4\pi}{3}R^3\Delta\rho_{\mathrm{m}}gz \quad (10)$$

where $\Delta\rho_{\mathrm{m}}$ is the particle excess mass density and g is the acceleration of gravity.

For all the calculated data presented in Sections 4.1.2 and 4.2 we replaced the particle radius by the hydrodynamic radius as determined by dynamic light scattering, since for the particles with surface roughness (RSi) a radius cannot be defined meaningfully.

3.3 Particle shape and polydispersity

If the investigated particles have a size distribution, $P(R)$, with a significant width, the expression for the initial slope of the correlation function becomes more complex than eqn (5). In this case the near wall form amplitude $B(Q, R)_{\mathrm{nw}}$ does not cancel from the expression for Γ as in the monodisperse case, and an integration over the size distribution of the numerator and denominator is required to obtain the expression for the size averaged initial slope

$$\langle\Gamma\rangle_{\mathrm{R}} = \frac{\int_0^\infty \mathrm{d}R B_{\mathrm{nw}}{}^2(Q,\kappa,R)P(R)\int_R^\infty \mathrm{d}z\exp\{-\beta\Phi(z)\}\exp\{-\kappa z\}D(Q,\kappa,R)}{\int_0^\infty \mathrm{d}R B_{\mathrm{nw}}{}^2(Q,\kappa,R)P(R)\int_R^\infty \mathrm{d}z\exp\{-\beta\Phi(z)\}\exp\{-\kappa z\}}, \quad (11)$$

where $D(Q, \kappa, R) = D_\parallel Q_\parallel{}^2 + D_\perp(Q_\perp{}^2 + \kappa^2/4)$. For our calculations we used a Gaussian normal distribution with mean value μ and relative standard deviation σ. It is important to note that eqn (11) cannot be strictly reduced to a linear relation similar to eqn (6).

Due to the exponential illumination profile, the form amplitude of a spherical particle cannot be written in a closed analytical form, it is rather given by

$$\begin{aligned}B_{\mathrm{nw}}(Q,\kappa,R) &= 2\pi R^3\left[\int_{-1}^1 \mathrm{d}\mu\int_0^1 \mathrm{d}y\, y^2\cos(Q_\perp y\mu R)\right.\\ &\quad\times\exp\left\{-\frac{y\mu\kappa R}{2}\right\}J_0\left(Q_\parallel\sqrt{1-\mu^2}yR\right)\\ &\quad+i\int_0^1 \mathrm{d}y\, y^2\sin(Q_\perp y\mu R)\\ &\quad\left.\times\exp\left\{-\frac{y\mu\kappa R}{2}\right\}J_0\left(Q_\parallel\sqrt{1-\mu^2}yR\right)\right]\end{aligned} \quad (12)$$

where J_0 refers to the zero order Bessel-function of the first kind. For a spherical core–shell particle with a core radius, R_C, outer radius, R, and scattering length densities of the core, ρ_C, and of the shell, ρ_S, the form amplitude is given by

$$B_{nw}(Q_\parallel, Q_\perp, \kappa, R_C, R) = 2\pi R^3 \left(\int_{-1}^{1} d\mu \rho_C \left[\int_0^{\chi} dy\, y^2 \cos(Q_\perp y\mu R) \exp\left\{ -\frac{y\mu\kappa R}{2} \right\} J_0\left(Q_\parallel \sqrt{1-\mu^2}\, yR \right) + i \int_0^{\chi} dy\, y^2 \sin(Q_\perp y\mu R) \exp\left\{ -\frac{y\mu\kappa R}{2} \right\} J_0\left(Q_\parallel \sqrt{1-\mu^2}\, yR \right) \right] + \rho_S \left[\int_{\chi}^{1} dy\, y^2 \cos(Q_\perp y\mu R) \exp\left\{ -\frac{y\mu\kappa R}{2} \right\} J_0\left(Q_\parallel \sqrt{1-\mu^2}\, yR \right) + i \int_{\chi}^{1} dy\, y^2 \sin(Q_\perp y\mu R) \exp\left\{ -\frac{y\mu\kappa R}{2} \right\} J_0\left(Q_\parallel \sqrt{1-\mu^2}\, yR \right) \right] \right) \quad (13)$$

where $\chi = R_C/R$. Details of the derivations are given in the ESI.† For the rough particles we could not derive a general expression for the form amplitude. For the limiting case of the particle size being very large compared to the size of the asperities and the asperities being randomly distributed on the particle surface, the form amplitude can be approximated by that of a spherical core particle plus a shell with the scattering length density of the asperities and an effective thickness which is very small compared to the wavelength.

4 Results and discussion

4.1 Experimental findings

4.1.1 Particle characterisation. A thorough characterisation of the used particles was done applying simultaneous static and dynamic light scattering as well as electron microscopy experiments. TEM micrographs and 3D-reconstruction from TEM tomography are shown in Fig. 2 for the RSi and the SSi particles together with TEM and REM images of HSi shells.

From the 3-D reconstructions, it is evident that SSi particles are, although not perfectly, to a good approximation spherical. The RSi particles consist of spherical main bodies carrying asperities on their surface which are irregularly distributed but approximately equal in height. TEM and SEM images from the HSi particles indicate a perfectly spherical shape and a narrow distribution of radii and shell thicknesses. The geometrical parameters and their relative standard deviation are listed in Table 1 together with the results from light scattering measurements. In all cases we observed that the hydrodynamic radius, $\langle R_H \rangle$, is larger than the radius measured in TEM, $\langle R \rangle_{TEM}$. For the rough particles this is intuitively understood, as the TEM radius is that of the central spherical body, which is identical with the SSi radius. The hydrodynamic radius is expected to be larger since the asperities will contribute to the hydrodynamic drag, additionally. In the case of SSi and HSi the discrepancy is explained in part by the fact that the two methods measure different averages of the size distribution. For a Gaussian distribution the ratio of both quantities is related to the relative standard deviation σ by $\langle R_H \rangle / \langle R \rangle_{TEM} = (1 + 3\sigma^2)/(1 + \sigma^2)$, since TEM measures the number average and DLS the z-average of a size distribution. However, for the SSi sample this would account only for about a two percent discrepancy, based on the relative standard deviation observed in TEM. For the HSi sample the expected difference is even smaller. Most likely the discrepancy is explained by the presence of a small fraction of aggregates. In the case of HSi the presence of aggregates with a hydrodynamic radius of $2 \times \langle R \rangle_{TEM}$, the same relative standard deviation as the main population and a relative volume fraction of 5% would account for the deviation.

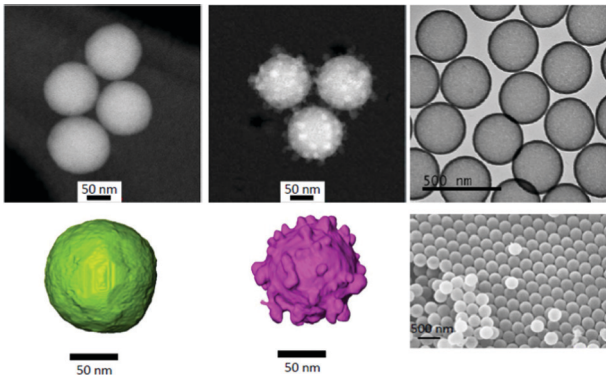

Fig. 2 Micrographs and 3D-reconstructions of SSi (left) and RSI (middle) particles. TEM and REM images of HSi are shown on the right. Scale bars are 50 nm in the left and middle panels and 500 nm in the right column.

The electron microscopy and DLS findings were further underpinned by static light scattering measurements. The radius of gyration, $\langle R_G \rangle$, for the three particle types listed in Table 1 were obtained from Guinier extrapolations. For the HSi particles the ratio $\rho = \langle R_G \rangle / \langle R_H \rangle = 0.71$, which is about ten percent smaller than the expected value for a perfect sphere of $\sqrt{3/5}$. While for the RSi particles we found an intermediate value of $\rho = 0.86$, the value for HSi $\rho = 0.91$, which is about ten percent smaller than expected for an infinitely thin shell. Although these ratios appear reasonable, it has to be noted that the particles sizes (in particular for HSi) are beyond the limits where Guinier's approximation can be safely applied and the values for $\langle R_G \rangle$ should be taken with care. More detailed information can be obtained from the SLS data by analysing the particle form factor. In Fig. 3 we present the experimentally determined $P(Q)$ *vs.* Q data for the SSi and HSi. While the SSi form factor is featureless, the data from the HSi particles show a distinct minimum around $Q \approx 0.022$ nm^{-1}. Non-linear least squares fitting with the form factor for polydisperse spheres and spherical shells[50] resulted in values for radius, shell thickness and relative standard deviations, which are in very good agreement with the TEM data.

4.1.2 EWDLS-data. The experimental findings from evanescent wave DLS are collected in Fig. 4 where we plot the diffusion constants parallel to the interface for the three particle types normalized by their respective bulk diffusion constant as a function of the evanescent wave penetration depth normalized by the bulk hydrodynamic radius.

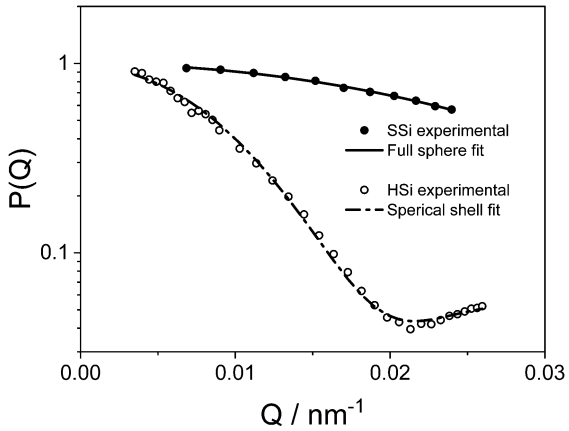

Fig. 3 Particle form factors from static light scattering data of SSi and HSi. Symbols are the experimental data and the lines are non linear least squares fits with the form factor for polydisperse spheres and spherical shells respectively.

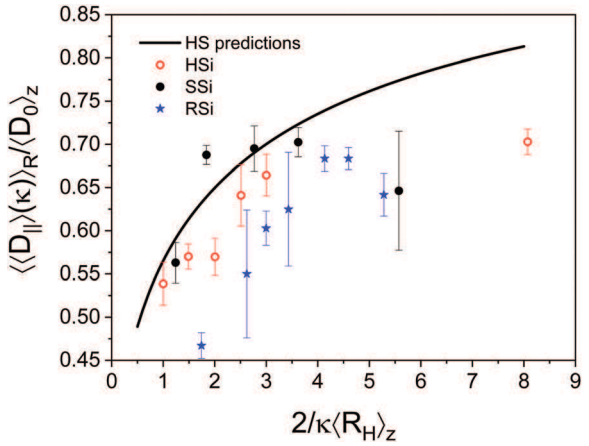

Fig. 4 Normalized parallel diffusion coefficients *versus* normalized penetration depth for three types of particles as indicated in the legend. The symbols are the experimental data and the error bars represent standard deviations from three consecutive experiments. The full line is the prediction for hard sphere particles according to ref. 46.

The data from the SSi particles may be considered to agree, except for one outlier at high penetration depth, with the theoretical reference curve for hard spheres (HS)[46] within experimental scatter. The HSi data are systematically, though not much, smaller than the HS-prediction, while the RSi particles show a significantly slower near wall diffusion than hard sphere particles. While the HSi data follow the trend of the HS-predictions at a somewhat lower level, the RSi data show a qualitatively different behaviour. Except for the outlier at the highest penetration depth, the gradient of the experimental data is always larger than that predicted for the reference system. It is tempting to assign this observation to the particle shape, *i.e.* the surface roughness. However, hydrodynamic theory predicts that surface roughness will reduce the wall drag effect as compared to smooth spherical particles with the same hydrodynamic radius.[37–39]

An alternative interpretation is based on the static interaction between the particles and the glass surface. The theoretical prediction for the near-wall dynamics of hard sphere particles shown in Fig. 4 is based on the assumption that the particle number density, $n(z)$, is constant throughout the entire sample down to the wall. This assumption is invalid, if static interactions other than the excluded volume are effective, as the density depends on the potential by Boltzmann's law. The effect of a DLVO interaction potential plus a gravitational contribution between monodisperse spheres and the wall on $n(z)$ is demonstrated in Fig. 5 for particles with 100 nm radius and fixed Hamaker constant $A_H = 0.5k_BT$. For $B_{er} > A_H$ the near surface region is significantly depleted of particles up to a range of about three particle radii, while an enrichment of particles occurs, if B_{er} is of the order of or smaller than the Hamaker constant. Since the near wall diffusion coefficient increases with separation distance according to eqn (1) it is expected that the experimental values for $\langle D_{\parallel}\rangle(\kappa)/D_0$ are larger than those predicted for hard spheres, if the static interaction with the wall is mainly repulsive and *vice versa*. We will discuss this effect quantitatively in Section 4.2.

It is worth noting that the gravitational contribution to the interaction potential (*i.e.* sedimentation) causes a shallow (secondary) minimum in the potential, which causes a small (secondary) maximum in the particle density distribution. However, for the particle sizes and density mismatches considered here, the effect of sedimentation on the particle dynamics is negligible as compared to the DLVO interactions.

There are two further effects which might cause the observed deviations of our experimental dynamic data from the hard sphere prediction, *i.e.* particle polydispersity and the resulting influence of the particle form amplitude on the experimental $\langle\Gamma\rangle$-values according to eqn (11) and particle aggregation in combination with enhanced sedimentation of the aggregates. Both effects will also be analysed in detail in Section 4.2.

4.2 Numerical calculations

4.2.1 Polydispersity and form amplitudes. For polydisperse systems the particle form amplitudes do not cancel from the expression for the initial slope of the time correlation function

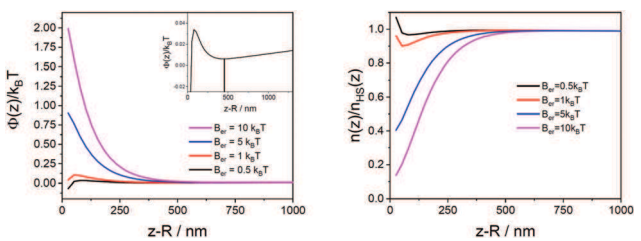

Fig. 5 Left: Sphere-wall interaction potentials calculated with eqn (7) for R = 100 nm, $A_H = 0.5k_BT$, $\lambda_D^{-1} \approx 100$ nm, $\Delta\rho_m = 1$ g mL^{-1} and amplitudes of the electrostatic repulsion B_{er} as indicated in the legend. The inset highlights the shallow minimum, marked by the vertical line for the potential with $B_{er} = 0.5k_BT$ which is due to the gravitational contribution. Right: Particle number densities normalized by the value for hard spheres *versus* separation distance, calculated with Boltzmann's law, using the potentials shown in the left panel.

(eqn (11)). If the particles are large enough to cause a strong variation of the scattered field with the scattering angles, significant deviations from the linear $\langle\Gamma\rangle_R$ *vs.* $Q_\parallel{}^2$ relation will occur, as is shown in the inset of Fig. 6, where the subscript R indicates integration over the distribution of particle sizes. This would lead to artefacts, if eqn (6) was applied to determine $\langle D_\parallel\rangle$ (κ) over the full range of scattering vectors. However, for $Q_\parallel R \ll 1$ the linear relation may still be used to determine a mean diffusion coefficient, $\langle\langle D_\parallel\rangle(\kappa)\rangle_R$. Resulting normalized data, calculated using eqn (1), (2), (6), (11) and (13) for a system of hollow shell particles with constant shell thickness and a Gaussian distribution of the outer radius are shown in Fig. 6. The number average outer particle radius, μ, and the shell thickness were chosen to roughly match the HSi particle size determined by TEM. To warrant comparability with the experimental EWDLS data, the calculated data have to be normalized by the z-average of the radius $\langle R\rangle_z$ and the corresponding diffusion coefficient $\langle D_0\rangle_z$, since light scattering experiments measure these quantities.

In all calculations concerning polydisperse or aggregating (Section 4.2.2) systems a density mismatch of $\Delta\rho_m = 1$ g mL^{-1} was incorporated to consider the enhanced sedimentation of larger particles. At low penetration depths systematic deviations from the prediction for monodisperse hard spheres towards slower dynamics are observed. However, the deviation is smaller than typical experimental scatter. Only at the largest polydispersity, and high penetration depths a significant deviation towards faster diffusion coefficients occurs. Similarly small effects are observed for spherical particles, where generally, the effect of polydispersity becomes larger with decreasing particle size, which is shown in the ESI.†

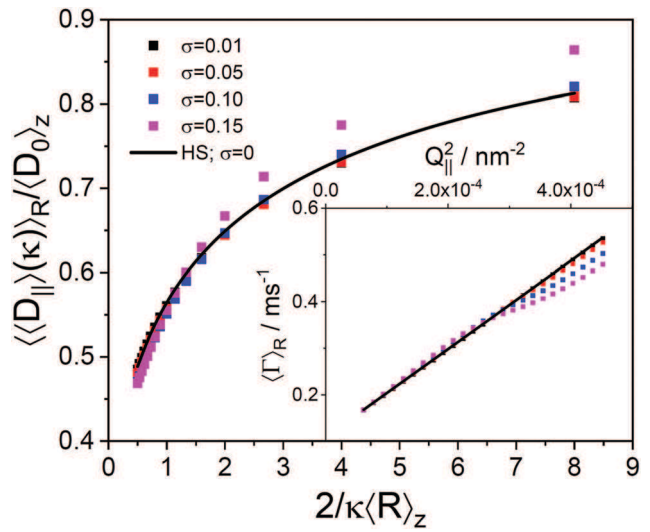

Fig. 6 Normalized parallel diffusion coefficients *versus* normalized penetration depth for hollow shells interacting only by excluded volume, with a constant shell thickness of 20 nm and a Gaussian distribution of the outer radius with μ = 150 nm and relative standard variations as indicated in the legend. Inset: Dependence of the initial relaxation rate on $Q_\parallel{}^2$. Symbols are the data calculated using eqn (1), (2), (6), (11) and (13). The full line is the prediction for monodisperse hard sphere particles according to Brenner.[46]

An analytical expression for $B(Q)$ of rough particles is in general not available. However, assuming that the asperities are small compared to the overall particle size, their average separation distance is small compared to the laser wavelength and they are randomly distributed, the form amplitude can be approximated by that of a spherical core particle plus a thin shell with the scattering length density of the asperities and an effective thickness which is very small compared to the reciprocal scattering vector. We may therefore assume that the effect of form amplitude and polydispersity is similarly small as observed for spheres and spherical shells.

4.2.2 Particle aggregation. As we realized that the three particle types, which we investigated experimentally, had a high tendency to form irreversible aggregates at salt concentrations as low as 0.1 mM, we tested what effect the presence of aggregates and their enhanced sedimentation would have on the near-wall dynamics. To simply mimic the aggregates, we used a bimodal Gaussian size distribution and the form amplitude of spheres to calculate initial slopes with eqn (11). The distribution of the population representing the aggregates is characterized by the mean μ_{agg} which was chosen to be an integer multifold of μ and the relative standard deviation $\sigma_{agg} = \sigma$. Furthermore, the relative volume fraction of the aggregates was varied over a range of $10^{-4} \leq \phi_{agg} \leq 0.05$. Larger volume fractions were not considered, since they would have been detected in the bulk DLS experiments, which were performed after the EWDLS measurements. Similar to the observations on the effect of polydispersity, we found that the linear dependence of $\langle\Gamma\rangle$ on $Q_\parallel{}^2$ is violated by the presence of aggregates, nevertheless it is possible to determine the near wall diffusion coefficient from the linear slope at sufficiently low $Q_\parallel$.

Calculated data of the normalized diffusion coefficients *vs.* normalized penetration depth are shown in Fig. 7 for a system consisting of a major population with μ = 100 nm and minor populations with μ_{agg} varying up to 1000 nm and ϕ_{agg} = 0.05 (left panel). Obviously, the presence of aggregates causes a strong slowing down of the system's near wall dynamics, even if the average hydrodynamic radius of the aggregates is only twice the size of the single particles. Data for this size ratio and varying relative volume fraction of the minor population is shown in the right panel of Fig. 7. The dynamics of the system with $\mu_{agg} = 2\mu$ and $\phi_{agg} \approx 0.03$ shows a similar deviation from the monodisperse reference system as the experimental HSi data. However, in all cases the calculated data show a smaller gradient than the reference systems which is clearly different from the trend of the experimental RSi data.

4.2.3 Static particle–wall interaction. The effect of static particle wall interactions on the near wall dynamics is demonstrated in Fig. 8 for spherical particles and selected interaction potentials. In the left panel, we plot the dynamic data for the interaction potentials shown in Fig. 5. At a typical Hamakaer constant of $A_H = 0.5k_BT$, the dynamics are slower than that of the reference hard sphere system at small penetration depths. At high penetration depths, the calculated data approach the hard sphere data for low electrostatic repulsion and the dynamics become even faster,

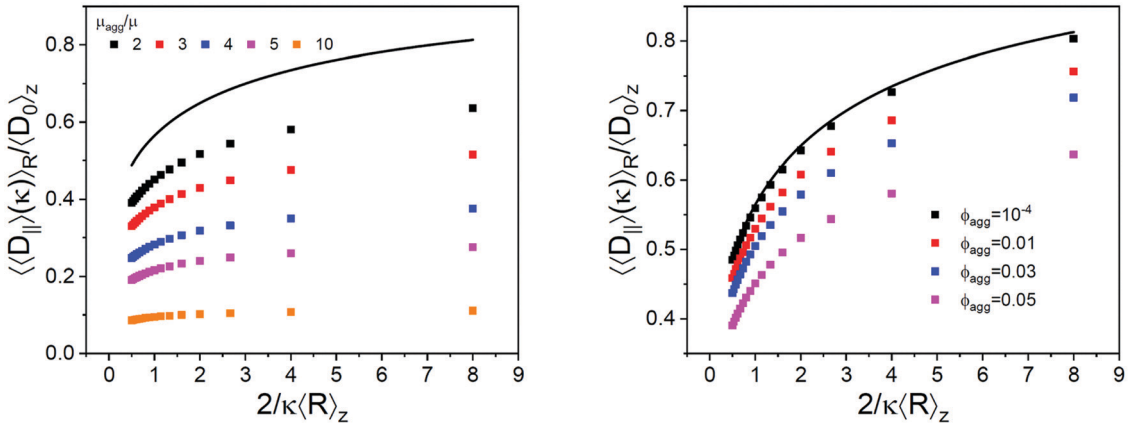

Fig. 7 Normalized parallel diffusion coefficients *versus* normalized penetration depth for systems of spheres with a bimodal Gaussian size distribution. The major population has a number average size of μ = 100 nm and both populations have a relative standard deviation of σ = 0.05. Left panel: The minor population has a relative volume fraction of ϕ_{agg} = 0.05 and their mean size μ_{agg} is varied as indicated in the legend. Right panel: The minor population has a number average size of $\mu_{agg} = 2\mu$ and varying relative volume fractions as indicated in the legend. Symbols are the data calculated using eqn (1), (2), (6), (11) and (12). The full line is the prediction for monodisperse hard sphere particles according to Brenner.[46]

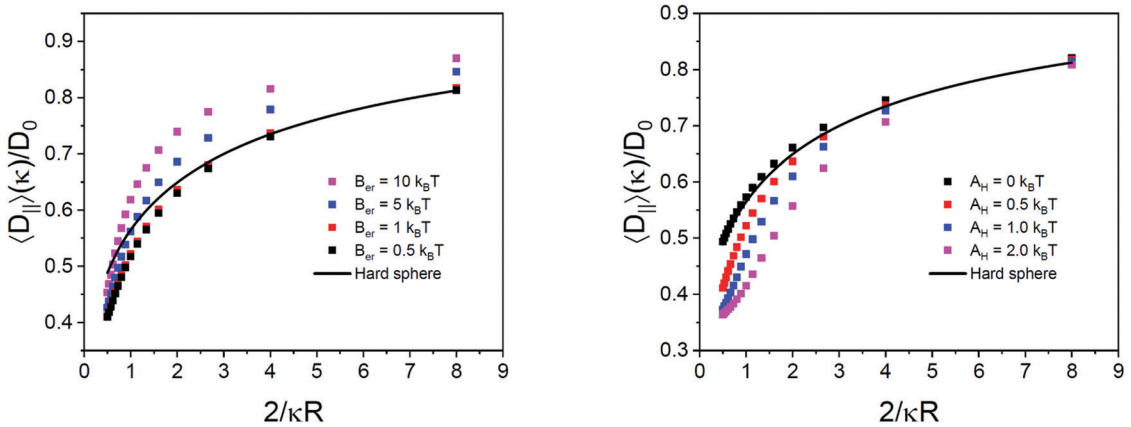

Fig. 8 Normalized parallel near wall diffusion coefficients *versus* normalized penetration depth for spherical particles interacting with the wall by the potentials displayed in Fig. 5 (left) and with $B_{er} = 1k_BT$ (right) and varying Hamaker constants as indicated in the legend. In all cases the excess mass density was chosen $\Delta\rho_m$ = 1 g mL^{-1}. Symbols are data calculated using eqn (1), (2), (6), (11) and (12). The full line represents the prediction for the hard sphere reference system according to Brenner.[46]

if the amplitude of the electrostatic repulsion significantly exceeds the Hamaker constant. The penetration depth at which the crossover of the calculated data with the reference data occurs shifts to smaller penetration depths with increasing electrostatic repulsion.

In the right panel of Fig. 8 we show the influence of varying Hamaker constants at a constant moderate electrostatic repulsion on the near-wall dynamics. At finite Hamaker constants, the calculated values are slower than those of the reference system, for almost all penetration depths. Only at the largest penetration depth investigated, the calculated dynamics appear to converge towards the reference data. At Hamaker constants $A_H \geq B_{er}$ the calculated data deviate from the reference data similarly to the experimental data of the RSi system.

4.2.4 Comparison of experimental EWDLS data with the calculated data. In Fig. 9 we show the experimental EWDLS result from Fig. 4 again, together with sets of calculated dynamic data, which match the measured data within the experimental scatter. The data were calculated with eqn (1), (2), (6), and (11) and the near wall form amplitude of spherical particles. Eqn (12) is a reasonable approximation, since the influence of the form amplitude together with polydispersity is minor as discussed in Section 4.2.1. Additionally we applied a bimodal size distribution to mimic the effect of a small fraction of aggregates, which were assumed to have the double size of the monomeric sphere and the same polydispersity. The parameters used for the calculations are listed in Table 2 and in all cases we applied an excess mass density of $\Delta\rho_m$ = 1 g mL^{-1} and a Debye screening length of λ_D^{-1} = 96 nm. Furthermore, the particles mimicking aggregates were subject to the same interaction potential as the monomers.

For the SSi- and HSi-system we could obtain a reasonable match of calculated with experimental data using an amplitude of the electrostatic repulsion of the order of k_BT and some

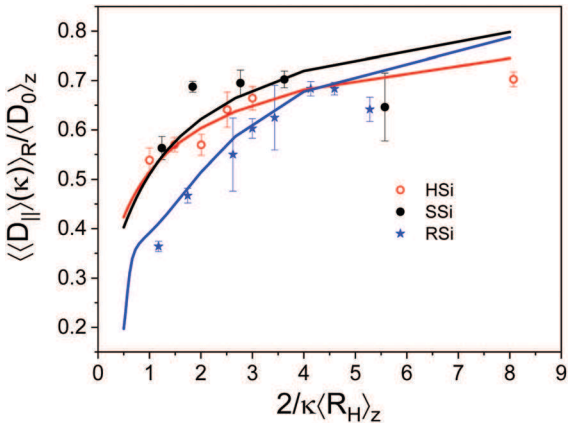

Fig. 9 Normalized parallel diffusion coefficients *versus* normalized penetration depth. Symbols are experimental data from the SSi-, the HSi- and the RSi-system, as indicated in the legend. Full lines represent data calculated using eqn (1), (2), (6), (11) and (12) and the parameters listed in Table 2.

Table 2 System parameters used to calculate the dynamic data shown in Fig. 9

Particle type	$\langle R_H\rangle_z$ (nm)	σ	B_{er} (k_BT)	A_H (k_BT)	ϕ_{agg}
SSi	71	0.05	1.5	0.5	5×10^{-3}
HSi	154	0.05	1.0	0.25	0.03
RSi	80	0.05	1.5	2.75	5×10^{-3}

fraction of k_BT for the Hamaker constant. The electrostatic amplitude of the particle–wall interaction corresponds to an effective surface potential $\Psi_{p,w} \approx -2$ mV which is about an order of magnitude smaller than that reported in the literature[51–53] based on total reflection microscopy measurements of the interaction potential between 2 μm Stöber–Silica particles and fused silica microscopy slides. Similarly, the ζ-potentials of all three systems are in the range of −30 to −40 mV. However it is important to note that the value of B_{er} is determined by the product of the particle's and wall's surface potentials. In the present case, the wall consists of a special high refractive index quartz glass (SF10) and there are indications in the literature that the surface charge density of quartz may[54] be one to two orders of magnitude lower than that of silica.[55] We therefore reckon that the small value of B_{er} is due to the low surface potential of the wall. Finally, the B_{er}-values for all three systems investigated here are about equal, which makes us confident that they are reliable. The found Hamaker constants of order $A_H \leq k_BT$ are in the range expected for non-retarded van der Waals interactions calculated based on the Lifshitz theory[56] for silica interacting with quartz across water.

In the case of the HSi-system, we had to allow for a higher relative volume fraction of "aggregates" to obtain a satisfying match of the calculated data with experiments. This is probably due to the fact that HSi particles were calcined and thus dried during synthesis to remove the organic core onto which the silica shell had been grown.[42] The probability of aggregates, which were not properly dispersed, being present is therefore higher than in samples which were never dried. Furthermore, spinning down aggregates is less effective than with full body particles due to the reduced excess mass density.

The most striking finding is, however, that for the RSi-particles the Hamaker constant required to allow for a match of calculated with experimental data is an order of magnitude larger than for the HSi- and SSi-systems. This implies that surface roughness plays an important role for the particle wall interaction and the resulting near wall dynamics. It is known from simulation work that surface roughness will enhance both electrostatic repulsion and van der Waals attraction, simply because the effective surface to surface separation is reduced by asperities. Walz *et al.* reported a lowering of the stabilisation barrier of the resulting DLVO-potential by about 10 to 15%, due to the different distance dependence of attraction and repulsion.[31] A similar reduction of the stabilization barrier was reported by Bhattacharjee *et al.*[30] Furthermore, these authors observe that the primary minimum of the DLVO interaction potential completely vanishes due to asperities. This might explain why our rough particles do not stick irreversibly to the glass surface, despite the large Hamaker constant. In this respect our findings may be regarded as additional experimental evidence for the predicted roughness effects on DLVO interaction energies. The resulting deviation of the dynamic data from the predictions for the reference hard sphere system are a mere consequence of the particle wall interaction potential and the resulting variation of number density with separation distance over which EWDLS inherently integrates.

Our findings might pave the way to a new method for the measurement of static particle wall interactions. Although the technique, especially the data analysis by comparison to model calculations, is cumbersome and not very efficient at this time, it might provide an extension of the classical total internal reflection microscopy (TIRM) technique.[57] While TIRM requires particle sizes which are typically in the range of several micrometres, EWDLS allows measurements on particles as small as 30 nm in radius.[14]

5 Conclusions

The Brownian near wall dynamics of different types of suspended silica particles were examined by evanescent dynamic light scattering. While the experimental averaged diffusion coefficients parallel to the wall for smooth full spheres (SSi) and hollow spherical porous shells (HSi) might be considered to be in qualitative agreement with theoretical predictions for the hard sphere reference system, particles with a rough surface (RSi) show significant deviations. The averaged diffusion constants are significantly smaller than for smooth non-interacting particles which is in conflict with hydrodynamic theory.[37–39] To interpret these observations, systematic numerical calculations were performed to investigate the effect of particle polydispersity, the presence of aggregates and static particle–wall interactions on the dynamics. By comparison with experimental data we found that

for the SSi and HSi systems very good agreement can be obtained by including a small fraction of aggregates and a particle–wall DLVO interaction, with a Hamaker constant and an amplitude of the electric double layer repulsion, both in the range of $\approx k_BT$. For the RSi system, at least a five times higher Hamaker constant needs to be taken into account to match the calculated data to the experimental results. Despite the high Hamaker constant the rough particles do not adsorb to the wall irreversibly. Both findings are consistent with the simulation results, which show that the DLVO stabilization barrier is significantly reduced by surface roughness[31] and that the primary DLVO minimum completely vanishes for rough particles.[30] We conclude that particle near wall dynamics are very sensitive to surface roughness where the theoretically predicted reduction of the flow resistance can be largely overcompensated by the effect of static particle wall interaction and the resulting particle number density profile.

Author contributions

J. Alejandro Rivera-Morán: investigation, formal analysis, writing – review and editing; Yi Liu: investigation, formal analysis, validation, writing – review and editing; Samuel Monter: investigation, formal analysis, software, validation, writing – review and editing; Chiao-Peng Hsu: resources, writing – review and editing; Pia Ruckdeschel: resources; Markus Retsch: resources, writing – review and editing; Maciej Lisicki: funding acquisition, conceptualization, writing – review and editing; Peter R. Lang: conceptualization, funding acquisition, software, supervision, writing – original draft.

Conflicts of interest

There are no conflicts to declare.

Acknowledgements

We thank Sara Bals, Qiongyang Chen and Hans Vanrompay from EMAT at the University of Antwerp for the TEM-investigation of the SSi and RSi particles and we gratefully acknowledge helpful discussions with Jan Dhont, Gerhard Nägele and Gunwoo Park from Forschungszentrum Jülich GmbH, IBI-4. This work has received funding from the European Union's Horizon 2020 research and innovation programme under grant agreement No 731019 (EUSMI).

Notes and references

1 H. A. Lorentz, *Abhandlung über Theoretische Physik: Ein allgemeiner Satz, die Bewegung einer reibenden Flüssigkeit betreffend, nebst einigen Anwendungen desselben*, B.G. Teubner, Leipzig and Berlin, 1907.
2 H. Faxén, *Ark. Mat. Astron. Fys.*, 1923, **17**, 1.
3 Z. Adamczyk, M. Adamczyk and T. van de Ven, *J. Colloid Interface Sci.*, 1983, **96**, 204–213.
4 K. H. Lan, N. Ostrowsky and D. Sornette, *Phys. Rev. Lett.*, 1986, **57**, 17–20.
5 B. Lin, J. Yu and S. A. Rice, *Colloids Surf., A*, 2000, **174**, 121–131.
6 B. H. Lin, J. Yu and S. A. Rice, *Phys. Rev. E: Stat. Phys., Plasmas, Fluids, Relat. Interdiscip. Top.*, 2000, **62**, 3909–3919.
7 H. B. Eral, F. Mugele and M. H. G. Duits, *Langmuir*, 2011, **27**, 12297–12303.
8 J. Y. Walz and L. Suresh, *J. Chem. Phys.*, 1995, **103**, 10714–10725.
9 L. Joly, C. Ybert and L. Bocquet, *Phys. Rev. Lett.*, 2006, **96**, 046101.
10 M. Hosoda, K. Sakai and K. Takagi, *Phys. Rev. E: Stat. Phys., Plasmas, Fluids, Relat. Interdiscip. Top.*, 1998, **58**, 6275–6280.
11 M. I. Feitosa and O. N. Mesquita, *Phys. Rev. A: At., Mol., Opt. Phys.*, 1991, **44**, 6677–6685.
12 N. Garnier and N. Ostrowsky, *J. Phys. II*, 1991, **1**, 1221–1232.
13 P. Holmqvist, J. K. G. Dhont and P. R. Lang, *Phys. Rev. E: Stat., Nonlinear, Soft Matter Phys.*, 2006, **74**, 021402.
14 P. Holmqvist, J. K. G. Dhont and P. R. Lang, *J. Chem. Phys.*, 2007, **126**, 044707.
15 M. Lisicki, B. Cichocki, J. K. G. Dhont and P. R. Lang, *J. Chem. Phys.*, 2012, **136**, 204704.
16 M. Lisicki, B. Cichocki, S. A. Rogers, J. K. G. Dhont and P. R. Lang, *Soft Matter*, 2014, **10**, 4312–4323.
17 Y. Liu, J. Blawzdziewicz, B. Cichocki, J. K. G. Dhont, M. Lisicki, E. Wajnryb, Y.-N. Young and P. R. Lang, *Soft Matter*, 2015, **11**, 7316–7327.
18 Y. Liu, N. Claes, B. Trepka, S. Bals and P. R. Lang, *Soft Matter*, 2016, **12**, 8485–8494.
19 V. N. Michailidou, G. Petekidis, J. W. Swan and J. F. Brady, *Phys. Rev. Lett.*, 2009, **102**, 068302.
20 V. N. Michailidou, J. W. Swan, J. F. Brady and G. Petekidis, *J. Chem. Phys.*, 2013, **139**, 164905.
21 D. Grasso, K. Subramaniam, M. Butkus, K. Strevett and J. Bergendahl, *Rev. Environ. Sci. Biotechnol.*, 2002, **1**, 17–38.
22 D. Kleshchanok, R. Tuinier and P. R. Lang, *Smart Colloidal Mater.*, 2008, **20**, 073101.
23 Q. Li, U. Jonas, X. S. Zhao and M. Kappl, *Asia-Pac. J. Chem. Eng.*, 2008, **3**, 255–268.
24 V. Dahirel and M. Jardat, *Curr. Opin. Colloid Interface Sci.*, 2010, **15**, 2–7.
25 M. Zanini, C.-P. Hsu, T. Magrini, E. Marini and L. Isa, *Colloids Surf., A*, 2017, **532**, 116–124.
26 L. C. Hsiao, S. Jamali, E. Glynos, P. F. Green, R. G. Larson and M. J. Solomon, *Phys. Rev. Lett.*, 2017, **119**, 158001.
27 L. C. Hsiao and S. Pradeep, *Curr. Opin. Colloid Interface Sci.*, 2019, **43**, 94–112.
28 C.-P. Hsu, S. N. Ramakrishna, M. Zanini, N. D. Spencer and L. Isa, *Proc. Natl. Acad. Sci. U. S. A.*, 2018, **115**, 5117–5122.
29 D. Lootens, H. van Damme, Y. Hémar and P. Hébraud, *Phys. Rev. Lett.*, 2005, **95**, 268302.
30 S. Bhattacharjee, C.-H. Ko and M. Elimelech, *Langmuir*, 1998, **14**, 3365–3375.
31 J. Y. Walz, *Part. Surf.*, 2002, **7**, 151–169.

32 L. Suresh and J. Y. Walz, *J. Colloid Interface Sci.*, 1996, **183**, 199–213.
33 L. Suresh and J. Y. Walz, *J. Colloid Interface Sci.*, 1997, **196**, 177–190.
34 C. Jin, T. Glawdel, C. L. Ren and M. B. Emelko, *Sci. Rep.*, 2015, **5**, 17747.
35 N. J. Wagner and J. F. Brady, *Phys. Today*, 2009, **62**, 27–32.
36 B. Schroyen, C.-P. Hsu, L. Isa, P. van Puyvelde and J. Vermant, *Phys. Rev. Lett.*, 2019, **122**, 218001.
37 B. Cichocki and R. B. Jones, *Phys. A*, 1998, **258**, 273–302.
38 G. C. Abade, B. Cichocki, M. L. Ekiel-Jeżewska, G. Nägele and E. Wajnryb, *J. Chem. Phys.*, 2012, **136**, 104902.
39 J. Riest, T. Eckert, W. Richtering and G. Naegele, *Soft Matter*, 2015, **11**, 2821–2843.
40 C. Kunert, J. Harting and O. I. Vinogradova, *Phys. Rev. Lett.*, 2010, **105**, 016001.
41 O. I. Vinogradova and A. V. Belyaev, *J. Phys. Condens. Matter*, 2011, **23**, 184104.
42 P. Ruckdeschel, M. Dulle, T. Honold, S. Förster, M. Karg and M. Retsch, *Nano Res.*, 2016, **9**, 1366–1376.
43 P. A. Midgley and M. Weyland, *Ultramicroscopy*, 2003, **96**, 413–431.
44 T. K. Moon, *IEEE Signal Process. Mag.*, 1996, **13**, 47–60.
45 A. J. Goldman, R. G. Cox and H. Brenner, *Chem. Eng. Sci.*, 1967, **22**, 637–651.
46 H. Brenner, *Chem. Eng. Sci.*, 1961, **16**, 242–251.
47 M. A. Bevan and D. C. Prieve, *J. Chem. Phys.*, 2000, **113**, 1228–1236.
48 H. C. Hamaker, *Physica*, 1937, **4**, 1058–1072.
49 S. Lin and M. R. Wiesner, *Langmuir*, 2010, **26**, 16638–16641.
50 J. S. Pedersen, *Adv. Colloid Interface Sci.*, 1997, **70**, 171–210.
51 H.-J. Wu and M. A. Bevan, *Langmuir*, 2005, **21**, 1244–1254.
52 H.-J. Wu, T. O. Pangburn, R. E. Beckham and M. A. Bevan, *Langmuir*, 2005, **21**, 9879–9888.
53 T. D. Iracki, D. J. Beltran-Villegas, S. L. Eichmann and M. A. Bevan, *Langmuir*, 2010, **26**, 18710–18717.
54 X. Shen, A. E. Wang, R. M. Sankaran and D. J. Lacks, *J. Electrost.*, 2016, **82**, 11–16.
55 S. H. Behrens and D. G. Grier, *J. Chem. Phys.*, 2001, **115**, 6716–6721.
56 B. Lennart, *Adv. Colloid Interface Sci.*, 1997, **70**, 125–169.
57 D. C. Prieve, *Adv. Colloid Interface Sci.*, 1999, **82**, 93–125.